A Study of the Crystallographic, Magnetic and Electronic properties of selected ZrM_2- H systems

Laura Richard

A thesis submitted for the degree of

Doctor of Philosophy

University of Oxford

September 2010

Department of Inorganic Chemistry and Linacre College

TABLE OF CONTENTS

Chapter 1: Introduction **1**

1.1 A Brief Introduction to Intermetallic Hydrides 1

1.1.1 Thermodynamic Aspects of Hydride Formation 2

1.1.2 Crystal Chemistry of the Intermetallic Hydrides 4

1.1.3 Electronic and Magnetic Properties of the Intermetallic Hydrides 6

1.2 The ZrM_2 (M = V, Cr, Mn) alloys and their hydrides 7

1.2.1 The $ZrMn_{2+x}-$ H system 7

1.2.2 The ZrV_2- H system 10

1.2.3 The $ZrCr_2-$ H system 13

1.3 Objectives of the Thesis 16

Chapter 2: Characterisation and Synthetic Techniques **18**

2.1 Crystallographic Characterisation 18

2.1.1 Introduction to Crystallography 18

2.1.1.1 Phase transitions and superstructures 20

2.1.1.2 Principles of Diffraction 20

2.1.1.3 Reciprocal Space and the Ewald Sphere 21

2.1.1.4 Line Broadening and The Peak Profile 23

2.1.1.5 Peak Intensities 24

2.1.2 X-ray Powder Diffraction 26

2.1.2.1 Instrumentation 26

2.1.3 Neutron Powder Diffraction 29

2.1.3.1 Instrumentation 31

2.1.4 Rietveld Refinement Technique 32
2.1.4.1 The Rietveld Method 32
2.1.4.2 Computational details 33
2.2 Magnetic Characterisation 35
2.2.1 Introduction to Magnetism 35
2.2.1.1 Diamagnetism 36
2.2.1.2 Paramagnetism 36
2.2.1.3 Effect of Field and Temperature 37
2.2.2 Localised Moment Model 38
2.2.3 Magnetic Materials 39
2.2.3.1 Domains and Hysteresis 40
2.2.4 Néel Theory of Ferrimagnetism 42
2.2.5 Itinerant Electron Theory 44
2.2.6 Superconductivity and Magnetism 45
2.2.7 The Superconducting Quantum Interference Device (SQUID) 46
2.2.7.1 SQUID Measurements 46
2.2.8 Magnetic Crystal Structure 47
2.2.9 Computational Modelling 48
2.3 Electronic Characterisation 49
2.3.1 Introduction to Electronic and Dielectric Characterisation . 49
2.3.2 Cavity Perturbation Theory 50
2.3.3 The "Collapsed Cylinder" Model 53
2.3.4 Instrumentation 55
2.3.4.1 Model Development 57
2.4 Synthetic Techniques 60
2.4.1 Raw Materials 60
2.4.2 Handling of Air Sensitive Materials 60
2.4.3 Metallurgical Techniques 60
2.4.4 Annealing Methods 61

2.4.4.1 Sealed Evacuated Tubes 61
2.4.4.2 Flowing Gas Reaction 62
2.4.4.3 Anneal Regimes 62
2.4.5 Hydriding and Dehydriding Reactions 63
2.4.5.1 Instrumentation 63
2.4.5.2 Measurement Errors 65
2.4.5.3 Hydriding Reaction 66
2.4.5.4 Dehydriding Reaction 67
2.4.6 Other Experimental Methods 67

Chapter 3: Crystallographic, Magnetic and Electronic Properties of the $ZrMn_{2+x}$ system and its hydrides 69

3.1 Introduction and Scope 69
3.2 Synthesis of the $ZrMn_{2+x}$ alloys 70
3.3 Crystallographic Features of the $ZrMn_{2+x}$ alloys 71
3.3.1 Structure of the nearly stoichiometric $ZrMn_{2+x}$ alloy 71
3.3.2 Structure of the superstoichiometric $ZrMn_{2+x}$ alloys 73
3.3.3 Structure of the substoichiometric alloy 74
3.4 Synthesis of the $ZrMn_{2+x}$ hydrides ($-0.35 \leq x \leq 0.44$) and the dehydriding process 79
3.4.1 The hydriding process 79
3.4.2 Cycling and the dehydriding reaction 81
3.4.3 Influence of x on the hydriding and dehydriding properties . 83
3.5 Hydriding Thermodynamics of the $ZrMn_{2+x}H_3$ ($-0.35 \leq x \leq 0.31$) system 86
3.6 Crystallographic Features of the $ZrMn_{2+x}H_3$ ($-0.35 \leq x \leq 0.44$) hydrides 89
3.6.1 Structure of the nearly stoichiometric hydride $ZrMn_{2.06}H_3$ . . 90

3.6.2 Structure of the superstoichiometric $ZrMn_{2+x}H_3$ ($0.13 \leq x \leq 0.31$) hydrides 93
3.6.3 Structure of the substoichiometric hydride 97
3.7 Crystallographic Features of the cycled, dehydrided $ZrMn_{2+x}$ ($0.06 \leq x \leq 0.44$) materials 100
3.7.1 Structure of the nearly stoichiometric, dehydrided $ZrMn_{2.06}$. 100
3.7.2 Structure of the superstoichiometric $ZrMn_{2+x}$ ($0.13 \leq x \leq 0.44$) dehydrided materials 102
3.8 Effect of x on the crystallographic features of $ZrMn_{2+x}$ and $ZrMn_{2+x}H_3$ 104
3.8.1 The effect of x on structure when $x > 0$ 104
3.8.2 The effect of x on structure when $x < 0$ 108
3.8.3 Peak profile analysis of the $ZrMn_{2+x}$ system and its hydrides 109
3.9 Neutron Diffraction studies on $ZrMn_{2+x}D_y$ ($-0.35 \leq x \leq 0.13$, $y \approx 3$) 111
3.9.1 Refinement of the nuclear structure of $ZrMn_{2+x}D_y$ at 300 K 112
3.9.2 Refinement of the magnetic structure of $ZrMn_{2+x}D_y$ at 10 K 121
3.10 Magnetic behaviour and ordering in $ZrMn_{2+x}$ ($-0.35 \leq x \leq 0.44$) and its hydrides 122
3.10.1 Magnetism of nearly stoichiometric $ZrMn_{2.06}$ and its hydride 123
3.10.1.1 Proposed model for magnetic order in $ZrMn_{2.06}$ and $ZrMn_{2.06}H_3$ 131
3.10.2 Magnetism of the superstoichiometric $ZrMn_{2+x}-$ H ($0.13 \leq x \leq 0.44$) system 135
3.10.2.1 Proposed model for magnetic order in $ZrMn_{2+x}$ and $ZrMn_{2+x}H_3$ 150
3.10.3 Magnetism of the substoichiometric $ZrMn_{1.65}-$ H system . . 156
3.10.3.1 Proposed model for magnetic order in substoichiometric $ZrMn_{1.65}$ and its hydride 162
3.11 The Magnetic Crystal Structure of the $ZrMn_{2+x}-$ H system 164

3.12 Electronic and Dielectric Properties of $ZrMn_{2+x}$ ($-0.35 \leq x \leq 0.44$) and its hydrides . . . 175
3.12.1 Model Verification *via* Microwave Studies on nearly stoichiometric $ZrMn_{2.06}-$ H . . . 175
3.12.2 Microwave Studies on the $ZrMn_{2+x}-$ H ($-0.35 \leq x \leq 0.44$) series . . . 179
3.13 Summary and Conclusions . . . 184
3.14 Future Work . . . 189

Chapter 4: Crystallographic, Magnetic and Electronic Properties of ZrV_2 and its hydrides 191

4.1 Introduction and Scope . . . 191
4.2 Formation of the ZrV_2 alloy . . . 192
4.3 Crystallographic Features of the ZrV_2 alloy . . . 193
4.4 Synthesis of the ZrV_2 hydride and the dehydrided material . . . 195
4.4.1 Hydriding ZrV_2 . . . 195
4.4.2 Cycling and the Dehydriding Reaction . . . 196
4.5 Crystallographic Features of the ZrV_2- H hydrides . . . 199
4.5.1 Published Structures of ZrV_2H_x . . . 199
4.5.2 Structural study on the hydride of ZrV_2- H system . . . 203
4.6 Crystallographic Features of the cycled, dehydrided ZrV_2 . . . 208
4.7 Magnetic and Superconducting Behaviour in the ZrV_2- H system . 212
4.7.1 Magnetic behaviour of ZrV_2 and $ZrV_2H_{2.8}$ . . . 213
4.8 Electronic and Dielectric Properties of the ZrV_2- H system . . . 220
4.9 Summary and Conclusions . . . 225
4.10 Future Work . . . 228

Chapter 5: Crystallographic, Magnetic and Electronic Properties of $ZrCr_2$ and its hydrides 230

5.1 Introduction and Scope . . . 230

5.2 Formation of the $ZrCr_2$ alloy 231
5.3 Crystallographic Features of the $ZrCr_2$ alloy 232
5.3.1 Published structures of the $ZrCr_2$ intermetallic compound . 232
5.3.2 Structural study of the $ZrCr_2$ alloy 233
5.4 Synthesis of the $ZrCr_2$ hydride and the dehydrided material 235
5.4.1 Hydriding of $ZrCr_2$ 235
5.4.2 Cycling and the dehydriding reaction 237
5.5 Hydriding Thermodynamics of the $ZrCr_2-$ H system 239
5.6 Crystallographic Features of the $ZrCr_2H_x$ hydride 241
5.6.1 Published Structures of $ZrCr_2H_x$ 241
5.6.2 Structural study of the $ZrCr_2$ hydride 242
5.7 Crystallographic Features of the cycled, dehydrided $ZrCr_2$ 246
5.8 Magnetic and Superconducting Behaviour in the $ZrCr_2-$ H system . 249
5.8.1 Magnetic behaviour of $ZrCr_2$ and $ZrCr_2H_3$ 250
5.9 Electronic and Dielectric Properties of the $ZrCr_2-$ H system 258
5.10 Summary and Conclusions 264
5.11 Future Work 267

Chapter 6: Summary and Conclusions 269
6.1 Summary of the results obtained 269
6.2 General Conclusions 272

Bibliography 277

Appendix A: Supplemental Crystallographic, Thermodynamic and Magnetic Data for the $ZrMn_{2+x}-$ H systems 288
A.1 Supplemental Crystallographic Data 288
A.1.1 X-ray Diffraction Data for the $ZrMn_{2+x}$ (x = 0.13, 0.18, 0.31, 0.44) alloys 288

A.1.2 X-ray Diffraction Data for hydrided $ZrMn_{2+x}H_3$ ($x = 0.13$, 0.18, 0.31) 291
A.1.3 X-ray Diffraction Data for the cycled, dehydrided $ZrMn_{2+x}$ ($x = 0.13$, 0.18, 0.31, 0.44) materials 293
A.1.4 Neutron Diffraction Data for $ZrMn_{1.69}D_{2.63}$ 296
A.2 Supplemental Hydriding Thermodynamic Data 297
A.2.1 Hydriding Pressures and Temperatures across the $ZrMn_{2+x}-$ H ($x = -0.35$, 0.06, 0.13, 0.18, 0.31, 0.44) systems 297
A.3 Supplemental Magnetic Data 298
A.3.1 Inverse Susceptibility Data for the $ZrMn_{2+x}-$ H ($x = 0.13$, 0.18, 0.31, 0.44) systems 298
A.3.2 Magnetic Hysteresis of the $ZrMn_{2+x}-$ H ($x = 0.13$, 0.18, 0.44) systems 300

ACKNOWLEDGMENTS

Firstly, I owe thanks to my doctorate supervisor, Peter Edwards, for allowing me to carry out this work within his research group.

I am also grateful to the assistance of several senior members of the Edwards group: I owe thanks to Martin Jones, for reading this thesis in its entirety and providing feedback, and also for occasional guidance over the course of my D. Phil. I would also like to thank Simon Johnson and Matthew Lodge, for their willingness to demonstrate the use of various pieces of instrumentation and also for many fruitful discussions over the course of this thesis.

The other students within the Edwards group have also played their role in helping me to complete this work. I would like to thank both past and present members of the group for both companionship and useful scientific input.

Outside of the Edwards group, I would like to thank David Book and Alex Bevan at the University of Birmingham for their assistance with the arc-melting of the alloys prepared in this thesis. I also owe many thanks to Adrian Porch at Cardiff University for teaching me the use of the microwave resonator technique, and helping me to understand the theory behind it.

I am extremely grateful to the Clarendon Fund for the financial support they provided for the first three years of this doctorate work, and also the Canadian Centennial Scholarship Fund for partially funding my fourth year.

Finally, I would like to thank my family in Canada for the love and support that they have never ceased to give. I particularly want to thank my mother, for always believing in me - without her, this thesis could not have materialised.

And eternal gratitude to Dennis, for much love, friendship, and compassion.

Chapter 1

INTRODUCTION

> It is in our nature to travel into our past, hoping thereby to illuminate the darkness that bedevils the present. *Farley Mowat*

1.1 A Brief Introduction to Intermetallic Hydrides

Hydrogen reacts with almost every element in the periodic table in an enormous variety of fashions, often bringing about drastic changes [1]. Compounds of the elements with hydrogen can be generally pigeonholed into one of three groups: the saline or ionic hydrides, covalent compounds, and metal-hydrogen systems. The ionic hydrides are characterised by the presence of a distinct hydrogen anion H^-, stabilised by an electropositive metal cation; in contrast, compounds containing bonds between hydrogen and a second element in which the electron pairs are shared are defined as covalent [1]. A metal-hydrogen system is defined as containing a metal, hydrogen in a gaseous or condensed phase, and an interface in between these two [2].

The general description of metal-hydrogen systems can be subdivided to consider just the intermetallic compound-hydrogen systems, where an intermetallic compound AB_x is defined as an ordered, single-phase alloy with a different structure to either of the parent metals A or B and a stoichiometric (or near stoichiometric) elemental ratio [3].

The solution of hydrogen in intermetallic compounds characteristically occurs at the interstitial sites of the bulk metal, often with little change to the base

metal substructure, excepting a lattice expansion to accommodate the hydrogen [2]. The formation of a hydride phase can; however, strongly affect the host metal's electronic and magnetic properties: the addition of an extra proton and electron from the hydrogen, combined with the concomitant lattice expansion, strongly perturbs the phonon distribution and electronic structure of the system and can lead to metal-semiconductor transitions and the creation or destruction of magnetic order and superconductivity [2]. Cases of these hydrogen-induced transitions are numerous [4], where examples include La_2Ni_7, which transforms from an antiferromagnet to a Pauli paramagnet upon hydriding [5], and Hf_2Fe, a Pauli paramagnet which is converted to a ferromagnet on hydrogen absorption [6].

Despite the large number of intermetallic compound-hydrogen systems that have been studied, the provenance of the property changes that occur in these systems is not as well understood as for the saline and covalent hydrides [7]. The hydrogen-induced alterations in the intermetallic hydrides are interesting not just in regards to technological applications, but also on the level of fundamental research. The diverse action of hydrogen on intermetallic compounds provides a tool to study many of the key phenomena in solid state chemistry and physics – *e.g.* magnetism, conductivity, ordered and disordered structures, superconductivity, *etc.* – and determining how and why these states arise could contribute greatly to the body of academic knowledge [2].

1.1.1 Thermodynamic Aspects of Hydride Formation

Figure 1.1 illustrates the absorption of hydrogen over time for a typical intermetallic compound – *viz.* $ZrMn_2$ – at a temperature of 120°C and a constant rate of hydrogen addition of 15 sccm. This flow rate corresponds to an expected linear pressure increase of 0.22 bar/min; however, absorption of hydrogen by the sample decreases the rate at which pressure rises.

The interaction of hydrogen with an intermetallic compound generally begins by the formation of a solid solution phase at some favourable temperature and

pressure that is highly dependent on the nature of the intermetallic [8]. The concentration of hydrogen that dissolves in the metal is typically low, on the order of 0.5 H/ formula unit (f.u.) of the intermetallic, and increases concurrently with the hydrogen pressure: this is exemplified in the region labelled AB in Figure 1.1.

As the hydrogen pressure rises, the $H - H$ interaction becomes locally important and growth of the distinct hydride phase begins: region BC depicts the area in which the solid solution phase and the hydride phase coexist [8]. The length of the plateau in the two phase region characterises the amount of hydrogen reversibly absorbed by the intermetallic, whilst thermodynamic aspects of the $M - H$ interaction determine its slope [8]. Once the pure hydride phase has formed (point C) no further hydrogen is absorbed and the rate at which the hydrogen pressure rises returns to its nominal rate of 0.22 bar/min.

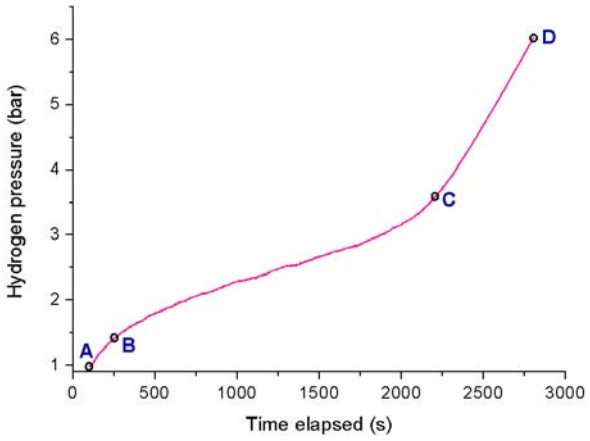

Figure 1.1: *Data from a hydriding cycle of $ZrMn_2$ at $120°C$, showing the change in hydrogen pressure over time for the course of the cycle. The point A indicates the start of the hydriding cycle, with 1 bar of hydrogen gas over the unhydrided alloy. Additional hydrogen was then added at a rate of 15 sccm and pressure in the sealed reaction chamber increased until line pressure (6 bar) was reached at point D.*

The metal-hydrogen system is naturally an equilibrium between the parent intermetallic compound, hydrogen gas, and the intermetallic hydride, and may be appropriately described by the hydriding enthalpy, ΔH [8]. Variations in pressure, p_H, and temperature, T_H, will alter the balance of this equilibrium, as the van't Hoff relationship shows [9]:

$$\ln p_H = \frac{-\Delta H}{RT_H} + \frac{\Delta S}{R} \tag{1.1}$$

Where a plot of $\ln p_H$ versus T_H^{-1} (a van't Hoff construction) should yield a

straight line with intercept equal to $\frac{-\Delta S}{R}$ and slope equal to $\frac{\Delta H}{R}$. A technologically important consequence of this equilibrium balance is that most intermetallic hydrides are reversible: that is, the hydrogen can be removed and the parent intermetallic returned *via* simple alteration of the environmental parameters [8].

The cycling of an intermetallic hydride through repeated hydrogen absorption and desorption cycles often leads to a reduction in particle sizes as a result of the lattice expansion and contraction that occurs concomitant to the hydriding and dehydriding processes; the strain induced by the hydrogen insertion and the inherent brittleness of intermetallic compounds may also play a role in this particle crumbling [3]. This hydrogen-induced particle disintegration is known as *decrepitation*, from the Latin *crepare*, meaning to crack or burst, and occurs to a varying extent across metal-hydrogen systems. After a suitable number of cycles, usually five to ten, the material is fully decrepitated and the hydriding process induces no further size reduction [3].

1.1.2 Crystal Chemistry of the Intermetallic Hydrides

Hydride-forming intermetallics have the general formula AB_n, where A is always an elemental capable of forming a binary hydride, and B is not so restricted; common metal atom ratios include AB, A_2B, AB_2, A_6B_{23}, AB_5 *etc.* [10]. The AB_2 intermetallics are of particular interest to the crystallographer due to their tendency to crystallise in one of three closely related structures known as Friauf-Laves or just *Laves phases* [11]. The Laves phases are tetrahedrally closed packed structures with an ideal atomic size ratio $r_a/r_b = \sqrt{\frac{3}{2}}$; the arrangement of the tetrahedra creates either a cubic C15 structure or one of two hexagonal structures, C14 and C36 [12]. Figure 1.2 shows the layered relationship of these structures and it can be readily discerned that the Laves phase polymorphs are interrelated *via* a simple series of displacements.

The electron concentration in the AB_2 system is an important factor in determining which Laves phase structure is adopted [13]. It has been shown [11] that

the electron concentration in transition metal Laves phases can be approximated by using the total number of valence electrons in the AB_2 system; under this estimation, the C14 phase is preferred for an electron total between 16 and 20, and, for a total between 11 and 13, the C15 phase is preferred. For the intermediate case of 14 or 15 valence electrons, the C15 phase is marginally more stable, but it can be expected that significant stacking faults will occur in these borderline cases during the course of crystallisation.

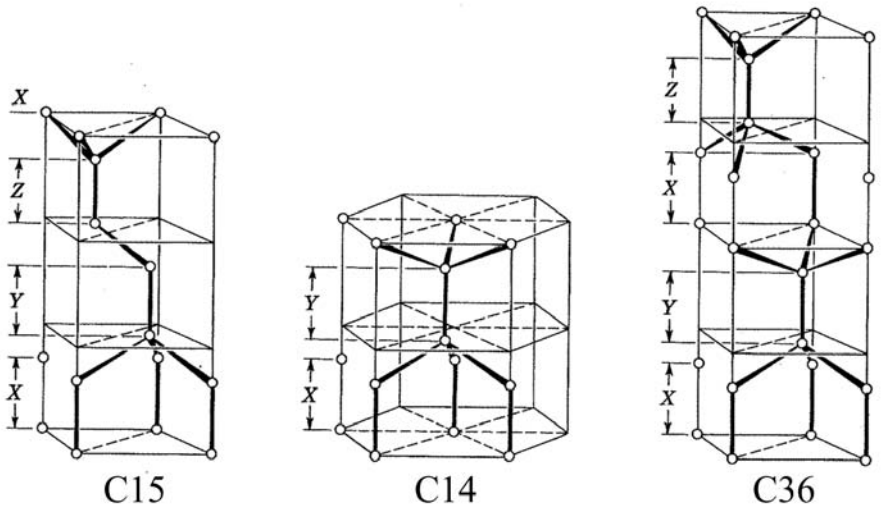

Figure 1.2: *A diagram showing the distribution of the A atoms and stacking of X, Y, and Z layers in the three Laves phase AB_2 structures. The B atoms are not shown for clarity. Figure from* [12].

In the C14 and C15 AB_2 intermetallics, there are 17 interstitial tetrahedral sites, per formula unit, which may be occupied by hydrogen [14]. These are composed of twelve *2A2B* sites (the interstice in the centre of a tetrahedron containing 2 A atoms and 2 B atoms), four *1A3B* sites, and one *4B* site [14]. The nature of the A and B atoms governs the hydrogen site preference: both the interstitial hole size, and the electronic structure of the compounds, are important factors [14]. The Westlake criteria [15] explain the discrepancy between the theoretical hydrogen capacity in these compounds (AB_2H_{17}) and the experimentally observed maximum capacities of 6 hydrogen atoms per formula unit [10]: *via* a geometrical

model, it was shown that there exists a minimum interstitial hole size of 0.4 Å and minimum distance between neighbouring hydrogen atoms of 2.1 Å, effectively limiting the capacity to $6\frac{1}{3}$ hydrogens per formula unit.

1.1.3 Electronic and Magnetic Properties of the Intermetallic Hydrides

When hydrogen enters a metal lattice, it contributes two states and one electron to the system, and electrons can either leave metal states to occupy those contributed by hydrogen – the anionic model [16] – or electrons from the hydrogen atoms can enter metal states – the proton model [16]. Both of these models are an oversimplification, and early band structure calculations by Switendick *et al.* [16] indicated that hydrogen most likely carries a partial charge in metal-hydrogen systems. More recent calculations by Smithson *et al.* [17] on the 3*d* binary dihydrides show that the addition of hydrogen to the metal inserts a low-lying band below the Fermi level, with significant H 1*s* character and an M 3*d* contribution from the formation of $M-H$ bonds. The width and position of these low lying bands is strongly dependent on the metal radius and the lattice constant, and furthermore varies as hydrogen is added to/removed from the hydride and the lattice parameters of the phase change [17] .

The consideration of magnetism adds additional complexity to the electronic structure of the metal-hydrogen systems, as the introduction of hydrogen to the metal lattice may affect the magnetism in several ways. Firstly, the lattice expansion induced in order to accommodate the hydrogen atoms may drastically alter the observed magnetism, as atomic moments are highly dependent on the local environment, *e.g.* changes in interatomic distances [4]. Secondly, the creation of a metal-hydrogen bonding interaction may result in an indirect exchange effect [4]. Thirdly, the change in Fermi level can strongly modify the magnetic interactions between the A and B atoms [4]. A recent DFT study on the C15 system YFe_2-H exemplifies this: Singh and Gupta [18] reported that the observed increase in magnetisation in the ferromagnetic YFe_2 upon hydriding to YFe_2H_4 resulted both

from the lattice expansion and from the hydrogen-induced distortions in the host metal band structure.

These findings suggest that construction of a general model of the hydrogen-metal interaction in intermetallic hydrides would be challenging —perhaps explaining why one does not yet exist. Moreover, this diversity complicates the prediction and explanation of the electronic and magnetic changes that occur concomitant to the hydriding process. Unfortunately, there exist few detailed studies into the role of hydrogen in the magnetism and electronic properties of Laves phase hydrides, despite the range of intriguing qualities they exhibit.

1.2 The ZrM_2 (M = V, Cr, Mn) alloys and their hydrides

1.2.1 The $ZrMn_{2+x}$– H system

Svechnikov and Petkov [19] were the first researchers to observe the hydrogen absorption properties of $ZrMn_2$; sparking a flurry of research into the $ZrMn_2$– H system. The intermetallic compound absorbs approximately 3.4 hydrogen atoms per formula unit with a plateau pressure of 0.03 bar at 80°C, and exhibits no tendency towards disproportionation upon repeated cycling [20].

$ZrMn_2$ crystallises in the C14 Laves phase structure, space group $P6_3/mmc$, with cell parameters as shown in Table 1.1 [21]. This metal substructure is preserved upon the addition of hydrogen: $ZrMn_2H_3$ retains the $P6_3/mmc$ space group, with an anisotropic lattice expansion in order to accommodate the hydrogen atoms [22]. The cell parameters of the hydride phase are also given in Table 1.1. Hydrogen atoms preferentially occupy the *2A2B* interstices which, due to the symmetry of the structure, are spread over four non-equivalent sites [23]. The occupancies of these sites are unequal as a consequence of the choice of hydrogen diffusion paths in the structure [23]; quasielastic neutron scattering has shown that the activation energy for long range hydrogen motion in $ZrMn_2H_3$ is one of the

lowest among the Laves phase hydrides and is coupled with a fast jump between pairs of closely spaced hydrogen sites [24].

The phase diagram of the binary alloy system is shown in Figure 1.3, where it can be immediately discerned that the C14 $ZrMn_2$ compound is not a line phase, and in fact exists over an extremely large homogeneity range. The exact width of this range is a matter of some dispute [25], with the most recently published phase diagram [26] stating that $ZrMn_{2+x}$ exists over the limits $-0.5 < x < 1.8$. The substoichiometric ($x < 0$) and superstoichiometric ($x > 0$) compounds retain the same C14 structure as the parent intermetallic compound, excepting a small lattice expansion and contraction, respectively [27, 28]. Density measurements coupled with structural studies have shown that the superstoichiometry is accomplished by the partial replacement of zirconium on the $4f$ site with manganese [22, 29]; however, the mechanism of the substoichiometry is not known. The non-stoichiometric $ZrMn_{2+x}$ intermetallics readily absorb hydrogen analogously to $ZrMn_2$, where the hydrides of the manganese deficient species are slightly more stable than $ZrMn_2H_3$, and the hydrides of the manganese excess species are slightly less stable [28].

The $ZrMn_2$ intermetallic compound has been reported to behave as a Pauli paramagnet down to 5 K [30]; however, theoretical studies [21, 31, 32] suggest that $ZrMn_2$ should be magnetically ordered at low temperatures. *Ab initio* calculations suggest a magnetostructural degeneracy in this system that has not yet been observed experimentally, possibly as a result of frustration of the magnetic moments [21]. The superstoichiometric $ZrMn_{2+x}$ compounds were also observed to behave as Pauli paramagnets [30]. Upon hydriding, the intermetallic compound transforms into a spin-glass magnet with $T_c = 143$ K for $ZrMn_2H_3$; the superstoichiometric hydrides exhibit a qualitatively similar magnetic ordering with a drop in T_c and increase in χ as the manganese content rises [30]. The magnetic behaviour of the substoichiometric compound and its hydride has not been studied.

Parameter	$ZrMn_2$ [21]	$ZrMn_2D_3$ [23]
a (Å)	5.0293(2)	5.391(3)
c (Å)	8.2669(3)	8.748(8)
V (Å^3)	181.087	220.18
Zr1, $4f$ site $(\frac{1}{3}, \frac{2}{3}, z)$	0.06340(5)	0.0661(8)
B_{eq} (Å^3)	0.64(2)	1.4
Mn1, $2a$ site $(0, 0, 0)$	-	-
B_{eq} (Å^3)	0.63(2)	1.4
Mn2, $6h$ site $(x, 2x, \frac{1}{4})$	0.83507(5)	0.8357(7)
B_{eq} (Å^3)	0.61(2)	1.4
D1 on $24l$ site (x, y, z)		0.042(2), 0.325(2), 0.562(1)
D1 occ.		0.179(4)
B_{eq} (Å^2)		1.4
D2 on $12k$ site $(x, 2x, z)$		0.456(1), 0.632(1)
D2 occ.		0.376(4)
B_{eq} (Å^2)		1.4
D3 on $6h$ site $(x, 2x, \frac{1}{4})$		0.463(2)
D3 occ.		0.312(1)
B_{eq} (Å^2)		1.4
D4 on $6h$ site $(x, 2x, \frac{1}{4})$		0.202(9)
D4 occ.		0.052(2)
B_{eq} (Å^3)		1.4

Table 1.1: *The room temperature structural parameters of the stoichiometric alloy $ZrMn_2$ and its deuteride $ZrMn_2D_3$, as reported in the published literature* [21, 23]. *Both phases crystallise in the $P6_3/mmc$ space group.*

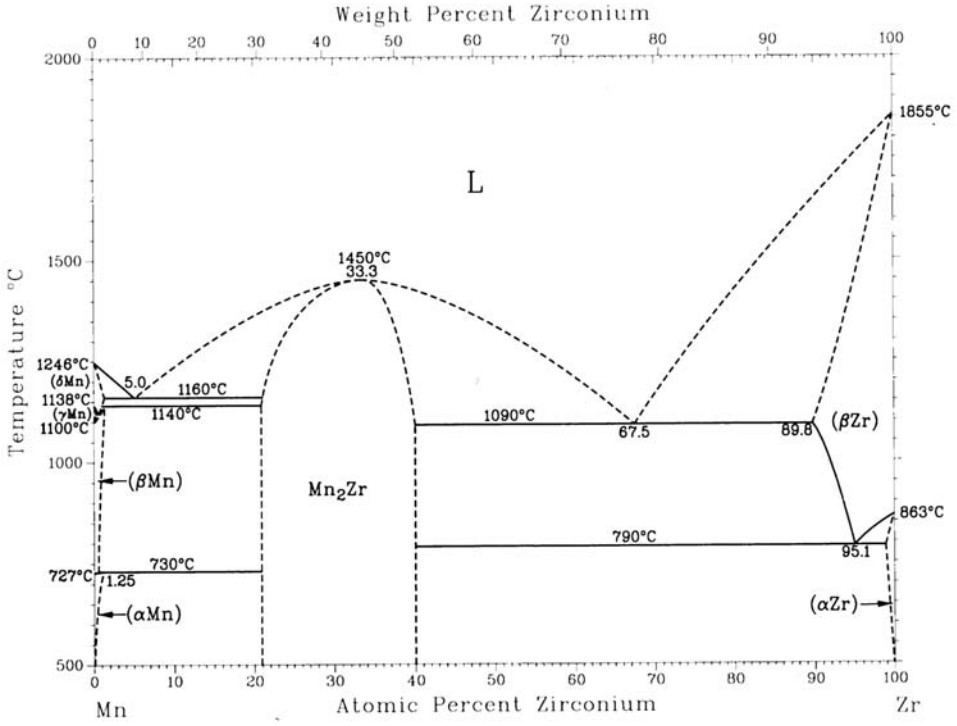

Figure 1.3: *The Zr-Mn binary phase diagram. Of particular interest is the $ZrMn_2$ intermetallic compound, which crystallises in the C14 Laves phase structure over a wide homogeniety range. Figure from* [26].

The nature of the magnetic ordering in the $ZrMn_{2+x}-$ H system remains a mystery. Measurement of the magnetic behaviour over a range of temperatures and fields suggest that the hydride is ferro- or ferrimagnetic, but the magnetic structure of this system is not known [30, 33, 34]. Although a low-temperature neutron diffraction study was carried out by Didisheim *et al.* [35] in attempt to elucidate the magnetic structure of $ZrMn_2D_3$, a full structural refinement could not be completed and these authors concluded that the magnetic structure was one of great complexity.

1.2.2 The ZrV_2- H system

Academic interest in the ZrV_2 Laves phase intermetallic compound was sparked by Matthias *et al.* [36] at Bell Laboratories when, in 1961, they observed its transition

to superconductivity below 8.8 K. Shortly thereafter, the hydrogen absorption properties of ZrV_2 were also revealed [37]: the hydride ZrV_2H_6 readily forms at very low hydrogen pressures, with a plateau pressure estimated to be less than 10^{-8} bar at 80°C [20].

As the binary Zr-V phase diagram in Figure 1.4 shows, ZrV_2 is the only intermetallic compound formed in this system, with relatively little variation from the line phase 2:1 atomic ratio [26]. ZrV_2 preferentially crystallises in the C15 Laves phase structure, with structural parameters as given in Table 1.2, but demonstrates significant lattice instabilities and may alternatively crystallise in the allotropic C14 structure if rapidly cooled from the eutectic melt [38, 39]. These lattice instabilities further result in a cubic-to-orthorhombic martensitic transition at $T_m = 116.7$ K [38].

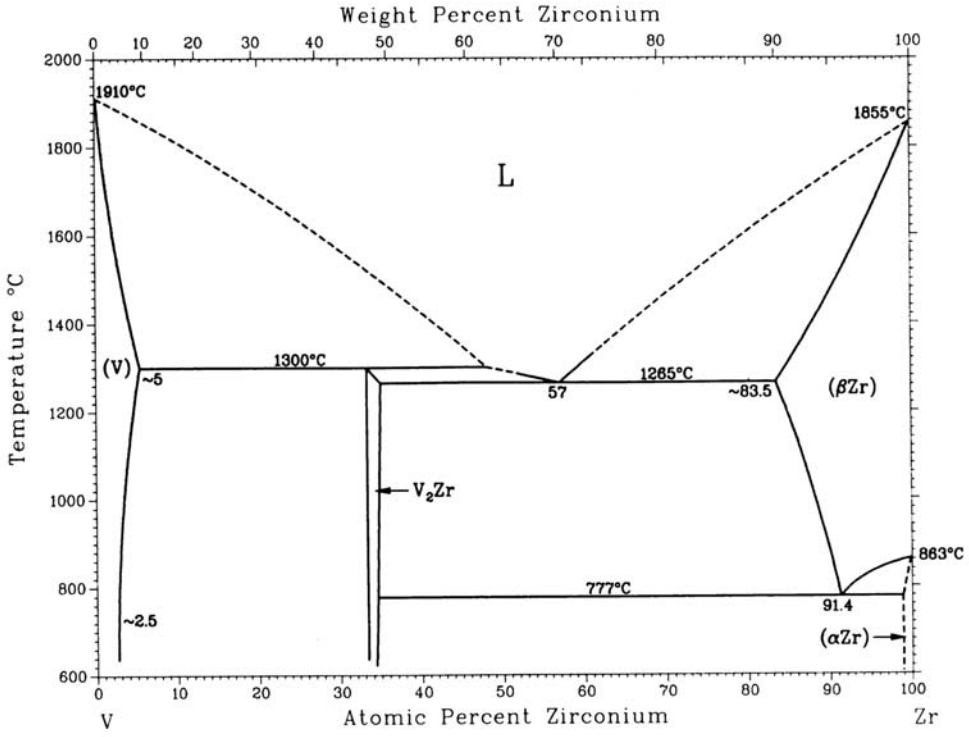

Figure 1.4: *The Zr-V binary phase diagram. Of particular interest is the ZrV_2 intermetallic compound, which crystallises in the C15 Laves phase structure over a narrow homogeniety range. Figure from* [26].

Parameter	ZrV_2 [38]	$ZrV_2D_{4.5}$ [40]
a (Å)	7.4414(5)	7.913(2)
V (Å^3)	412.063	495.47
Zr1, 8a site $(0,0,0)$	-	-
B_{eq} (Å^3)	0	0.89(9)
V1, 16d site $(\frac{5}{8},\frac{5}{8},\frac{5}{8})$	-	-
B_{eq} (Å^3)	0	0.89(9)
D1 on 96g site (x,x,z)		0.1859(3), 0.9993(5)
D1 occ.		0.249(4)
B_{eq} (Å^2)		0.89(9)
D2 on 32e site (x,x,x)		0.3989(2)
D2 occ.		0.387(4)
B_{eq} (Å^3)		0.89(9)

Table 1.2: *The room temperature structural parameters of the intermetallic compound ZrV_2 and its deuteride $ZrV_2D_{4.5}$, as reported in the published literature* [38, 40]. *Both phases crystallise in the $Fd\bar{3}m$ space group.*

Unlike the two-phase $ZrMn_2$−H system discussed earlier, hydrogen dissolves continuously as a solid solution in ZrV_2, up to a maximum of 6 hydrogen atoms per formula unit [37, 41]. At room temperature, the hydrogen behaves as a lattice gas and is distributed over the *2A2B* sites and *1A3B* sites in the C15 structure, causing a lattice expansion of the $Fd\bar{3}m$ unit cell but no other alterations to the base metal substructure [40]. The order in which these sites are occupied is dependent on the hydrogen concentration, which is in turn a factor of the temperature and pressure of the hydriding reaction [40]. Structural parameters of the disordered $ZrV_2D_{4.5}$ phase are given in Table 1.2.

At low temperatures, a complex series of hydrogen-ordered phases can form as hydrogen superstructures of lower lattice symmetry than the parent metal arise; the stability of these phases is factor of both the hydrogen concentration and the temperature. Four of these Lifshitz-type superstructures of ZrV_2H_x are known: $ZrV_2H_{1<x<2.2}$ with $k = (\frac{1}{2}, \frac{1}{2}, \frac{1}{2})$ [42], $ZrV_2H_{2.8\leq x<3.5}$ with the variable vector $k = (0, 0, 1-\delta)$ where $0 \leq \delta \leq 0.5$ [43],$ZrV_2H_{3.5<x<4}$ with $k = (0)$ [43], and $ZrV_2H_{5.6<x<6}$ with $k = (001)$ [41].

ZrV_2 is a type II superconductor with a high critical field of approximately 230 kOe [44]. The intermetallic compound possesses a particularly high density of states at the Fermi level, which decreases as the hydrogen content in the solid solution phase rises; as both materials are Pauli paramagnets, this corresponds to a hydrogen-induced reduction in χ [45]. A drop in the superconducting T_c readily occurs concomitant to the hydrogen absorption, such that at a concentration of $ZrV_2H_{1.3}$, susceptibility measurements suggest a low (less than 2 K) or vanishing T_c [45]. At higher hydrogen concentrations, ZrV_2H_x behave as a simple Pauli paramagnet down to 2 K [46].

1.2.3 The $ZrCr_2$– H system

The existence of the Laves phase $ZrCr_2$ has been known for over fifty years [47] and its polymorphism has been a matter of particular interest. As the Zr-Cr binary phase diagram in Figure 1.5 shows, the intermetallic $ZrCr_2$ is the only intermediate phase in this system and it can crystallise in any of the three Laves phase structures; although the C15 phase is the most stable structure at room temperature, the C14 and C36 phases can be readily obtained by rapidly cooling the eutectic melt [26]. As a result of this structural degeneracy, stacking faults can lead to the formation of metastable structures based on five- and nine-layer modifications of the parent Laves phase structures [48].

Both the hexagonal and the cubic allotropes of $ZrCr_2$ have been shown to absorb hydrogen to an equivalent extent, where the temperature and pressure of

hydride formation are independent of the structure type. Pebler and Gulbransen [37] showed that the C14 intermetallic compound absorbed 3.6 hydrogens per formula unit, with a plateau pressure of 0.09 bar at 98.7°C; similarly, Shaltiel *et al.* [20] demonstrated that the C15 polymorph absorbed 4 hydrogen atoms per $ZrCr_2$ unit with a plateau pressure of 0.05 bar at 80°C. In both cases, $ZrCr_2-H$ was observed to be a two phase system, forming the hydride $ZrCr_2H_3$, but at higher pressures additional hydrogen can be dissolved in the hydride phase, up to the concentration $ZrCr_2H_4$ [20, 37].

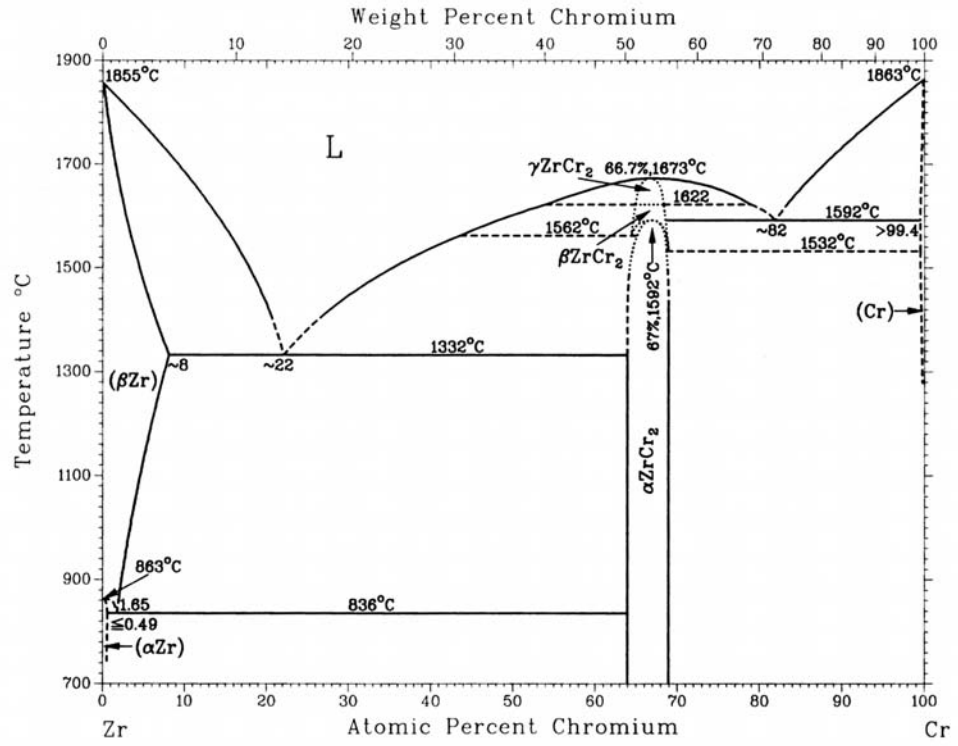

Figure 1.5: *The Zr-Cr binary phase diagram. Of particular interest is the* $ZrCr_2$ *intermetallic compound, which preferentially crystallises in the C15 Laves phase structure, but can be stabilised as the C14* ($\beta ZrCr_2$) *or the C36* ($\gamma ZrCr_2$) *polymorph. Figure from* [26].

Neutron diffraction studies of cubic $ZrCr_2D_{3.8}$ phase revealed that the C15 base metal substructure is retained upon the absorption of deuterium with a concomitant lattice expansion; deuterium preferentially occupies *2A2B* interstices, with

Parameter	$ZrCr_2$ [49]	$ZrCr_2D_{3.8}$ [49]
a (Å)	7.203(1)	7.6913(1)
V (Å^3)	373.72	454.98(1)
Zr1, 8a site $(0,0,0)$	-	-
B_{eq} (Å^3)	0	0.49(3)
Cr1, 16d site $(\frac{5}{8},\frac{5}{8},\frac{5}{8})$	-	-
B_{eq} (Å^3)	0	0.59(3)
D1 on 96g site (x,x,z)		0.1894(1), 0.9953(1)
D1 occ.		0.2844(4)
B_{eq} (Å^2)		1.11(4)
D2 on 32e site (x,x,x)		0.3434(5)
D2 occ.		0087(1)
B_{eq} (Å^3)		1.11(4)

Table 1.3: *The room temperature structural parameters of the C15 allotrope of the intermetallic compound $ZrCr_2$ and its deuteride $ZrCr_2D_{3.8}$, as reported in the published literature* [49]. *Both phases crystallise in the $Fd\bar{3}m$ space group.*

an additional small occupancy of the *1A3B* sites [49]. Moreover, $ZrCr_2D_{3.8}$ undergoes a low temperature order-disorder transition to form a monoclinic $C2/c$ modification at 250 K [49]. The full structural parameters of the room temperature deuteride, along with the parent C15 phase, are given in Table 1.3. Of further interest is the hydrogen mobility in the $ZrCr_2-$ H system: the fast localised motion of hydrogen enhances the hydrogen diffusivity down to anomalously low temperatures [50].

Both $ZrCr_2$ and its hydride are simple Pauli paramagnets down to 4.2 K, with

an observed three-fold susceptibility increase upon the addition of hydrogen [51]. Although the conductivity of $ZrCr_2$ and its hydride have not been previously investigated, a very recent theoretical study [52] on the hydrided C15 phase showed, *via* an *ab initio* calculation, that the electron associated with the hydrogen atoms remains bound to the proton: that is, the electron can be considered localised. This may have interesting implications for the influence of hydrogen on the electrical properties of the $ZrCr_2$ system, a topic which has yet to be explored experimentally.

1.3 Objectives of the Thesis

The objectives of this thesis are to:

- Synthesise the alloys ZrV_2, $ZrCr_2$ and $ZrMn_2$ and their corresponding hydrides. In the case of $ZrMn_{2+x}$, it will be desirable to synthesise a range of alloys with varying x and hydride them accordingly.

- Observe the thermodynamic aspects of how these intermetallic compounds interact with hydrogen, and comment on the capacity for hydrogen absorption, the temperature-pressure dependence of hydrogen absorption, and enthalpy and entropy of hydride formation.

- Describe the crystal structure of these intermetallic compounds and their hydrides at room temperature, and clarify the hydrogen-induced structural changes.

- Explore the magnetic behaviour of the intermetallic compounds and their hydrides across a range of temperatures and applied magnetic fields, in order to determine the effect of hydrogen on susceptibility and, where applicable, magnetic ordering. In the case of magnetically ordered structures, it will be interesting to examine the nature of the ordering and describe the magnetic crystal structure.

- Investigate the room-temperature dielectric and electronic properties of these intermetallic compounds and their hydrides, and, in particular, reveal the effect that hydrogen has on the conductivity of these intermetallic compounds.

The final objective of this thesis will be to comment on the crystallographic, magnetic, and electronic properties of the ZrM_2- H systems, where M = V, Cr, Mn, with a view towards constructing a general model of the effect that hydrogen has on these Laves phase intermetallic compounds.

Chapter 2

CHARACTERISATION AND SYNTHETIC TECHNIQUES

I shall be telling this with a sigh
Somewhere ages and ages hence:
Two roads diverged in a wood, and I—
I took the one less traveled by,
And that has made all the difference.
-Robert Frost, "The Road Not Taken" (Mountain Interval, 1920)

2.1 Crystallographic Characterisation

2.1.1 Introduction to Crystallography

The diffraction of X-rays and neutrons by crystalline materials is a powerful tool for answering a whole host of structural and magnetic questions. Crystalline materials are defined as solids which possess long-range order; an order that can be broken into translational repeats of a *unit cell*. The unit cell is described by parameters that outline its shape and dimensions (length of the sides a, b, c and the angles between them, α, β, γ) and the arrangement of the atoms within it (defined by atomic coordinates x, y, z). Alternately, the structure can be described as a *lattice*, composed of an infinite pattern of points on which an atom or a group of atoms can be located – only 14 distinct arrangements are possible, and these are called the Bravais lattices.

A lattice is further defined by the number and type of *symmetry elements* within it. The possible operators in three dimensions for a point are a mirror plane

m, rotation axes (1, 2, 3, 4, and 6 fold), inversion points $\bar{1}$, improper rotation axes $\bar{n}$, and the identity operator E. The collection of symmetry elements that operate on a point can be grouped into just 32 *point groups*, which when combined with the 14 Bravais lattices yield 73 *space groups*. Once translational symmetry elements are also included (screw axes and glide planes) a total of 230 distinct space groups are generated.

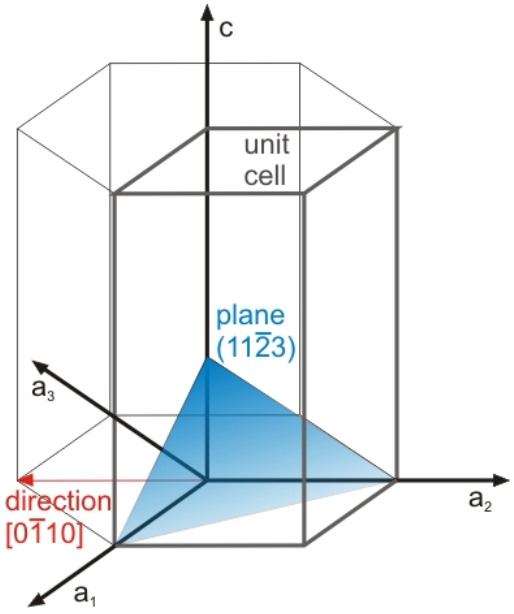

Figure 2.1: *The Miller-Bravais indexing system as used for hexagonal crystals, with four axises a_1, a_2, a_3, and c. Shown in blue is a plane described using this four index system. A vector in red demonstrates direction notation in this system.*

The ordered atomic arrangement of a crystal can be visualised as families of planes. A set of identical parallel planes can be described by *Miller indices* (hkl) where the values of h, k and l are reciprocals of the fractions of the unit cell edge a, b and c intersected by the plane. The interplanar spacing (also called the *d-spacing*) is given by d_{hkl}. Similarly, a set of parallel directions is given by $[uvw]$, where the indices u, v,and w describe a vector pointing from the unit cell origin in units of lattice cell repeats a, b, and c. These concepts are illustrated in Figure 2.2.

However, the Miller indices are ambiguous in the case of hexagonal crystals, as several sets of indices can often be given for identical planes. In this case a four axis coordinate system, a_1, a_2, a_3, and c can be used with four *Bravais-Miller indices* $(hkil)$, where h, k, and i are cyclically permutable – this is illustrated in Figure 2.1. Directions can also be specified with a four-index system using the Weber indicies $[u'v'tw']$. [53]

2.1.1.1 Phase transitions and superstructures

Phase transitions which occur with a change in the symmetry of the crystal structure are second-order transitions and can be understood on the basis of Landau's thermodynamic theory as detailed in [54]. Such a second-order transition may lead to the formation of a *superstructure*, where the unit cell of the new structure has dimensions superior to that of the parent unit cell, but retains a closely related structure [55]. If this 'superlattice' and the parent structure are then defined by two triplets of vectors defining the unit cells in these lattices, an appropriate matrix **Q** can be found which relates them:

$$\begin{pmatrix} a \\ b \\ c \end{pmatrix}_{\text{superlattice}} = \mathbf{Q} \begin{pmatrix} a \\ b \\ c \end{pmatrix}_{\text{parent lattice}} \tag{2.1}$$

where the nature of **Q** and its determinant describe the type of structural transition that occurs [55].

2.1.1.2 Principles of Diffraction

The regular atomic arrangement of a crystalline material can diffract a beam of radiation (with wavelength, λ, comparable to the atomic spacing) in a precise pattern due to its ordered nature. This is described by *Bragg's Law* (see Figure 2.2) which states that a beam of radiation impinging at angle θ on a set of planes with spacing d_{hkl} will only be diffracted if the following geometric condition is fulfilled [53]:

$$n\lambda = 2d_{hkl} \sin\theta \text{ where } n \in \mathbb{Z} \tag{2.2}$$

Although Bragg's Law defines the 2θ values at which radiation is diffracted, it does not give the intensity of the diffracted beam: to obtain this it is necessary to consider the scattering of all the atoms in the unit cell. This is described by the structure factor, $\mathbf{F}(hkl)$, for each hkl reflection, with direction given by the phase angle ϕ_{hkl} and magnitude $|\mathbf{F}(hkl)|$ proportional to the intensity of the

reflection. [56]

$$\mathbf{F}(hkl) = \sum_{n=1}^{N} f_n \exp[2\pi \cdot i(hx_n + ky_n + lz_n)] = |\mathbf{F}(hkl)|\, e^{i\phi_{hkl}} \tag{2.3}$$

The scattering power of each atom n in the unit cell is given by the form factor f_n, and the term $2\pi(hx_n + ky_n + lz_n)$ gives the phase of the diffracted wave from atom n at position x, y, z into the hkl plane. The f_n term is affected not only by the type of atom, but also by the nature of the radiation used and the angle of the diffracted beam. Relevant details on f_n for X-rays are given in Section 2.1.2 and for neutrons in Section 2.1.3.

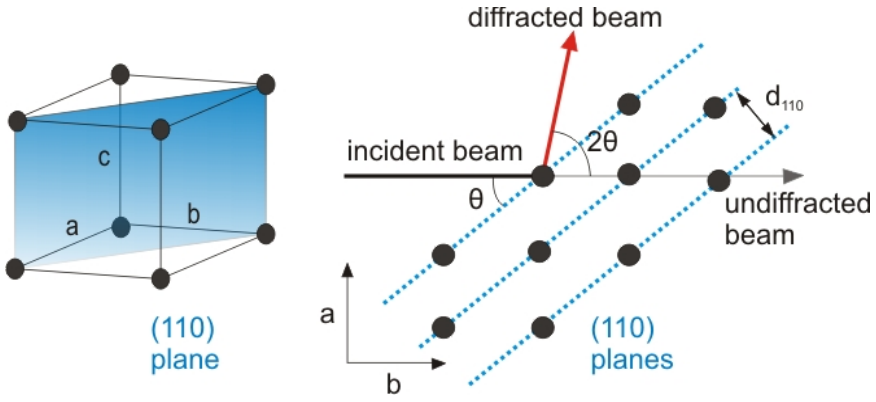

Figure 2.2: *On the left is shown a simple unit cell, with the (110) plane highlighted in blue. An 2D view of this crystal lattice is shown on the right, with the family of (110) planes illustrated and an incident beam diffracting off it in accordance with Bragg's Law.*

2.1.1.3 Reciprocal Space and the Ewald Sphere

The *reciprocal lattice* is a mathematical representation through which the principles of diffraction are more easily understood. This lattice is defined by basis vectors a^*, b^*, c^* and is related to the real space lattice parameters a, b, c and end faces *via*

$$a^* = \frac{1}{d_{100}} \qquad b^* = \frac{1}{d_{010}} \qquad c^* = \frac{1}{d_{001}} \tag{2.4}$$

It can be shown [56] that a family of planes (hkl) in a real space lattice corresponds to a row of reciprocal space lattice points of the same indices; furthermore, that the spacing of the reciprocal lattice points r^*_{hkl} is equal to the inverse of the real space lattice plane spacing d_{hkl}. This powerful relation, along with a geometrical construct called the *Ewald Sphere* can be used to visualise the diffraction process: if the reciprocal lattice and incident beam are sketched and a vector of length $\frac{1}{\lambda}$ is drawn from the origin in opposite direction, a sphere around this vector will intersect reciprocal lattice points in accordance with Bragg's Law. All points on the surface of this sphere are hkl reflections that will produce diffracted beams – this is illustrated in Figure 2.3. A screen placed in such a way as to intercept these diffracted beams will register a pattern of spots, where the size of the dots is equal to the intensity of the diffracted beam: a series of such images through various slices of the reciprocal lattice can be collated together to form a *diffraction pattern.* [53]

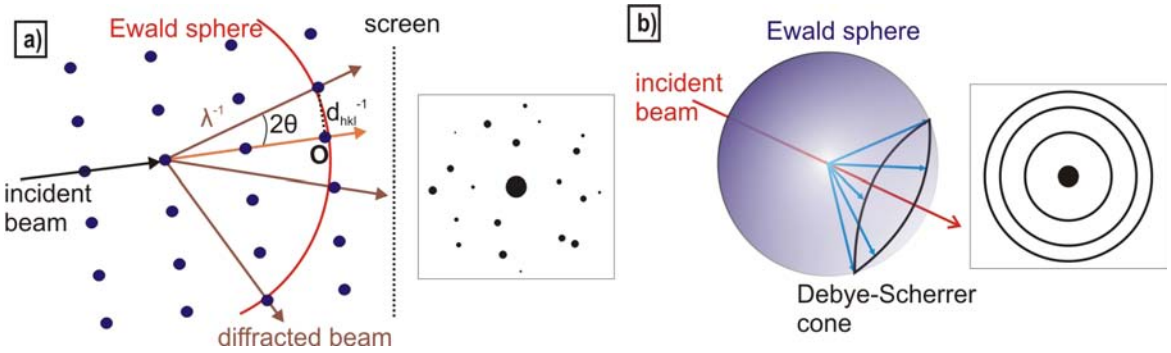

Figure 2.3: *On the left, a) illustrates the formation of an Ewald sphere by showing a 2D slice of a reciprocal lattice, and the image that would be formed if a screen was placed in front of the diffracted beams. The Ewald sphere and resulting Debye-Scherrer cone formed by a powder sample (and the resulting image that would be formed) is shown in b)*

In a material consisting of a collection of randomly oriented crystallites (such as a powder) each crystallite will produce its own Ewald sphere, also randomly oriented. Diffraction through these Ewald spheres will not produce a discrete

collection of spots, but rather rings, which arise from the *Debye-Scherrer cones* produced by the simultaneous irradiation of all families of hkl planes at every incident angle [53]. Figure 2.3 illustrates one such cone generated on the surface of an Ewald sphere; in reality, a set of concentric cones for each family of hkl planes would be generated. The two-dimensional nature of detectors means that all hkl reflections with the same d-spacing will appear at the same 2θ value – such an overlapped peak is said to have a multiplicity, p, which depends on the structure and the reflection in question [53].

2.1.1.4 Line Broadening and The Peak Profile

Equation 2.2 suggests that each hkl reflection will correspond to a discrete value of 2θ; however, Heisenburg's uncertainty principle shows that even in a single crystal a reflection will have a finite width [56]. Instrumental broadening and microstructural effects further increase the range of angles $\Delta\theta$ over which a reflection occurs [57]. If we also add in the collapse of the three-dimensional reciprocal lattice onto the 2θ axis for powdered samples, it is clear that the separation of the overlaid reflections will become very difficult. A *peak profile function* $H(2\theta)$ can deconvolute these factors by separating the sample profile function $f_{hkl}(2\theta)$ from the instrumental profile function $g(2\theta)$ [57]:

$$H_{hkl}(2\theta) = f_{hkl}(2\theta) * g(2\theta) \tag{2.5}$$

The instrumental line profile, which can be approximated by using samples relatively free of microstructural defects, varies continuously with 2θ and arises from factors relating the physical instrumentation (*e.g.* wavelength variation in the incident beam, geometry of source and detector alignment, slit width) [57]. The sample profile function adjusts for the fact that 'real structures' are not perfectly periodic and may contain defects, vacancies, strains, aberrations, *etc.* [58]. A full description of a real structure would require a large number of parameters; fortunately, the materials discussed in this thesis can be appropriately modelled just with the application of size and strain induced broadening terms.

Crystalline strain, ϵ, in a crystal represents the variation in d_{hkl} for a set of planes which may arise from lattice distortions due to internal stress distributions, dislocations, *etc.* This varies with 2θ as:

$$\Delta\theta = 4\epsilon \tan\theta \tag{2.6}$$

The strain is dependent on the order of reflection (*i.e.*, varies with hkl) and the broadening effect is more pronounced at higher angles [58]. The broadening effect of a finite crystallite size, D can be approximated as:

$$\Delta\theta \approx \frac{\lambda}{2D\cos\theta} \tag{2.7}$$

but the exact expression depends upon the crystal shape and is usually only significant for $D < 1\mu m$ [58]. Unlike strain, the size induced broadening is order-independent [58]. These differences allow the separation of size and strain induced broadening in powder diffraction data – the mathematics of deconvoluting these factors will be shown in Section 2.1.4.

2.1.1.5 Peak Intensities

The intensity, I, of a diffracted beam depends on the experimental conditions and the crystal structure:

$$I_{hkl} = sL\left|\mathbf{F}(hkl)\right|^2 PA \tag{2.8}$$

where s is the 'scale factor', accounting for the volume fraction of the phase in a multi-phase material as well as the multiplicity of the reflection, A is the absorption factor (a correction that accounts for the partial absorption of the incident beam by some materials), L is the Lorentz polarisation factor and the polarisation correction, and P accounts for any preferred orientation in polycrystalline samples. L is generally a θ-dependent function defined for a particular type of radiation and instrument, whereas $\mathbf{F}(hkl)$ (and in particular, the atomic form factor f_n included in this function) is subject to a number of material-dependent corrections. [58]

The most significant of these modifications is perhaps the thermal vibration correction, which accounts for the problem of atomic vibration at temperatures

greater than 0 K. This atomic displacement effectively smears the electron density of atom, leading to a decrease in the observed intensity; the stationary atomic form factor f_n can be suitably adjusted with the *Debye-Waller factor* B

$$f_{adjusted} = f_n \exp\left[-B\left(\frac{\sin\theta}{\lambda}\right)\right] \tag{2.9}$$

Clearly, the thermal motion of atoms in the crystal structure (and the observed decrease in I) is more significant at higher diffracted beam angles. B is numerically related to the mean displacement of the atom from its normal crystallographic site, $\langle \bar{r}^2 \rangle$, *via*

$$B = 8\pi^2 U \text{ with } U = \langle \bar{r}^2 \rangle \tag{2.10}$$

where U is the isotropic temperature factor [53].

The atomic form factor is further influenced by the occupancy factor of the site. Normally, a site is taken to be fully occupied by a single type of atom (occupancy = 1), but it is possible for an atom to incompletely occupy a site (expressed as a fractional occupancy, where some percentage of that site will be left empty) or for a mixture of atoms to randomly distribute over a single crystallographic site. The form factor in this case can be constructed from a linear summation of form factors f_n for each atom n on that crystallographic site, appropriately modified by their fractional occupancy o_n [58]:

$$f = \sum^{n} o_n f_n \tag{2.11}$$

A diffraction pattern provides information on the 2θ positions and intensities of reflections, but does not yield the phase angle ϕ_{hkl} – this is known as the phase problem [56]. Determining the structure of an unknown material is therefore an iterative process known as *refinement*, where a model structure is repeatedly adjusted to fit the experimental data. This procedure is discussed in detail in Section 2.1.4.

2.1.2 X-ray Powder Diffraction

As discussed in Section 2.1.1.2, the atomic form factor f_n is a function dependent not only on the nature of the atom n but also the angle of diffraction θ and the type of radiation used. The *X-ray form factor* is simply proportional to the atomic number Z_n and θ [57]:

$$f_n(\theta) \propto \frac{Z_n}{2}(1 + \cos 2\theta) \tag{2.12}$$

This introduces several limitations in the use of X-rays as a structural probe:

- Isoelectronic ions and atoms that are adjacent in the periodic table are difficult to distinguish.
- The diffraction pattern will be dominated by scattering from the heaviest elements in the structure, meaning that information about light elements will be difficult to extract in the presence of a transition metal.
- As X-rays are scattered by the electron cloud around an nucleus, the scattering cross section is significant, especially for heavy elements. As Equation 2.12 indicates, this results in a marked angular dependence of the intensity. In practice, the drop in intensity of the diffracted beam as 2θ increases restricts the useable range to $2\theta < 90$.

Although these factors limit the usefulness of X-ray powder diffraction (XRPD), it was used extensively in this thesis for the routine characterisation of unknown materials. Where the restrictions above were problematic in structure identification, neutron radiation was used (see Section 2.1.3).

2.1.2.1 Instrumentation

A *PANalytical X'Pert PRO* lab-based X-ray diffractometer was used for standard characterisation of all the materials studied in this work – its intensity and resolution enabled accurate determination of lattice parameters and an assessment of

phase purity, but the data for air-sensitive samples were generally insufficient to allow a full structural refinement due to the limitations of the sample holder. This diffractometer functions in Bragg-Brentano geometry with a fixed X-ray source operated at a current of 40 mA, a voltage of 45 kV, and with a detector on the 2θ axis. A focusing beam Johansson monochromator uses Ge (111) to select only the Cu $K\alpha_1$ radiation with wavelength $\lambda = 1.54059$ Å. The divergence slit is automatically adjusted to maintain a fixed sample irradiation area throughout the scan. [59]

Measurements of air-stable materials were conducted by mounting finely ground samples on a greased (High Vacuum Grease, Dow Corning GMBH) quartz wafer, which was then mounted in a spinner carousel rotated at 60 rpm during the diffraction measurement. Air-sensitive samples were prepared in an argon filled glove box, where they were finely ground, mounted on a greased glass slide and then inserted into an airtight aluminum sample holder with an acetate window. Measurements were carried out between $2\theta = 10^\circ - 80^\circ$ with a step size of 0.008° and an average scan length of $1 - 3$ hours.

High resolution X-ray powder diffraction data, suitable for full structural refinement, were collected on many samples using the *ID31 beamline at the European Synchrotron Radiation Facility (ESRF)* in Grenoble, France. This beamline operates with energies between 5 and 60 keV, leading to wavelengths in the range $0.2 - 2.5$ Å (the exact wavelength is selected by a double Si (111) monochromator; values of λ for the measurements in this thesis ranged from $0.7 - 0.9$ Å) [60]. The intensity of the diffracted beam as a function of 2θ is measured by a bank of nine scintillation detectors (spaced at 2° intervals). Each of these detectors is preceded by a Ge (111) crystal analyser, with all nine crystals mounted on one rotation stage so that only a single adjustment is needed when a wavelength is selected [60]. Diffraction measurements were carried out with a step size of 0.003° over the range $2\theta = 3^\circ - 48^\circ$ with an average scan length of 15 minutes.

The *I11 beamline at the Diamond Light Source* in Harwell, England was also

used to collect high resolution X-ray powder diffraction on some of the materials in this thesis. This beamline operates with energies between 5 and 30 keV, leading to wavelengths in the range $0.4 - 2.5$ Å (the exact wavelength is selected by a double Si (111) monochromator; values of λ for the measurements in this thesis ranged from $0.8 - 1.0$ Å) [61]. Two different detector arrangements were used:

1. For the data measured during the beamtime with $\lambda = 0.82497$ Å, the detector design was similar to that discussed above for ID31. Rather than one set of nine detectors which scanned the whole 2θ range, though, five sets were used, and each detector set scanned only a portion (approx. 18°) of the 2θ circle [61]. Every detector is preceded by a Ge (111) crystal analyser, with all nine crystals of a set mounted on the same rotation stage [61]. Measurements were carried out with a step size of 0.001° over the range $2\theta = 5° - 61°$ with an average scan length of 10−15 minutes.

2. For the data measured during the beamtime with $\lambda = 0.82656$ Å, the position sensitive detector (PSD) was used. The PSD is a wide angle, fixed position detector with a 90° aperture and a step size of 0.00375°, allowing high throughput of samples (a full scan is completed in 1 s) due to the fast-shutter speed of I11 [61]. Measurements were carried out over the range $2\theta = 5° - 95°$ with data 'blanks' (due to the detector edges) of 0.2° at 5° intervals. Each diffraction pattern consists of at least 10 separate scans merged together.

Both beamlines operate in Debye-Scherrer transmission geometry with the samples in a rotating $0.7 - 1.0$ mm borosilicate glass capillary. The finely ground samples were loaded into these tubes inside a nitrogen-filled glove bag, where the capillaries were also fitted with a glass rod and sealed with grease. After removal from the glove bag the capillaries were flame sealed and placed in the diffractometer.

2.1.3 Neutron Powder Diffraction

Thermal neutrons (kinetic energy corresponding to approx. 290 K) are useful probes of crystal structure as their wavelengths span a range that is comparable to interatomic distances [62]. The atomic form factor, f_n, for neutron diffraction is referred to as the *coherent scattering length,* b_n, and relative values of this for the elements studied in this work are given in Table 2.1 . Neutrons interact with the nucleus of an atom (rather than its electron cloud) which offers several advantages over X-ray diffraction:

- The nucleus is a point scatterer; thus, the neutron scattering cross section is generally independent of scattering angle 2θ and refineable data can be measured for a large range of d-spacings. Additionally, the neutron scattering length is not proportional to Z_n and thus elements with similar Z_n, which are undistinguishable with X-rays, may be readily separated; as well, light elements (*e.g.* H) may be distinguished even when mixed with heavier elements [57].

- As neutrons carry a magnetic moment ($S = \frac{1}{2}, \mu = -9.66 \times 10^{-27}$ J/T), they can interact with unpaired electrons in a magnetic material and therefore also describe the magnetic structure [62].

- Relative to X-rays, the penetrating power of neutrons is strong and thus complex environments around the sample (*e.g.* furnaces and cryostats) may be used without significantly affecting the diffraction from the sample [57].

However, the relatively weaker scattering power of neutrons also means that large sample sizes and long collection times must be used. A further disadvantage of neutron diffraction is that is the apparatus required (*viz.* large scale infrastructure, like a nuclear reactor) may not be readily available. Consequently, neutron radiation has only be used in this work in cases where its advantages over more accessible X-ray radiation are clearly required.

Isotope	Natural Abundance (%)	Coherent Scattering Length (1×10^{-15} m)	Coherent Scattering Cross-Section (1×10^{-24} cm)	Absorption Cross-Section (for 2200 m/s)
^{1}H	99.99	−3.74	1.76	0.33
^{1}H	-	*25.27*	*80.27*	*(incoherent)*
^{2}H (D)	0.015	6.67	5.59	0.00052
^{51}V	99	−0.402	0.0203	4.9
^{52}Cr	84	4.92	3.04	0.76
^{55}Mn	100	−3.73	1.75	13.3
^{90}Zr	51	6.4	5.1	0.011

Table 2.1: *Neutron scattering cross-sections and scattering lengths, along with the absorption cross-section, for the most abundant natural isotopes of the elements studied in this work. Deuterium is included as a comparison to hydrogen. All values given are for coherent scattering, except for the incoherent values noted.* [63]

The intensity of the Bragg reflections in a neutron diffraction experiment is determined by a combination of two types of scattering: that which is *coherent* with other nuclei and can produce interference, and that which is *incoherent* [62]. Incoherent scattering, in which there is no phase relation between the contributions from neighbouring nuclei, largely contributes to diffuse scattering in the pattern [62]. For elements where the incoherent scattering length is large compared to the coherent scattering length (*e.g.* H^1) the diffuse scattering contribution is visible as a large background and may obscure the Bragg diffraction peaks. When an isotope with more favourable properties is available (*e.g.* H^2), isotopic enrichment may be preferred. In this thesis, all neutron diffraction work was carried out on deuterided (rather than hydrided) materials.

It should be noted that in the case of vanadium, the incoherence is very large and overwhelms the weak coherent scattering – therefore, V is often used as a sample holder since it contributes so little intensity to a diffraction pattern [62]. Thus, ZrV_2 and its hydrides are not suitable to study with neutron diffraction.

2.1.3.1 Instrumentation

The neutron powder diffraction data presented in this thesis were collected using the GEneral Materials (GEM) diffractometer at the ISIS pulsed neutron source. At ISIS, the neutrons are produced *via* spallation of a tungsten target and are then moderated and collimated for use in time-of-flight measurements. In this technique, the neutrons travel a known distance L from the source to the sample, and then to a fixed-position detector which records the neutron's arrival time (time-of-flight, t). The incident beam contains a range of wavelengths, which can be related to the neutron momentum p and its mass m through the de Broglie relationship [62]:

$$\lambda = \frac{h}{p} = \frac{ht}{mL} \tag{2.13}$$

When combined with Bragg's Law (Equation 2.2) and substituted with appropriate values for m and h, a simple relationship of t and d_{hkl} is revealed:

$$t = 505.56 L d_{hkl} \sin\theta \tag{2.14}$$

Unlike the methods discussed for X-ray diffraction, where detectors scan part of a 2θ circle, the time-of-flight technique measures an entire diffraction pattern with a set of fixed detectors arranged in a series of *banks*, characterised by their resolution, d-spacing range and count rate. The GEM diffractometer has 6 banks, covering an area of 7.27 m^2 and a 2θ range of $1.2° - 117.4°$; the banks typically used for structural refinement in this work are bank 3 ($25° - 45°$), bank 4 ($50° - 75°$), bank 5 ($79° - 104°$, the so-called '90° bank') and bank 6 ($142° - 169°$) [64]. The finely ground samples used for neutron diffraction on GEM in this thesis were loaded, in an argon filled glovebox, into 8 mm vanadium cans which were sealed with indium wire. The diffractometer was outfitted with a cryostat to allow temperatures below 300 K to be accessed; typical collection times at each temperature measured were approximately 3 hours.

2.1.4 Rietveld Refinement Technique

2.1.4.1 The Rietveld Method

In the earlier discussion of powder diffraction (see page 24) the difficulty of separating overlapping *hkl* peaks and deconvoluting the individual intensity contributions was touched upon. Assignment of the Bragg reflections can be accomplished *via* a number of different techniques; in this thesis, the widely-used *Rietveld refinement method* [65] was exclusively employed for all crystallographic structure determinations.

In the Rietveld method, a series of least-squares refinements are carried out to minimise the difference between experimental diffraction data (given as a set of intensities, y_i, at even step sizes of 2θ, time-of-flight, d-spacing, *etc.*) and calculated diffraction data that include an input structural model, instrumental corrections, and other sample characteristics as required. The key feature of the method is feedback of the minimisation results into the refinement loop to modify the initial calculated structural model until a best fit is obtained. [65]

The method is one of structure refinement and makes no attempt to resolve overlapping reflections or assign peaks to particular *hkl*s —thus, a good starting model is needed. With an initial structure model for all the phases present, including space group, lattice parameters and atomic sites, an initial value of $\mathbf{F}(hkl)$ can then be provided for calculation of the intensity at each data point i [65]:

$$y_{ci} = s \sum_{hkl} L_{hkl} \left|\mathbf{F}(hkl)\right|^2 H(2\theta_i - 2\theta_{hkl}) P_{hkl} A + y_{bi} \tag{2.15}$$

The above is simply an expanded form of Equation 2.8 with additional parameters for the peak profile function $H(2\theta)$ and the diffraction background, y_{bi} (which is modelled using high order polynomials). In the following least-squares refinement of this calculated y_{ci} versus the experimental y_i, the residual S_y is minimised [65]:

$$S_y = \sum_i \frac{1}{y_i}(y_i - y_{ci})^2 \tag{2.16}$$

Minimisation is accomplished by refining the variables that define y_{ci} in Equation 2.15. Inherent in the structure factor for each reflection, $\mathbf{F}(hkl)$, is the ability to refine the provided structural model as well. The choice of which parameters to refine and the order in which this is carried out is key to a successful refinement [65].

The quality of a refinement is best judged by visual examination of the experimental data versus the calculated model, but several statistical parameters also exist to quantify this. In this thesis, the *weighted pattern reliability factor* R_{wP} [65] is used:

$$R_{wP} = \sqrt{\frac{\sum_i \frac{1}{y_i}(y_i - y_{ci})^2}{\sum_i y_i}} \tag{2.17}$$

A stumbling block in the Rietveld method is *parameter correlation*: there exist sets of parameters that affect the calculated intensity in very similar ways and cannot be reliably refined if one attempts to minimise the whole set simultaneously [65]. The correlations between the temperature factor B_n and occupancy factor o_n for a given n site are well known [65] and in a calculated model where both of these are to be refined, the minimisation must be carried out separately, with appropriate limits on the values in order to stabilise the refinement.

2.1.4.2 Computational details

The structural refinements presented in this thesis were carried out using TOPAS Academic [66], a software suite employing the Rietveld method discussed above. The general refinement process followed a stepwise process in order to ensure both the stability of the refinement and the accuracy of refined parameters:

1. Begin by fitting the background with an appropriate number of parameters (to be increased in later stages of the refinement). Include suspected phases, with initial structure model as those given on the Inorganic Crystal Structure Database [67].

2. The lattice parameters and scale factors of the phases are refined, along with the global parameters of zero-point error (in the case of X-ray diffraction), axial divergence correction, and absorption parameter.

3. The peak profile of each phase is then modelled, following which the thermal parameters, site occupancies and atomic positions are separately considered.

For several materials studied in this thesis, the contributions to $H(2\theta)$ from crystallite size D and strain ϵ were significant and deconvolution of these parameters was desirable. To accomplish this, the peak profile $H(2\theta)$ was modelled using a Voigt function (the convolution of a Gaussian peak by a Lorentzian peak) and the integral breadth, β, which is simply the ratio of peak area to peak height, was determined as a function of 2θ [68]. For each of the Gaussian (G) and Lorentzian (L) functions the apparent crystallite size can then be calculated (*via* Equation 2.7):

$$\beta_G(2\theta) = \frac{\lambda}{D_G \cos 2\theta} \text{ and } \beta_L(2\theta) = \frac{\lambda}{D_L \cos 2\theta} \tag{2.18}$$

An approximation for the real crystallite size, D, is then obtained by combining these two determinations using the Voigt integral breadth β_V and adding a shape parameter k (for the materials discussed in this thesis, the shape of the grains were approximated as spheres) [68]:

$$D = \frac{k}{\beta_V(D_G, D_L)} \tag{2.19}$$

With the same calculated peak profile we can also determine the contributions from strain, except in this case the peak widths, Γ, are used in combination with Equation 2.6 [68]:

$$\Gamma_G(2\theta) = \epsilon_G \tan 2\theta \text{ and } \Gamma_L(2\theta) = \epsilon_L \tan 2\theta \tag{2.20}$$

The total strain within the crystal is then calculated *via* [68]:

$$\epsilon = \frac{1}{2\Gamma_V(\Gamma_G, \Gamma_L)} \tag{2.21}$$

2.2 Magnetic Characterisation

2.2.1 Introduction to Magnetism

Magnetism, in its vast and diverse range of behaviours, arises simply from electrical charge in motion [69]. Just as a macroscopic current loop can generate a magnetic field, one can envisage the movement of an electron in its orbit around an atom generating a magnetic moment m. This interpretation, although convenient on a qualitative level, breaks down on further inspection due to the quantisation of the electron's angular momentum, as it implies that the electron's magnetic moment must also be quantised. The orbital angular momentum p_o is defined by the quantum number l ($l = 0, 1, 2...(n-1)$) and the spin angular momentum p_s by the quantum number s (for an electron, $s = \frac{1}{2}$):

$$p_o = \left(\frac{h}{2\pi}\right)\sqrt{l(l+1)} \text{ and } p_s = \left(\frac{h}{2\pi}\right)\sqrt{s(s+1)} \tag{2.22}$$

The total angular momentum of an electron p_j is similarly calculated, except the quantum number j (simply the vector sum $l + s$) is used.

Larmor's Theorem states that an electron moving in an orbit will precess about an applied magnetic field, with the component of the momentum along the field axis given by $m\cos\theta$ [69]. When this is combined with the quantised angular momenta given above, there arises discrete values of the magnetic quantum numbers m_o and m_s:

$$m_o = -\left(\frac{eh}{4\pi m_e}\right)\sqrt{l(l+1)} = -\mu_B\sqrt{l(l+1)} \text{ and } m_s = -2\mu_B\sqrt{s(s+1)} \tag{2.23}$$

The Bohr magneton, μ_B, is simply a combination of constants including the electron mass m_e and the unit of elementary charge e [69]. As before, a total magnetic moment m_j can be defined, where the Lande splitting factor g describes the relative contributions from the spin components and the orbital components:

$$m_j = -g\mu_B\sqrt{j(j+1)} \tag{2.24}$$

2.2.1.1 Diamagnetism

The total angular momentum j for the collection of electrons in an atom can be summed (by a variety of methods, depending on the coupling between l and s) to give $\mathbf{J}$. Regardless of the method chosen, for a closed shell of electrons the individual j will sum to zero [69], meaning that only those partially filled shells – those with unpaired electrons – need be considered.

Materials in which all electrons are paired as described above have no net atomic magnetic moment. However, an applied magnetic field will affect the orbital momentum of the electrons, due to their charged nature, and bring about a change in their velocity in such a way that a moment will be induced that opposes the applied field [56]. The bulk magnetisation, M, in this case is slightly negative and independent of temperature. This is known as *diamagnetism* [69] and is exhibited by all atoms; however, the effect is so small that in systems where some sort of magnetic order also exists the diamagnetic contribution is often neglected.

2.2.1.2 Paramagnetism

The quantised energy levels of electrons within an atom are 'split' in the presence of an applied magnetic field H in a phenomenon known as the *Zeeman Effect*, with the difference in energy E given by [69]:

$$\Delta E = -\mu_0 m H \tag{2.25}$$

If Equation 2.25 is combined with Equation 2.24, then, for the case of an isolated, non-interacting atom:

$$\Delta E = -\mu_B \mu_0 \sqrt{\mathbf{J}(\mathbf{J}+1)} H \tag{2.26}$$

If the orbital contribution is ignored (an approximation that is appropriate for transition metals due to quenching of the orbital momentum [56]) then $\mathbf{J} = \mathbf{S}$ and, for an atom with one unpaired electron, there exist then only two energy levels with the electron aligned either parallel ($m_s = \frac{1}{2}$) or antiparallel ($m_s = -\frac{1}{2}$) to the

applied field. Then E becomes the energy cost of aligning that unpaired electron for all the atoms in the sample with the applied field. Using Boltzmann statistics, the bulk magnetisation M (magnetic moment per unit volume) can be estimated as [69]:

$$M = \frac{Nm^2\mu_0 H}{k_B T} \tag{2.27}$$

where N is the number of atoms per unit volume and m, the magnetic moment per atom, is given by Equation 2.24. Rearrangement to isolate the susceptibility, $\chi(= \frac{M}{H})$, yields the well-known *Curie Law* [69]:

$$\chi = \frac{C}{T} \text{ with } C = \frac{Nm^2\mu_0}{k_B} \tag{2.28}$$

In the case of an atom with multiple unpaired electrons, the derivation is similar [69].

2.2.1.3 Effect of Field and Temperature

In experimental determinations of magnetism, a relation must be found between the atomic magnetic moment, m, and the macroscopic observable M. The bulk magnetisation of a material is a factor of its size and shape, the applied field, and the temperature, which affect the atomic moment m in differing ways depending on the type of magnetic order (additionally, the nature of the ordering can change as a function of H and T).

As mentioned in Section 2.2.1.1, the magnetisation of a diamagnet is slightly negative and nearly temperature independent. For paramagnets, Equation 2.27 suggests that at $H = 0$, $M = 0$ (the magnetic moments will be randomly oriented, yielding a net spin of zero) and that, once a field is present, M will increase as T decreases (reduction in thermal motion allows electron spins to better align with field). The magnetisation will increase as a function of H, but subsequent removal of the field will return the system to a state of $M = 0$ as the spins are non-interacting. This is illustrated in Figure 2.4.

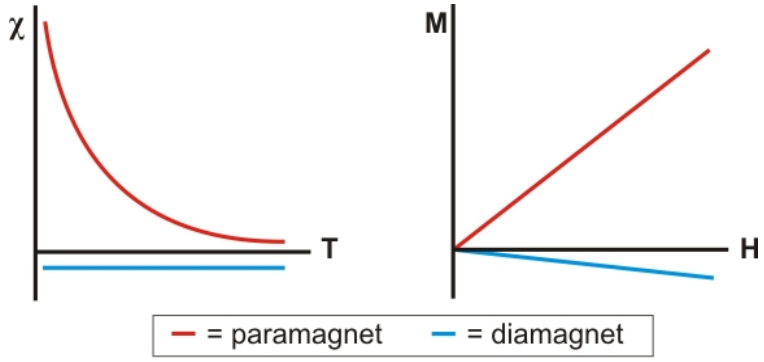

Figure 2.4: *The effect of temperature on the magnetic susceptibility at constant field is shown on the left for a typical paramagnet (red) and a typical diamagnet (blue). On the right, the effect of a varying field on the magnetisation (at constant temperature) is shown for the same materials.*

2.2.2 Localised Moment Model

The models discussed to this point assume that spins on neighbouring atoms are non-interacting. A simple model for the interaction of spins is the Heitler-London approximation: for two one-electron neighbouring atoms, approximate the orbital wave function of the two electrons together by a linear combination of the atomic orbital wave function of each electron localised on its own atomic site [70]. This is the localised moment model, and the energy of this system is given by:

$$E = \iint \Psi(r_i, r_j) \langle H \rangle \Psi^*(r_i, r_j) d\tau_1 d\tau_2 \tag{2.29}$$

The Hamiltonian $\langle H \rangle$ must contain the separate Hamiltonians $\langle H_i \rangle$ and $\langle H_j \rangle$ for each electron as well as an *exchange Hamiltonian* $\langle H_{ij} \rangle$. One form for this exchange Hamiltonian is to express it in terms of an exchange integral J_{ij} and the spins on the two electrons, s_i and s_j [56]:

$$\langle H_{ij} \rangle = -2 J_{ij} s_i \cdot s_j \tag{2.30}$$

J_{ij} is an energy which arises from the exchange of the electrons on the two sites – when $J > 0$, the two electrons will be aligned parallel, and when $J < 0$, they will align antiparallel. For a solid containing many atoms, the exchange Hamiltonian should be summed over all electrons which contribute to the exchange energy [56]:

$$\langle H_{ij} \rangle = -2 \sum \sum J_{ij} s_i \cdot s_j \tag{2.31}$$

In practice, the summation is carried only over nearest neighbours with the assumption that J is invariant for all nearest-neighbour pairs. If J is large enough to make the reduction from the exchange coupling energy greater than the energy needed to achieve spin alignment, such a solid possess magnetic ordering.

2.2.3 Magnetic Materials

Of the many kinds of magnetic order in solids, *ferromagnetism* (spins aligned parallel), *antiferromagnetism* (spins aligned antiparallel) and *ferrimagnetism* (spins mostly antiparallel with cancellation incomplete) are perhaps the most common. However, every magnetically ordered material undergoes a transition at some higher temperature T_C where the ordering is lost (thermal motion becomes larger than the exchange energy) and the material is paramagnetic [69].

The generalised dependence of susceptibility, χ, on temperature for these classes of magnetic materials are shown in Figure 2.5. Above T_C (T_N for antiferromagnets by convention after Néel – see Section 2.2.4) the susceptibility curve resembles that of a paramagnet. Below this ordering temperature, the susceptibility a) *decreases* for the antiferromagnet as the magnetic moments begin to align antiparallel, b) *increases* for the ferromagnet as the moments align with the field or c) *increases* for the ferrimagnet (but to a lesser extent) as the moments align antiparallel but do not completely cancel out. In reality, the rotation of magnetic moments occurs in groups known as *domains* [69].

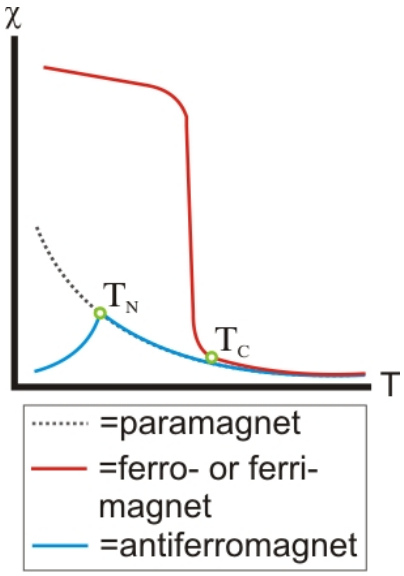

Figure 2.5: *Susceptibility behaviour of a typical paramagnet, antiferromagnet and a ferro- or ferrimagnet versus temperature in a constant magnetic field.*

2.2.3.1 Domains and Hysteresis

In the demagnetised state, a magnetically ordered solid consists of a collection of volumes or *domains* as a consequence of magnetostatic energy minimisation [56]. Within these domains, the atomic magnetic moments are aligned, but on the macroscopic scale the magnetic moments of the domains are randomly oriented and cancellation occurs. In the presence of a field, these volumes are simply rearranged until the moment of each domain (and therefore of all the atoms) are aligned.

There exist finite boundaries between these domains where the change in direction of moment between one domain to the next takes place gradually over many atoms. The width of these walls is determined from the interplay between the exchange energy and the anisotropy energy (a reduction in energy when the magnetisation is directed along certain crystallographic axes called *easy axes*) [56]. When a field is applied, those domains favourably oriented to this field will gradually increase in size *via* translational domain wall motion at the expense of domains unfavourably aligned [56].

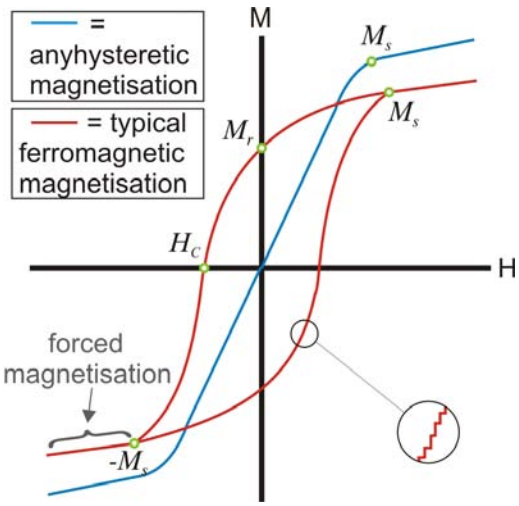

Figure 2.6: *Hysteresis curve for a typical ferromagnet - an anhysteretic curve is shown for comparison. The hysteresis parameters indicated on the curve are described in the text.*

Although a wall can bend in a reversible fashion at low field strengths, domain wall motion is an irreversible effect. The potential energy of a wall across a material is generally inhomogeneous (due to defects, microstrains, grain boundaries, *etc.*) and the wall thus becomes 'pinned' onto energy minima and a discontinuous energy jump is required to 'unpin' it [69]. At higher field strength (greater than the anisotropy energy) the moments within a domain can irreversibly rotate into the

field direction and, at very high fields, the angle of precession of the moments about the field direction is reversibly reduced [69].

In a perfect ferromagnet free of defects, the change in magnetisation with applied field would follow a completely reversible *anhysteretic magnetisation curve* [69] as shown in Figure 2.6. However, in magnetically ordered real materials, the presence of strains and anisotropy leads to discontinuous jumps in the magnetisation and creates a hysteresis – M is not a unique function of H. The hysteresis of a material can be characterised by various parameters [69]:

- The loss W_H (area enclosed by the hysteresis loop), can be used to describe the amount of hysteresis in a material and is related to the number of strains and defects as well as the amount of anisotropy present.

- The coercive field H_C (field required to reduce M to zero) directly relates to the amount of strain and defects in a material – H_C is proportional to the product of the number of domains and the density and average energy of the pinning sites. A *hard* magnet has $H_C > 125$ Oe, whilst a *soft* magnet generally has $H_C < 12.5$ Oe.

- The magnetic remanence M_r (magnetisation remaining when field is reduced to zero) is a factor of the degree of magnetocrystalline anisotropy: the magnetic moments aligned along a crystallographic easy axis become trapped in a energy minima, and can only be shifted in a discontinuous and irreversible rotation. It is also dependent on the saturation magnetisation.

- The saturation magnetisation M_s (maximum magnetisation) is the magnetisation of the material when all domains are aligned in the same direction. It is defined at absolute zero, but is typically measured at some finite low T. Once M_s has been reached, the magnetisation can still increase very slowly *via forced magnetisation* where the moments' angle of precession around the applied field is reduced.

It is important to note that all magnetically ordered materials contain domains and that they behave in a similar fashion as the characterisation above for a ferromagnet.

2.2.4 Néel Theory of Ferrimagnetism

The Néel treatment of ferrimagnetism [71] uses the Weiss molecular field approach, where it assumed that the field acting on any atom in a magnetically ordered material is the sum of the applied field and the internal molecular fields arising from interatomic interactions. The material can be considered as consisting of interpenetrating sublattices k, with the field experienced by the atom i on the k sublattice given by:

$$H_i = H_0 + \sum_{k=1}^{n} \gamma_{ik} M_k \tag{2.32}$$

where the summation is over n sublattices and γ is a constant called the molecular field coefficient [72]. A positive value of γ suggests a parallel arrangement of moments, and a negative value an antiparallel arrangement. For a antiferromagnet, there are two sublattices, composed of the same magnetic ion, with equal but opposite net magnetisations. In the case where there are two types of magnetic ions A and B, with λ as the fraction of A sites and μ as the fraction of B sites, there exist two unequal sublattices where the total fields acting on the A and B atoms can be described by

$$H_a = H_0 + \gamma_{aa} M_a + \gamma_{ab} M_b \text{ and } H_b = H_0 + \gamma_{bb} M_b + \gamma_{ab} M_a \tag{2.33}$$

which is of course a ferrimagnet [72]. Above the ordering temperature T_C, the inverse susceptibility χ^{-1} for this system can be described by the Néel hyperbola (also illustrated in Figure 2.7):

$$\frac{1}{\chi} = \frac{T}{C} + \frac{1}{\chi_o} - \frac{\sigma}{T - \theta^*} \tag{2.34}$$

A result which is quite different from antiferromagnets and ferromagnets, both of which show a linear dependence of χ^{-1} on T above T_C [69]. The coefficients

describing the hyperbola relate directly to the molecular field coefficients *via* [72]

$$\frac{1}{\chi_o} = \gamma_{bb}\lambda\mu\left(2 + \frac{\lambda\gamma_{ab}}{\gamma_{aa}\mu} + \frac{\gamma_{bb}\mu}{\gamma_{ab}\lambda}\right) \tag{2.35}$$

$$\theta^* = -C\gamma_{ab}\lambda\mu\left(2 - \frac{\gamma_{aa}}{\gamma_{ab}} - \frac{\gamma_{bb}}{\gamma_{ab}}\right) \tag{2.36}$$

$$\sigma = C\gamma_{ab}^2\lambda\mu\left(\lambda(1 - \frac{\gamma_{aa}}{\gamma_{ab}}) - \mu(1 - \frac{\gamma_{bb}}{\gamma_{ab}})\right)^2 \tag{2.37}$$

$$T_C = \frac{1}{2}C\gamma_{ab}\left(\lambda\frac{\gamma_{aa}}{\gamma_{ab}} + \mu\frac{\gamma_{bb}}{\gamma_{ab}} + \sqrt{\left(\lambda\frac{\gamma_{aa}}{\gamma_{ab}} - \mu\frac{\gamma_{bb}}{\gamma_{ab}}\right)^2 + 4\lambda\mu}\right) \tag{2.38}$$

The Weiss molecular field coefficient is simply a primitive representation of the exchange interaction discussed in Section 2.2.2, and as such can be transmuted into exchange integrals J *via*

$$\gamma_{ij} = \frac{\frac{1}{2}Z_{ij}J_{ij}}{g_i g_j \mu_B^2 N_j} \tag{2.39}$$

where Z_{ij} is the number of nearest neighbours on the j^{th} sublattice for an atom on the i^{th} sublattice and N_j is the number of j atoms per mol of material [70].

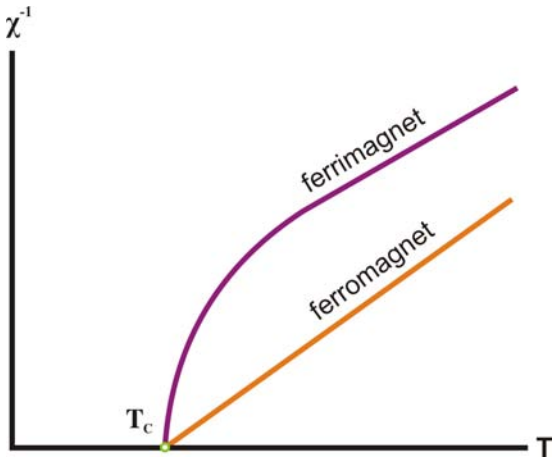

Figure 2.7: *Inverse susceptibility versus temperature for a typical ferrimagnet (in purple) with the trace for a ferromagnet with the same T_C shown in orange for comparison.*

2.2.5 Itinerant Electron Theory

For materials in which electron bands form a better description than localised atomic orbitals, the localised model discussed in Section 2.2.2 does not accurately predict magnetic properties and an itinerant electron model is preferred [56]. For example, some paramagnetic metals demonstrate a temperature-independent weak susceptibility, called *Pauli paramagnetism*, contrary to expectations of Equation 2.28. If the unpaired electrons contributing to this susceptibility are contained in the conduction band, then most will have no possibility of spin flipping under an applied field as nearly all orbitals in the band with parallel spins will already be occupied. Only electrons in the range ϵ_F(Fermi energy) to $\epsilon_F - k_B T$ will be able to populate new parallel spin orbitals and thus only a fraction of the total number of electrons can contribute to the observed magnetism [56]. The Pauli paramagnetic susceptibility is thus directly proportional to the density of states at the Fermi level, $D(\epsilon_F)$:

$$\chi \propto \mu_0 D(\epsilon_F) \tag{2.40}$$

Some metals and alloys possess characteristics of both the localised and the itinerant model – an apparent contradiction that can be explained by consideration of *correlation effects*. In these cases the electron bands are considered to be narrow enough to concentrate the charge density in the vicinity of the atomic sites and thus electron spins are correlated to varying extents [69].

The relation between H and M in some itinerant electron systems can be described by the Arrott equation [73]:

$$M^2 = M_s^2 \left(1 - \frac{T^2}{T_C^2}\right) + 2\chi_0 \frac{H}{M} \tag{2.41}$$

where the degree to which experimental data agree with this formulation (*i.e.*, the linearity of an M^2 versus $\frac{H}{M}$ plot) provides a useful indication of the interplay between localisation and itinerancy of the electrons [74]. However, spatial inhomogeneities, spin fluctuations, and other phenomena can also cause deviations

from linearity. The intercept of the Arrott plot can also be used to extract the saturation magnetisation, M_s.

2.2.6 Superconductivity and Magnetism

Generally speaking, superconductivity and magnetism are mutually exclusive phenomena: conventional superconductivity is attributed to *Cooper pairs* [56] of electrons with opposing spins and momenta, whereas magnetic order arises from a co-operative exchange interaction forcing electrons in alignment with their neighbours. In weak magnetic field, a superconductor acts as a perfect diamagnet ($\chi = -1$) and, when cooled in a magnetic field from $T > T_C$ (the superconductor transition temperature) to $T < T_C$, a bulk superconductor will eject lines of induction such that the field inside is zero [56]. However, at a sufficiently strong magnetic field called the critical field, $H_c(T)$ (which varies with temperature), the superconductivity will be destroyed. As shown in Figure 2.8, this happens in a sharp fashion for type I superconductors; type II superconductors demonstrate a vortex region $H_{c1} < H < H_{c2}$ where flux exclusion is incomplete yet the superconducting electrical properties remain.

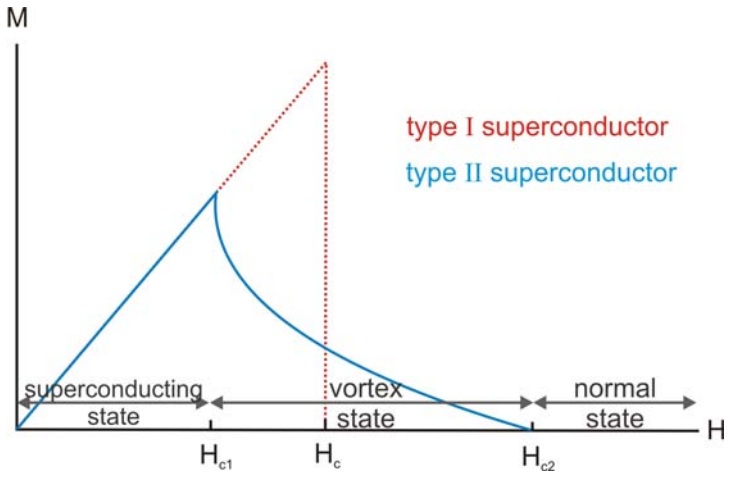

Figure 2.8: *Destruction of superconductivity via application of a critical field for both type I and type II superconductors. The labelling of superconducting, vortex and normal state refer to the type II material. Figure adapted from* [56]

2.2.7 The Superconducting Quantum Interference Device (SQUID)

An *MPMSXL Superconducting Quantum Interference Device (SQUID)* was used in this thesis to measure changes in magnetisation as a function of both field and temperature. A SQUID is inherently more accurate, with higher resolution, than other magnetometers (*e.g.*, a VSM) as it uses a Josephson junction to count flux quanta [69].

The Josephson junction device in a SQUID consists of a poorly conducting material sliced into a superconducting ring so as to create two insulating barriers. A potential difference applied across the superconductor-insulator barrier allows the tunneling of Cooper pairs such that the junction itself becomes weakly superconducting [69]. The magnetic flux exhibited by a sample inserted into the SQUID induces a phase difference across the junction, which in turns allows quantum tunneling. The current in the ring is a periodic function of this magnetic flux; thus, by measuring the current changes, the flux (and therefore the magnetisation) can be monitored [69].

2.2.7.1 SQUID Measurements

A small quantity of sample (typically $30 - 80$ mg) was placed inside a gelatin capsule and then inside a plastic straw marked with diamagnetic tape (the straw was prepared in an argon filled glovebox in the case of air-sensitive samples). This was then mounted on a sample rod with diamagnetic tape, pushed through the SQUID air-lock and purged with He, and then inserted into the centre of a superconducting magnet, typically operating at $-50 \leq H \leq 50$ kOe and $T = 2 - 350$ K for the measurements in this thesis. The chamber enclosing the sample was filled with He, a diamagnetic gas, to ensure that O_2 (paramagnetic) did not affect the reading. The magnetisation in the sample was detected by moving the sample within a superconducting coil, which then passed the signal to the SQUID in order to shield it from high fields. Each data point obtained represents the average of four separate magnetisation scans to ensure a precise reading.

2.2.8 Magnetic Crystal Structure

As was mentioned in Section 2.1.3, the scattering of neutrons by nuclei contains not only a structure factor component $\mathbf{F}(hkl)$ but also a magnetic structure factor $\mathbf{S}(hkl)$ on account of the interaction between the neutron magnetic moment and the magnetic moment of an atom. Thus, the total neutron scattering of a magnetic material will be a sum of Bragg structure peaks ($\mathbf{F}(hkl)$) and magnetic structure peaks ($\mathbf{S}(hkl)$) [62]. The magnetic structure factor is defined similar to $\mathbf{F}(hkl)$ (See Equation 2.3):

$$\mathbf{S}(hkl) = \sum_{n=1}^{N} q_n p_n \exp[2\pi \cdot i(hx_n + ky_n + lz_n)] \tag{2.42}$$

where q_n is the magnetic interaction vector and p_n is the magnetic scattering amplitude, defined by [62]:

$$p_n = s f_m \left(\frac{e^2\gamma}{mc^2}\right) \tag{2.43}$$

The factor enclosed in brackets is the product of the radius of the electron and the magnetic moment of the neutron. The magnitude of magnetic scattering thus depends on the electron spin s and the magnetic form factor f_m. Much like the X-ray form factor, this magnetic f_m falls off rapidly with 2θ as the electrons creating the magnetic moment are distributed over some volume of space. As the magnetic cross-sections are defined by the valence electron cloud, they differ from nuclear scattering lengths and in some cases may even be larger [62].

The introduction of a reversal symmetry operation R to describe the spin flip between coupled magnetic moments necessitates the use of a *magnetic unit cell,* of larger and lower symmetry than the chemical unit cell. The R operation adds to the existing 230 normal space groups (see Section 2.1.1) an extra 1421 space groups to describe magnetically ordered structures, giving a total 1651 *Shubnikov space groups* [62].

When the R operation is not present in a magnetic structure (*i.e.* in a ferromagnet, where the spins are aligned parallel) the magnetic unit cell is identical to

the chemical unit cell, creating magnetic structure peaks that are overlaid on the chemical structure peaks. Note that the relative intensities of the magnetic *hkl* peaks are not equal to the intensities of the structural peaks as $f_m \neq b_n$. In those magnetically ordered structures where a reversal operation takes place – namely, ferrimagnets and antiferromagnets – the chemical unit cell and magnetic unit cell will be non-equivalent and there will arise new diffraction peaks that can entirely be attributed to the magnetic structure. An example of both types of structure is shown in Figure 2.9.

The uncorrelated collection of magnetic moments that occur in a paramagnet do not diffract neutrons in any coherent fashion as they have no long range order. Paramagnetic scattering is thus completely incoherent and, rather than generating magnetic *hkl* peaks, it adds to the background scattering with non-constant intensity that is dependent on 2θ [62].

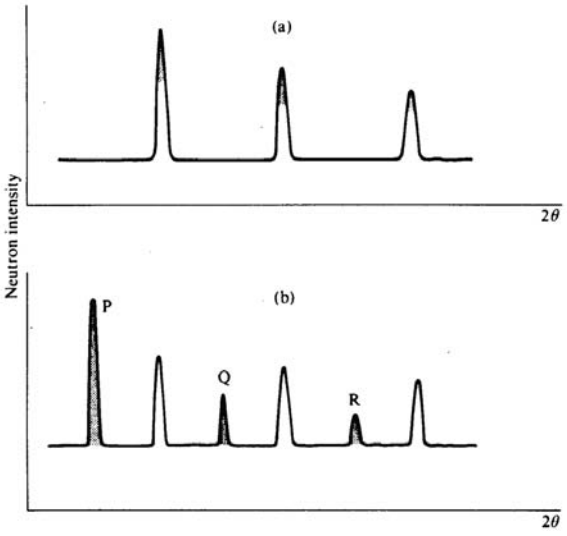

Figure 2.9: *Neutron diffraction from idealised magnetic crystals. a) shows the diffraction for a ferromagnet, with nuclear diffraction unshaded and magnetic diffraction shaded, and b) shows the same for a simple antiferromagnet. Figure from* [62]

The magnetic neutron diffraction data presented in Chapter 3 were analysed using the GSAS package [75] with EXPGUI [76]. GSAS is a software package that performs structural refinements using the Rietveld Method (see Section 2.1.4) and is capable of handling magnetic diffraction as well as nuclear diffraction. Details of the refinement process are discussed with the magnetic structure refinement.

2.2.9 Computational Modelling

A mean field Monte Carlo modelling program called McPhase [77] was used to predict possible magnetic structures in Chapter 3. Given the crystal structure and

exchange interaction constants, the McPhase program calculates the properties of a magnetic system. For the specified temperature and magnetic field, the program calculates the free energy for all possible magnetic structures that are stabilised by a mean field algorithm modified by a Monte Carlo process. Details of the calculation are given with results in Chapter 3.

2.3 Electronic Characterisation

2.3.1 Introduction to Electronic and Dielectric Characterisation

The electrical resistivity, ρ, of a material can be simply defined for most materials *via* Ohm's Law [78]:

$$V = I\rho \tag{2.44}$$

The van der Pauw 4-point probe method allows the resistivity of an unknown material to be determined by passing a current I through a pair of contacts attached the sample and then measuring the resulting voltage V developed across another pair of contacts. As long as the thickness of the piece of material is known, ρ can be readily obtained [78]. In the case of a powdered sample, where attachment of four contacts to an individual particle would prove impossible, the van der Pauw method can be used on pellet created from the pressed powder. Grain boundaries will significantly affect the measured resistivity, but can be partially avoided *via* high-temperature sintering of the pellet [78].

The interaction of hydrogen with the ZrM_2 alloys studied in this thesis generates finely divided powders due to decrepitation. The interparticle contacts in such a fine powder would create significant error contributions in a conventional four-point probe conductivity determination and high-temperature sintering cannot be used with these metal hydrides as the temperatures necessary would also cause hydrogen desorption. Thus, the conductivity measurements for hydrides presented in this thesis were obtained *via* a nonstandard contactless microwave method, called the *cavity perturbation technique* [79], detailed here.

In this technique, the characteristics of a microwave resonator cavity are measured both before and after a sample is inserted into the cavity. The material to be measured may be in any state (powdered solid, liquid. *etc.*) and the presence of a sample holder, *e.g.* a glass tube, may be easily accounted for, which allows the sample environment to be readily controlled. As long as the sample is small compared to the spatial variation of the field and does not cause a jump from the unperturbed cavity mode, the change in cavity properties can be directly related to the dielectric properties of the sample [79].

Although a resonant cavity can sustain several standing waves near each resonant frequency, in practice only the primary resonant mode is followed. The power absorption spectrum of the mode has a Lorentzian line shape and can be effectively described by its centre frequency, f, and Γ, the 3 dB bandwidth (width of the peak measured 3dB below the peak maximum) [79]. The response of the sample to the electromagnetic excitation, which is quantified by Δf and $\Delta\Gamma$, can then be related to its fundamental dielectric properties: both the electric permittivity, ϵ, and the magnetic permeability, μ, can be derived [79]. The presence of a distinct electric field antinode (in which only an electric field is generated and $H = 0$) and magnetic field antinode in the cavity enable a separate measurement of the sample's electric and magnetic response. Using the complex permittivity,

$$\hat{\epsilon} = \epsilon_1 + i\epsilon_2 = \epsilon_\infty + 4\pi i\frac{\hat{\sigma}}{\omega} \tag{2.45}$$

the complex conductivity of a material, $\hat{\sigma}$, and thus its resistivity ρ $(= \sigma^{-1})$, can be calculated from a microwave resonance measurement [79].

2.3.2 Cavity Perturbation Theory

The quality factor of a resonating structure, Q, is defined by [79]

$$Q = \frac{f}{\Gamma} = \frac{\omega}{L}\langle W\rangle \tag{2.46}$$

where $\langle W \rangle$ is the time-averaged energy stored in the cavity and L is the energy loss per cycle and ω describes the complex frequency [79],

$$\hat{\omega} = \omega - i\frac{\omega}{2Q} \text{ where } \omega = 2\pi f \tag{2.47}$$

The energy stored in the cavity is simply the intensity of the applied magnetic and electronic fields (H_o and E_o) integrated over the volume of the cavity, V_c, for all positions r [79]:

$$\langle W \rangle = \frac{1}{16\pi}\int_{V_c} (|E_o(r)|^2 + |H_o(r)|^2)dv \tag{2.48}$$

As briefly mentioned above, the sample size is small enough compared to the spatial variation of the field that a quasi-static approximation can be made, and thus $E_o(r) = E_o$ and $H_o(r) = H_o$ at all values of r.

As a consequence of the linearity of Maxwell's equations [56], the field inside the sample (H_{in} and E_{in}) is simply equal to the externally applied field modified by a depolarisation field:

$$E_{in} = E_o - 4\pi n \cdot P \tag{2.49}$$

$$H_{in} = H_o - 4\pi n \cdot M \tag{2.50}$$

Except in a good conductor, where the local field is zero, E_{in} and H_{in} are non-uniform within the sample [56]. n is a tensor related to the geometry of the sample [79], and P and M are the polarisation and magnetisation of the sample and are defined as dipole moment/magnetic moment per unit volume. P and M can be expressed as factors of both the susceptibility of the material, χ, and the polarisability, α [56]:

$$P = \chi_e E_{in} = \alpha_e E_o \tag{2.51}$$

$$M = \chi_m H_{in} = \alpha_m H_o \tag{2.52}$$

The susceptibility is related to intrinsic properties of the material, whereas the polarisability is an extrinsic factor expressing the field magnification caused by the sample geometry [79].

The change in energy stored when a sample of volume V_s is inserted into a cavity, $\Delta \langle W \rangle$, is expressed as [79]:

$$\Delta \langle W \rangle = \frac{-1}{4} \int_{V_s} (P \cdot E_o + M \cdot H_o) dv \tag{2.53}$$

If the insertion of a sample into the cavity, with a frequency change $\Delta\hat{\omega}$, is assumed to be adiabatic, then the ratio $\frac{\langle W \rangle}{\hat{\omega}}$ is invariant [79] and therefore

$$\frac{\Delta\hat{\omega}}{\hat{\omega}_o} = \frac{\Delta \langle W \rangle}{\langle W \rangle} \tag{2.54}$$

The expression for complex frequency in the electric field antinode ($H = 0$), is yielded *via* substitution of Equations 2.48, 2.53, and 2.51 in the above:

$$\frac{\Delta\hat{\omega}}{\hat{\omega}_o} = \frac{\Delta \langle W \rangle}{\langle W \rangle} = \frac{\frac{-1}{4} \int_{V_s} (P \cdot E_o) dv}{\frac{1}{16\pi} \int_{V_c} (|E_o(r)|^2) dv} = -\frac{2\pi\alpha_e V_s}{V_{eff}} \tag{2.55}$$

The derivation for the magnetic field is similar. Note that in this thesis, only the permittivity of the samples was determined – the permeability was not calculated. Thus from this point only derivations for the electric field antinode are discussed.

The factor V_{eff} (the *effective volume*) is a constant that depends only on the resonant mode of cavity and is equal to

$$V_{eff} = \frac{\int_{V_c} (|E_o(r)|^2) dv}{E_o^2} \tag{2.56}$$

V_{eff} can be determined by appropriate calibration of the resonator with a material of known permittivity – this is discussed further in Section 2.3.4.

Since the complex frequency (Equation 2.47) is composed of the measured parameters of f and Γ,

$$\frac{\Delta\hat{\omega}}{\hat{\omega}_o} = \frac{\Delta f}{f_o} - i\frac{\Delta\Gamma}{2f_o} \tag{2.57}$$

Equation 2.55 can directly relate the experimentally obtained data with the sample polarisability, α_e. Therefore, if the sample geometry is known and an expression for the dipole moment p of the sample can be formulated, the permittivity of an unknown sample can be calculated from f and Γ_o.

2.3.3 The "Collapsed Cylinder" Model

The dipole p of a particle of size a in an electric field can be solved under the quasistatic limit of potential theory, provided that boundary conditions are met [80]:

1. $a \ll \lambda$ (or, $f \ll \frac{c}{a}$)

2. $a \ll \delta$

Where f, λ refer to the applied electromagnetic field and δ is the skin depth. In a conducting material, an applied field decays exponentially as it penetrates into a sample and δ describes the distance over which the field varies [79]:

$$\delta = \sqrt{\frac{\rho}{\pi \mu_0 f}} \tag{2.58}$$

The quasistatic modelling avoids the need for full solutions to Maxwell's time dependent equations and allows the use of Laplace's equation $\nabla^2 \varphi = 0$ to solve for the electrostatic potential with the following boundary conditions [80]:

1. The parallel component of the electric field, E, is continuous across any boundary between media.

2. The perpendicular component of the electric flux density, D $(= \epsilon_0 \epsilon E)$, is also continuous across any boundary.

Consider an assembly of spheres inside a hollow cylinder (*viz.*, a powder packed in a glass tube). Solving Laplace's equation for the dipole moment of this system, even with the assumption that the spheres are non-interacting, would require finite element analysis and dedicated computational resources. However, a simplifying assumption can be made that this assembly of spheres collapses into a solid cylinder, herein called the *'collapsed cylinder' model.* The model does not factor in the density of packing of the spheres and ignores the presence of a third media (air or other material filling the spaces between the spheres), thus the permittivities and

conductivities derived using the model can only be considered relative and are not the values of the bulk material. Nevertheless, for a series of materials with similar particle sizes and morphologies, and for which particle interactions are similar, these effective ϵ and σ values will follow the trends of the bulk values. The group of ZrM_2 alloys and hydrides explored in this thesis is such a series, and therefore relative differences in ϵ_{eff} and σ_{eff} between these materials will reflect bulk $\Delta\epsilon$ and $\Delta\sigma$ values.

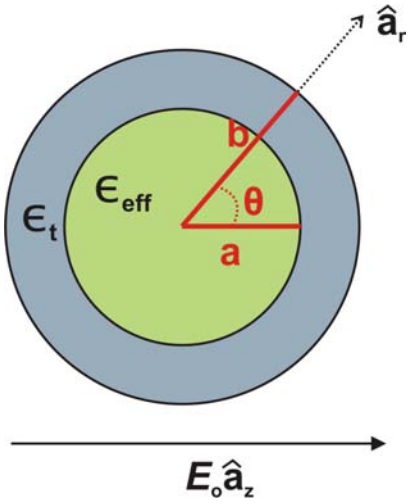

Figure 2.10: *2D cross section of the collapsed cylinder model. The grey circle shows the tube enclosing the sample, of radius b, and the green circle shows the collapsed cylinder, of radius a. The direction of the field is shown.*

Figure 2.10 shows the construction of this collapsed cylinder, of length L, where the tube containing the sample has some known permittivity ϵ_t. There exist three separate regimes for the potential a distance r from the centre of the dipole:

$$\varphi = -E_o r\cos\theta + \frac{p\cos\theta}{2\pi r} \text{ for } r > b \tag{2.59}$$

$$\varphi = -Ar\cos\theta + \frac{B\cos\theta}{r} \text{ for } a < r \leq b \tag{2.60}$$

$$\varphi = -E_{in} r\cos\theta \text{ for } r \leq a \tag{2.61}$$

where A, B represent the unknown electric field and dipole moment, respectively, in the tube wall region. E_{in} and p are properties of the sample. Using Laplace's equation in cylindrical co-ordinates and the boundary conditions outlined above, a solution for p solely in terms of $E_o, \hat{\epsilon}_t, \hat{\epsilon}_{eff}, a$ and b can be found:

$$p = 2\pi b^2 E_o \left(\frac{-\hat{\epsilon}_t^2 a^2 - \hat{\epsilon}_t a^2 - b^2\hat{\epsilon}_t + b^2\hat{\epsilon}_t^2 + \hat{\epsilon}_{eff}\hat{\epsilon}_t a^2 + \hat{\epsilon}_{eff} a^2 - b^2\hat{\epsilon}_{eff} + b^2\hat{\epsilon}_{eff}\hat{\epsilon}_t}{b^2\hat{\epsilon}_t + b^2\hat{\epsilon}_t^2 + b^2\hat{\epsilon}_{eff} + b^2\hat{\epsilon}_{eff}\hat{\epsilon}_t - \hat{\epsilon}_t^2 a^2 + \hat{\epsilon}_t a^2 + \hat{\epsilon}_{eff}\hat{\epsilon}_t a^2 - \hat{\epsilon}_{eff} a^2} \right) \tag{2.62}$$

From the definition of polarisation [56] and Equation 2.51:

$$\frac{p}{E_o \pi b^2 L} = \alpha_e \tag{2.63}$$

Thus Equation 2.62 can be directly used with Equations 2.55 and 2.57 to calculated ϵ_{eff} of a powdered sample packed in a tube from a measured value of f and Γ in the electric field antinode. In practice, desktop mathematics software is needed to carry out this calculation and deconvolute the real and imaginary components of $\hat{\epsilon}_{eff}$.

2.3.4 Instrumentation

The microwave resonator used in this work was a copper hairpin resonator, approximate dimensions 20 x 24 x 4.5 mm, designed such that an electric field antinode ($H = 0$) exists at the top of the hairpin and a magnetic field antinode ($E = 0$) exists at the bottom. In normal use, the hairpin is surrounded by a copper radiation shield, into which the input and output coupling loops feed, and is covered with a removable copper lid. Holes drilled in the shield allow the placement of a sample directly in either the E or H antinode of the hairpin. The resonator, shown in Figure 2.11, was custom designed and built by Professor Adrian Porch of Cardiff University[1] and has a primary resonant frequency of ~ 2.5 GHz and an unloaded quality factor Q of about 1600.

In accordance with the collapsed cylinder model, the samples were packed in precision quartz capillaries (sealed at one end) supplied by Hilgenberg Glass Gmbh., with dimensions of outside diameter 2.0±0.1 mm, inside diameter 1.6±0.1 mm, and length 120±0.5 mm. Air sensitive samples were packed inside an argon-filled glovebox. The tubes were filled to a depth of at least 3 cm, such that the length of tube inside the hairpin would consistently be filled with a well-packed powder. The tubes were temporarily sealed with vacuum grease (then removed from the glovebox if necessary) and the open end permanently flame sealed.

---

[1] Cardiff School of Engineering, Cardiff University
Queen's Buildings, The Parade
CARDIFF CF24 3AA

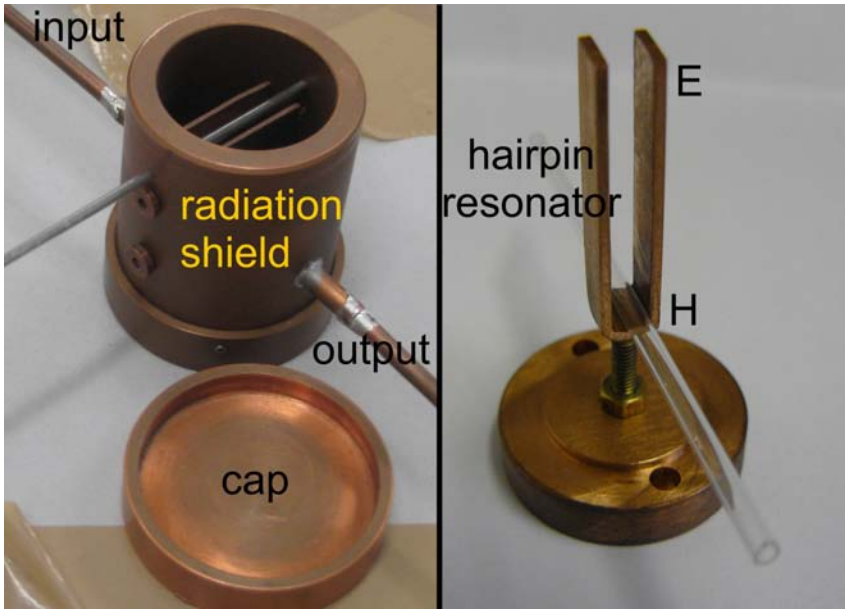

Figure 2.11: *The hairpin resonator used for the dielectric measurements in this thesis. On the left is a photograph of the resonator in normal use (with its radiation shield) and with a sample inserted in the E field antinode. On the right is a photo of just the hairpin, with the shield removed for clarity - the electric and magnetic field antinode locations are at E and H, respectively.*

The effective volume (see Equation 2.56) for this resonator was determined *via* calibration with materials of known permittivity: a 1 mm stainless steel ball (Type 302, Alfa Aesar), 0.25 mm diameter molybdenum wire (Alfa Aesar), a 0.25 mm and a 0.50 mm tin wire (Alfa Aesar) were each independently measured in the resonator. The dipole moment of these simple geometrical shapes was easily determined and used with Equation 2.55, along with tabulated conductivity values (from which $\hat{\epsilon}$ was obtained) from [81] in order to calculate V_{eff} for each material. The values were averaged together to give

$$V_{eff} = 1.9 \times 10^{-6} \text{ m}^3 \tag{2.64}$$

A vector network analyser (Agilent 5071B Network Analyser), or VNA for short, was used to determine the power transmitted across the coupling loops in the frequency domain. A typical spectrum produced by the VNA is shown in Figure 2.12. For each sample measurement, a determination of f and Γ of the empty resonator was also carried out in order to obtain Δf and $\Delta\Gamma$; in general, this

was repeated at least six times and then averaged for each sample. The averaged values for Δf and $\Delta\Gamma$ thus obtained, along with the calibrated V_{eff} value, were then used with Equations 2.57, 2.55 and 2.62 to obtain the real and imaginary components of $\hat{\epsilon}_{eff}$. The computational package Maple (Maplesoft Inc., version 13) was used to ease these calculations.

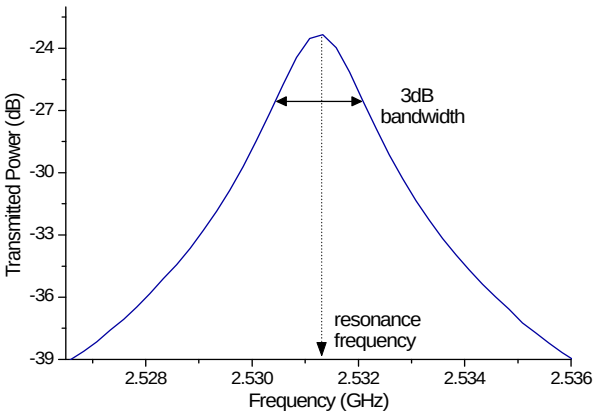

Figure 2.12: *Typical microwave resonance spectrum, showing transmitted power versus frequency. The spectra for the empty cavity, collected by the VNA, is shown, with arrows indicating the resonance frequency and the 3dB bandwidth.*

2.3.4.1 Model Development

It can be easily shown that the boundary conditions of the collapsed cylinder model (see page 54) are satisfied for the ZrM_2 series when measured on the microwave resonator described above. For a resonant frequency $f = 2.5$ GHz, condition 1 will be satisfied for a particle radius $a < 0.12$ m. Clearly, the materials measured in this thesis are easily below this limit.

Analysis of condition 2 requires a knowledge of the skin depth of the material, which is calculated from the conductivity: this presents a catch-22 situation as it is indeed the conductivity that we wish to find. However, there exist bulk resistivity measurements in the literature for the alloys ZrV_2 and $ZrMn_2$ from which a value for δ may be obtained, as shown in Table 2.2. Since no bulk resistivity measurements have been published for $ZrCr_2$ or any of the hydrides, we must make the assumption that resistivity and therefore δ will be similar to these two known values. Particle sizes can be estimated from diffraction data, as discussed on page 25, and it will be duly shown in the relevant Chapters for each ZrM_2 system that the effect of decrepitation ensures that all the samples measured had average particle sizes well below these skin depths.

	$\boldsymbol{\rho}_{bulk}$ at 300 K	**calculated** δ
$ZrMn_2$	195 $\mu\Omega$ cm [21]	12 μm
ZrV_2	95 $\mu\Omega$ cm [82]	10 μm

Table 2.2: *Published bulk resistivity values and calculated skin depths for ZrV_2 and $ZrMn_2$*

The viability of this 'collapsed cylinder' model was first tested by measuring a well-characterised insulator (MnO) and metal (V) as powders packed into a sealed quartz tube. Table 2.3 gives the measured microwave parameters and calculated dielectric properties for these materials, along with their published literature values. The 'effective' values for permittivity and conductivity are much lower than the bulk measurements due to the inclusions of gas pockets and the powder packing fractions; nonetheless, the metallic V powder is easily distinguishable from the insulator MnO. As an additional check of the calculation method, measurement of an empty tube yields $\hat{\epsilon} \simeq 1$ as would be expected from a tube filled with air.

In order to estimate the error inherent in the permittivity, loss tangent and conductivity calculations, eighteen measurements from the same sample, $ZrMn_{2.06}$ (cycled and dehydrided) were performed. The measurements were performed in sets of six, on three individually prepared quartz tubes measured on 3 different dates each separated by a period of several weeks. Each sample's spectra was then compared to a separate measurement of the empty cavity, taken at the same time. From each calculation of $\Delta\Gamma$ and Δf, the 'effective' values for ε_1, ε_2, $\tan\delta$, and σ were determined. Table 2.4 lists the statistical data for this series of measurements. The relative standard deviations are likely an overestimate but can be considered as the outside limits of the error in this conductivity determination.

This Work:	Δf (Hz)	$\Delta\Gamma$ (Hz)	ε_{1eff}	ε_{2eff}	σ_{eff} (Ω^{-1} m^{-1})
MnO	-2.070×10^7	1.7×10^3	2.60	-2.20×10^{-4}	3.06×10^{-5}
	$\pm 5.5 \times 10^4$	$\pm 5.9 \times 10^3$			(300 K)
V	-3.11×10^7	8.69×10^5	9.86	-0.823	0.114
	$\pm 1.4 \times 10^5$	$\pm 9.9 \times 10^3$			(300 K)
Empty	-1.071×10^7	-2.5×10^4	0.970	1.23×10^{-3}	1.71×10^{-4}
Tube	$\pm 1.2 \times 10^5$	$\pm 6.9 \times 10^3$			(300 K)
Literature:			ε_1	ε_2	σ_{bulk} (Ω^{-1} m^{-1})
MnO			12.8 [81]		12.5 [83]
					(1273 K)
V					5.08×10^6 [81]
					(298 K)
Air			1		3×10^{-15} [84]
					(298 K)

Table 2.3: *Measured microwave resonance parameters for an empty tube, and MnO and V powders packed into quartz tubes, along with dielectric properties calculated as described in the text. Selected literature values are shown for comparison.*

	Mean	*Standard Deviation*	*r.s.d.* (%)	*Highest Value*	*Lowest Value*
$\Delta\Gamma$ (Hz)	1.6×10^6	1.2×10^5	7.5	1.81×10^6	1.46×10^6
Δf (Hz)	-3.07×10^7	6.9×10^5	2.3	-2.96×10^7	-3.15×10^7
ε_{1eff}	9.2	1.1	11.4	10.4	7.52
ε_{2eff}	-1.4	0.37	25.8	-0.89	-1.90
σ_{eff} (Ω^{-1} m^{-1})	0.19	0.052	25.8	0.265	0.124
$\tan\delta$	0.15	0.024	15.5	0.184	0.118

Table 2.4: *Error statistics for a set of 18 microwave resonance measurements* ($N = 18$) *performed on a cycled, dehydrided sample of* $ZrMn_2$

2.4 Synthetic Techniques

2.4.1 Raw Materials

The ZrM_2 alloys (M = V, Cr, Mn) described in this thesis were prepared from the elements: the same zirconium crystal bar turnings (99.5% pure, Lot J07M24, Alfa Aesar) were used for all the samples studied, with the addition either of manganese granules ($0.8-3.0$ mm, Lot E30S027, Alfa Aesar), chromium pieces ($3.0-8.0$ mm, 99.99% pure, Lot I07S001, Alfa Aesar), or vanadium crystal bar turnings (99.7% pure, Lot 08214DD, Sigma Aldrich).

Hydriding and deuteriding of these alloys was accomplished by passing the pure gases over the alloys: both the hydrogen (research grade, 99.9995% pure) and the deuterium (99.8% pure) were purchased from BOC Gases. Research grade Ar (BOC Gases, 99.9995% pure) was used for dehydriding and inert gas cycles during these syntheses.

2.4.2 Handling of Air Sensitive Materials

Many of the materials studied in this thesis – namely, the hydrided and deuterided materials, as well as the finely divided dehydrided samples – were both air and moisture sensitive. Unless expressly stated otherwise, all materials were stored and handled in an argon-filled glovebox, in which oxygen and water vapour levels were monitored and maintained at average levels of $O_2 < 10$ ppm and $H_2O < 0.1$ ppm.

2.4.3 Metallurgical Techniques

The ZrM_2 alloys used in this work were prepared from the elements *via* arc melting [3], using a custom-built arc furnace in Dr David Book's group at the University of Birmingham. To produce an ingot of total mass 4 - 5 grams, an approximately 2 g charge of zirconium was accurately weighed and this weight then used to

calculate the amount of the alloying element M required. In the case of M = Mn, an extra 10% above the stoichiometric amount was included to account for the high vapour pressure of Mn at the temperatures needed to form the alloy [81] and evaporative losses thus expected. The metal lots were combined and loaded onto a water cooled copper hearth within the arc furnace, along with a small ingot of Ti in a separate boat to act as a getter, and the system was evacuated. After three cycles of evacuation and Ar flushing, the arc furnace was then filled with 800 mbar Ar. In order to remove any trace O_2 or H_2O, the Ti getter was melted for three minutes at an arc current of 90 amps; after this purification, the samples themselves could then be melted. Each sample was melted several times (flipping the ingot in between each melt) in order to produce a homogeneous microstructure.

2.4.4 Annealing Methods

To secure the appropriate phase of the alloy, it was necessary to anneal the as-cast ingots; appropriate annealing temperatures and times were determined from published phase diagrams [26] and repeated experimentation. In order to avoid the formation of oxides and other impurity phases, this was carried out either under a flow of Ar gas or in a sealed evacuated tube, the procedures for both of which are described below.

2.4.4.1 Sealed Evacuated Tubes

The ground ingot was placed in an alumina crucible, which was then placed inside a quartz tube. Using a Swagelok ® fitting along with a pair of O-rings to effect an air-tight seal, this tube could then be closed off with a greaseless vacuum tap ('Young's tap' from J. Young Ltd, London, England) to control the tube atmosphere —this is illustrated in Figure 2.13 (a). The tube, thus sealed, could then be removed from the glovebox and connected to a vacuum line, where it was evacuated to a pressure of $\sim 5 \times 10^{-4}$ mbar using an Oerlikon TurboVac 50

(Leybold Vacuum) over 1 to 2 hours. The tube was then permanently sealed using an oxygen-natural gas torch and heated in a muffle furnace as required.

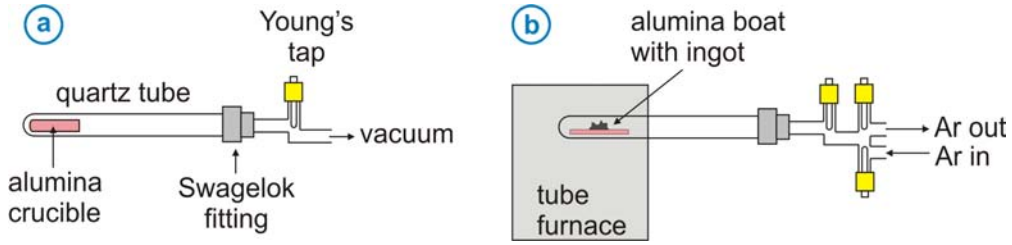

Figure 2.13: *Tube reactions for annealing metal alloys. On the left, a), is the set-up for a evacuated tube capped with a single Young's tap. On the right, b), is the set-up for a flowing gas reaction in a horizontal tube furnace.*

2.4.4.2 Flowing Gas Reaction

The solid ingot was placed in an alumina boat, which was then placed inside a quartz tube. Using a Swagelok ® fitting along with a pair of O-rings to effect an air-tight seal, this tube could be capped with a set of triple Young's taps to control the flow of gas through the tube as illustrated in Figure 2.13 (b). The tube was placed inside a horizontal tube furnace and Ar gas, after passing through a sulphuric acid bubbler to remove water, was flown into one of the Young's taps with PVC tubing, with the other tap, acting as a gas outlet, attached to a paraffin bubbler to prevent the suck-back of atmospheric air. A continuous flow of gas was established such that a steady stream of bubbles was sustained in the paraffin bubbler.

2.4.4.3 Anneal Regimes

The annealing process for each alloy is outlined below:

- $ZrMn_{2+x}$: as-cast ingots were ground in the glovebox and placed in sealed evacuated tubes. In the muffle furnace, the sealed tubes were heated to 1000°C at 2°C/min and held at that temperature for 3 hours. Samples with higher manganese concentrations ($x = 0.31, 0.44$) required an additional

annealing step to secure single-phase samples: these samples were annealed again in sealed evacuated tubes for an additional 10 hours at 1000°C.

- ZrV_2: the as-cast ingots were ungrindable, so the solid ingots were annealed under flowing Ar at 1050°C for 48 hours. The ingots were heated at a rate of 2°C/min and, once cool, brought into the glovebox and ground into a fine powder.

- $ZrCr_2$: As for ZrV_2, the solid ingots were annealed under flowing Ar at 1100°C for 7 hours. The ingots were heated at a rate of 10°C/min and, once cool, brought into the glovebox and ground into a fine powder.

2.4.5 Hydriding and Dehydriding Reactions

2.4.5.1 Instrumentation

Hydriding and dehydriding of samples was carried out on a purpose built high-pressure hydriding apparatus that was designed and constructed by the author (see Figure 2.14 for a block diagram, and Figure 2.15 for a photograph). This equipment allows the control of the pressure, flow and temperature of gases interacting with a sample, and the monitoring of the evolution or absorption of gas.

Gases (hydrogen and argon) enter the apparatus from cylinder points beside the equipment. Regulators on the cylinders control the input pressure, and Valves 1, 2 and 3 allow flow to be quickly turned on or off. The additional 'spare' point allows other gases (*e.g.* deuterium) to be admitted. A BOC Edwards TIC Vacuum system (backing diaphragm pump + turbo pump), controlled by Valve 4, allows the line to be evacuated to $\sim 10^{-5}$ bar. A scrubber (Agilent, OT3-4-SS) removes trace O_2 and H_2O vapour. Valves 5 and 6 allow the scrubber to be sealed off and protected from the atmosphere in the event that the line needs to be opened up. To purge gas in the lines, Valves 7 and 13 can opened to vent to atmosphere.

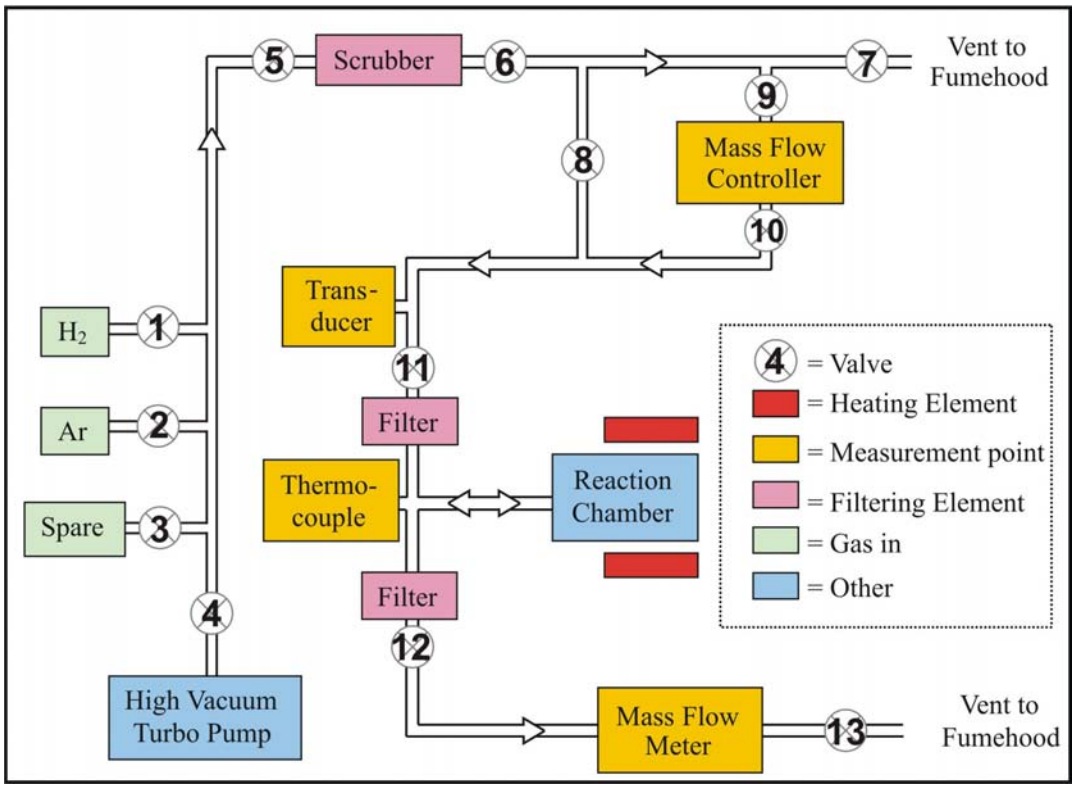

Figure 2.14: *Block diagram of the author's custom built hydriding apparatus. Operation of the apparatus and details of the components are described in the text.*

A Brooks Model 5850S mass flow controller (MFC) regulates the flow of gas into the reaction chamber. The controller can be set between 5 and 250 mL/min, or can be bypassed entirely by closing valves 9 and 10 and opening valve 8. A Brooks Model 5850 mass flow meter (MFM) monitors the flow of gas exiting the chamber and can record flows between 5 and 250 mL/min. The transducer (Gems Sensors, 2200 series) measures absolute pressure between 0 and 15 bar. If valves 8, 10 and 12 are closed (and valve 11 is open) the pressure measured is the pressure in the reaction chamber.

The reaction chamber itself is a small stainless steel pot (Swagelok ®) with a volume of 20 cm^3. A band heater (TC Direct) wrapped around this pot can be ramped up to a maximum of 375 ^oC through manual temperature control. A k-type thermocouple (Omega) bored through the stainless steel line and pushed into contact with the powdered sample at the bottom of the reaction chamber

allows a measure of the temperature of the sample. Two filters (Swagelok ®) prevent the sample from possibly being blown through the line when exposed to sudden changes in pressure. Finally, valves 11 and 12 can be closed to seal the reaction chamber and allow it to be removed from the line in order to load and unload samples in a glovebox.

Figure 2.15: *Photograph of the author's custom built hydriding apparatus. On the lower left of the photo, the electronic controls and data acquistion box can be seen.*

Data from the transducer, the thermocouple, the MFC and MFM are collected using a data acquisition card (Omega, OMB-DAQ-3000) and transferred to a computer. Acquisitions occur once per second with an oversample rate of 4, such that the final recorded value for each second is actually an average of 4 individual readings.

2.4.5.2 Measurement Errors

Equilibration between the measurement devices and the sample can be a problem, particularly for temperature. As mentioned above, the thermocouple is in direct contact with the sample, but as the samples are unpacked powders, the measurement may not be exact. The samples are heated by a band heater wrapped around

the sample pot, and thus the thermal lag before the interior of the sample reaches the desired temperature must be also taken into account. The sample sizes used in the apparatus are small – ranging from 300 to 1000 mg – which minimizes the equilibrium time. Repeated experimentation allows the time for temperature equilibration between the sample and the heater to be estimated as between 100 and 200 seconds.

The pressure transducer is quite close to the reaction chamber, and the small internal volume that exists between this transducer and the sample itself allows pressure equilibrium to be rapidly reached. Repeated experimentation suggests that this occurs in (at most) a few seconds.

2.4.5.3 Hydriding Reaction

In order for the as-annealed metal alloys to react with hydrogen, an activation step was generally required. This involved heating the alloy (up to 375°C) alternately under a high pressure of hydrogen (up to 8 bar) and in vacuo until the metal began to react with hydrogen. Once activated, the ZrM_2 alloys could be repeatedly hydrided and dehydrided in a process known as *cycling*. Each alloy was cycled at least 20 times, sufficient to achieve full decrepitation, and a variety of pressures and temperatures of reaction were explored in order to explore the hydriding and dehydriding thermodynamics.

The procedure for hydriding was as follows: the reaction chamber, whilst filled with inert gas, was heated to the desired hydriding temperature. If the expected hydriding pressure, p_H, was below 1 bar, the chamber was evacuated; otherwise, it was filled with hydrogen at atmospheric pressure. The chamber outlet (valve 12) was closed, and a controlled flow of hydrogen into the chamber established - generally between 5 and 25 sccm. With the outlet shut, hydrogen pressure built in the chamber until p_H was reached. At this point, the pressure reached a plateau as the added hydrogen was consumed to form the hydride, and, once the

hydriding reaction was complete, the pressure continued to rise until line pressure was reached.

In a similar process, deuterium can be flown into the chamber rather than hydrogen to generate the deuterided compound.

2.4.5.4 Dehydriding Reaction

In order to dehydride the sample, the reaction chamber was first cooled to a temperature at which $p_H < 1$ bar. A hydrogen flow was established (typically 25 sccm) and the outlet, valve 12, was opened to establish a flowing gas system at atmospheric pressure. As no hydrogen would be desorbed under these conditions, the flow leaving the mass flow controller (MFC) was equal to the flow into the mass flow meter (MFM). To remove the hydrogen from the system in a controlled fashion, the reaction chamber was gradually heated until $p_H > 1$ bar, at which point hydrogen desorption was registered as an increase in the MFM reading (whilst the MFC reading remained steady). Dehydriding was judged to be complete when the MFM reading was once again equal to the MFC reading.

2.4.6 Other Experimental Methods

Dehydriding of ZrM_2H_x samples was also accomplished in some cases on the benchtop vacuum line. As per the sealed evacuated tube reactions described in Section 2.4.4.1, hydrided samples were loaded into alumina crucibles in the glovebox. These were then placed in quartz tubes capped with a single Young's tap and evacuated. Once a vacuum was established, the tube was lowered into a vertical tube furnace (whilst still on the vacuum line) and heated in order to desorb the hydrogen. The heating programs for each system are as follows:

- $ZrMn_{2+x}$: The tube was heated under vacuum, at a rate of 5°C/min, to 275°C and held there for 1 hour.

- ZrV_2: The tube was heated under vacuum, at a rate of 20°C/min, to 650°C and held there for 1 hour.

- $ZrCr_2$: The tube was heated under vacuum, at a rate of 20°C/min, to 550°C and held there for 1 hour.

Once the sample had cooled to $T < 100$°C, the Young's tap was closed and the tube brought back into the glovebox, where the now-dehydrided sample could be extracted. This method was used to prepare the dehydrided samples for crystallographic analysis, magnetic measurements and microwave resonator experiments.

Chapter 3

CRYSTALLOGRAPHIC, MAGNETIC AND ELECTRONIC PROPERTIES OF THE ZRMN$_{2+X}$ SYSTEM AND ITS HYDRIDES

Experience is the name everyone gives to their mistakes. *Oscar Wilde*

3.1 Introduction and Scope

The intermetallic Laves phase compound $ZrMn_2$, which was first introduced in Section 1.2.1, has been actively researched for approximately forty years [19, 85], yet there remain many fundamental questions about the nature of this material. It is known to crystallise in the C14 Laves phase structure, space group $P6_3/mmc$, and magnetic studies have shown that it is a Pauli paramagnet down to 5 K [30]. There exist an entire group of theoreticians who suggest that this structure must be magnetically ordered at low temperatures [21, 31, 32]; however, this has never been experimentally observed. $ZrMn_2$ is not just a line phase, existing in the same C14 structure over the range $ZrMn_{2+x}$ [26]; and although the details of the superstoichiometric ($x > 0$) structure have been previously described [22], the substitutional model of the substoichiometric version ($x < 0$) remains a mystery.

This intermetallic compound also readily absorbs hydrogen to form the hydride series $ZrMn_{2+x}H_3$ at accessible temperatures and pressures [34]. A range of studies on these hydrides have been published, but lack a cohesive approach and fail to succinctly describe the variation in structural and thermodynamic properties with x [27, 28, 86]. Moreover, although initial magnetic studies have shown that the hydride is a spin glass magnet at low temperatures [30], no model for the magnetic ordering in this system has yet been proposed.

The following chapter will present a detailed examination of the $ZrMn_{2+x}-H$ system, carefully examining, over a multitude of fundamental properties, the effect of varying both the manganese and hydrogen content. This will include hydriding thermodynamics, crystal structure, magnetic behaviour, magnetic structure, dielectric properties and electrical conductivity. Important novel contributions to the body of academic knowledge will include determination of the crystal structure of substoichiometric $ZrMn_{2+x}$ and its deuteride; observation of magnetic order in the $ZrMn_{2+x}$ system; the magnetic structure of the $ZrMn_{2+x}$ system and how this changes upon hydriding, which is validated *via* low temperature neutron diffraction; and a study of the dielectric properties and electrical conductivity for $ZrMn_{2+x}$ compounds and their hydrides. The chapter will conclude with a summary and discussion of these properties and their variation across the $ZrMn_{2+x}-H$ system.

3.2 Synthesis of the $ZrMn_{2+x}$ alloys

A series of six $ZrMn_{2+x}$ alloys were synthesised *via* arc-melting as described in Section 2.4.3, with inclusion of an annealing step to help to secure homogeneous single-phase alloys. From the mass of zirconium used in the arc-melting and the weight of the melted ingot, with the difference between these two assumed to be entirely due to manganese, the nominal composition of the six alloys is as follows:

$$ZrMn_{1.67},\ ZrMn_{2.02},\ ZrMn_{2.17},\ ZrMn_{2.20},\ ZrMn_{2.30},\ ZrMn_{2.43}$$

These nominal compositions do not reflect the actual elemental ratios in the alloys as at 1500°C – a temperature close to that used in the alloy synthesis – manganese has a vapour pressure of approximately 0.03 bar [81] and thus significant evaporative losses occurred over the course of synthesis. The ratio of zirconium to manganese in the resulting ingot therefore could not be accurately predicted from the amounts of the starting materials.

3.3 Crystallographic Features of the $ZrMn_{2+x}$ alloys

As was introduced in Section 1.2.1, at room temperature $ZrMn_2$ is known to crystallise in a hexagonal C14 Laves phase structure belonging to the space group $P6_3/mmc$; the structural details of the reported structure are given in Table 1.1. This hexagonal structure is retained over a wide homogeneity range $ZrMn_{2+x}$, $-0.5 < x < 1.8$ [26], with a small lattice expansion or contraction accompanying the manganese depletion or substitution, respectively [27, 28]. Coupled density measurements and crystallographic studies have revealed that excess manganese in the $ZrMn_{2+x}$ superstoichiometric alloys ($x > 0$) is accommodated in the C14 structure *via* partial replacement of zirconium on the $4f$ site with manganese [22, 29]. The mechanism by which excess zirconium is stabilised in the C14 lattice in the substoichiometric alloys ($x < 0$) has not yet been elucidated.

3.3.1 Structure of the nearly stoichiometric $ZrMn_{2+x}$ alloy

The crystalline structure of the as-synthesised alloy with nominal composition $ZrMn_{2.02}$ (see Section 3.2 for synthetic details) was examined on the ID31 beamline at the ESRF – a full description of the instrument and the experimental parameters can be found in Section 2.1.2.1. The collected synchrotron data were analysed using the Rietveld method described in Section 2.1.4; an R_{wP} of 23.683 was obtained for a fit using only the C14 Laves phase structure of $ZrMn_2$ described above. In the refinement process, the metal atoms were constrained to the $4f$, $2a$, and $6h$ sites as in the reported structure [21]; those atomic coordinates not constrained by the site symmetry were freely refined, as were the global lattice parameters and the thermal parameter of each atom. The observed diffraction pattern and calculated fit are shown in Figure 3.1.

As noted in Section 3.2, the exact composition of the alloy could not be accurately determined solely from the ratio of the starting materials due to ready evaporation of manganese. However, with suitably intense and well-resolved diffraction data – *e.g.* from a synchrotron X-ray source – the relative atomic percentages of

zirconium and manganese on each lattice site can be refined and the value of x in $ZrMn_{2+x}$ determined. The relative scattering powers of the manganese and zirconium atoms (as determined by the X-ray form factor, Equation 2.12) allow the two atoms to be readily distinguished. As the excess manganese is accommodated *via* partial replacement of zirconium [22], the $4f$ site in the structural model of the $ZrMn_{2+x}$ phase was described as simultaneously occupied by manganese and zirconium, with the sum of the fractional occupancies of these atoms equal to one:

$$occ(Mn3) + occ(Zr1) = 1 \tag{3.1}$$

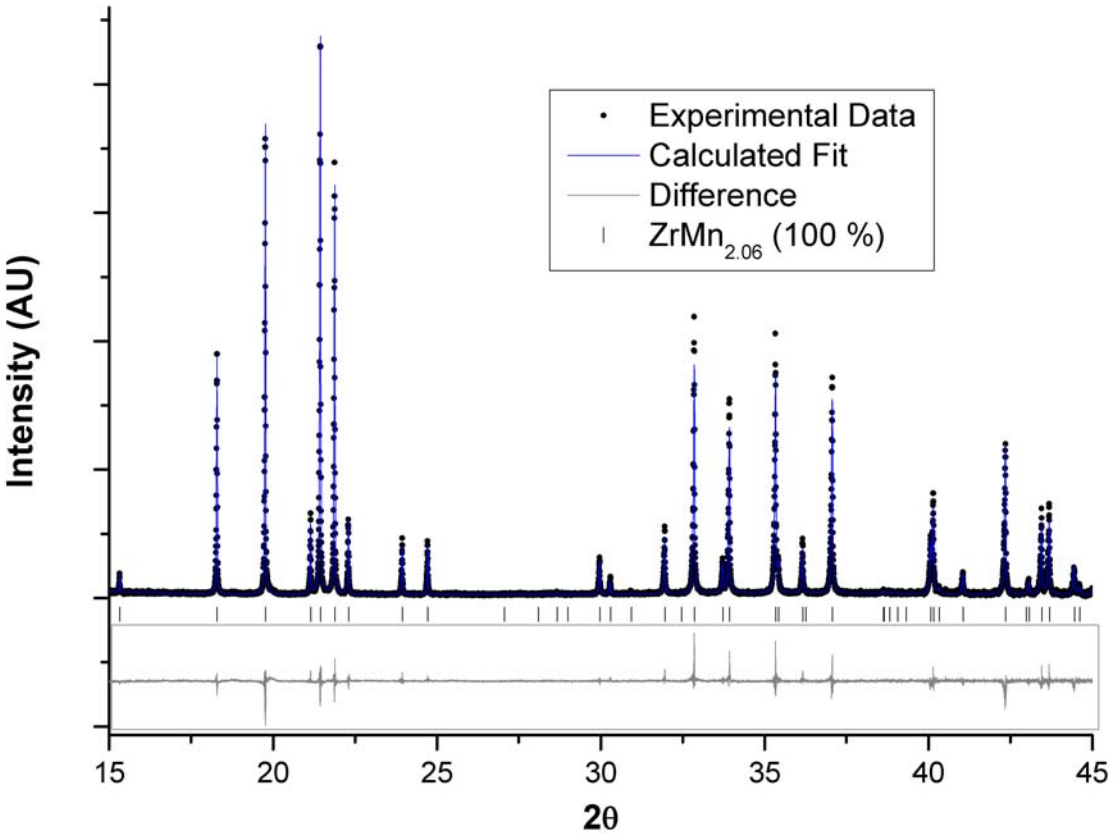

Figure 3.1: *Synchrotron diffraction pattern for the alloy $ZrMn_{2.06}$, which was fitted with solely the C14 $ZrMn_{2.06}$ phase. The ticks marks for this phase are shown at the bottom of the diagram. The difference plot between the observed experimental data (black points) and calculated fit (blue solid line) is shown as a grey line enclosed in a box. $R_{wP}(alloy) = 23.683$.*

Under the restriction of Equation 3.1, the Mn3 and Zr1 occupancies were refined from the alloy diffraction data and converged at a composition of $ZrMn_{2.06}$, with an error on x of ± 0.02. The alloy of nominal composition $ZrMn_{2.02}$ will therefore be referred to from this point on as $ZrMn_{2.06}$ or the 'nearly stoichiometric' alloy, using this accurately refined value as the correct composition.

The structural parameters of the refined $ZrMn_{2.06}$ phase are presented in Table 3.3 (on page 92); this refined structure agrees excellently with the reported structure for the stoichiometric alloy [21]. The close agreement supports the refinement of the excess manganese atoms to a nearly stoichiometric composition of $ZrMn_{2.06}$. A satisfactory fit ($R_{wP} = 23.683$) to the collected diffraction data of the alloy was accomplished using only this $ZrMn_{2.06}$ phase; no phase fraction of any oxide or traces of the starting materials could be reliably refined.

3.3.2 Structure of the superstoichiometric $ZrMn_{2+x}$ alloys

X-ray diffraction data on the as-synthesised $ZrMn_{2+x}$ alloys (the method of preparation is detailed in Section 3.2) with nominal compositions $ZrMn_{2.17}$, $ZrMn_{2.20}$, $ZrMn_{2.30}$ and $ZrMn_{2.43}$, were collected at two different synchrotron radiation facilities. The alloys were measured either on the ID31 beamline at the ESRF or the I11 beamline at Diamond; instrumental details of both these beamlines, as well as the conditions under which the diffraction patterns were collected, can be found in Section 2.1.2.1. The data were analysed using the Rietveld method (see Section 2.1.4) and in each case were successfully fitted with only the hexagonal $ZrMn_{2+x}$ structure. No phase fraction of any oxide, or lingering starting material, could be reliably refined in the superstoichiometric alloy diffraction data.

During the refinement of the $ZrMn_{2+x}$ phase of the superstoichiometric alloys, the metal atoms were restrained to the $4f$, $2a$, and $6h$ sites as in the reported structure [22]; those atomic coordinates not constrained by the site symmetry were freely refined, as were the global lattice parameters and the thermal parameter of

each atom. Excess manganese was accommodated on the $4f$ site using the restriction introduced in Equation 3.1, and the relative occupancies of zirconium and manganese on this site were refined. From the refined Mn3 and Zr1 occupancies, the global x value for each $ZrMn_{2+x}$ phase was calculated, allowing an accurate determination of the alloy composition. These newly refined compositions, with an uncertainty on x of approximately 0.02, are as follows:

$$ZrMn_{2.13},\ ZrMn_{2.18},\ ZrMn_{2.31},\ ZrMn_{2.44}$$

and will be taken to replace the nominal compositions of the alloys that were estimated previously from the weight of the ingots.

The structural parameters of the refined $ZrMn_{2+x}$ phases are presented in Table 3.1; these refined structures agree well with previously published crystallographic studies on the superstoichiometric $ZrMn_{2+x}$ intermetallic compounds of comparable compositions [27, 28, 86]. The observed diffraction pattern and calculated fit for each superstoichiometric alloy can be found in Appendix A; all are extremely similar to the pattern presented in Figure 3.1 for the $ZrMn_{2.06}$ alloy.

3.3.3 Structure of the substoichiometric alloy

In order to determine the sites and relative distributions of zirconium and manganese in the substoichiometric $ZrMn_{2+x}$ compound, diffraction data on the as-synthesised alloy with nominal composition $ZrMn_{1.67}$ were collected on the I11 beamline at Diamond. The details of this instrument and the experimental parameters under which the data were collected can be found in Section 2.1.2.1; the collected data were then analysed using the Rietveld method (see Section 2.1.4).

The diffraction data were initially fitted with the same hexagonal C14 structure as stoichiometric $ZrMn_2$; however, there was a mismatch in peak intensities which indicated that some difference might exist between the model ($ZrMn_2$) and the actual structure. In order to determine the manganese and zirconium sites

and occupancies, four possible models which conserve the original base metal substructure but allow for a manganese deficiency were tested.

Parameter	$ZrMn_{2.13}$	$ZrMn_{2.18}$	$ZrMn_{2.31}$	$ZrMn_{2.44}$
Instrument	ESRF	ESRF	ESRF	Diamond
Wavelength, λ (Å)	0.79986	0.79986	0.79986	0.824971
a (Å)	5.0310(1)	5.0223(1)	5.0064(1)	4.9944(5)
c (Å)	8.2687(3)	8.2390(3)	8.2232(4)	8.2036(8)
V (Å^3)	181.251(1)	179.973(9)	178.49(1)	177.21(4)
R_{wP}	10.320	10.184	11.043	17.118
$4f$ site $(\frac{1}{3}, \frac{2}{3}, z)$	0.0635(1)	0.0643(3)	0.0639(2)	0.0642(2)
Zr1 occ.	0.96(1)	0.944(5)	0.907(7)	0.873(7)
Mn3 occ.	0.04(1)	0.057(5)	0.093(7)	0.111(7)
B_{eq} (Å^3)	0.17(3)	0.85(9)	0.62(8)	0.68(4)
Mn1, $2a$ site $(0, 0, 0)$	-	-	-	-
B_{eq} (Å^3)	0.17(5)	0.26(8)	0.68(9)	0.56(7)
Mn2, $6h$ site $(x, 2x, \frac{1}{4})$	0.8299(1)	0.8309(4)	0.8298(2)	0.8312(3)
B_{eq} (Å^3)	0.34(3)	0.12(9)	0.40(7)	0.66(5)

Table 3.1: *Refined structural parameters of the hexagonal $ZrMn_{2+x}$ phase, with $x = 0.13, 0.18, 0.31, 0.44$. The structural parameters were determined from the room temperature synchrotron diffraction patterns of the superstoichiometric alloys.*

The tested substoichiometric models were:

1. A partial manganese vacancy on the $2a$ site.

2. A partial manganese vacancy on the $6h$ site.

3. Substitution of zirconium for manganese on the $2a$ site.

4. Substitution of zirconium for manganese on the $6h$ site.

Each of these possible models was separately tested whilst holding all other refineable parameters constant. To examine the suitability of models 1. and 2., the occupancy of the manganese atom on the site in question was allowed to freely refine without any restrictions. In both cases; however, the occupancy converged at a value of 1, indicating that the site was fully occupied and that these vacancy models were invalid. To test models 3. and 4., an extra zirconium atom (Zr2) was entered, with identical coordinates to the site on which it was substituting with a restriction on the relative manganese and zirconium occupancy as per Equation 3.1. For both models, the refinement returned a fractional zirconium occupancy of approximately 0.15 which suggested that either substitutional scenario might be valid. It is worthwhile to note that a model in which zirconium substitution was allowed to occur at both sites simultaneously did not reach a satisfactory convergence. Further analysis revealed that model 4. refined to an R_{wP} that was 0.44 lower than that found for model 3. Therefore, the best possible fit to the observed diffraction data of the substoichiometric alloy was a hexagonal structure similar to that observed for $ZrMn_2$ but with a partial substitution of zirconium for manganese on the $6h$ site.

With this initial model, the collected diffraction data for $ZrMn_{1.67}$ could then be analysed. The metal atoms in the $ZrMn_{2+x}$ phase were restrained to the $4f$, $2a$, and $6h$ sites as in the reported stoichiometric structure [21]; those atomic coordinates not constrained by the site symmetry were freely refined, as were the global lattice parameters and the thermal parameter of each atom. Excess zirconium was accommodated *via* substitution onto the $6h$ site; the occupancies of the manganese and zirconium atoms on this site were refined within a restraint analogous to that in Equation 3.1, and the refinement subsequently converged at

a composition of $ZrMn_{1.65}$, with an error on x of ± 0.02. This refined value will be taken as the accurate composition of the substoichiometric $ZrMn_{2+x}$ alloy. The full structural details of this $ZrMn_{1.65}$ phase are reported in Table 3.5 (on page 98); the lattice parameters agree well with the only reported partial refinement of a similar structure, $ZrMn_{1.8}$ [27].

This proposed substitutional model for $ZrMn_{1.65}$ is novel, but there exists a precedent for the accommodation of excess A atoms on the one of the B sites in C14 AB_2 intermetallics. The hexagonal Laves phase $TiMn_{2+x}$ is characterised by a large compositional range much like $ZrMn_{2+x}$, and a detailed neutron diffraction study on a substoichiometric member of this phase has been carried out by Fruchart *et al.* [87]. The work in question found that the substoichiometric $TiMn_{1.45}$ retained the original C14 structure of $TiMn_2$, with the change in composition accomplished *via* a partial replacement of Mn by Ti solely on the $2a$ site; a statistical distribution of the excess Ti between both the $2a$ and the $6h$ site was shown to be less favourable [87].

The diffraction pattern for the $ZrMn_{1.65}$ alloy, along with the calculated fit, is shown in Figure 3.2. It evident from the data that this is not a single phase material: additional peaks that could not be assigned to $ZrMn_{1.65}$ were found at 2θ = 16.03, 17.47, 19.66, 20.86, 22.72, 28.79, 34.37 and 40.54°. Previous workers [25, 86] have found the same set of unmatched peaks in diffraction data of substoichiometric $ZrMn_{2+x}$; energy dispersive X-ray analysis [25] suggested that this minor secondary phase had the composition ZrMn, with structure unknown. The Zr-Mn binary phase diagram (shown in Figure 1.3) does not, however, indicate the existence of any 'ZrMn' compound and in fact suggests that, at room temperature, the only phases possible in the system are $ZrMn_{2+x}$, α-Zr dissolving at most 1 at. % Mn, and α-Mn dissolving 1.25 at. % Zr [26].

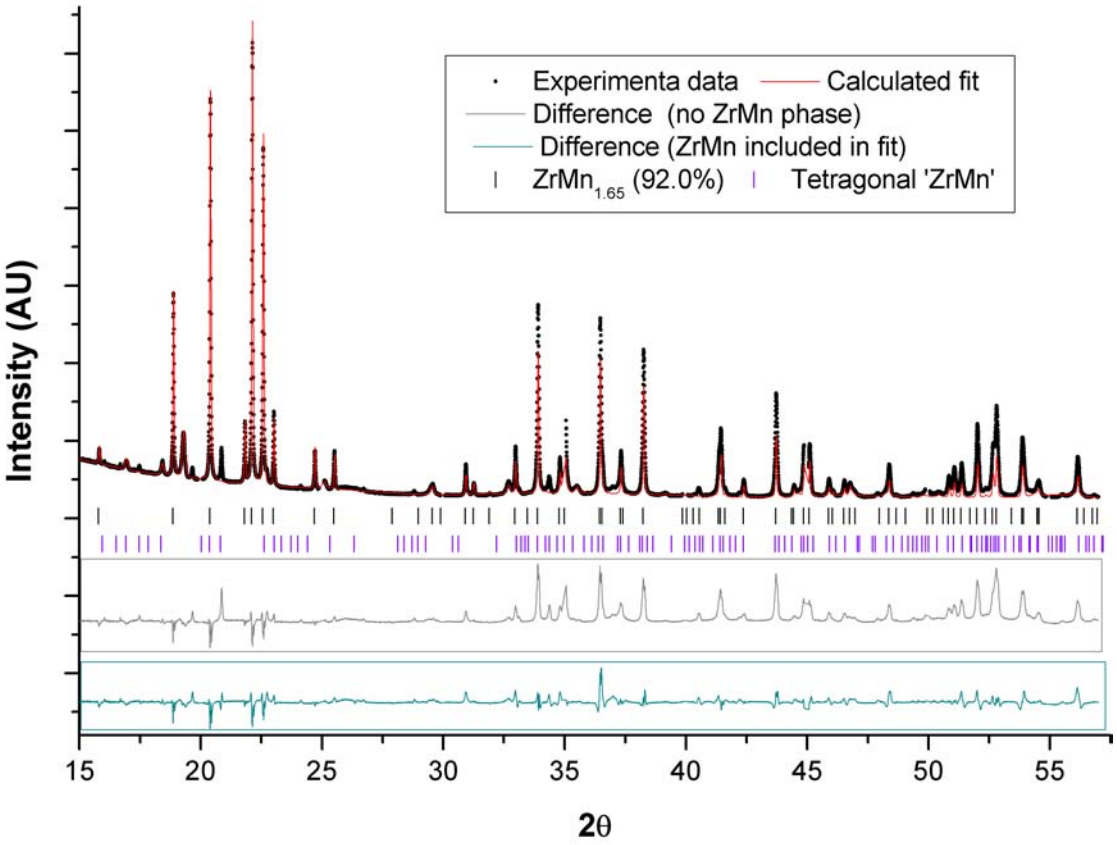

Figure 3.2: *Synchrotron diffraction pattern for the alloy* $ZrMn_{1.65}$*, collected at room temperature. The pattern was fitted with a mixture of phases; the major phase (92.0 weight percent) is C14* $ZrMn_{1.65}$*, with tick marks for the Bragg peak positions of this structure given below in black;* α*-Zr is the main impurity, at 7.9 weight percent (tickmarks not shown). The red line indicates the calculated fit* ($R_{wP} = 15.775$)*, with the difference between the calculated and observed pattern given in a grey enclosed line below. The peak mismatch is significant; however, if a P4 'ZrMn' phase (tick marks in purple) is included, the fit improves significantly, as demonstrated by the enclosed turquoise difference plot with* $R_{wP} = 5.983$.

In order to determine the structure of this possible ZrMn phase, reference is once again made to the binary Ti-Mn system. Waterstrat *et al.* [88] have demonstrated the existence of a stable TiMn phase at room temperature and, whilst it has not been fully indexed, the diffraction data of this material suggest that it crystallises in a large tetragonal unit cell. Correspondingly, an attempt was made to fit the unmatched peaks in the $ZrMn_{1.65}$ data to a tetragonal cell using the *Pawley method* [53] – this refinement technique uses only the unit cell

dimensions and the crystal symmetry to determine hkl positions, and then arbitrarily assigns intensities to match the observed data. This technique was used, rather than the preferred Rietveld method, as a full indexing of the unknown phase was complicated by the low peak intensity and the partial overlap with some $ZrMn_{2+x}$ reflections. An initial refinement of the ZrMn phase in the $P4$ unit cell yielded a satisfactory fit ($R_{wP} = 5.983$) to a cell with dimensions $a = 8.4309(1)$ Å, $c = 2.8782(1)$ Å. It is likely that the actual structure contains more symmetry elements than this simplistic refinement suggests; however, a full determination of the ZrMn structure could not be accomplished at this time.

The nature of the Pawley refinement, *viz.* calculating a fit using an empty unit cell, necessitates that the relative percent of the ZrMn phase cannot be determined from its X-ray diffraction data; however, the low intensity of the ZrMn diffraction peaks, as compared to the $ZrMn_{1.65}$ phase, suggests that it is not a major phase. A further impurity was also present in the alloy diffraction data: 7.99 wt. % of α-Zr (space group $P6_3/mmc$ [89]) was included in the initial Rietveld refinement of the data. This zirconium is likely unreacted starting material from the arc-melting of the alloy.

3.4 Synthesis of the $ZrMn_{2+x}$ hydrides ($-0.35 \leq x \leq 0.44$) and the dehydriding process

3.4.1 The hydriding process

The hydrides $ZrMn_{2+x}H_3$ were generated from the annealed alloys using the hydriding apparatus described in Section 2.4.5 at a variety of hydriding temperatures and pressures. Figure 1.1 on page 3 illustrates the absorption of hydrogen over time for $ZrMn_{2.06}$ at a temperature of 120°C and a constant hydrogen flow rate of 15 sccm. These data can be translated into a pressure-temperature-composition (pcT) plot in order to compare hydriding reactions carried out at differing temperatures and flow rates. The hydrogen content in the sample can be continuously

calculated by comparing the actual pressure against the known flow rate and time elapsed; if this is then plotted against the measured pressure, and the process repeated at several temperatures, a series of isotherms is generated. This is illustrated in Figure 3.3 for the alloy $ZrMn_{2.06}$.

There is, however, a caveat to this method of calculating composition: as the pressure determinations are taken continuously, without allowing the system to reach equilibrium after each aliquot of hydrogen is added, the amount of hydrogen thus determined will always be less than the amount that was actually absorbed. As accurate hydrogen concentrations could be easily obtained on the subsequent dehydriding cycle, the calculated hydrogen composition was scaled to its actual value and all the pcT compositions presented in this thesis are adjusted in this manner.

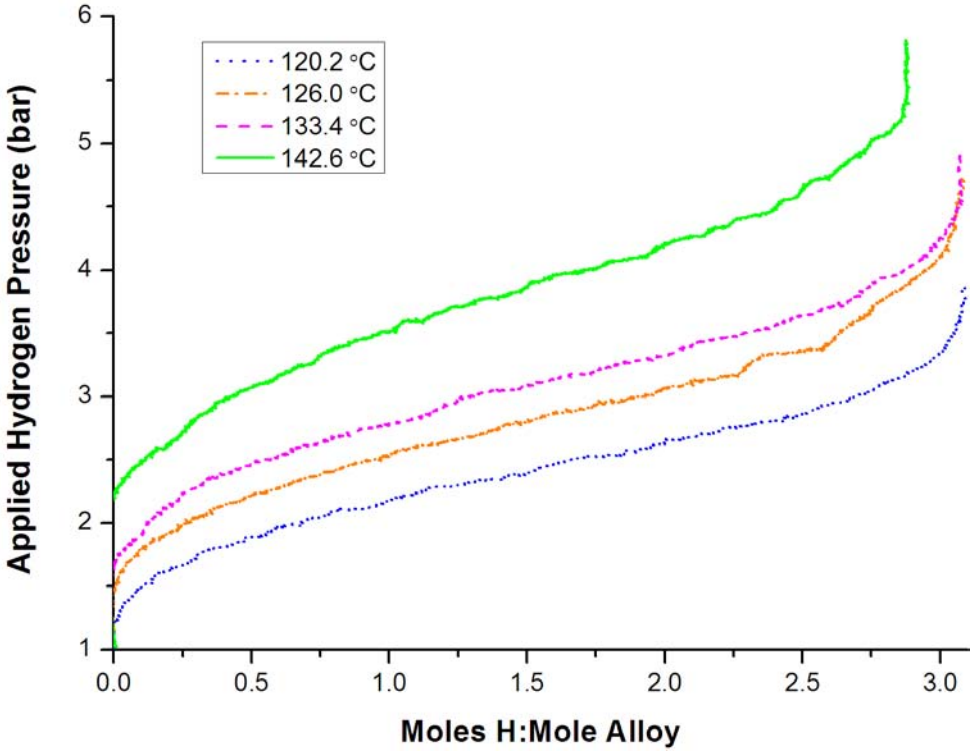

Figure 3.3: *A pressure-composition-temperature (pcT) plot for $ZrMn_{2.06}$, illustrating the change in plateau pressure of the hydriding reaction as temperature is increased. Shown are isotherms for hydriding reactions carried out at 120.2 (dotted blue line), 126.0 (dot-dash orange line), 133.4 (dashed pink line) and 142.6 (solid green line) °C.*

The nearly stoichiometric compound $ZrMn_{2.06}$ absorbs hydrogen readily —at temperatures below 100°C, the hydride forms at less than 1 bar of applied hydrogen gas. This is in agreement with the literature, which suggests that around 100°C the hydriding pressure for $ZrMn_2$ is approximately $0.2 - 0.6$ bar [28, 90]. Figure 3.3 shows that, as expected, the pressure required to hydride the alloy increases as temperature increases. This hydriding pressure can be quantified by taking the pressure measurement in the region of the two-phase plateau of the pcT (this is then called the *plateau pressure*). In the case of a sloping plateau, as occurs for the $ZrMn_{2+x}-$ H series, the plateau pressure is approximated as the pressure at the plateau's midpoint [8]. Thus, the plateau pressure at 142.6°C for $ZrMn_{2.06}$ was found to be approximately 3.7 bar; slightly higher than the value of 2.5 bar found by Luo *et al.* [28] for the stoichiometric compound at 150°C. The deviation between these two values should not be taken as significant: previous workers have shown that the plateau pressure for $ZrMn_{2+x}$ hydrides is strongly dependent on the exact manganese content and the microstructure of the system, and thus measured values differ significantly when the synthesis method and annealing program are altered [28, 34]. Nonetheless, the hydriding properties that were measured for the $ZrMn_{2.06}$ alloy in this thesis agree well with the trends reported in the literature for the stoichiometric compound, and a full table of measured plateau pressures at a variety of temperatures can be found in Appendix A.

Figure 3.3 also suggests that $ZrMn_{2.06}-$ H is a miscibility gap system,with no intermediate phases existing between the fully hydrided version ($ZrMn_{2.06}H_3$) and the hydrogen-free alloy. Moreover, the gap decreases with increasing temperature, although the hydriding temperatures tested here were all well below the critical temperature.

3.4.2 Cycling and the dehydriding reaction

Data from the dehydriding reactions of the $ZrMn_{2+x}$ hydrides were also collected using the apparatus described in Section 2.4.5; Figure 3.4 is a typical dehydriding

plot for $ZrMn_{2.06}H_3$. It can be assumed that all of the weight loss over the course of a dehydriding experiment is due to hydrogen gas released from the hydride, and indeed, the total loss corresponds to the weight percent of hydrogen in the compound $ZrMn_{2.06}H_{3.16}$. It is apparent from this figure that the rate at which hydrogen is lost is at first trivial, but, as the temperature is increased to the point where the hydride is unstable at atmospheric pressure ($> 100°$ C) significant hydrogen desorption occurs. Once this point has been reached, the reaction proceeds quickly and the hydrogen-free $ZrMn_{2.06}$ is returned within approximately three minutes.

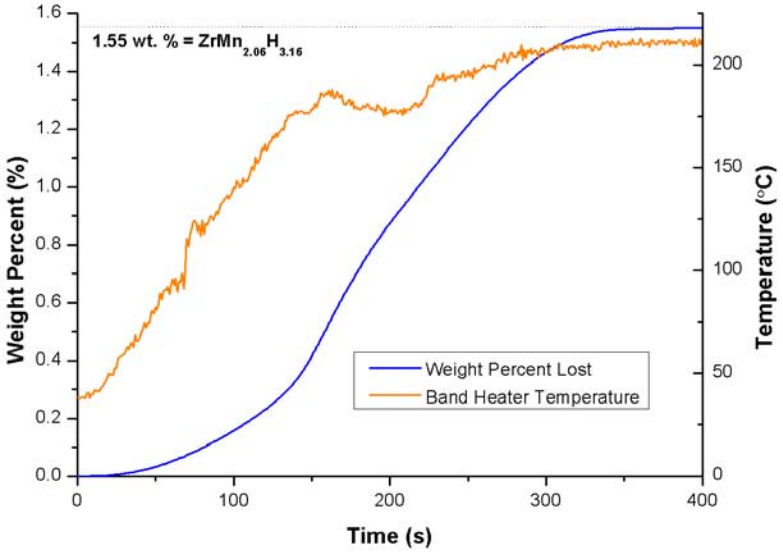

Figure 3.4: *A sample dehydriding trace for the $ZrMn_{2.06}$ hydride against time, showing applied temperature (orange) and weight percent lost from the sample (blue). The dashed line indicates the expected amount of hydrogen to be lost for a composition of $ZrMn_{2.06}H_{3.16}$.*

It was found that several hydriding and dehydriding cycles had to be carried out before the full capacity of the $ZrMn_{2+x}$ alloy could be realised; in general, this varied from eight to twelve. Figure 3.5 illustrates the increase in hydrogen capacity with the number of cycles for the $ZrMn_{2.13}-$ H system. After eight hydrogen absorption/desorption cycles, the alloy absorbs 3.1 hydrogen atoms per $ZrMn_{2.13}$ formula unit, which is judged to be its full capacity as this does not increase upon further cycling. Moreover, the amount of time elapsed during the

hydriding reaction becomes successively smaller as the number of cycles increases. This can be attributed to the particle size reduction that occurs concomitant to the hydriding reaction *via* the process of decrepitation; as the particle size is reduced, the surface area available to the exchange of hydrogen gas becomes larger and the reaction kinetics correspondingly increase. The eighth cycle can therefore also be viewed as the point of complete decrepitation of the sample as further cycling does not bring about any additional rise in dehydriding rate.

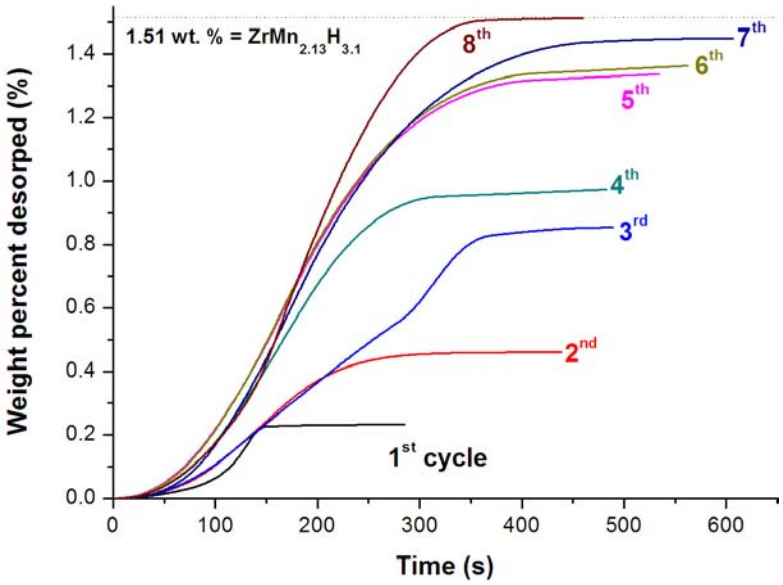

Figure 3.5: *A plot of the effect of cycling on* $ZrMn_{2.13} - H$*. The percentage of weight lost from the hydrided sample is shown on the y-axis, and the time elapsed is on the x-axis. Desorption traces, all carried out under identical conditions, are shown starting from the hydrided virgin alloy (*1^{st} *cycle) until the point of full decrepitation (*8^{th} *cycle). The dashed line indicates the expected amount of hydrogen to be lost for a final composition of* $ZrMn_{2.13}H_{3.1}$*.*

3.4.3 Influence of x on the hydriding and dehydriding properties

The hydriding properties of the $ZrMn_{2+x}$ system are found to be strongly dependent on the amount of excess manganese present. Figures 3.6 and 3.7 are comparative pcT plots for members of the $ZrMn_{2+x}$ system at ∼50°C and ∼120°C, respectively; further hydriding data at other temperatures can be found in Appendix A. It can be seen that the nearly line compound with $x = 0.06$ absorbs

the highest amounts of hydrogen and that as x increases, the pressure required for hydride formation grows and the amount of hydrogen absorbed drops. Moreover, the slope of the hydriding plateau in the two phase region also increases with x. It is evident that for some of the superstoichiometric alloys, the limitations of the equipment (maximum temperature of 375°C, maximum pressure of 8 bar) prevented collection of the full pcT: for $ZrMn_{2.44}$ at 65.1°C, $ZrMn_{2.31}$ at 117.0°C and $ZrMn_{2.18}$ at 126.5°C, the plateau had not reached its endpoint before the line pressure of 6.5 bar had been reached. It is expected that with the use of higher hydrogen pressures, more hydrogen absorption would be observed.

The manganese deficient system ($ZrMn_{1.65}$) absorbs approximately 3 hydrogen atoms per formula unit, as does the nearly stoichiometric alloy, $ZrMn_{2.06}$, and $ZrMn_{2.13}$. The more superstoichiometric alloys do not reach this capacity but as noted above, under higher hydrogen pressures these systems might also absorb 3 hydrogens per formula unit. The substoichiometric alloy hydrides at significantly lower pressures than the line phase analogue —as Figure 3.7 illustrates, the plateau pressure for $ZrMn_{1.65}-$ H is 0.5 bar lower than that for $ZrMn_{2.06}H_3$, even though the hydriding temperature is 34°C higher.

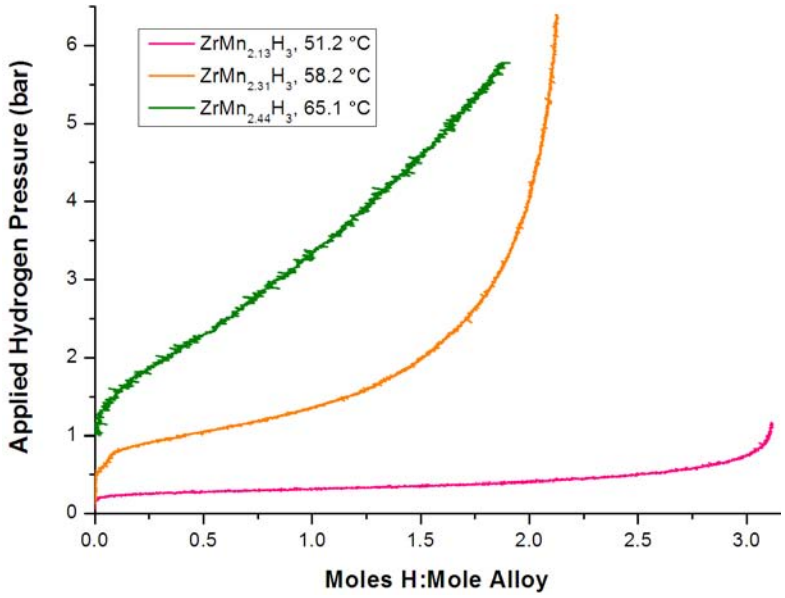

Figure 3.6: *A pcT plot of the $ZrMn_{2+x}$ series for $x = 0.13, 0.31, 0.44$, all hydrided at temperatures between 50 and 65°C. The exact hydriding temperature for each system is indicated in the legend.*

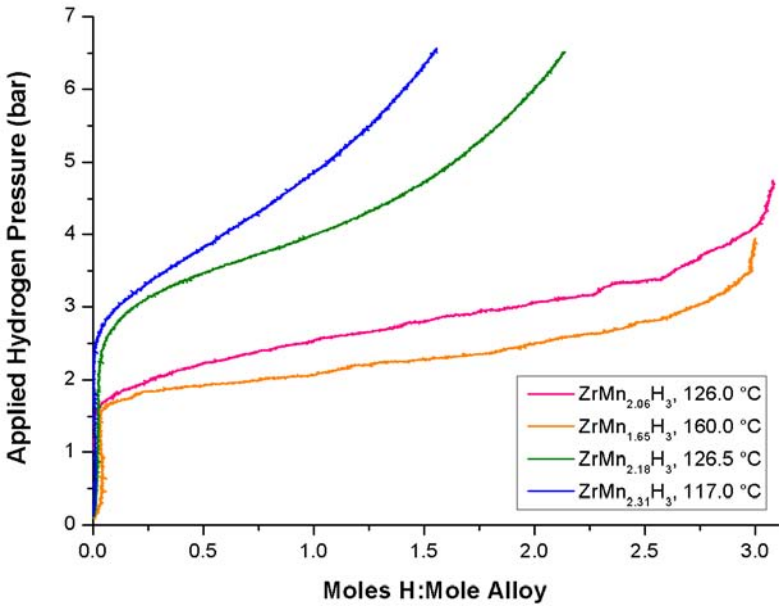

Figure 3.7: *A pcT plot of the $ZrMn_{2+x}$ series for $x = -0.35, 0.06, 0.18, 0.31$, all hydrided at temperatures between 115 and 160° C. The exact hydriding temperature for each system is indicated in the legend.*

As was noted for the nearly stoichiometric hydride, the $ZrMn_{2+x}-$ H series also appear to be miscibility gap systems. The pcT graphs (see Figures 3.6 and 3.7) show that the critical temperature, T_C, must decrease as x increases, and although values for T_C were not nominally determined, the pcT data for $ZrMn_{2.44}$ (fully detailed in Appendix A) clearly show that $T_c \approx 100°C$. For other values of x, T_C was above the highest hydriding temperatures tested.

Previous workers [28] have found the sloping plateaux of the $ZrMn_{2+x}-$ H system to be independent of annealing regime or preparation method: it appears to be an inherent property of the system. Luo *et al.* [28] have speculated on the thermodynamic significance of the sloping plateau and found that it was caused by a spread in the hydrogen chemical potential potential, μ_H, across the hydride on a macroscopic scale. This variation in μ_H is not created by inhomogeneities in the material, and is likely due to segregation of the alloy and hydride components in the vicinity of grain boundaries, or, in the case of the sub- and superstoichiometric hydrides, variations of the local manganese concentration around sites of atomic

substitution.

Just as the plateau pressure at a given temperature increased with x, it was found that the temperature required to remove hydrogen from the compound (at atmospheric pressure) decreased with x. Clearly, as the manganese concentration rises in the $ZrMn_{2+x}-$ H system, the hydride formed gradually becomes less stable. There may also be a decrease in the amount of hydrogen absorbed as x increases; however, this cannot be determined from the hydriding data collected herein alone.

3.5 *Hydriding Thermodynamics of the $ZrMn_{2+x}H_3$ ($-0.35 \leq x \leq 0.31$) system*

Although the pcT plots provide an initial view into the stability of the $ZrMn_{2+x}$ hydrides, translating these data into fundamental thermodynamic quantities like enthalpy and entropy can provide a quantitative picture of the hydriding reaction and how it varies with manganese content. A plot of the natural logarithm of the plateau pressure, p_H, against the hydriding temperature, T_H, should yield a linear trend and allow the determination of the hydriding enthalpy, ΔH_H, and entropy, ΔS_H, *via* Equation 1.1, the van't Hoff relationship.

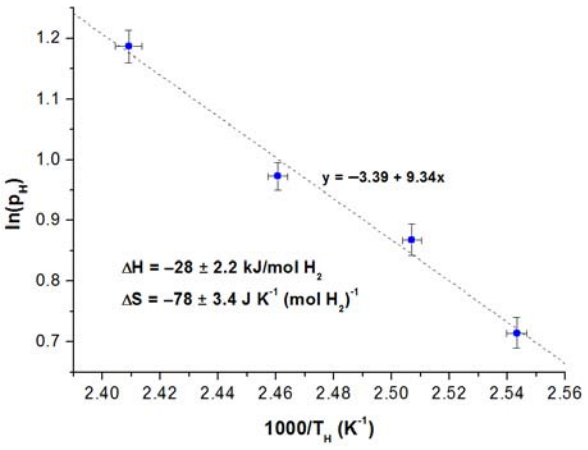

Figure 3.8: *A van't Hoff plot of the $ZrMn_{2.06} - H$ system, with the natural logarithm of the plateau pressure on the y-axis and the inverse of the hydriding temperature on the x-axis. Plateau pressures were taken at a concentration of 1.5 hydrogens per formula unit. A dashed line indicates the best fit to the experimental data (blue dots) and the hydriding enthalpy and entropy derived from this fit are given.*

Figure 3.8 illustrates a van't Hoff plot for $ZrMn_{2.06}-$ H, along with the best-fit linear trend line. As ΔH_H varies with the amount of hydrogen absorbed [91], plateau pressures on the slop-

ing plateau were consistently selected at each temperature for the concentration $ZrMn_{2.06}H_{1.5}$. Hydriding enthalpies and entropies for each member of the $ZrMn_{2+x}-$ H series, also selected at the plateau midpoint of H = 1.5, are given in Table 3.2; a compiled diagram of the van't Hoff plots from these values is shown in Figure 3.9. Note that for the most superstoichiometric member of the series, $ZrMn_{2.44}$, the highly sloped plateau and low hydrogen concentrations achieved at the temperatures and pressures measured prevented the construction of an accurate van't Hoff plot.

x **in** $\mathbf{ZrMn_{2+x}H_{1.5}}$	ΔH_H **(kJ/mol** $\mathbf{H_2}$**)**	ΔS_H **(J (K·mol** $\mathbf{H_2}$**)**$^{-1}$**)**
−0.35	−42(2)	−106(5)
0.06	−28(1)	−78(3)
0.13	−24.8(7)	−70(2)
0.18	−14.0(8)	−46(2)
0.31	−14.2(7)	−46.6(2)

Table 3.2: *Values of the hydriding enthalpy, ΔH_H, and the hydriding entropy, ΔS_H, for the $ZrMn_{2+x}-$ H system. The values were determined from van't Hoff constructions, with the hydriding pressures and temperatures taken at a hydrogen concentration of $H = 1.5$.*

The calculated enthalpy values for the $ZrMn_{2+x}-$ H series show a clear trend with x: as the amount of manganese in the system increases, the stability of the resulting hydride decreases. For the $ZrMn_{2.18}$ and the $ZrMn_{2.31}$ hydrides, ΔH_H and ΔS_H are not statistically different, which suggests that the increase in the hydriding enthalpy with x may reach a maximum. The hydriding entropies show a similar trend, with the absolute value of the entropy decreasing as x increases.

The reported hydriding enthalpies for the $ZrMn_{2+x}-$ H system mirror the trends found in this work, but differ in value slightly: Zhang and Wallace [90] report a ΔH_H of −22.2 kJ (mol H_2)$^{-1}$ for stoichiometric alloy, compared to the value calculated here of −28.2 kJ (mol H_2)$^{-1}$ for the nearly stoichiometric alloy,

$ZrMn_{2.06}$. It should be noted that there exists little agreement in the literature as to the actual value of the hydriding enthalpy for $ZrMn_2-$ H: Luo *et al.* [28] found it be -18.7 kJ (mol $H_2)^{-1}$, whilst Shaltiel *et al.* [20] noted a value of -26.6 kJ (mol $H_2)^{-1}$. However, the studies on the dependence of ΔH_H with x agree that the hydriding enthalpy of superstoichiometric hydrides successively increases as the manganese content increases [28, 91]. For the manganese deficient system, there is little published data on its hydriding thermodynamics: Luo *et al.* [28] found it to be slightly more stable than the stoichiometric alloy, in agreement with the results herein, but did not compute its entropy. There is a similar spread in the published entropy values: Luo *et al.* [28] reported $|\Delta S_H|$ for $ZrMn_2-$ H to be 47.0 J (K·mol $H_2)^{-1}$, and Shaltiel *et al.* [20] noted it to be 61.0 J (K·mol $H_2)^{-1}$. In the case of the hydriding entropy, there is no agreement on the relationship between $|\Delta S_H|$ and x: according to Luo *et al.* [28], the entropy decreases as x increases; however, Pourarian *et al.* [91] found the reverse to be true.

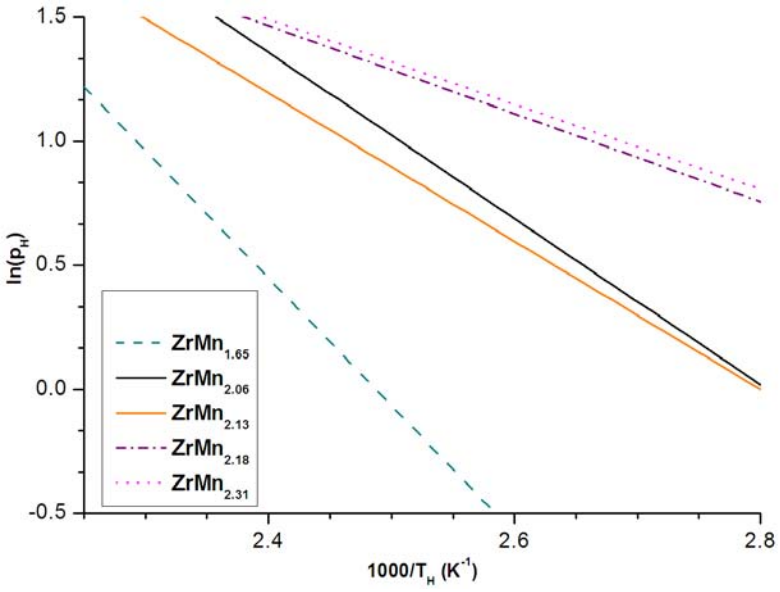

Figure 3.9: *A plot of the compiled van't Hoff constructions for the* $ZrMn_{2+x} - H$ *system, with the natural logarithm of the plateau pressure on the y-axis and the inverse of the hydriding temperature on the x-axis. Plateau pressures were taken at a concentration of 1.5 hydrogens per formula unit. Solid and dashed lines indicate the best fits to the experimental data; the data and its relative errors are not shown for clarity.*

Contrary to the conflicting published results, this work shows a clear dependence of the hydriding enthalpy and entropy upon the level of manganese substitution: as x increases, $|\Delta S_H|$ decreases and ΔH_H increases, indicating that the hydride becomes less stable.

3.6 Crystallographic Features of the $ZrMn_{2+x}H_3$ ($-0.35 \leq x \leq 0.44$) hydrides

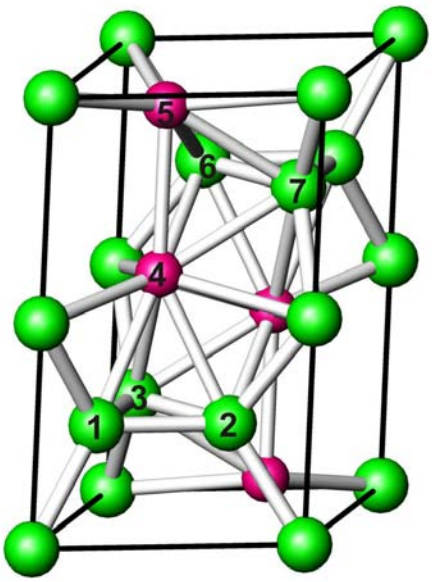

Figure 3.10: *A diagram of the C14 hexagonal structure of $ZrMn_2$, showing the arrangement of the zirconium atoms (pink spheres) and manganese atoms (green spheres) within the unit cell (heavy black lines). Nearest-neighbour atoms are connected by thin white cylinders as a guide to the eye. The atoms labelled 1, 2, 3 and 4 form a 1A3B type tetrahedral interstice, whilst the atoms 4, 5, 6 and 7 form a 2A2B interstice.*

The crystal structure of $ZrMn_2H_3$, which was introduced in Section 1.2.1, is reported [23] to retain the same $P6_3/mmc$ symmetry as the parent Laves phase intermetallic compound $ZrMn_2$. Hydrogen addition occurs with no change in the C14 metal sublattice, excepting an anisotropic lattice expansion to accommodate the hydrogen atoms at interstitial sites [23]. Three types of tetrahedral interstices exist in this hexagonal structure: one surrounded by one zirconium atom and three manganese atoms (*1A3B*), one with two manganese atoms and two zirconium atoms (*2A2B*), and one surrounded by four manganese atoms (*4B*). Didisheim *et al.* [23] have shown that only the *2A2B* site is occupied, as it is surrounded by the highest number of zirconium atoms: these show a stronger chemical affinity to hydrogen than manganese. Due to the sym-

metry of the structure, there are four non-equivalent *2A2B* sites. A diagram of the atomic sites in the C14 structure is given in Figure 3.10, with some of these interstices illustrated; the reported structural parameters for the stoichiometric deuteride can be found in Section 1.2.1.

3.6.1 Structure of the nearly stoichiometric hydride $ZrMn_{2.06}H_3$

The hydrided analogue of the nearly stoichiometric alloy $ZrMn_{2.06}$ was examined on the ID31 beamline at the ESRF —a full description of the instrument and the experimental parameters can be found in Section 2.1.2.1. The synthesis of this material is described in Section 3.4, where the hydride that was chosen for analysis at the synchrotron had been subjected to 14 hydriding/dehydriding cycles and was thus considered to be fully cycled. The collected synchrotron diffraction data were analysed using the Rietveld method described in Section 2.1.4; an R_{wP} of 7.810 was obtained for a fit using three crystalline phases, with the major phase being the hydride $ZrMn_{2.06}H_3$ at 75.2 wt. %. A trace impurity of ZrO_2, amounting to 0.6 wt. %, was also present, along with a minor phase component consisting of unreacted $ZrMn_{2.06}$ with identical structural parameters to the $ZrMn_{2.06}$ phase in the diffraction data of the alloy sample reported in Table 3.3.

The hydride phase crystallised in an expanded analogue of the $ZrMn_{2.06}$ $P6_3/mmc$ structure, and its lattice parameters were freely refined. As compared to the hydrogen-free structure, the hydride underwent an anisotropic lattice expansion of 22.1 %, consisting of an 6.20 % expansion in the direction of the c-axis and a 7.22 % expansion in the direction of a-axis. As the base metal substructure is conserved upon hydriding, with no significant change in the relative atomic positions of the zirconium and manganese atoms [23], the metal atoms were constrained to the positions described in Section 3.3.1 for the hydrogen-free alloy. Only those atomic sites not restricted by symmetry were freely refined, along with the thermal parameters of each atom. Atomic positions and occupancies of the hydrogen atoms could not be determined (see Section 2.1.2 for a discussion of the difficulty

in determining hydrogen locations using X-ray diffraction) but have been determined independently using neutron diffraction as will be shown in Section 3.9. The hydrogen content is approximated as $ZrMn_{2.06}H_3$ at this stage, based on the observed hydrogen absorption in the pressure-composition isotherm.

The structural parameters of the refined $ZrMn_{2.06}H_3$ phase are reported in Table 3.3. Figure 3.11 displays the observed synchrotron diffraction pattern for the $ZrMn_{2.06}-$ H sample, along with the calculated fit.

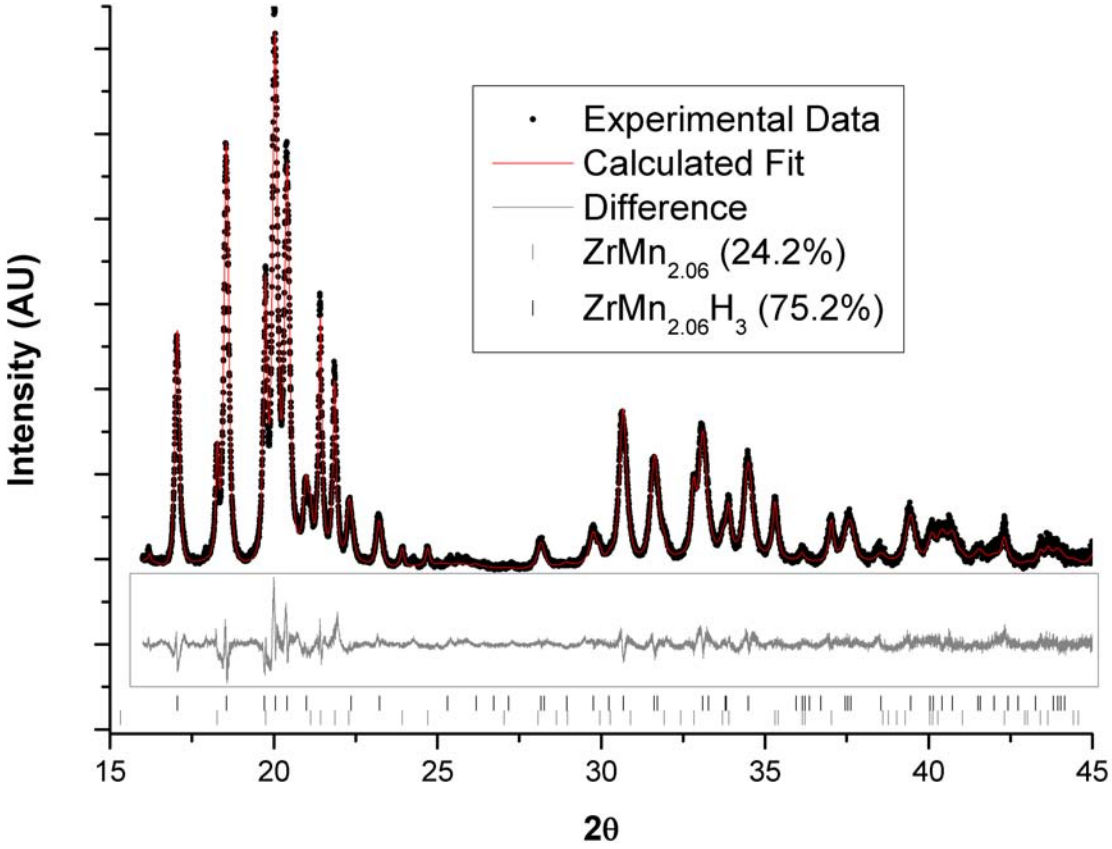

Figure 3.11: *Room temperature synchrotron diffraction pattern for* $ZrMn_{2.06} - H$. *The major phase is the C14 hydride, 75.2 weight percent, with 24.2 weight percent* $ZrMn_{2.06}$ *- ticks marks for both are shown at the bottom of the diagram. The difference plot between the observed experimental data (black points) and calculated fit (solid red line) is shown as a grey boxed line.* $R_{wp} = 7.810$.

The lattice parameters of the hydrogen-free minority phase $ZrMn_{2.06}$, also crys-

tallising in the space group $P6_3/mmc$, were freely refined. As these refined cell parameters did not differ significantly from the $ZrMn_{2.06}$ structure described in Table 3.3, the atomic positions and thermal parameters were not determined and were taken to be equal to those refined earlier for the $ZrMn_{2.06}$ phase in the alloy.

Parameter	*$ZrMn_{2.06}$ (alloy)*	*$ZrMn_{2.06}$ (dehydride)*	*$ZrMn_{2.06}H_3$*
Instrument	ESRF	Diamond	ESRF
Wavelength, λ (Å)	0.79986	0.824971	0.79986
a (Å)	5.0318(1)	5.0278(1)	5.3953(2)
c (Å)	8.2704(1)	8.2628(2)	8.7830(4)
V (Å^3)	181.351(9)	180.89(1)	221.41(2)
R_{wP}	23.683	16.965	7.810
$4f$ site $(\frac{1}{3}, \frac{2}{3}, z)$	0.0636(2)	0.0641(1)	0.0629(1)
Zr1 occ.	0.98(1)	0.98	0.98
Mn3 occ.	0.02(1)	0.02	0.02
B_{eq} (Å^3)	0.3	0.12(2)	0.46(2)
Mn1, $2a$ site $(0, 0, 0)$	-	-	-
B_{eq} (Å^3)	0.3	0.32(4)	1.69(6)
Mn2, $6h$ site $(x, 2x, \frac{1}{4})$	0.8319(4)	0.8319(2)	0.8394(2)
B_{eq} (Å^3)	0.3	0.02(2)	0.24(3)

Table 3.3: *Structural parameters for the nearly stoichiometric alloy $ZrMn_{2.06}$, its hydride $ZrMn_{2.06}H_3$, and the corresponding dehydrided compound.*

The diffraction peaks of both the $ZrMn_{2.06}$ phase and the $ZrMn_{2.06}H_3$ phase ex-

hibited significant peak broadening as compared to the peak width of the $ZrMn_{2.06}$ phase in the parent alloy (see Figure 3.1). This peak broadening, along with the concomitant reduction in Bragg peak intensity, prevented the determination of the manganese-to-zirconium ratio in both phases. However, a satisfactory fit to the data ($R_{wP} = 7.810$) was achieved using the manganese and zirconium occupancies refined from the alloy diffraction data in Section 3.3.1. The refined structure of $ZrMn_{2.06}H_3$ agrees excellently with the reported structure for the stoichiometric deuteride [22], which is summarised in Section 1.2.1 for ease of reference.

3.6.2 Structure of the superstoichiometric $ZrMn_{2+x}H_3$ ($0.13 \leq x \leq 0.31$) hydrides

Synchrotron X-ray diffraction data for the hydrided members of the $ZrMn_{2+x}$ series were collected at either the ID31 beamline at the ESRF or the I11 beamline at Diamond; instrumental details of both these beamlines, as well as the conditions under which the diffraction data were taken, can be found in Section 2.1.2.1. The synthesis of these hydrides is described in Section 3.4; for all compositions, the material was subjected to 14 hydriding/dehydriding cycles before diffraction data were collected. The data were analysed using the Rietveld method (see Section 2.1.4) and fitted with a mixture of three phases. In each case, the major phase was $ZrMn_{2+x}H_3$; some amount of the hydrogen-free $ZrMn_{2+x}$ and a trace impurity of ZrO_2 were also present in each data set. Details of the relative ratios of these phases for each composition, along with the collected diffraction patterns and calculated fits, can be found in Appendix A.

During refinement, the metal atoms of the $ZrMn_{2+x}$ phase were restrained to the $4f$, $2a$, and $6h$ sites as in the reported structure [22]; those atomic coordinates not constrained by the site symmetry were freely refined, as were the global lattice parameters and the thermal parameter of each atom. The metal atoms in the hydride phase were constrained in the same fashion as above, in accordance with the reported structure of the deuteride [22]. Excess manganese

in both phases was accommodated *via* replacement of zirconium on the $4f$ site; unfortunately, the relative ratio of manganese to zirconium on this site could not be satisfactorily refined due to the width of the diffraction peaks. The value of x for both the $ZrMn_{2+x}$ phase and the $ZrMn_{2+x}H_3$ phase was therefore assumed to be the same as that refined for the corresponding alloy and a satisfactory fit in each case ($R_{wP}(ZrMn_{2.13}{-}H) = 8.141$, $R_{wP}(ZrMn_{2.18}{-}H) = 16.685$, $R_{wP}(ZrMn_{2.31}{-}H) = 15.991$) was obtained with this assumption.

As discussed in Section 2.1.2 , it is difficult to unambiguously distinguish hydrogen in X-ray diffraction data when metal atoms are also present; thus, the hydride positions and occupancies were not refined in these data sets. As per the stoichiometric hydride, the hydrogen content can be approximated as $ZrMn_{2+x}H_3$; a neutron study determining the actual hydrogen content and atomic positions of one of the superstoichiometric hydrides will be presented in Section 3.9. The full refined structural parameters for $ZrMn_{2.13}H_3$, $ZrMn_{2.18}H_3$ and $ZrMn_{2.31}H_3$ are reported in Table 3.4, diffraction patterns with calculated fit are given in Appendix A but were very similar to that shown for the stoichiometric hydride in Figure 3.11.

It was not possible in the course of this work to collect synchrotron diffraction data on the hydride $ZrMn_{2.44}H_3$. Although initial laboratory X-ray diffraction experiments on the freshly hydrided material indicated the formation of $ZrMn_{2.44}H_3$, the hydride was metastable at atmospheric pressure and slowly released hydrogen gas to reform the $ZrMn_{2.44}$ phase *via*:

$$ZrMn_{2+x} + \frac{3}{2}H_2 \leftrightarrows ZrMn_{2+x}H_3 \tag{3.2}$$

In the case of the stoichiometric hydride, the equilibrium of the above reaction under standard conditions strongly favours the right-hand side and little of the hydride dissociates to reform $ZrMn_2$. However, as shown in Section 3.5, the presence of excess manganese destabilises the hydride and shifts the equilibrium to make the hydride dissociation more favourable. This is manifested in the gradual

loss of hydrogen from the hydrided sample over time, until eventually the sample is entirely converted back to $ZrMn_{2+x}$. Quantifying the length scale of this conversion was beyond the scope of this work; herein it is simply noted that as the manganese concentration of the phase increased, the ease with which the hydride dissociation occurred also accelerated.

Parameter	$ZrMn_{2.13}H_3$	$ZrMn_{2.18}H_3$	$ZrMn_{2.31}H_3$
Instrument	ESRF	Diamond	Diamond
Wavelength, λ (Å)	0.79986	0.824971	0.824971
a (Å)	5.3741(1)	5.3713(2)	5.3669(1)
c (Å)	8.7469(3)	8.7409(4)	8.7335(3)
V (Å^3)	218.78(1)	218.39(2)	217.85(1)
R_{wP}	8.141	16.685	15.991
$4f$ site $(\frac{1}{3}, \frac{2}{3}, z)$	0.0630(1)	0.0634(1)	0.0645(1)
Zr1 occ.	0.96	0.944	0.907
Mn3 occ.	0.04	0.057	0.093
B_{eq} (Å^2)	0.53(2)	0.69(3)	0.5
Mn1, $2a$ site $(0, 0, 0)$	-	-	-
B_{eq} (Å^2)	0.80(5)	0.94(6)	0.5
Mn2, $6h$ site $(x, 2x, \frac{1}{4})$	0.8369(2)	0.8396(2)	0.8395(2)
B_{eq} (Å^2)	0.12(2)	0.64(3)	0.5

Table 3.4: *Refined structural parameters for the hydrided, cycled phases of the $ZrMn_{2+x}H_3$ series, for $x = 0.13, 0.18, 0.31$.*

Figure 3.12 tracks the equilibrium of Equation 3.2 for the $ZrMn_{2.31}-$ H system

with a series of laboratory X-ray diffraction patterns collected at varying time intervals after the initial hydriding reaction. Details of the laboratory X-ray instrument and the experimental parameters under which the diffraction data were collected can be found in Section 2.1.2.1; the data were analysed using the Rietveld method described in Section 2.1.4. Each data set was fitted to a two-phase mixture of $ZrMn_{2.31}$ and $ZrMn_{2.31}H_3$: the ratio of these two phases was freely refined but their structural parameters were fixed to those given in Tables 3.1 and 3.4.

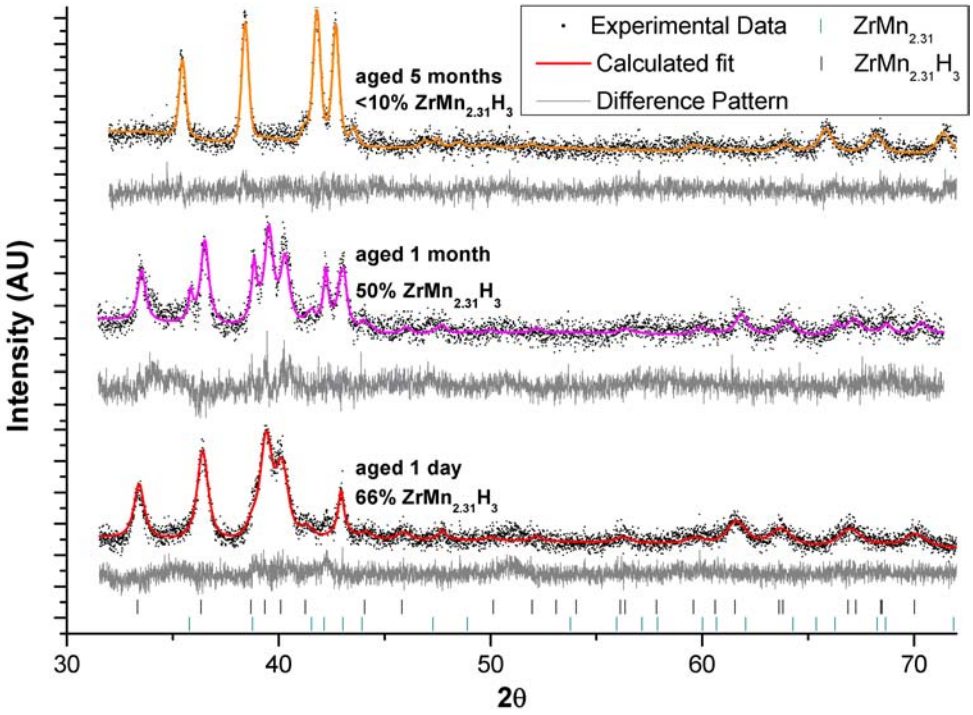

Figure 3.12: *A series of laboratory X-ray diffraction patterns for $ZrMn_{2.31} - H$, collected over a period of 5 months after its initial hydriding. The major phases in the samples are the C14 hydride $ZrMn_{2.31}H_3$ and the corresponding hydrogen-free $ZrMn_{2.31}$ - ticks marks for both are shown at the bottom of the diagram and structural details are given in the text. The relative weight percents of these two phases vary with the age of the sample as indicated on the diagram. Difference plots between the experimental data (black points) and calculated fits (solid coloured lines) are shown as grey lines.*

As Figure 3.12 shows, five months after the material was first hydrided, the $ZrMn_{2.31}H_3$ phase has almost entirely disappeared. The situation is correspondingly worse for $ZrMn_{2.44}$ —brief laboratory X-ray scans unsuitable for detailed

refinement indicate that the hydride completely dissociates over the course of several days. Thus in-house characterisation measurements could be quickly carried out freshly prepared samples of $ZrMn_{2.44}H_3$; however, it was not possible to prepare such a sample in advance for measurement at a synchrotron facility.

3.6.3 Structure of the substoichiometric hydride

The $ZrMn_{2+x}-$ H substoichiometric hydride was also examined *via* X-ray diffraction at the I11 beamline of Diamond; details of the instrument and the experimental parameters can be found in Section 2.1.2.1. Synthetic details for this hydride are described in Section 3.4; the sample was passed through 14 hydriding/dehydriding cycles before measurement at the synchrotron. The collected data were analysed using the Rietveld method (see Section 2.1.4) and the calculated model contained two phases: C14 $ZrMn_{1.65}$ (described in Section 3.3.3), and a hydrided $ZrMn_{1.65}H_3$ phase. Figure 3.13 presents the collected pattern of the hydride along with the calculated fit.

In the refinement process for both phases, the metal atoms were restrained to the $4f$, $2a$, and $6h$ sites as in the reported structure of the stoichiometric analogues [21,23]; those atomic coordinates not constrained by the site symmetry were freely refined, as were the global lattice parameters and the thermal parameter of each atom. Excess zirconium was accommodated on the $6h$ site using a restriction similar to that introduced in Equation 3.1. Significant peak broadening, and consequent reduction in peak intensity, prevented accurate refinement of the atomic occupancies on the $6h$ site for either phase; however, use of the relative Zr:Mn ratio determined *via* refinement of the alloy gave a satisfactory fit ($R_{wP} = 5.267$). Atomic positions and occupancies of the hydrogen atoms could not be determined (see Section 2.1.2 for a discussion of the difficulty in determining hydrogen locations using X-ray diffraction) but have been determined independently using neutron diffraction as will be shown in Section 3.9. Based on the observed hydrogen absorption in the pressure-composition isotherm, the hydrogen content can be approximated as $ZrMn_{1.65}H_3$. Full structural parameters for this $ZrMn_{1.65}H_3$

phase are reported in Table 3.5; the cell parameters agree with the only reported partial refinement of a similar structure, $ZrMn_{1.8}-$ H [27].

Parameter	*$ZrMn_{1.65}$*	*$ZrMn_{1.65}H_3$*
Instrument	Diamond	Diamond
Wavelength, λ (Å)	0.82656	0.82656
a (Å)	5.0482(2)	5.3862(8)
c (Å)	8.2966(6)	8.7705(3)
V (Å^3)	183.106(3)	220.35(1)
R_{wP}	5.983	5.267
Zr1, $4f$ site $(\frac{1}{3}, \frac{2}{3}, z)$	0.0629(2)	0.0640(1)
B_{eq} (Å^3)	0.3	0.19(2)
Mn1, $2a$ site $(0, 0, 0)$	-	-
B_{eq} (Å^3)	0.3	0.22(5)
Mn2, $6h$ site $(x, 2x, \frac{1}{4})$	0.8296(3)	0.8371(2)
Mn2 occ.	0.867(9)	0.867
Zr2 occ.	0.133(9)	0.133
B_{eq} (Å^3)	0.3	0.72(2)

Table 3.5: *Refined structural parameters for the hydrided, cycled $ZrMn_{1.65}H_3$ and for the alloy $ZrMn_{1.65}$.*

As compared to the diffraction data collected for the alloy (see Figure 3.2), no amount of α-Zr nor of the tetragonal ZrMn phase could be reliably detected in the diffraction data of the hydride. The strongest reflections of the suspected ZrMn phase overlap with many of the broad $ZrMn_{1.65}H_3$ peaks; when combined with the

already low weight percent of the impurity, this makes the detection of ZrMn in the hydride difficult. Flanagan *et al.* [86] suggest that ZrMn may dissociate under hydrogen pressure, with the zirconium forming a hydride ZrH_2 and the manganese atoms atoms migrating into the existing substoichiometric $ZrMn_{2+x}$ phase. This theory is not supported by the findings in this work, as no ZrH_2 phase was found in the diffraction data for the hydride.

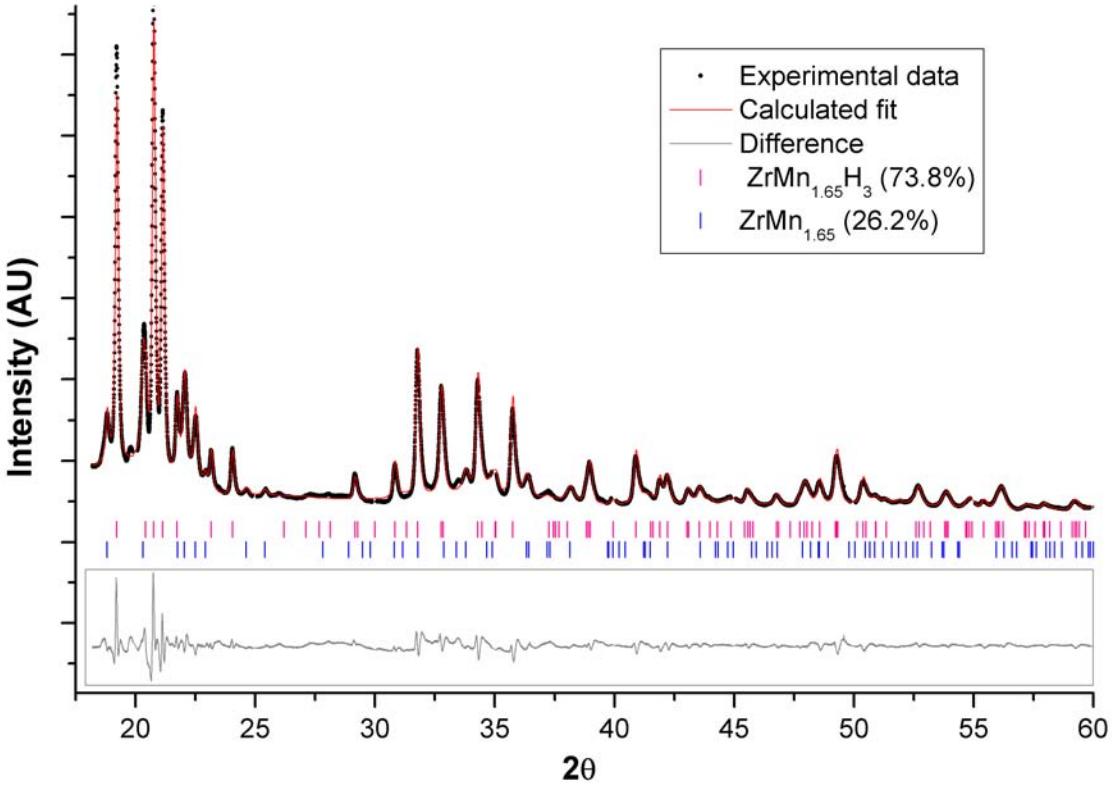

Figure 3.13: *Synchrotron diffraction pattern collected at room temperature for the substoichiometric hydride, $ZrMn_{1.65}H_3$. A succesful fit ($R_{wP} = 5.267$) was obtained using just the C14 $ZrMn_{1.65}$ phase (tick marks in blue, 26.2 weight percent) and the expanded C14 hydride $ZrMn_{1.65}H_3$ (tick marks in pink, 73.8 weight percent). The difference plot between the calculated fit (solid red line) and the observed experimental data (black dots) is shown as a grey line enclosed in a box.*

It may instead be postulated that the large number of hydriding cycles carried out on this system (greater than 15) has mimicked the effect of a long annealing program: the trace impurities of zirconium and ZrMn may have combined with

the existing $ZrMn_{2+x}$ to form a new, slightly more substoichiometric phase. As mentioned above, however, the atomic occupancies on the $6h$ site for both the hydrided and hydrogen-free $ZrMn_{2+x}$ phases could not be reliably refined; thus, the actual compositions of these phases could not be determined. The satisfactory fit ($R_{wP} = 5.267$) obtained for $x = -0.35$ does suggest that the actual composition does not deviate greatly from this value.

3.7 Crystallographic Features of the cycled, dehydrided $ZrMn_{2+x}$ ($0.06 \leq x \leq 0.44$) materials

3.7.1 Structure of the nearly stoichiometric, dehydrided $ZrMn_{2.06}$

The X-ray diffraction data for the cycled, dehydrided $ZrMn_{2.06}$ material were collected at the I11 beamline at Diamond; instrumental details of this beamline, as well as the conditions under which the diffraction data were taken, can be found in Section 2.1.2.1. The synthesis of this material is described in Section 3.4; where the sample used for synchrotron diffraction was passed through 15 hydriding/dehydriding cycles before measurement. The collected data were analysed using the Rietveld method (see Section 2.1.4) and were fitted with the C14 $ZrMn_{2.06}$ phase; the structural parameters were freely refined in the manner described above for the nearly stoichiometric alloy in Section 3.3.1. The collected diffraction pattern, along with the calculated fit, are shown in Figure 3.14.

Table 3.3, which gives a full account of the structural parameters for the $ZrMn_{2.06}$ phase for both the alloy and dehydrided sample, shows that the refined structures of both these materials are very similar, with only slightly differing lattice parameters and atomic coordinates. The dehydrided material was not single phase: it was found to contain approximately 1.6 weight percent of ZrO_2 which was not present in the original alloy. It is suspected that this minor oxide phase arose as a result of minute oxygen exposures that may have occurred during repeated transfers between the glovebox and the hydriding apparatus. The hydride phase,

$ZrMn_{2.06}H_3$, could not be satisfactorily fitted to the diffraction data, indicating that the dehydriding reaction went to completion.

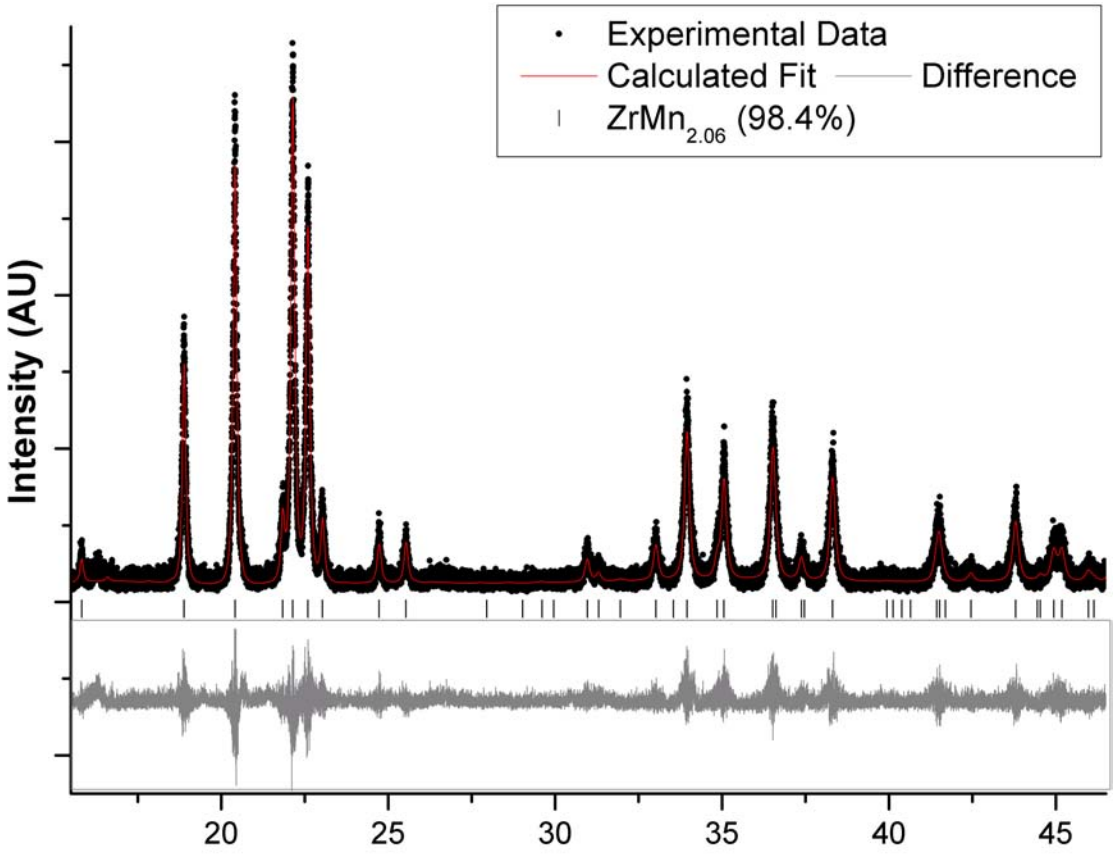

Figure 3.14: *Synchrotron diffraction pattern, collected at room temperature, for the cycled, dehydrided $ZrMn_{2.06}$ material. The pattern has been fitted with the C14 $ZrMn_{2.06}$ phase, the ticks marks for which are shown at the bottom of the diagram. Tickmarks for the minor ZrO_2 phase (1.6 wt. %) are not shown. The difference plot between the experimental data (black points) and calculated fit (red solid line) is shown as a grey line enclosed in a box.* $R_{wP} = 16.965$.

From a visual comparison of Figures 3.1 and 3.14, it is evident that the dehydrided material exhibits significant peak broadening as compared to the original alloy. The broadened peaks of the $ZrMn_{2.06}$ phase in the dehydrided material, combined with the reduction in intensity brought about by the increased peak width, did not allow the accurate refinement of the manganese and zirconium occupancies on the $4f$ site in this phase. However, a satisfactory fit ($R_{wP} = 16.965$)

was obtained using the relative occupancies previously refined for the $ZrMn_{2.06}$ phase in the alloy material in Section 3.3.1.

3.7.2 Structure of the superstoichiometric $ZrMn_{2+x}$ ($0.13 \leq x \leq 0.44$) dehydrided materials

X-ray diffraction data for the cycled, dehydrided $ZrMn_{2+x}$ materials were collected at two different synchrotron radiation facilities. The materials were measured either on the ID31 beamline at the ESRF or the I11 beamline at Diamond; instrumental details of both these beamlines, as well as the conditions under which the diffraction data were collected, can be found in Section 2.1.2.1. The synthetic details of the dehydriding process are detailed in Section 3.4; all the materials used for this diffraction study were subjected to fifteen hydriding/dehydriding cycles before measurement. The collected diffraction data were analysed using the Rietveld method (see Section 2.1.4) and were fitted with the hexagonal $ZrMn_{2+x}$ structure and an additional trace impurity of ZrO_2.

In the refinement process for the $ZrMn_{2+x}$ phase of the superstoichiometric dehydrided compounds, the metal atoms were restrained to the $4f$, $2a$, and $6h$ sites as in the reported structure [22]; those atomic coordinates not constrained by the site symmetry were freely refined, as were the global lattice parameters and the thermal parameter of each atom. Excess manganese was accommodated on the $4f$ site using the restriction introduced in Equation 3.1.

Table 3.6 gives the refined structural parameters of the $ZrMn_{2+x}$ phase for the cycled, dehydrided compounds; no significant difference was found between the structural parameters of the dehydrided material and the alloy for any of the compositions studied. The observed diffraction pattern and calculated fit for each dehydrided material can be found in Appendix A; all are extremely similar to the pattern presented in Figure 3.14 for dehydrided $ZrMn_{2.06}$.

Parameter	$ZrMn_{2.13}$	$ZrMn_{2.18}$	$ZrMn_{2.31}$	$ZrMn_{2.44}$
Instrument	ESRF	Diamond	Diamond	Diamond
Wavelength, λ (Å)	0.79986	0.82656	0.824971	0.82656
a (Å)	5.0264(1)	5.0241(6)	5.0134(1)	5.0071(1)
c (Å)	8.2559(2)	8.2542(1)	8.2386(3)	8.2240(2)
V (Å^3)	180.64(1)	180.435(5)	179.33(1)	178.560(8)
R_{wP}	8.376	3.268	15.526	3.809
$4f$ site $(\frac{1}{3}, \frac{2}{3}, z)$	0.0645(1)	0.0640(1)	0.0640(1)	0.0641(1)
Zr1 occ.	0.96	0.944	0.907	0.873
Mn3 occ.	0.04	0.057	0.093	0.111
B_{eq} (Å^3)	0.39(2)	0.10(1)	0.14(1)	0.11(1)
Mn1, $2a$ site $(0, 0, 0)$	-	-	-	-
B_{eq} (Å^3)	0.38(5)	0.24(2)	0.25(4)	0.21(3)
Mn2, $6h$ site $(x, 2x, \frac{1}{4})$	0.8308(2)	0.8303(1)	0.8307(1)	0.8298(1)
B_{eq} (Å^3)	0.05(2)	0.17(1)	0.10(2)	0.21(2)

Table 3.6: *Refined structural parameters for the dehydrided, cycled phases of the* $ZrMn_{2+x}$ *series, for* $x = 0.13, 0.18, 0.31, 0.44$.

Significant peak broadening, and consequent reduction in peak intensity, prevented accurate refinement of the atomic occupancies on the $4f$ site of the $ZrMn_{2+x}$ phase for the dehydrided materials. As the corresponding phases in the alloy diffraction data were not so restricted (see Section 3.3.2) the zirconium and manganese occupancies for each $ZrMn_{2+x}$ phase was thus determined from the diffraction data of the alloy and used to model the $ZrMn_{2+x}$ phase in the dehydrided materials. A satisfactory fit ($R_{wP}(ZrMn_{2.13}) = 8.376$, $R_{wP}(ZrMn_{2.18}) = 3.268$, $R_{wP}(ZrMn_{2.31}) = 15.526$, $R_{wP}(ZrMn_{2.44}) = 3.809$) using the alloy composition was obtained in each case.

3.8 Effect of x on the crystallographic features of $ZrMn_{2+x}$ and $ZrMn_{2+x}H_3$

The crystallographic data detailed above in Sections 3.3, 3.6, and 3.7 present a complex picture of the effects of both hydrogen absorption and variations in manganese content on the crystal structure of the $ZrMn_{2+x}$ system. A summary of the variation in each of the cell parameters for both the $ZrMn_{2+x}$ and the $ZrMn_{2+x}H_3$ series can be used to elucidate the nature of these structural changes.

3.8.1 The effect of x on structure when $x > 0$

The variation in unit cell parameters with x for the cycled, dehydrided $ZrMn_{2+x}$ C14 phase is shown in Figure 3.15; data for the variation in unit cell volume are given in the inset. The corresponding data for the hydride series $ZrMn_{2+x}H_3$ can be found in Figure 3.16. Note that data for the substoichiometric member of the series ($ZrMn_{1.65}$) are not included in these compilations and will be separately compared against the nearly stoichiometric alloy and hydride. Although this separation of sub- and super-stoichiometric compounds was not followed in previous studies [27,28] of the dependence of structure on composition in the $ZrMn_{2+x}-$ H system; it is basic metallurgical knowledge that the chemical composition dependencies of the lattice parameters for intermetallic compounds differ between sub- and superstoichiometric regions [92].

As Figure 3.15 shows, there is a linear relationship between the manganese content and the lattice parameters for the superstoichiometric $ZrMn_{2+x}$ phase. The dependence of V on x has been previously noted, and the best-fit line in this work agrees excellently with these earlier determinations [27, 28, 86]. This agreement also validates the method used in this thesis of determining x from the diffraction data and shows that the separate use of atomic absorption spectroscopy or energy dispersive spectroscopy – two of the most commonly used methods of elucidating x in $ZrMn_{2+x}$ [25, 28] – is unnecessary, as well-refined diffraction data can provide both the structure and the composition.

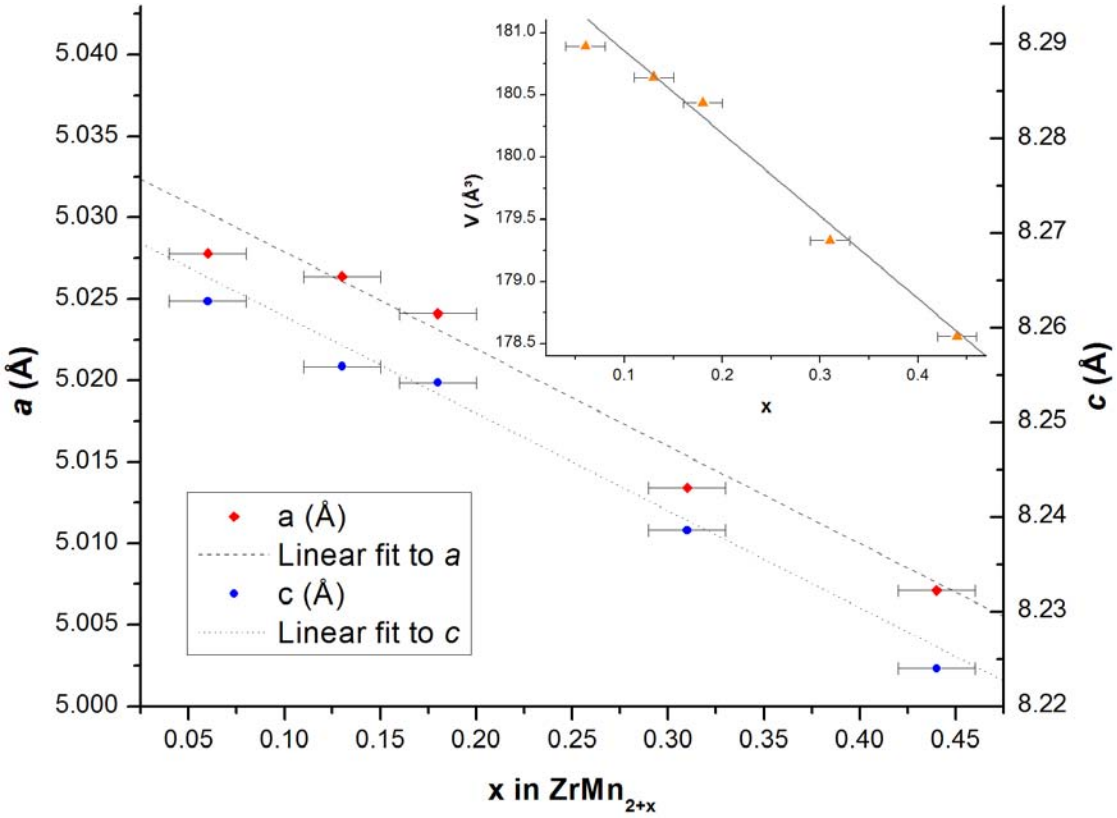

Figure 3.15: *Variation of a (red diamonds) and c (blue circles) lattice parameters versus x for the cycled, dehydrided $ZrMn_{2+x}$ C14 phase. The inset shows the variation in unit cell volume with x. The values for the lattice parameters and the errors indicated by bars on the graph were extracted via refinement of the synchrotron diffraction data; note that the y-axis error bars are smaller than the data points. For each data set, a linear regression was performed to find the best-fit line: for the variation of c vs x this is a dotted line, and for a vs. x this is a dashed line. The best-fit line to the unit cell volume is a solid grey line.*

The superstoichiometry in the $ZrMn_{2+x}$ series is accomplished by the replacement of a zirconium atom on the $4f$ site by a manganese atom as discussed in Section 3.3.1. Since manganese has a smaller atomic radius than Zr (161 versus 206 pm [93]), this substitution is expected to cause a decrease in the unit cell size, as observed. Figure 3.17, a comparison of the synchrotron diffraction patterns for the cycled, dehydrided materials, is perhaps more illustrative of this lattice contraction.

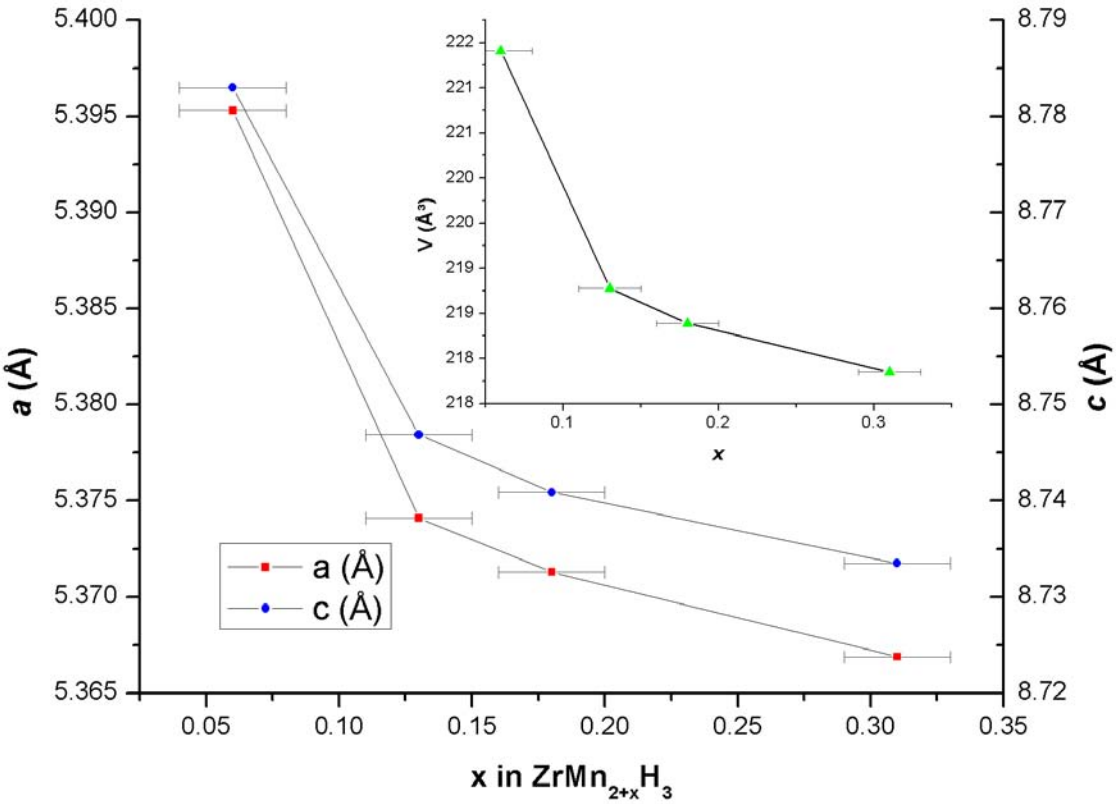

Figure 3.16: *Variation of a (red squares) and c (blue circles) lattice parameters versus x for the cycled, hydrided $ZrMn_{2+x}H_3$ series. The inset shows the variation in unit cell volume with x. The values for the lattice parameters and the errors indicated by bars on the graph were extracted via refinement of the synchrotron diffraction data; note that the y-axis error bars are smaller than the data points. The lines connecting the data points are simply a guide to the eye.*

The manganese substitution is expected to have a similar effect on the $ZrMn_{2+x}H_3$ series; indeed, the unit cell shrinks as the manganese content rises in the hydrides,

as shown in Figure 3.16. Hydrogen absorption has, however, caused a significant lattice expansion compared to the $ZrMn_{2+x}$ phase – *viz.* 21.1% for the $ZrMn_{2.13}$–H series – as the hydrogen atoms are accommodated in interstitial sites. Unlike the $ZrMn_{2+x}$ phase, the relationship between V and x is not linear for the hydrides: the unit cell of the nearly stoichiometric hydride $ZrMn_{2.06}H_3$ is much larger than that of the more superstoichiometric members of the series.

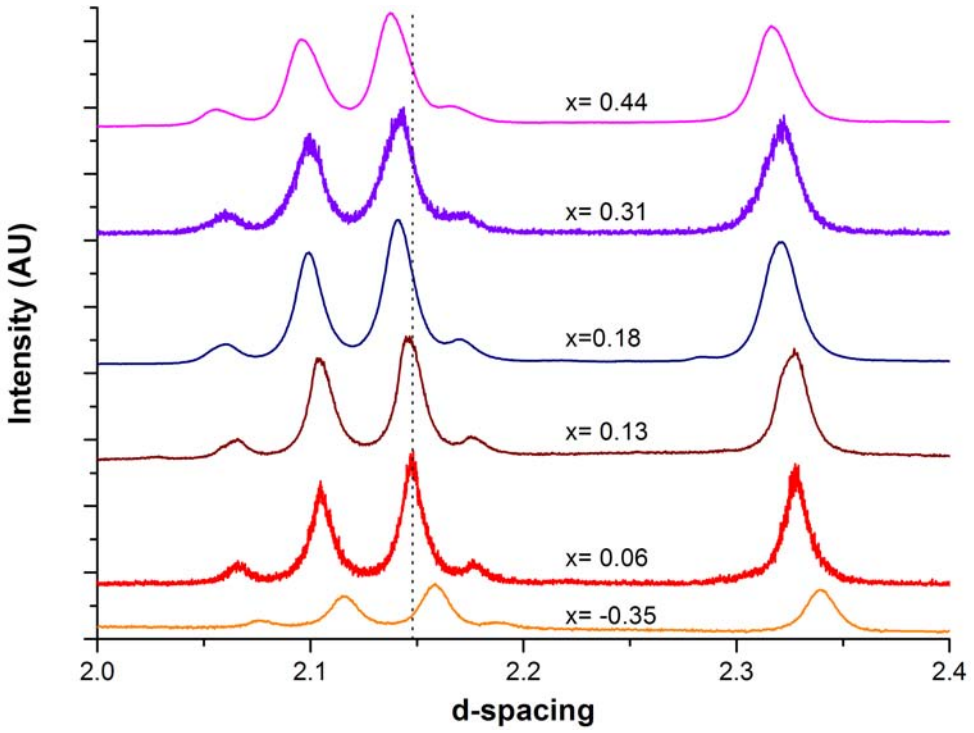

Figure 3.17: *A plot of a selected area of the synchrotron X-ray diffraction patterns for the cycled and dehydrided $ZrMn_{2+x}$ materials, showing the shift in the hkl reflections with the manganese content, x. The dotted line at $d = 2.148$ indicates the position of the $(11\bar{2}2)$ peak in the $x = 0.06$ sample. Note that for the phase with $x = -0.35$ a laboratory X-ray diffraction pattern has been used.*

The cause of this phenomenon is simplified if the chemical formulae of the superstoichiometric hydrides are re-written; for example, instead of $ZrMn_{2.13}H_3$, consider $Zr_{0.96}Mn_{0.04}Mn_2H_{2.88}$. Although the two forms are equivalent, the more complex notation makes it clear that there are less hydrogens atoms per unit cell

as compared to the stoichiometric hydride $ZrMn_2H_3$. It is easily shown that the number of hydrogen atoms per unit cell continues to decrease as the manganese content increases; this finding is supported by crystal chemistry considerations which suggest that the substitution of Mn for Zr will reduce the number of *2A2B* sites available for hydrogen absorption. Correspondingly, the superstoichiometric alloys show less lattice expansion upon hydrogen absorption than the stoichiometric alloy: $ZrMn_{2.06}$ expands 22.4% upon hydriding, whilst $ZrMn_{2.18}$ expands only 21.0%. The observed non-linear relationship of $V(x)$ in the $ZrMn_{2+x}H_3$ series therefore results from the combination of two connected factors, (1) the decrease in the amount of hydrogen per unit cell as x increases, resulting in less lattice expansion as compared to $ZrMn_2$ and (2) the increase in the amount of manganese per unit cell as x increases, also resulting in a smaller unit cell.

3.8.2 The effect of x on structure when $x < 0$

The unit cell parameters of the substoichiometric alloy $ZrMn_{1.65}$ and its hydride can be found in Table 3.5. Comparison of these values with the corresponding cell parameters of the nearly stoichiometric alloy and hydride (shown in Table 3.3) reveals two key differences:

1. Reduction in manganese content from $ZrMn_{2.06}$ to $ZrMn_{1.65}$ has resulted in a slight lattice expansion of the C14 phase in the alloy.

2. Conversely, the hydride $ZrMn_{1.65}H_3$ has a slightly smaller unit cell than $ZrMn_{2.06}H_3$.

As shown in Section 3.3.3, the manganese deficient structure is achieved *via* partial substitution of Zr for Mn on the $6h$ site. Since the zirconium atom is larger than the manganese, it is expected that this substitution will cause a slight expansion of the unit cell, as observed for the $ZrMn_{1.65}$ alloy. Figure 3.17 illustrates the shift in the $(11\bar{2}2)$ reflection of $ZrMn_{1.65}$ as compared to $ZrMn_{2.06}$.

In the case of the hydrided compound, the reduction in the size of the unit cell of $ZrMn_{1.65}H_3$ is somewhat surprising. Performing the same formulaic rewrite as was carried out for the superstoichiometric hydrides gives $Zr_{1.13}Mn_{1.87}H_{3.39}$, suggesting that the substoichiometric alloy absorbs slightly more hydrogen per unit cell than $ZrMn_2$. This increase in hydrogen absorption capacity is easily explained, as the substitution of Zr for Mn will create additional *2A2B* sites favourable to hydrogen absorption, and may even lead to the appearance of a few *3A1B* sites of high hydrogen affinity. The expanded unit cell of the substoichiometric alloy, combined with an increased hydrogen absorption capacity – as compared to the nearly stoichiometric alloy – should make the unit cell of $ZrMn_{1.65}H_3$ slightly larger than that of $ZrMn_{2.06}H_3$; instead, it is slightly smaller. At the moment, this discrepancy cannot be explained.

3.8.3 Peak profile analysis of the $ZrMn_{2+x}$ system and its hydrides

A full peak profile analysis using the method described in Section 2.1.4 was carried out on the synchrotron diffraction data of the cycled, dehydrided members of the $ZrMn_{2+x}$ series in order to determine the provenance of the observed peak broadening. The data of the $ZrMn_{2+x}H_3$ hydrides were also analysed *via* this peak profile method. A full peak profile analysis could not be carried out on the substoichiometric $ZrMn_{1.65}-$ H system, however, as the diffraction data for these materials were not fully refined (see Section 3.3.3 and 3.6.3). There exists no published information on the nature of the peak broadening in the $ZrMn_{2+x}-$ H series, although many workers have noted it in their diffraction data [22, 25, 35].

The peak profile analysis revealed that, in all cases, the increased peak width can be largely ascribed to a size-induced broadening effect, with less significant strain contributions. In the dehydrides, the crystallite size of the $ZrMn_{2+x}$ phase showed no dependence on x; rather, the sizes were scattered about a mean of 55 nm with a standard deviation of 12 nm. Likewise, no relationship was found between particle size and manganese content in the $ZrMn_{2+x}H_3$ phase; the hydrides'

crystallite sizes were described by precisely the same mean of 55 ± 12 nm. It should be noted that these values for the crystallite size do not describe actual particle sizes, as the calculation method simply yields an approximation.

The computed strain values for both the $ZrMn_{2+x}$ and the $ZrMn_{2+x}H_3$ phases are plotted against x in Figure 3.18. The dehydrided compounds show a distinct variation in strain with manganese content: although the strain value for the nearly stoichiometric phase is quite low, a gradual increase in the strain with x is evidenced for the superstoichiometric compounds. The substitutional model for these non-stoichiometric compounds may be the cause of this increased strain, as the accommodation of a smaller manganese atom onto the existing zirconium site of the C14 lattice deforms the parent structure. Kodama *et al.* [25] also postulated that atomic substitution would cause an increase in lattice strain for both the sub- and superstoichiometric compounds but did not perform a full peak profile analysis to verify this. Figure 3.18 clearly demonstrates for the first time that a deviation from the stoichiometric $ZrMn_2$ composition increases the strain in the C14 crystal structure for an increased manganese content.

It can be seen from Figure 3.18 that the trend in lattice strain against x is substantially different for the $ZrMn_{2+x}H_3$ phases. For the nearly stoichiometric and superstoichiometric hydrides, the lattice strain is larger in the hydrogen-free compounds and is not significantly different across the series. These data suggests that the hydrogen-induced lattice expansion relieves the strain caused by the atomic substitution for the non-stoichiometric hydrides. In all cases, the strain value is larger than was observed for the parent compounds, indicating that the hydriding process has created new strains in the structure.

Cycling the $ZrMn_{2+x}$ system through multiple hydrogen absorption/desorption steps clearly leads to highly decrepitated compounds, as the crystallite size data above show. The anisotropic nature of the hydrogen-induced lattice expansion, combined with the large crystal strain in the hydride structure, creates a situation favourable to the development of extensive cracks and faults in the material.

As the cycling process continues, these faults expand and expose fresh surfaces, accelerating the decrepitation process. It is interesting to note that the superstoichiometric compounds do not decrepitate more significantly than the $ZrMn_{2.06}$ phase; this observation supports the hypothesis that the particle size reduction is largely a result of the crystal strain in the hydride.

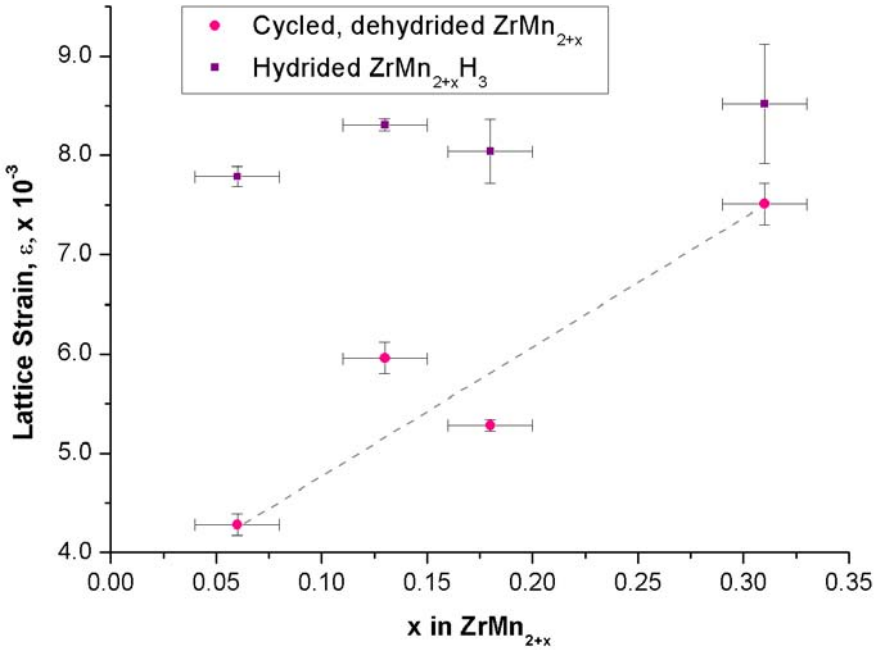

Figure 3.18: *A plot showing the influence of x on the lattice strain in cycled, dehydrided $ZrMn_{2+x}$ (pink circles) and $ZrMn_{2+x}H_3$ (purple squares). The lattice strain was derived from a peak profile analysis of the diffraction data. The grey dotted line serves as a guide to the eye in describing the variation of the lattice strain with x for the dehydrided materials.*

3.9 Neutron Diffraction studies on $ZrMn_{2+x}D_y$ ($-0.35 \leq x \leq 0.13$, $y \approx 3$)

Neutron diffraction data on the $ZrMn_{1.65}-$ D, $ZrMn_{2.06}-$ D, and $ZrMn_{2.13}-$ D deuterides were collected at 300 K in order to determine the deuterium positions in these compounds. Additional data were also collected at 10 K to assist in the determination of a magnetic structure for the $ZrMn_{2+x}-$ H system. All of these diffraction data were collected during beamtime number RB920147 on the GEM

instrument at ISIS —Section 2.1.3.1 describes the instrument and the parameters under which the data were obtained.

3.9.1 Refinement of the nuclear structure of $ZrMn_{2+x}D_y$ at 300 K

For the nuclear structure refinement, the data taken at 300 K were analysed using the Rietveld method (see Section 2.1.4). Due to care taken to deuteride the samples under high pressure promptly before measurement, the hydrogen-free $ZrMn_{2+x}$ phase could not be detected in any of the three materials. The major phase in all cases was $ZrMn_{2+x}D_y$, with small contributions from the vanadium can and the cryostat adding to the background; for $ZrMn_{2.06}-$ D, an additional impurity phase of 1.2 weight percent of MnO was included in the refinement. Figure 3.19 and 3.20 shows the collected diffraction pattern on banks 3 and 4 and the calculated fits, for the $ZrMn_{2.06}-$ D system at 300 K; likewise, Figure 3.21 corresponds to the same data for the $ZrMn_{2.13}-$ D system on bank 3. Neutron diffraction patterns with calculated fits for the $ZrMn_{1.65}-$ D system can be found in Appendix A.

In the refinement process for the $ZrMn_{2+x}D_y$ phase, the metal atoms were restrained to the $4f$, $2a$, and $6h$ sites as in the reported structure of the stoichiometric deuteride [23]; those atomic coordinates not constrained by the site symmetry were freely refined, as were the global lattice parameters and the thermal parameter of each atom. Using the constraints and atomic sites for manganese and zirconium substitution in the $ZrMn_{2+x}$ alloys that were described in Sections 3.3.1 and 3.3.3, respectively, the occupancies of the metal atoms on the $4f$ site ($ZrMn_{2.06}-$ D, $ZrMn_{2.13}-$ D) or the $6h$ site ($ZrMn_{1.65}-$ D) were refined. It is interesting to note that these refined compositions independently converged at values very near ($x \pm 0.04$) to those found for the alloys using X-ray diffraction —this close agreement further validates the determination of composition in $ZrMn_{2+x}$ *via* crystallographic analysis. The refined parameters for the $ZrMn_{2+x}D_y$ phases can be found in Table 3.7.

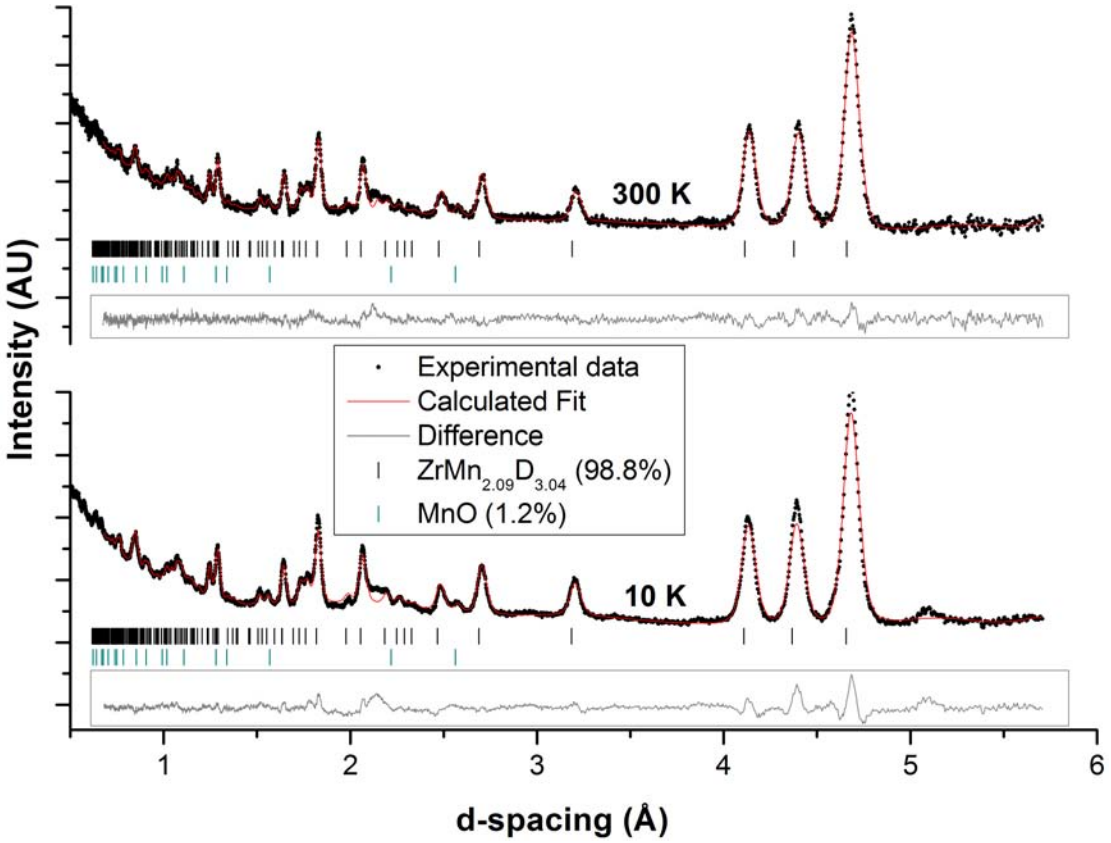

Figure 3.19: *Experimental data (black dots), calculated fits (red lines) and difference plots (grey lines enclosed in boxes) for the structural refinement of* $ZrMn_{2.09}D_{3.04}$ *from neutron diffraction data collected at bank 3 of the ISIS GEM diffractometer. Shown are data collected at 300 K and 10 K. The Bragg peak positions of both the major deuteride phase and a trace MnO impurity are shown by vertical tick marks.* $R_{wP} = 1.084(300\ K), R_{wP} = 1.378(10\ K)$.

For the superstoichiometric and the nearly stoichiometric deuterides, the deuterium atom positions were initially fit to the *2A2B* interstitial sites as calculated by Didisheim *et al.* [23]: these were the $24l$, $12k$, and two $6h$ sites. The atomic coordinates not constrained by site symmetry were then freely refined, as were the deuterium occupancies and the thermal parameters.

For the substoichiometric deuteride, there existed no previous study on the deuterium atom positions and relative occupancies; as such, an initial model was developed in which six deuterium sites were included:

- The four deuterium sites at *2A2B* interstices occupied in the stoichiometric deuteride.

- Two new deuterium sites at *1A3B* interstices, as substitution of zirconium for manganese on the $6h$ site would turn a fraction of these sites into new *2A2B*-type interstices

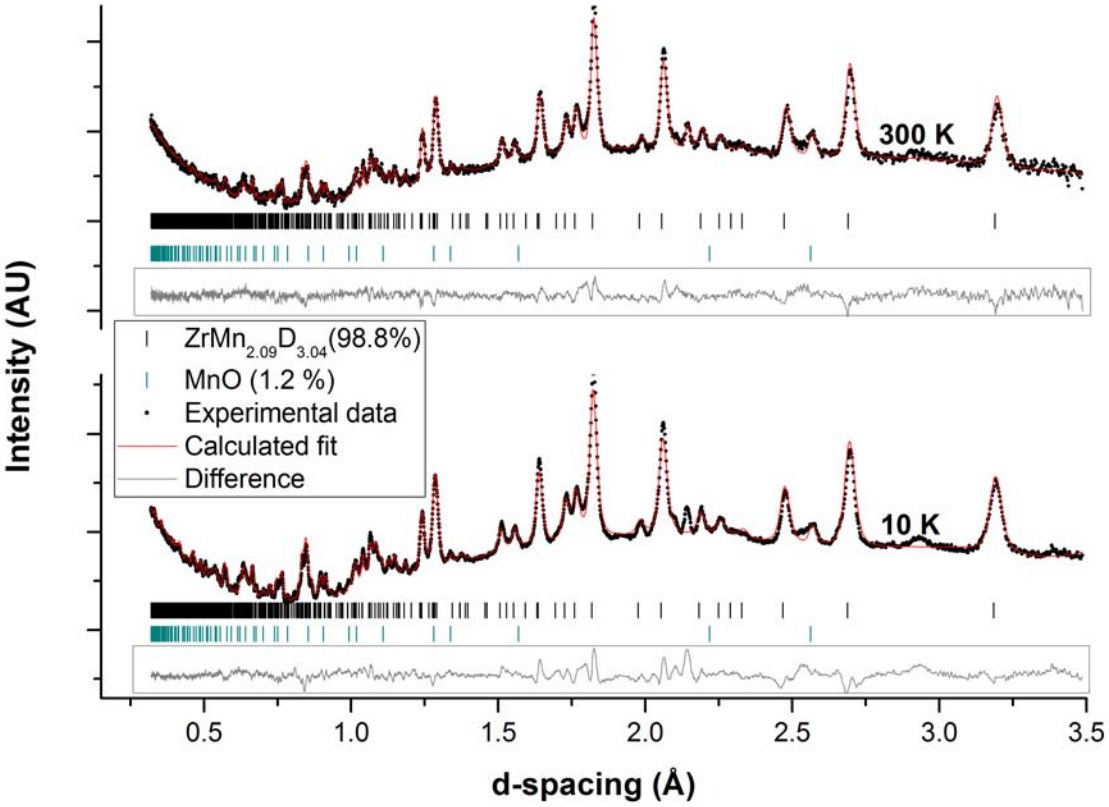

Figure 3.20: *Experimental data (black dots), calculated fits (red lines) and difference plots (grey lines enclosed in boxes) for the structural refinement of* $ZrMn_{2.09}D_{3.04}$ *from neutron diffraction data collected at bank 4 of the ISIS GEM diffractometer. Shown are data collected at 300 K and 10 K. The Bragg peak positions of both the major deuteride phase and a trace MnO impurity are shown by vertical tick marks.* $R_{wP} = 1.087(300\ K), R_{wP} = 1.914(10\ K)$.

From inspection of the refined structure of the $ZrMn_{1.65}$ alloy (discussed in Section 3.3.3) it was determined that the structure contained two non-equivalent types of *1A3B* interstices, with one located on a $12k$ site ($x \simeq 0.132, z \simeq 0.138$) and

the other on a $4f$ site ($z \simeq 0.665$). These initial values for the $1A3B$ interstices were input into the $ZrMn_{1.65}D_y$ model, along with the atomic positions of the $2A2B$ interstices, and the atomic coordinates not constrained by site symmetry for all six D sites were freely refined. The occupancies and thermal parameters were also independently refined for each site. Table 3.8 gives the refined deuterium occupancies and atomic coordinates for all three of the materials studied.

Parameter	$ZrMn_{2.09}D_{3.04}$	$ZrMn_{2.13}D_{3.36}$	$ZrMn_{1.69}D_{2.63}$
a (Å)	5.3878(4)	5.3680(3)	5.392(1)
c (Å)	8.7538(8)	8.7315(6)	8.756(4)
V (Å^3)	220.07(3)	217.89(3)	220.5(1)
R_{wP}	1.501	1.888	1.536
$4f$ site $(\frac{1}{3}, \frac{2}{3}, z)$	0.0641(3)	0.0622(2)	0.0581(5)
Zr1 occ.	0.97(1)	0.96(1)	1
Mn3 occ.	0.03(1)	0.04(1)	-
B_{eq} (Å^2)	0.24(3)	0.96(2)	0.43(1)
Mn1, $2a$ site $(0, 0, 0)$	-	-	-
B_{eq} (Å^2)	0.24(8)	0.68(4)	0.6(1)
Mn2, $6h$ site $(x, 2x, \frac{1}{4})$	0.8259(4)	0.8364(2)	0.8285(8)
Mn2 occ.	1	1	0.884(3)
Zr2 occ.	-	-	0.116(3)
B_{eq} (Å^2)	0.08(1)	0.37(4)	0.23(8)

Table 3.7: *Refined unit cell parameters and metal atom positions, as determined via neutron diffraction at 300 K, for the deuterided, cycled $ZrMn_{2+x} - D$ series with $x = -0.35, 0.06, 0.13$.*

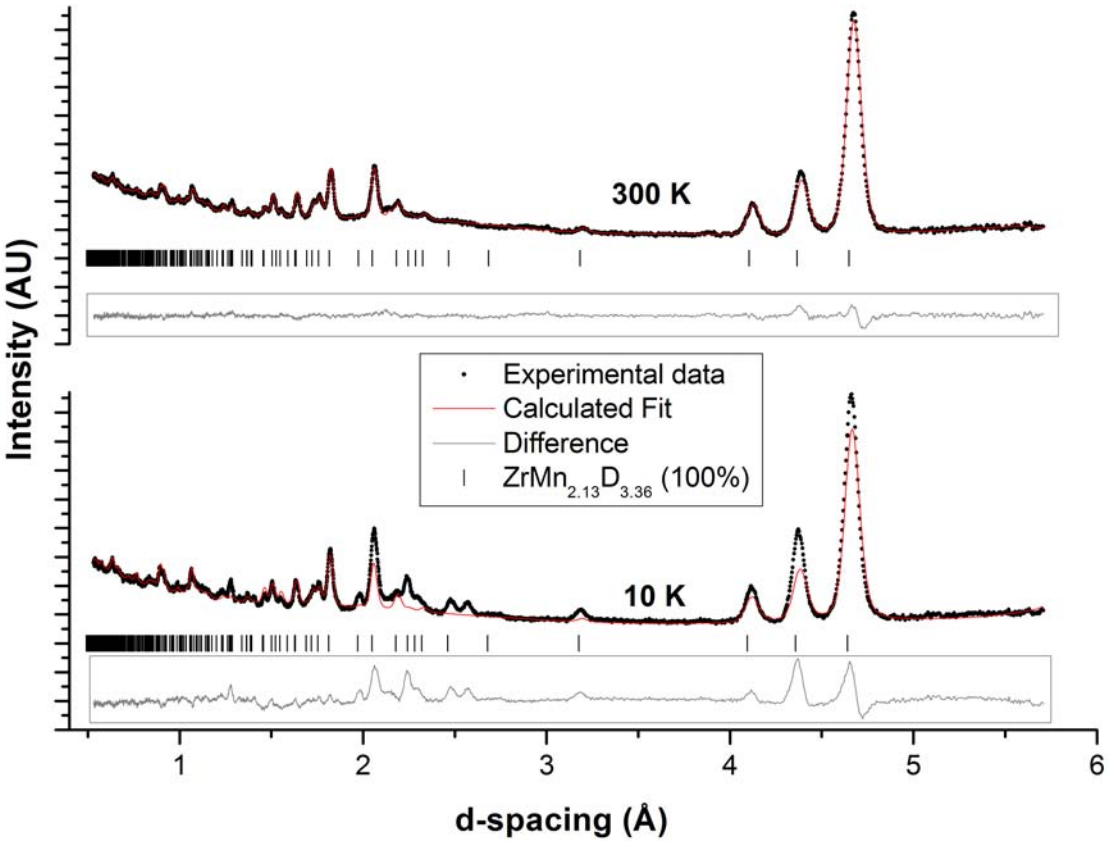

Figure 3.21: *Experimental data (black dots), calculated fits (red lines) and difference plots (grey lines enclosed in boxes) for the structural refinement of* $ZrMn_{2.13}D_{3.36}$ *from neutron diffraction data collected at bank 3 of the ISIS GEM diffractometer. Shown are data collected at 300 K and 10 K. The Bragg peak positions of the major deuteride phase is shown by vertical tick marks.* $R_{wP} = 1.550(300\ K), R_{wP} = 5.414(10\ K)$.

The refined structure of $ZrMn_{2.09}D_{3.04}$ agrees with those reported in the literature for the stoichiometric $ZrMn_2D_3$ [22, 23]; however, the atomic coordinates of the sites vary slightly (by approximately 10%) between the findings here and those published earlier. The refined deuterium positions of $ZrMn_{2.13}D_{3.36}$ concord almost exactly with these previous studies, suggesting the possibility that these earlier workers were in fact studying slightly superstoichiometric deuterides. The deviation may also simply be the result of high hydrogen mobility in the $ZrMn_{2+x}H_3$ structure at room temperature —a recent quasielastic neutron scattering study found that hydrogen in $ZrMn_2H_3$ is extremely mobile, even down to 225 K, with an activation energy for long-range hydrogen diffusion that is one of

the lowest observed for a Laves phase hydride [24]. Large B_{eq} values determined in the refinement of the deuterium atoms echo this tendency for hydrogen diffusion through the structure, showing that at room temperature, it is difficult to precisely fix the location of deuterium in these structures.

Contrary to the study by Pontonnier *et al.* [22] on the superstoichiometric deuterides, the neutron data refined herein show a clear trend in the decrease unit cell volume of $ZrMn_{2+x}H_3$ as x increases. The conclusion of these earlier workers was that the hydriding reaction brought about the disproportionation of the $ZrMn_{2+x}$ system, returning the stoichiometric $ZrMn_2$ hydride regardless of the composition of the original material; however, the work herein shows that this is not the case. The superstoichiometric deuteride $ZrMn_{2.13}D_{3.36}$ retains precisely the same zirconium to manganese ratio as the parent alloy, and the volume of the unit cell formed by this deuteride is significantly less than that of $ZrMn_{2.09}D_{3.04}$. This mirrors the trend in $V(x)$ demonstrated *via* X-ray diffraction studies on the $ZrMn_{2+x}$ hydrides in Section 3.8.1.

Refined deuterium concentrations for the three $ZrMn_{2+x}-$ D systems can be compared to the values of hydrogen absorption determined *via* pressure uptake in Section 3.4. The number of deuterium atoms per formula unit for the nearly stoichiometric deuteride was found to be 3.04, which agrees excellently with the pcT diagram – Figure 3.3 shows that 3.08 hydrogen atoms per formula unit is absorbed by $ZrMn_{2.06}$ at 126.0°C. For the superstoichiometric deuteride, the refined composition was slightly higher than expected: compare the refined value of 3.36 deuterium atoms per formula units with the volumetrically determined value of 3.11 (for hydrogen absorption at 51.2°C as shown in Figure 3.6). This perhaps may be related to the low thermal parameters obtained in the $ZrMn_{2.13}D_{3.36}$ refinement —as discussed in Section 2.1.4, there exist a well-known parameter correlation between the occupancy and thermal parameter of a given atom. Conversely, for the substoichiometric deuteride, the refined deuterium concentration of 2.63 atoms per formula unit was lower than expected, with hydrogen absorption measurements

indicating the uptake of 3.00 hydrogen atoms per formula unit (see the 160.0°C isotherm in Figure 3.7).

There exists precedent for these small discrepancies between the refined deuterium concentrations from the neutron diffraction experiment and those determined from the hydriding experiments; indeed, Pontonnier *et al.* [22] found the refined deuterium concentration in $ZrMn_{2+x}-$ D to always be lower than the amount found by volumetric measurement. As per Pontonnier's study, the uptake determined from pressure changes during the hydriding reaction is deferred to as the more accurate judge of the actual hydrogen or deuterium concentrations in the materials.

As it represents the first neutron diffraction study of the substoichiometric $ZrMn_{2+x}D_y$ deuteride, the refined structure of $ZrMn_{1.69}D_{2.63}$ warrants further comment. The atomic coordinates of the original four *2A2B* sites have shifted by approximately 10% from the values found for the stoichiometric deuteride —Table 3.9 tracks the changes in atomic separation between the zirconium and manganese atoms and these four sites, as well as the two new deuterium sites, for $ZrMn_{2.09}D_{3.04}$ and $ZrMn_{1.69}D_{2.63}$. The data reveal that, for the substoichiometric deuteride, the deuterium atoms D1 through D4 have shifted away from the nominal *2A2B* interstice and towards the zirconium vertex; the D2 atom is an exception, remaining fairly equidistant from all four atoms forming the interstice. Substitution of zirconium onto the $6h$ (Mn2) site generates a fraction of new *2A2B* interstices and two new deuterium sites: D5 is shifted from its nominal position towards the substituted $6h$ site, whilst D6 is drastically shifted towards the zirconium $4f$ site. The net effect of these displacements is the creation of a tighter network of deuterium atoms about the $4f$ site in the manganese deficient deuteride as compared to the stoichiometric $ZrMn_2D_3$ [23].

Parameter	$ZrMn_{2.09}D_{3.04}$	$ZrMn_{2.13}D_{3.36}$	$ZrMn_{1.69}D_{2.63}$
D1 on $24l$ site (x, y, z)	$x = 0.098(1)$	$x = 0.034(1)$	$x = 0.113(4)$
	$y = 0.291(1)$	$y = 0.337(1)$	$y = 0.373(3)$
	$z = 0.6017(9)$	$z = 0.5798(6)$	$z = 0.528(2)$
D1 occ.	0.21(1)	0.263(2)	0.159(2)
B_{eq} (Å^2)	2.8(2)	4.9(2)	1.2(3)
D2 on $12k$ site $(x, 2x, z)$	x =0.4171(3)	$x = 0.4581(5)$	$x = 0.3831(6)$
	$z = 0.6184(8)$	$z = 0.6300(6)$	$z = 0.528(2)$
D2 occ.	0.338(5)	0.331(7)	0.272(4)
B_{eq} (Å^2)	2.1(2)	0.53(4)	1.4(3)
D3 on $6h$ site $(x, 2x, \frac{1}{4})$	0.4018(6)	0.4657(3)	0.3864(8)
D3 occ.	0.368(4)	0.350(3)	0.322(6)
B_{eq} (Å^2)	2.7(2)	0.19(5)	0.18(7)
D4 on $6h$ site $(x, 2x, \frac{1}{4})$	0.193(2)	0.195(3)	0.227(1)
D4 occ.	0.082(7)	0.090(8)	0.199(7)
B_{eq} (Å^3)	2.6(7)	0.29(9)	1.7(3)
D5 on $12k$ site $(x, 2x, z)$			$x = 0.143(2)$
			$z = 0.24(1)$
D5 occ.			0.096(3)
B_{eq} (Å^2)			1.6(3)
D6 on $4f$ site $(\frac{1}{3}, \frac{2}{3}, z)$			0.583(5)
D6 occ.			0.093(7)
B_{eq} (Å^3)			0.6(4)

Table 3.8: *Refined deuterium atom positions, as determined via neutron diffraction at 300 K, for the deuterided, cycled $ZrMn_{2+x}-D$ series with $x = -0.35, 0.06, 0.13$. These atom positions correspond with the unit cells described in Table* 3.7.

Atom 1	Atom 2	Average separation (Å)	
		$ZrMn_{2.09}D_{3.04}$	$ZrMn_{1.69}D_{2.63}$
D1	Mn1	1.64(1)	1.80(1)
D2	Mn1	2.988(3)	2.919(6)
D3	Mn1		
D4	Mn1	2.83(1)	
D5	Mn1		2.56(2)
D6	Mn1		
D1	Mn2 (Zr2)	2.17(1)	2.39(1)
D2	Mn2 (Zr2)	2.155(3)	2.565(5)
D3	Mn2 (Zr2)	2.468(5)	2.507(6)
D4	Mn2 (Zr2)	2.34(1)	2.39(2)
D5	Mn2 (Zr2)		1.489(5)
D6	Mn2 (Zr2)		2.10(3)
D1	Zr1 (Mn3)	2.55(2)	1.97(2)
D2	Zr1 (Mn3)	2.089(2)	2.661(5)
D3	Zr1 (Mn3)	1.748(3)	1.752(3)
D4	Zr1 (Mn3)	2.09(1)	1.95(1)
D5	Zr1 (Mn3)		2.45(3)
D6	Zr1 (Mn3)		1.24(1)

Table 3.9: *Average distance, in angstroms, between selected pairs of atoms in the refined structures of $ZrMn_{2.09}D_{3.04}$ and $ZrMn_{1.69}D_{2.63}$. Separations of less than 1 Å and greater than 3 Å are not included in the calculation. Nominal manganese or zirconium sites in which substitution may occur are so indicated in brackets.*

The occupancies of the D1 through D4 atoms in $ZrMn_{1.69}D_{2.63}$ have shifted as compared to the nearly stoichiometric deuteride, with slightly lower fractional occupancies on the D1 and D2 sites, and slightly higher occupancies on the D3 and D4 site. This alteration in distribution may be due to the metamorphosis of a tiny fraction of nominally $2A2B$ sites into $3A1B$ sites, which would be highly favourable towards deuterium absorption.

Finally, it should be noted that the low occupancies of the D5 and D6 sites are exactly in accordance with expectations —consider the D6 interstice formed by three $6h$ sites and one $4f$ site, with 11.6% of the $6h$ sites occupied by zirconium instead of manganese. Therefore, there is a 34.8% chance that this nominally *1A3B* interstice will become a *2A2B* interstice and, if we assume that the *2A2B* interstices are $\frac{1}{4}$ to $\frac{1}{3}$ occupied by deuterium (as the refined structure of the nearly stoichiometric deuteride suggests), the predicted fractional occupancy of the D6 site is 0.116 to 0.087. This agrees excellently with the observed fractional deuterium occupancy of 0.093. Correspondingly, the D5 interstice, which is formed by two $6h$ sites, one $2a$ site and one $4f$ site, is predicted to contain 0.077 to 0.058 deuterium atoms. The refined value of 0.096 is slightly higher, but is not unreasonable, considering the high mobility of deuterium in this structure.

It was noted earlier in Section 3.6.3 that the volume of the $ZrMn_{1.65}$ hydride, as determined *via* X-ray diffraction, was lower than that of the stoichiometric hydride. This was an unexpected result, given that that unit cell of hydrogen-free $ZrMn_{1.65}$ is larger than that $ZrMn_2$, and the two compounds absorb a similar amount of hydrogen. In contrast, the findings of this neutron diffraction study suggest that the volume of the $ZrMn_{1.65}D_{2.63}$ unit cell is slightly larger than that of $ZrMn_{2.09}D_{3.04}$, which is now exactly in accordance with predictions.

3.9.2 Refinement of the magnetic structure of $ZrMn_{2+x}D_y$ at 10 K

It is evident from Figures 3.19 and 3.20 that a structural change occurs in the $ZrMn_{2.06}-$ D system between 300 K and 10 K: the stacked neutron diffraction

patterns collected at these two temperatures illustrates that the $ZrMn_{2.09}D_{3.04}$ structure outlined in Table 3.7 is not the only phase present in the material measured at 10 K. Additional peaks in the difference pattern suggest a low temperature transition. These additional low temperature reflections are more pronounced in the 10 K diffraction data for the superstoichiometric deuteride then the stoichiometric deuteride, as Figure 3.21 shows. The refinement of the 10 K data for $ZrMn_{2+x}D_y$ ($x = 0.06$ and 0.13) will be discussed in Section 3.11 in the context of a low temperature magnetic structure.

3.10 Magnetic behaviour and ordering in $ZrMn_{2+x}$ ($-0.35 \leq x \leq 0.44$) and its hydrides

Hydrogen absorption in the $ZrMn_{2+x}-$ H system causes an intriguing set of magnetic changes and, although oft commented on [30, 33, 51], the nature of these changes remains unclear. The hydrogen-free $ZrMn_{2+x}$ phase has been reported [30] to be Pauli paramagnetic down to 4.2 K with $\chi = 1.60 \times 10^{-3}$ emu/f.u. for the stoichiometric alloy, with susceptibility increasing slightly with x; however, theoretical studies [21,31] suggest a stable ferromagnetic or antiferromagnetic structure at low temperatures. In contrast, the hydrided $ZrMn_{2+x}H_3$ exhibits spin glass magnetism, with the observed moment increasing with x [30, 33]. The magnetic structure of the hydride has not been elucidated, but previous workers [30,35] have speculated that it is ferro- or ferrimagnetic.

In order to elucidate the magnetic behaviour of the $ZrMn_{2+x}$ system and clarify how the magnetic properties change both upon hydrogen absorption and variation in the manganese content, the as-synthesised $ZrMn_{2+x}$ alloys, their cycled hydrides and the cycled, dehydrided analogues were all examined at a variety of field strengths and temperatures using a SQUID magnetometer. The synthesis of these compounds is discussed in Section 3.2 and 3.4, whilst the operational details of the SQUID are covered in Section 2.2.7.1.

3.10.1 Magnetism of nearly stoichiometric $ZrMn_{2.06}$ and its hydride

The magnetic behaviour of the nearly stoichiometric $ZrMn_{2.06}-$ H system was examined over the temperature range 2 to 300 K; the as-synthesised alloy, as well the cycled hydride and dehydrided material, were all analysed. Figure 3.22 shows the variation in molar susceptibility with temperature for the three materials. The alloy and the dehydrided sample had very similar magnetic behaviour: the initial susceptibility ($\chi_{300K} = 1.82 \times 10^{-3}$ emu mol^{-1} Oe^{-1} (alloy), $\chi_{300K} = 3.25 \times 10^{-3}$ emu mol^{-1} Oe^{-1} (dehydride)) rose gradually as temperature decreased from 300 K, reaching approximately double its initial value by a temperature of 50 K. As the temperature decreased further the susceptibility rose rapidly, intensifying more than 10-fold by the time 5 K has been reached.

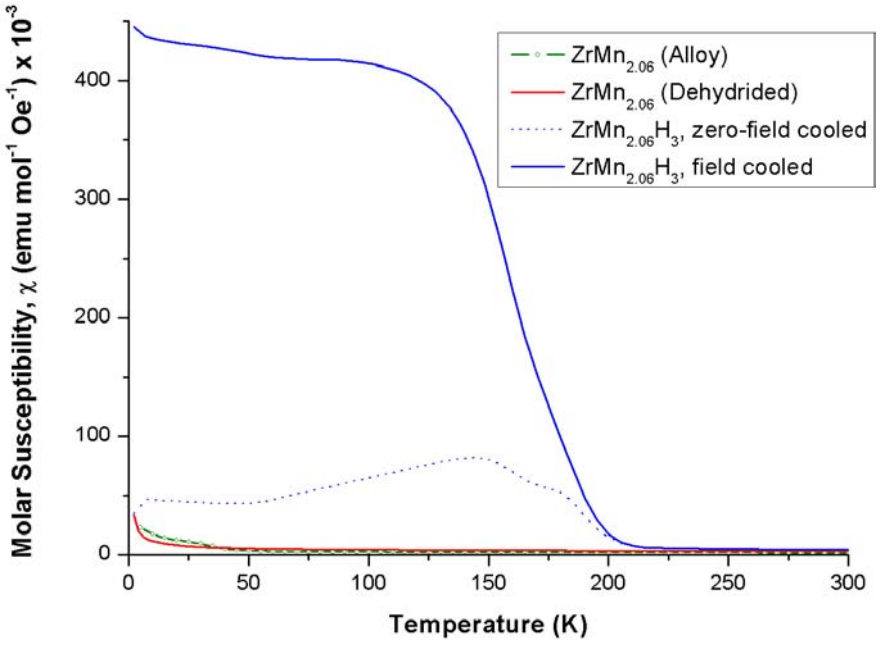

Figure 3.22: *Thermomagnetic analysis of the $ZrMn_{2.06} - H$ series from 2 K to 300 K. The alloy (green line with open circles) and dehydrided, cycled sample (red line) were cooled to 2 K in a field of 1000 Oe before measurement in the same field. The hydride $ZrMn_{2.06}H_3$ was measured both when cooled in absence of field (blue dashed line), and when cooled in field (blue solid line). Relative errors are smaller than the data points.*

For the hydride, the magnetic behaviour below 225 K mirrored that of the alloy with a susceptibility ($\chi_{300K} = 4.25 \times 10^{-3}$ emu mol^{-1} Oe^{-1}) that increased slowly with decreasing temperature. At $T = 224$ K, the hydride undergoes a magnetic transition, and the susceptibility below this point depended upon the thermal history: when cooled in a magnetic field prior to measurement, the susceptibility sharply escalates by a factor of 100 and then continues to rise slowly as the temperature is further reduced. However, when the hydride is cooled in the absence of a magnetic field, the susceptibility below the transition temperature peaks at 144 K and then decreases slowly with temperature. The excellent agreement between the χ_{300K} values reported above for $ZrMn_{2.06}$ and $ZrMn_{2.06}H_3$, and those given by Pourarian *et al.* for the stoichiometric system ($\chi_{300K} = 1.60 \times 10^{-3}$ emu mol^{-1} Oe^{-1} (alloy), $\chi_{300K} = 4.21 \times 10^{-3}$ emu mol^{-1} Oe^{-1} (hydride) [30]) should be noted.

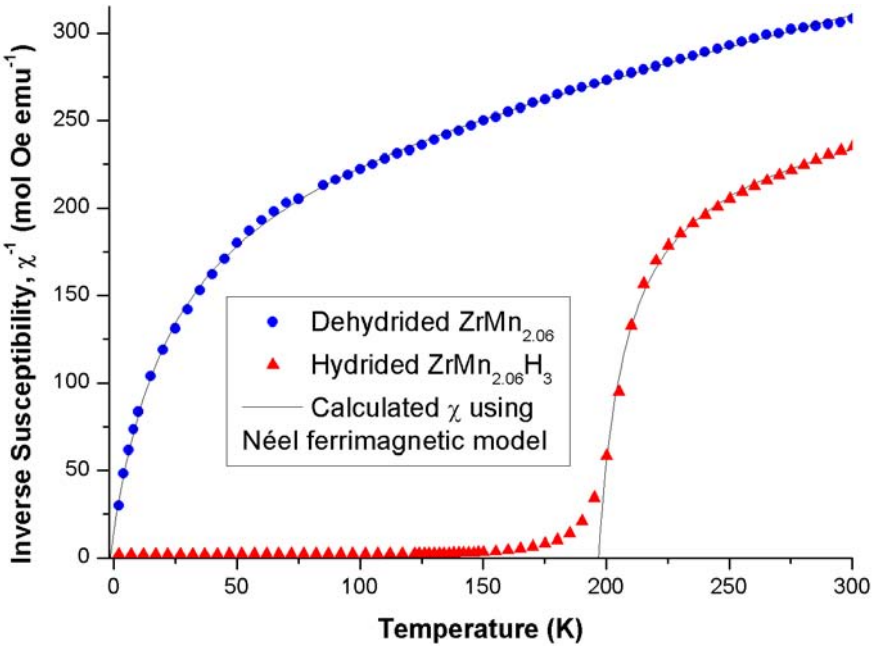

Figure 3.23: *A plot of the temperature dependence of the inverse molar susceptibility for cycled, dehydrided $ZrMn_{2.06}$ (blue dots) and cycled, hydrided $ZrMn_{2.06}H_3$ (red triangles), both cooled in and then measured in a field of 1000 Oe. The coloured symbols are experimental data (note that relative errors are smaller than the data points), whilst the solid black lines are fits of the data to the Néel ferrimagnetism model.*

Figure 3.23 plots the dependence of the inverse of the molar susceptibilities of the dehydrided $ZrMn_{2.06}$ and hydrided $ZrMn_{2.06}H_3$ against temperature. The sharp drop in χ^{-1} around the visually identified T_c of 224 K clearly shows that the hydride undergoes a magnetic transition; curiously enough, however, the dehydrided material unexpectedly exhibits this same rapid decrease in χ^{-1} as the measurement temperature approaches 2 K. Contrary to the published literature, $ZrMn_{2.06}$ is obviously not a Pauli paramagnet, as its susceptibility is far from temperature-independent. It is evident that the hydrogen-free phase undergoes a very low temperature transition with some T_C below 2 K that cannot be accessed under these experimental conditions; moreover, the similarity in shape of the inverse susceptibility curves for $ZrMn_{2.06}$ and $ZrMn_{2.06}H_3$ suggests that the nature of the magnetic ordering in the two materials may be related.

As outlined in Section 2.2.4, the shape of the non-linear χ^{-1} *vs.* T relationship that is described in Figure 3.23 is characteristic of a ferrimagnet. Indeed, the Néel ferrimagnetic model given by Equation 2.34 can be successfully fit to the experimental data for both $ZrMn_{2.06}$ and $ZrMn_{2.06}H_3$, with derived fitting parameters as shown in Table 3.10. The fittings parameters that describe the Néel hyperbola – $C, \chi_o, \sigma, \theta$ – can be directly related to the molecular field coefficients of the A and B sublattices – $\gamma_{AA}, \gamma_{AB}, \gamma_{BB}$ – as shown by Equations 2.35 through 2.38; additionally, these can then be transmuted into exchange integrals J_{ij} *via* the use of Equation 2.39. The results of these calculations (shown in Table 3.10) allow initial

	$ZrMn_{2.06}$	$ZrMn_{2.06}H_3$
C	3.33(7)	5.4(2)
χ_o	0.00422(4)	0.0050(7)
σ	$5.5(2) \times 10^3$	$2.6(3) \times 10^3$
θ	$-25.0(8)$	185(2)
γ_{AA}	$-4.5(3)$	$-18(3)$
γ_{AB}	$-2.5(1) \times 10^2$	$-2.1(4) \times 10^2$
γ_{BB}	0.42(2)	$1.8(3) \times 10^3$
J_{AB} (K)	$-2.3(1)$	$-30(5)$
J_{AA} (K)	$-189(9)$	$-1.7(3) \times 10^2$
J_{BB} (K)	0.32(2)	$8.3(6) \times 10^2$

Table 3.10: *Calculated fitting parameters from the Néel ferrimagnetism model used to describe the observed temperature dependence of the $\chi^{-1}(T)$ data for cycled, dehydrided $ZrMn_{2.06}$ and for $ZrMn_{2.06}H_3$.*

conclusions about the ordering in the $ZrMn_{2.06}-$ H system to be made:

- The $A-B$ coupling is slightly negative, increasing upon hydriding.
- The $A-A$ coupling strongly favours antiparallel alignment.
- The $B-B$ coupling is negligible in $ZrMn_2$, but very strongly favours parallel alignment in the hydride.

Further insight into the magnetic behaviour of the $ZrMn_{2.06}-$ H system can be gleaned from a hysteresis measurement; Figure 3.24 shows the variation in magnetisation against applied magnetic field strength at 2 K for the alloy, hydrided, and dehydrided members of this system. A paramagnet would be expected to display a shallow but linear increase in magnetisation as field strength is increased; but, as the figure shows, none of the three materials display such a linear $M(H)$ dependence. This observation lends further strength to the postulate that both the hydrogen-free and the hydrided members of the $ZrMn_{2.06}-$ H system are magnetically ordered at low temperatures.

The hysteresis plot in Figure 3.24 shows that at all field strengths, $ZrMn_{2.06}H_3$ exhibits a much higher magnetisation than the hydrogen-free phase. At low field strengths – that is, below 7 kOe – the magnetisation response of the cycled, dehydrided material and the virgin alloy cannot be distinguished. However, as the field is increased, a larger enhancement in magnetisation is observed for the dehydrided material than for the virgin alloy. This difference between the alloy and the dehydrided material at high field strengths may be due to a very small amount of hydrogen, existing as a solid solution within the metal matrix, which survived the dehydriding process; even traces of interstitial hydrogen in the $ZrMn_{2.06}$ lattice would affect the strength of the magnetisation. Figures 3.25 and 3.26 document in more detail the hysteresis of $ZrMn_{2.06}H_3$ and dehydrided $ZrMn_{2.06}$, respectively.

It is seen from the hysteresis plot in Figure 3.25 that $ZrMn_{2.06}H_3$ is a soft magnet with a very large magnetic remanence: this suggests that, although there

may be a contribution to the hysteresis loss from magnetic strain, the substantial magnetocrystalline anisotropy is the main loss component. For the hysteresis of the dehydrided $ZrMn_{2.06}$ at 2 K, as shown in Figure 3.26, this strong magnetocrystalline anisotropy is not manifested, as M_r and H_c are nearly zero. This minor hysteresis and the curvature of the $M(H)$ data at 2 K may be due to appearance of short range interactions and clusters of spins at the onset of a magnetic transition.

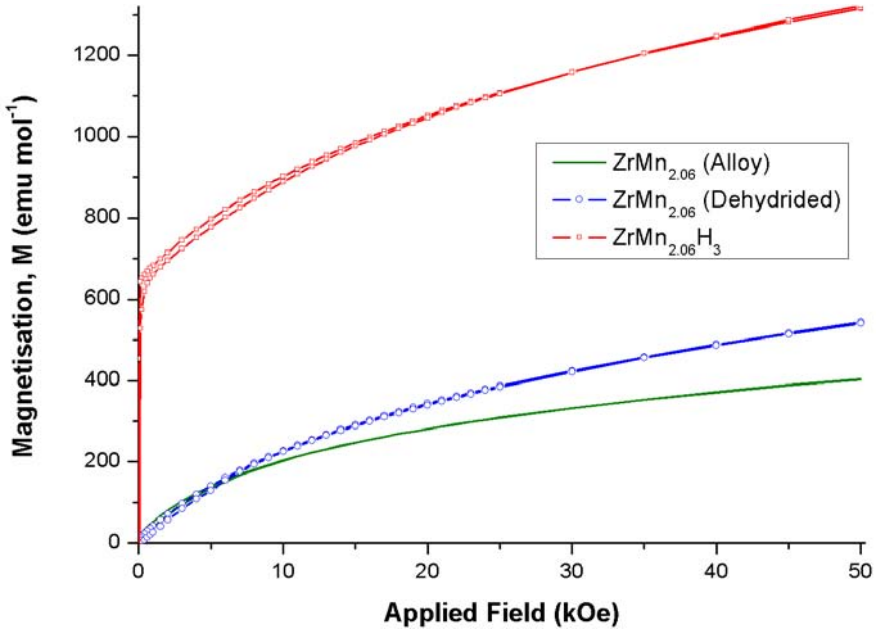

Figure 3.24: *A hysteresis plot at 2 K for the $ZrMn_{2.06}-H$ series, showing the first quadrant of data only. The field dependence of the molar magnetisation (up to 50 kOe) is shown for the alloy (green solid line), the cycled, dehydrided $ZrMn_{2.06}$ (blue line with open circles) and the hydride $ZrMn_{2.06}H_3$ (red line with open squares). Relative errors are smaller than the data points.*

The thermomagnetic data in Figure 3.23 suggest that at 2 K the hydrogen-free material is approaching a magnetic transition, thus, at lower temperatures, a more distinct hysteretic behaviour would be observed. The measured hysteresis of $ZrMn_{2.06}$ at higher temperatures (see Figure 3.26) indicates a linear relationship between magnetisation and field, as would be expected for a paramagnet; the difference between these data and those measured at 2 K is another indicator of the very low temperature magnetic transition that occurs in this material.

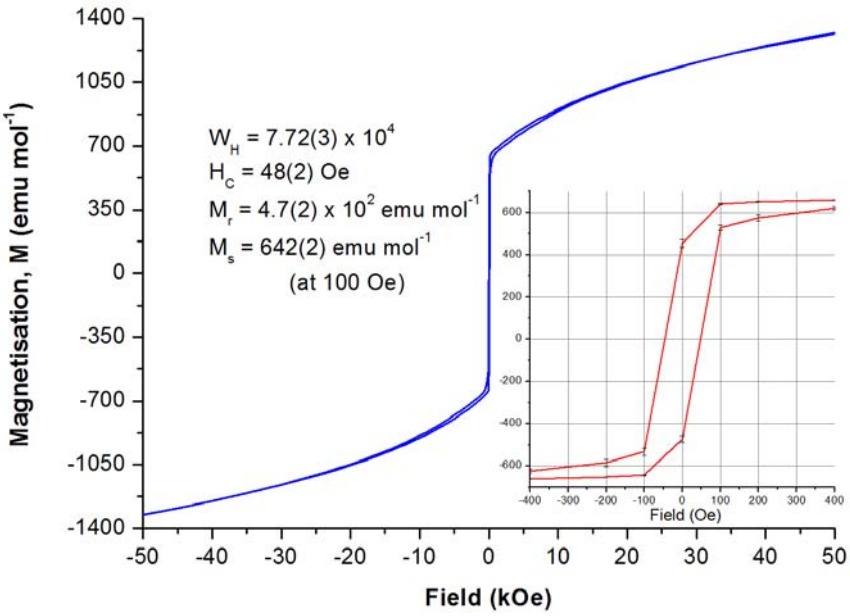

Figure 3.25: *A hysteresis plot at 2 K for $ZrMn_{2.06}H_3$, showing the field dependence of the molar magnetisation from -50 kOe to 50 kOe. Inset on the right is detail on the low-field hysteresis behaviour. The hysteresis parameters derived from the data are also shown on left.*

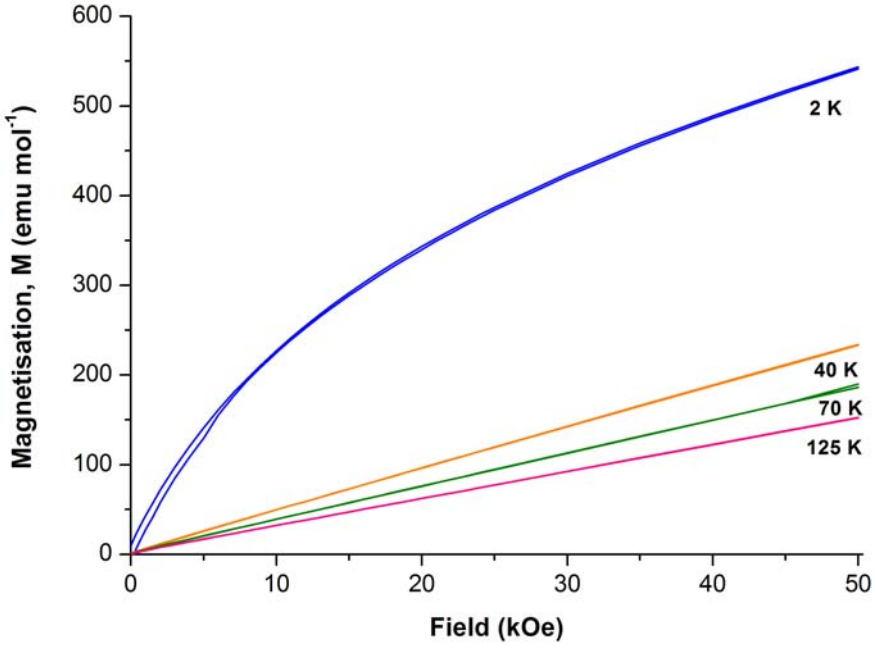

Figure 3.26: *A hysteresis plot at several temperatures for cycled, dehydrided $ZrMn_{2.06}$, showing data from the first quadrant only. Relative errors are smaller than the data points. The field dependence of the molar magnetisation (up to 50 kOe) is shown at 2 K, 40 K, 70 K and 125 K as indicated on the graph.*

The relationship between H and M describes the degree of itinerancy or localisation in a system, as discussed in Section 2.2.5; as well, the saturation magnetisation M_s can be extracted from a plot of M^2 against $\frac{H}{M}$ [73]. Figure 3.27 is an Arrott plot for the $ZrMn_{2.06}$ system, with the field dependence of the magnetisation for the both the alloy and the dehydrided phase shown at a variety of temperatures. For the dehydrided sample at 2 K, the $M(H)$ relation is quite linear; however, as temperature increases, substantial curvature in the Arrott plot develops. As the $ZrMn_{2.06}$ phase becomes magnetically ordered at some low temperature, it would be expected that the extrapolated $y-$intercept of the Arrott plot would gradually approach zero from below as the temperature is lowered to T_C. The linear fit to the 2 K data is negative, indicating that M_s is zero and the material is still paramagnetic; however, when compared to the extrapolated intercepts at higher temperatures, it is evident that a magnetic transition is imminent below 2 K.

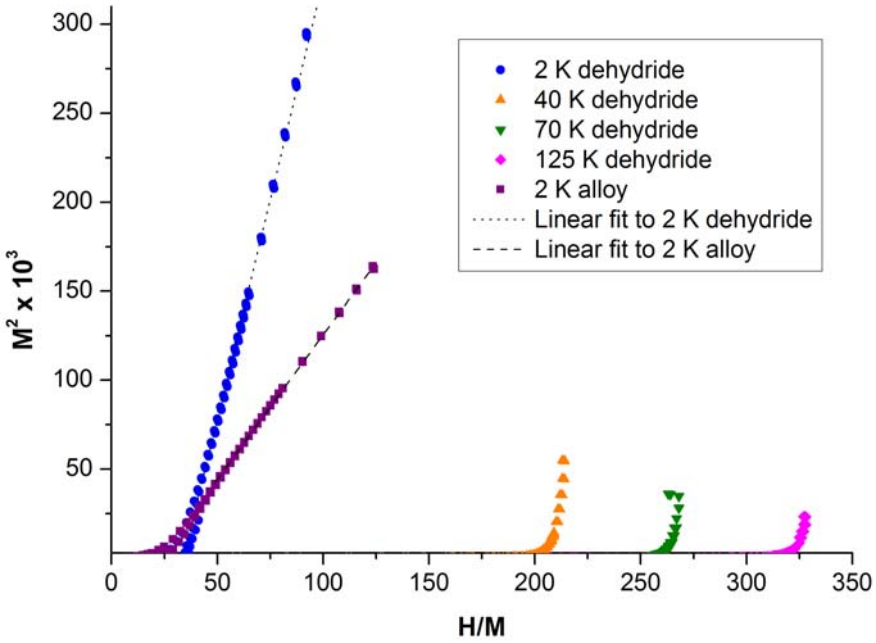

Figure 3.27: *An Arrott plot for cycled, dehydrided $ZrMn_{2.06}$, with the square of the molar magnetisation, M, on the y-axis and the applied field, H (in Oe), over M, on the x-axis. Relative errors are smaller than the data points. The linear fit to the 2 K data (blue circles) is shown as a dotted black line; however, the data at 40 K, 70 K and 125 K (coloured symbols) are all too curved to apply a linear fit. Also shown on the same plot is the $ZrMn_{2.06}$ alloy at 2 K (purple squares), with its corresponding linear fit (dashed black line).*

Figure 3.27 also charts the $M(H)$ relationship for the $ZrMn_{2.06}$ alloy at 2 K. Similar to the dehydrided material at this temperature, the Arrott plot for the alloy can be fitted to a linear trend; however, the slope of the linear fit is significantly higher in the dehydrided material and the value of the $y-$intercept follows suit. This suggests that the alloy is closer to the magnetic transition than the dehydrided material —it is possible that the reduction in particle size and increase in crystalline strain brought about by the cycling process has lowered the T_C in dehydrided $ZrMn_{2.06}$.

The Arrott plots for $ZrMn_{2.06}H_3$ measured between 2 K and 125 K can all be described by linear trends, as shown in Figure 3.28. In calculating the linear trendlines, it was necessary to exclude data for applied fields of less than 5 kOe due to some low field curvature. For all four temperatures measured, the $y-$intercepts are positive and indicate that the sample is magnetically ordered, which is in accordance with the observed T_C of 225 K. The spontaneous magnetisation of $ZrMn_{2.06}D_3$ is 636 emu mol^{-1}, as calculated from the Arrott plot at 2 K.

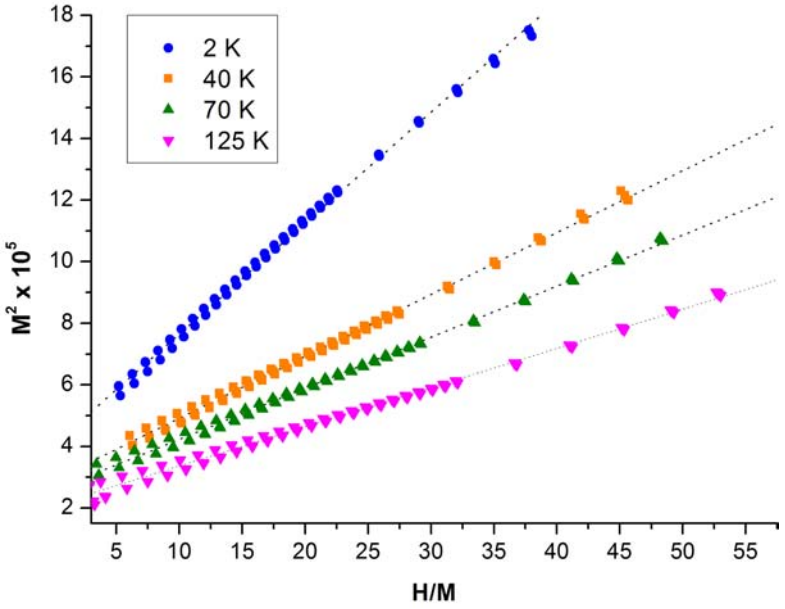

Figure 3.28: *An Arrott plot for $ZrMn_{2.06}H_3$, with the square of the molar magnetisation M on the y-axis and the applied field, H (in Oe), over M, on the x-axis. Relative errors are smaller than the data points. The 2 K, 40 K, 70 K and 125 K data sets are shown as colored symbols, whilst the linear fits to these data sets are shown as a dotted black lines.*

3.10.1.1 Proposed model for magnetic order in $ZrMn_{2.06}$ and $ZrMn_{2.06}H_3$

The experimental data reviewed in the previous section provide several powerful clues as to the nature of the magnetic ordering in the $ZrMn_{2.06}-$ H system, summarised here:

- The $\chi^{-1}(T)$ data for both the hydrided and the hydrogen-free phase can be fitted to the 'Néel hyperbola' described by Equation 2.34, indicating that these compounds are ferrimagnetic. A transition temperature of 224 K was identified for the hydride, whereas both the dehydride and the virgin alloy, which are magnetically very similar, appear to undergo a magnetic transition just below 2 K.

- Analysis of the magnetisation field dependence revealed that the hydride was a soft magnet with a large magnetocrystalline anisotropy. The magnetisation behaviour of the dehydrided material at 2 K revealed a very small hysteresis with substantial deviation from the expected linear $M(H)$ behaviour, suggesting the formation of short-range spin correlations at the threshold of long-range magnetic order.

- Arrott plots of the hydrided material verified its magnetism and provided a value for M_s; the Arrott plots of the dehydrided material showed that whilst M_s was zero for all temperatures measured, the system at 2 K was on the verge of manifesting a spontaneous magnetisation

Fitting parameters of the Néel hyperbolae were used to derive λ and μ, the relative fractions of atoms on the A and B sublattices, as well the exchange constants relating them. For the dehydrided and the hydrided material, μ was found to be 0.029 and 0.023, respectively, indicating that the A sublattice is much larger than the B sublattice. Assuming that the manganese atoms are those that carry the magnetic moment, the most plausible ferrimagnetic model that agrees with the experimental evidence is one in which is A sublattice consists of manganese

atoms on the $2a$ sites, and the B lattice is formed by the substituted manganese atoms on the $4f$ site.

Using this model, the value of μ identified above *via* fitting of the dehydrided experimental data would correspond to a composition $ZrMn_{2.05}$ – agreeing very well with the composition of $ZrMn_{2.06}$ that was derived from the crystallographic data (see Section 3.3.1). Conversely, a model where the A sublattice consisted of the $6h$ manganese atoms would generate a calculated composition of $ZrMn_{2.15}$, a value that lends support to the placement of the A sublattice of the $2a$ sites instead. Further support for a magnetic model with moments located on the $2a$ sites can be found in *ab initio* simulations of Chen *et al.* [31], where an arrangement of opposed moments on the manganese $2a$ sites was found to be the most stable antiferromagnetic structure for a perfect $ZrMn_2$ crystal at absolute zero.

Atom 1	Atom 2	Average separation (Å)	
		$ZrMn_{2.06}$	$ZrMn_{2.06}-$ D
Mn1	Mn1		
Mn1	Mn2	2.534(1)	2.736(2)
Mn1	Zr1(Mn3)	2.953(8)	3.16(1)
Mn2	Mn2	2.494(3)	2.574(3)
Mn2	Zr1(Mn3)	2.967(2)	3.148(2)
Zr1	Zr1(Mn3)	3.083(8)	3.27(1)

Table 3.11: *Average distance, in angstroms, between selected pairs of atoms in the refined structures of $ZrMn_{2.09}D_{3.04}$ (determined via neutron diffraction) and $ZrMn_{2.06}$ (determined via X-ray diffraction). Separations of less than 1.5 Å and greater than 3.5 Å are not included in the calculation. The nominal zirconium site in which manganese substitution may occur is so indicated in brackets.*

In this proposed magnetic model for the $ZrMn_{2.06}-$ H system, the chief difference between the hydrogen-free and the hydrided compound is an expanded lattice. As shown in Section 3.6.1, the base metal substructure, and therefore the relative positions of the manganese atoms, is unaffected by hydrogen absorption; however, the lattice expansion does increase the distances in between the metal atoms. Table 3.11 tracks the changes in metal-metal distance between $ZrMn_{2.06}$ and and its deuterided analogue. It can be seen that the manganese-

manganese distance for the neighbouring Mn2 atoms on the $6h$ site is quite short (less than 2.6 Å), as is the distance between the $2a$ site (Mn1) and the $6h$ site, for both the hydrided (deuterided) and hydrogen (deuterium)-free structure. Conversely, the distance between neighbouring Mn1 atoms on $2a$ sites are the largest manganese-manganese separations in both structures —greater than 3.5 Å. The distance between the substitutional manganese on the $4f$ (Mn3) site in $ZrMn_{2.06}$ and either nominal manganese site is approximately 3 Å, and slightly larger than this in the hydride (deuteride).

Variation in the relative manganese-manganese distances plays a role in the magnetic behaviour of two other Laves phase intermetallic compounds, YMn_2 and $LuMn_2$. These alloys reversibly absorb hydrogen at temperatures and pressures similar to those observed for the $ZrMn_2$ system, and also exhibit analogous magnetic behaviour —the parent intermetallics appear to be paramagnetic, but the hydrides exhibit a spin glass magnetism. For both YMn_2 and $LuMn_2$, the appearance of magnetic order in the hydride was attributed to a hydrogen induced lattice expansion that caused the Mn-Mn bond length to exceed a critical distance of 2.86 ± 0.06 Å [94]. Below this distance, the magnetic coupling is thought to be quenched, but above the critical distance a local moment on the manganese sites may form. A similar model was also proposed for the R_6Mn_{23} rare earth hydrides [94]. The *ab initio* study of Chen *et al.* [31] on a postulated antiferromagnetic structure of $ZrMn_2$ supports this concept of a critical Mn-Mn distance: the short distance between neighbouring Mn2 atoms on the $6h$ sites was found to quench their local moments due to increased hybridisation.

In view of this critical distance, re-examination of the manganese-manganese distances in Table 3.11 in consideration of the proposed ferrimagnetic structure suggests that both the hydrided and dehydrided phase of the $ZrMn_{2.06}-$ H system should manifest localised moments on the A sublattice (manganese on $2a$ sites) and on the B sublattice (substitutional manganese on the $4f$ site). The difference in transition temperature between these two materials suggests a large difference

in stability of the magnetically ordered structures.

A recent analysis of $ZrMn_2$ by Rotter *et al.* [21] has postulated that the intermetallic compound displays highly frustrated magnetism, perhaps as a result of the structural and magnetic degeneracy that low temperature *ab initio* calculations point to: DFT calculations have shown the degeneracy of at least three structures (C14, C15 and C36) at 0 K, with the ferromagnetically ordered phase more stable than a nonmagnetic or antiferromagnetic phase for each of these structures. The gain in magnetisation energy for spontaneous spin polarisation is different in each case, but is of the correct size to cause degeneracy, leading to the prediction that $ZrMn_2$ should be polymorphic at low temperatures, and undergo magnetic ordering as the temperature is reduced [21, 32]. However, neutron diffraction down to 6 K showed no evidence of the magnetostructural degeneracy suggested by these calculations, with the nonmagnetic C14 structure retained at low temperature [21]. Measurements of the temperature dependence of the resistivity revealed anomalous behaviour below 10 K, with significant deviation from the expected behaviour of a simple metal at low temperatures [21]. These variations in the electrical resistivity were ascribed to scattering of the charge carriers on the frustrated Mn moments, suggesting that the predicted magnetostructural degeneracy in $ZrMn_2$ is absent due to magnetic frustration in the system [21].

Much as the hydriding process has been shown in Section 3.8.3 to relieve the crystalline strain induced by the atomic substitution, it is possible that the absorption of hydrogen may reduce the frustration of the manganese moments and increase the transition temperature of the magnetically ordered state. This may occur simply as a result of the hydrogen-induced lattice expansion, although it is possible that an indirect exchange mechanism between manganese and hydrogen may also stabilise the magnetic ordering. Nevertheless, the observed spin glass behaviour of $ZrMn_{2.06}H_3$ below T_C indicates that it is still a system of significant frustration, in that cooling under an applied field is necessary in order to obtain the fully ordered state.

This model of a frustrated ferrimagnetic system that is relaxed by hydrogen absorption is in sharp contrast to the model proposed by Pourarian *et al.* [91] to explain the body of published experimental data on the magnetic behaviour of the $ZrMn_2-$ H system. Although the concept of a critical Mn-Mn distance is also invoked by these authors, they accommodate a local moment on both the $2a$ and the $6h$ manganese site, and fail to explain why the hydrogen-free material is nonmagnetic even though this critical distance has been exceeded in the $ZrMn_2$ structure.

3.10.2 Magnetism of the superstoichiometric $ZrMn_{2+x}-$ H ($0.13 \leq x \leq 0.44$) system

The magnetic behaviour of the superstoichiometric $ZrMn_{2+x}-$ H system was examined over the temperature range 2 to 300 K for $x = 0.13$, 0.18, 0.31 and 0.44. The as-synthesised alloys and the cycled hydrides were both analysed under identical conditions; for $x = 0.44$, the dehydrided material was also examined. Figure 3.29 shows the variation in molar susceptibility with temperature for the superstoichiometric hydride series; for ease of comparison, the thermomagnetic analysis of the nearly stoichiometric hydride is also shown on this graph. The $\chi(T)$ data for the alloys and the dehydrided materials are not shown but for all values of x the thermomagnetic behaviour was found to be very similar to that of $ZrMn_{2.06}$, which is shown in Figure 3.22. Table 3.12 summarises the results of the thermomagnetic analysis for the alloy, dehydrided, and hydrided members of the $ZrMn_{2+x}$ series.

For the superstoichiometric hydrides, the magnetic behaviour in the range $200 - 300$ K appeared paramagnetic, mirroring that of the original alloys, with susceptibilities that increased slowly with decreasing χ. As temperature dwindled, however, each of the hydrides underwent a magnetic transition and their T_c values, which were obtained from visual analysis of the thermomagnetic data, are reported in Table 3.12. Similar to $ZrMn_{2.06}H_3$, the superstoichiometric hydrides exhibited spin glass behaviour, as the susceptibility below T_c depended upon the thermal his-

tory. When the hydrides were cooled in absence of a field, the susceptibility peaked around 100 K, with the magnitude of this χ_{Max}, and the temperature at which it occurred, dependent on the manganese concentration. For hydrides cooled in a magnetic field, the susceptibility substantially increased below T_c and continued to rise as temperature decreased. The amount by which the room temperature susceptibility was amplified in the field cooled $ZrMn_{2+x}H_3$ as it was brought below its transition temperature was dependent on x, with the magnetisation at 2 K decreasing as x increased.

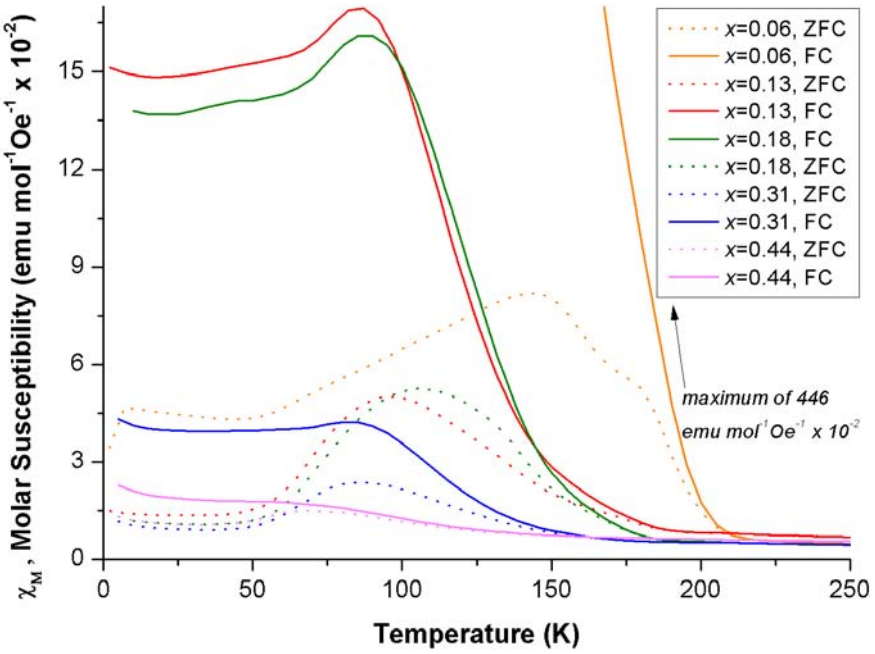

Figure 3.29: *A stacked plot of thermomagnetic analyses for the $ZrMn_{2+x}H_3$ hydrides, from 2 K to 250 K, for $x = 0.06, 0.13, 0.18, 0.31, 0.44$. Each compound was measured twice in a field of 1000 Oe, once after cooling to 2 K in the same field (solid lines labelled FC - field cooled), and once after cooling to 2 K in the absence of a field (broken lines labelled ZFC - zero field cooled). Relative errors are smaller than data points.*

Table 3.12 shows that the room temperature susceptibility of the $ZrMn_{2+x}$ alloy series is independent of x, increasing only slightly across the series; in all cases, the maximum susceptibility is 10 times larger. As the alloys are Pauli paramagnetic at room temperature, this increase in χ_{300K} with x may be attributed to an increase

in the Fermi level density of states with increased manganese substitution. When compared to the alloy, χ_{300K} for the dehydrided $ZrMn_{2.44}$ was slightly higher. The room temperature susceptibilities of the superstoichiometric hydrides followed the opposite trend, decreasing as the manganese content increased. In all cases, the room temperature susceptibilities of the hydrides were larger than those of the hydrogen-free material. These values show excellent agreement with those reported by Pourarian *et al.* [30] for the $ZrMn_{2+x}-$ H series.

Examination of $\chi^{-1}(T)$ data for the $ZrMn_{2+x}H_3$ system reveals that both the hydrided and the hydrogen-free phases can be described by the Néel hyperbola (see Equation 2.34), suggesting that $ZrMn_{2+x}$ and $ZrMn_{2+x}H_3$ are ferrimagnetic. The inverse susceptibility versus temperature graphs for the $ZrMn_{2+x}$ alloys are shown in Appendix A, but in all cases were extremely similar to that of the $ZrMn_{2.06}$ dehydrided sample shown in Figure 3.23. For all values of x, the ferrimagnetic transition temperature is predicted to be below 2 K —the lowest temperature that could be accessed in the experiment. The $\chi^{-1}(T)$ data for the superstoichiometric hydrides are also shown in Appendix A, but again were akin to that shown in Figure 3.23 for $ZrMn_{2.06}H_3$. The principal difference in the inverse susceptibility plots between the stoichiometric hydride and those with excess manganese was a shift in T_c to lower temperatures as Table 3.12 documents. Values for the Néel fitting parameters for the $ZrMn_{2+x}-$ H series are reported in Table 3.13.

The variation in transition temperature for the superstoichiometric hydrides is illustrated in Figure 3.30. Two sets of transition temperatures are shown: the 'experimental' T_c, which is recorded in Table 3.12, was derived in the conventional fashion by examination of the $\chi(T)$ data, with the transition temperature taken to be the point at which the susceptibility deviates from the expected paramagnetic value. Conversely, a different value of T_c can be extracted from the Néel hyperbolae fitted to the $\chi^{-1}(T)$ data; here, the transition temperature is taken to be the $x-$intercept of the fitted curve. The magnitude of the difference between these two values provides a measure of the temperature range over which the transition

	χ_{300K} $(\frac{emu}{mol \cdot Oe})$	[1]χ_{Max} $(\frac{emu}{mol \cdot Oe})$	T of χ_{Max} ±5 K	T_C ±2 K	[2]M_S $(\frac{emu}{mol})$	m per f.u. (μ_B)
alloys:						
$ZrMn_{2.06}$	$1.820(1) \times 10^{-3}$	0.02789(2)	5			
$ZrMn_{2.13}$	$2.395(1) \times 10^{-3}$	0.01662(2)	5			
$ZrMn_{2.18}$	$2.213(1) \times 10^{-3}$	0.01727(1)	5			
$ZrMn_{2.31}$	$2.252(1) \times 10^{-3}$	0.01504(1)	5			
$ZrMn_{2.44}$	$2.710(1) \times 10^{-3}$	0.01391(2)	5			
dehydrides:						
$ZrMn_{2.06}$	$3.248(1) \times 10^{-3}$	0.01570(1)	5			
$ZrMn_{2.44}$	$3.732(1) \times 10^{-3}$	0.01611(1)	5			
hydrides:						
$ZrMn_{2.06}H_3$	$4.247(1) \times 10^{-3}$	0.0817(1)	144	224	642(7)	0.109(1)
$ZrMn_{2.13}H_3$	$4.170(1) \times 10^{-3}$	0.0481(1)	97	190	343(9)	0.057(2)
$ZrMn_{2.18}H_3$	$3.813(1) \times 10^{-3}$	0.0525(1)	105	186	151(8)	0.037(2)
$ZrMn_{2.31}H_3$	$4.099(1) \times 10^{-3}$	0.0236(1)	85	180	206(9)	0.027(2)
$ZrMn_{2.44}H_3$	$3.592(1) \times 10^{-3}$	0.01014(8)	85	174	146(6)	0.024(1)

[1]For the hydrides, this is the peak in the ZFC data, otherwise, it is 5 K

[2]M_S was determined from the saturation at 2 K of the $M(H)$ data.

Table 3.12: *Experimentally observed susceptibilities, transition temperatures, saturation magnetisations and magnetic moments for the $ZrMn_{2+x} - H$ series. Data for the virgin alloys and hydrides are given at all values of x (0.13, 0.18, 0.31 and 0.44); however, the magnetic behaviour of the cycled, dehydrided phase was examined only for x = 0.44. Data for the nearly stoichiometric system, $ZrMn_{2.06} - H$, are shown for comparison.*

Néel ferrimagnetism model: $\frac{1}{\chi} = \frac{T}{C} - \frac{1}{\chi_o} - \frac{\sigma}{T-\theta}$

	C	$\chi_0(\times 10^{-3})$	$\sigma(\times 10^3)$	θ	γ_{AB}	$\gamma_{AA}(\times 10^2)$	γ_{BB}	${}^1J_{AB}$	${}^1J_{AA}(\times 10^2)$	${}^1J_{BB}$
alloys:										
$ZrMn_{2.13}$	2.7(1)	3.06(5)	7.7(6)	−23(1)	−529(9)	−0.033(4)	$-8.3(9) \times 10^2$	−264(9)	−2.5(3)	$-6.3(8) \times 10^2$
$ZrMn_{2.18}$	1.67(3)	3.48(4)	6.4(3)	−22(1)	−24(2)	−3.1(2)	−1.13(8)	−12.2(9)	−2.3(2)	−0.84(6)
$ZrMn_{2.31}$	1.66(2)	3.56(3)	5.7(2)	−20.8(7)	−2.3(1)	−3.1(1)	0.70(3)	−1.14(6)	−2.3(1)	0.52(3)
$ZrMn_{2.44}$	1.95(3)	4.36(5)	3.8(2)	−19(1)	−8.4(7)	−2.5(2)	0.40(3)	−4.2(3)	−1.9(2)	0.30(2)
dehydrides:										
$ZrMn_{2.44}$	3.52(2)	5.11(5)	4.16(6)	−26.0(3)	−10.9(2)	−2.10(4)	−0.137(3)	−5.5(1)	−1.57(3)	−0.103(2)
hydrides:										
$ZrMn_{2.13}H_3$	3.4(5)	5.1(3)	7.5	123(1)	−59(9)	−2.2(4)	$1.1(2) \times 10^3$	−30(4)	−1.7(3)	$8.3(9) \times 10^2$
$ZrMn_{2.18}H_3$	2.3(1)	6.48(8)	5.0	133(1)	−185(9)	−1.8(4)	$2.5(5) \times 10^3$	−92(7)	−1.3(1)	$1.8(4) \times 10^3$
$ZrMn_{2.31}H_3$	2.2(1)	7.0(3)	7.5	78(1)	−123(9)	−2.0(2)	$9.0(7) \times 10^2$	−61(4)	−1.5(1)	$6.7(5) \times 10^2$
$ZrMn_{2.44}H_3$	6.73(8)	4.15(7)	5.0	79.4(8)	−77(9)	−2.6(3)	$8.1(9) \times 10^2$	−39(4)	−2.0(2)	$6.0(7) \times 10^2$

Table 3.13: *Calculated fitting parameters from the Néel ferrimagnetism model used to describe the observed temperature dependence of the $\chi^{-1}(T)$ data for the $ZrMn_{2+x}$ alloys and their hydrides, $ZrMn_{2+x}H_3$. Thermomagnetic measurements were fit to the ferrimagnetic model for $x = 0.13$, 0.18, 0.31 and 0.44. The cycled, dehydrided $ZrMn_{2.44}$ was also analysed.*

occurs, as the experimental T_c marks the start of the transition from a paramagnetic to ordered compound, and the Néel T_c marks the end of this transition. As Figure 3.30 shows, the width of the transition of the $ZrMn_{2+x}H_3$ system expands as x increases, and is indicative of increased magnetic strain and disorder in the system [95].

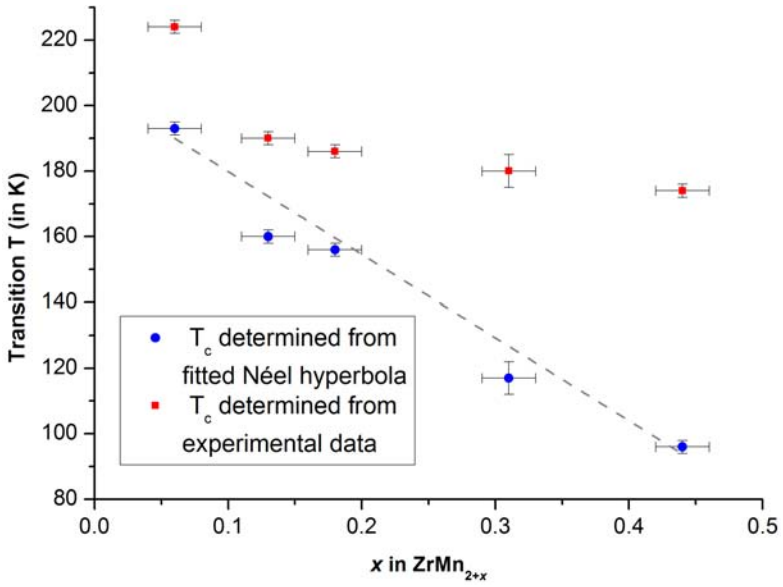

Figure 3.30: *Changes in the ferrimagnetic transition temperature with x across the series $ZrMn_{2+x}H_3$, for x = 0.13, 0.18, 0.31 and 0.44 (data for the nearly stoichiometric hydride are also shown). The set of transition temperatures derived from the experimental data are shown as red squares, whilst the set obtained from the fitted Néel hyperbolas are shown as blue circles. A dotted line shows the linear best fit trend to the Néel data. Uncertainties in x and in T_c are indicated by the error bars.*

Transition temperatures determined from the Néel hyperbolae for $ZrMn_{2+x}H_3$ can be fitted to a linear trend as demonstrated in Figure 3.30. Due to the increased magnetic disorder in the system and the expansion of the transition region, the experimental T_c values do not vary linearly with x. This transition width and its dependence on slight changes in manganese content explains the variation in reported T_c in the literature, and also the poor agreement with the values given here. Pourarian *et al.* [30] suggest a T_c of 143 K for $ZrMn_2H_3$ (their published TMA suggests they have taken an average temperature value at the midpoint of

the transition) whilst Didisheim *et al.* [35] give T_c = 175 K, and the results of Jacob *et al.* [51] suggest a T_c of 190 K. The higher T_c of 224 K that is reported here for $ZrMn_{2.06}H_3$ may also be a result of improved accuracy in the measurement technique since these earlier determinations, allowing subtle changes in χ to be explored and an accurate transition to be observed.

The fittings parameters that describe the Néel hyperbola – $C, \chi_o, \sigma, \theta$ – can be directly related to the exchange integrals J_{ij} for the coupling of the A and B sublattices, as described in Section 2.2.4. The results of these calculations for the $ZrMn_{2+x}-$ H system are shown in Table 3.13 and, for the hydride series, are graphically depicted in Figure 3.31. For the superstoichiometric alloys, the exchange integrals vary little with x; the negative (antiferromagnetic) $A-A$ exchange is the strongest in the system. The inter sublattice exchange is weak, but also antiferromagnetic, whilst J_{BB} is vanishingly small, suggesting there is no $B-B$ coupling at all.

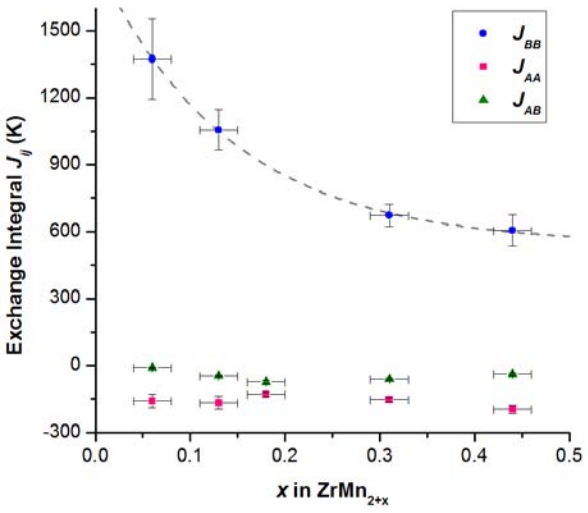

Figure 3.31: *A plot of the magnetic exchange integrals against x for the series* $ZrMn_{2+x}H_3$*, with x = 0.06, 0.13, 0.18, 0.31 and 0.44. The calculation of the exchange integrals is described in the text and assume a ferrimagnetic model with A and B sublattices. The* J_{BB} *coupling is described by blue circles and has been fitted to an exponential trend shown by a broken grey line - note that the x = 0.18 data is not shown as it appears erroneously high. Data for* J_{AA} *are shown by pink squares, and the data for* J_{AB} *are shown by green triangles.*

Upon hydriding, the $B-B$ coupling increases dramatically to became the strongest exchange in the system. The J_{AB} integral is slightly negative and is the smallest in magnitude of all three of the exchange integrals for this system. The J_{AA} integral is also negative, favouring antiparallel exchange, and is several times larger in magnitude than J_{AB}. Both of these coupling constants are

relatively constant against variation in x; however, as Figure 3.31 shows, the J_{BB} integral depends strongly on the manganese content. This exchange integral is positive across the series – favouring parallel spin alignment – and is largest for the nearly stoichiometric hydride. As the manganese content increases, J_{BB} decreases, but even for $x = 0.44$ the J_{BB} exchange is easily the strongest coupling in the system.

A graph of the relative magnetisation ($\frac{M}{M_s}$) against the reduced temperature ($\frac{T}{T_c}$) can be instructive in elucidating the nature of the magnetic ordering in a system —Figure 3.32 shows such a plot for the $ZrMn_{2+x}H_3$ series. Data for $x = 0.44$ has been omitted, as the thermomagnetic curve for the $ZrMn_{2.44}-$ H system was dominated by the contributions from the hydrogen-free $ZrMn_{2.44}$ phase. As discussed in Section 3.6.2, this highly superstoichiometric hydride is metastable at room temperature, releasing hydrogen to reform $ZrMn_{2.44}$ *via* the equilibrium described in Equation 3.2. The contribution from the hydride phase could be readily distinguished from the alloy due to differences in the onset of magnetic ordering; however, as the concentration of the hydride in the sample was low, the magnetisation was not of sufficient magnitude to overpower the minor paramagnetic contribution from the alloy.

In ferrimagnetic materials, the relative magnetisation can be thought of as the sum of the magnetisation on the A sublattice and that on the B sublattice. The shape of the $\frac{M}{M_s}$ *vs.* $\frac{T}{T_c}$ curve is characteristic of the magnitude of the sublattices' magnetisations, the nature of the A and B interactions (negative or positive) and the relative amounts of A and B atoms (λ and μ). The curve described by the nearly stoichiometric hydride in Figure 3.32 is similar to the Brillouin function, which models the relative magnetisation of ideal ferromagnets [72]. A perfect Brillouin function is characterised chiefly by an infinite slope at $\frac{T}{T_c} = 1$ and zero slope at $\frac{T}{T_c} = 0$ [72] —conditions which the $ZrMn_{2.06}H_3$ curve does not satisfy, suggesting that there may be minor additional contributions to the magnetisation. As the manganese content in $ZrMn_{2+x}H_3$ increases, this deviation from the

Brillouin function becomes more significant as several competing ordering tendencies alter the observed magnetisation. The 'humped' relative magnetisation curve of the hydrides with $x > 0.06$ is characteristic of a system where one sublattice exhibits a strong tendency for parallel alignment and the other, which is weakly antiferromagnetically coupled to it, has a smaller, negative magnetisation [72].

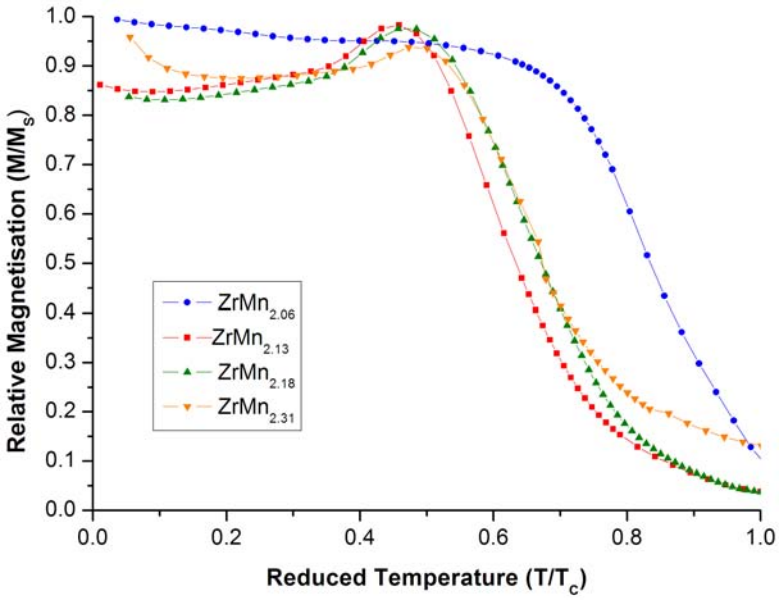

Figure 3.32: *A plot of the relative magnetisation versus reduced temperature for the series $ZrMn_{2+x}H_3$, with $x = 0.13$, 0.18, and 0.31. Shown are the data for the samples cooled in a field of 1000 Oe down to 2 K and then measured in the same field up to 300 K. Data for the nearly stoichiometric hydride ($x = 0.06$) are also shown. Values of T_c are taken from Table 3.12, and the M_S value in each case is taken as the maximum value of the magnetisation during the temperature sweep. Relative errors are smaller than the data points.*

Considering the exchange integrals outlined in Table 3.12, alongside the above trends in relative magnetisation, suggests that the B sublattice, with its very strongly positive J_{BB} exchange, is the dominant contributor to the observed magnetisation. As the manganese content increases, the competing $B - B$ exchange (parallel), $A - A$ exchange (antiparallel), and $A - B$ exchange (antiparallel) may create a small, negative magnetisation on the A sublattice as the system strives to satisfy the strong $B - B$ ferromagnetic coupling. This trend is manifested in

the $\frac{M}{M_s}$ *vs.* $\frac{T}{T_c}$ data for $ZrMn_{2+x}H_3$ in Figure 3.32 as a growing divergence from the Brillouin function as x increases.

The field dependence of the magnetisation for the $ZrMn_{2+x}$ hydrides and alloys is analogous to the data shown in Figure 3.24 for the $ZrMn_{2.06}-$ H system, exhibiting only minor changes in hysteresis parameters as the manganese content varies. Table 3.14 tracks these changes in hysteresis parameters for the whole of the $ZrMn_{2+x}-$ H series, with the data from the nearly stoichiometric alloy, hydride and dehydrided material shown for comparison. The $M(H)$ data for the $ZrMn_{2.31}-$ H system are shown in Figure 3.33; hysteresis graphs for $x = 0.13$, 0.18, and 0.44 can be found in Appendix A but are qualitatively very similar.

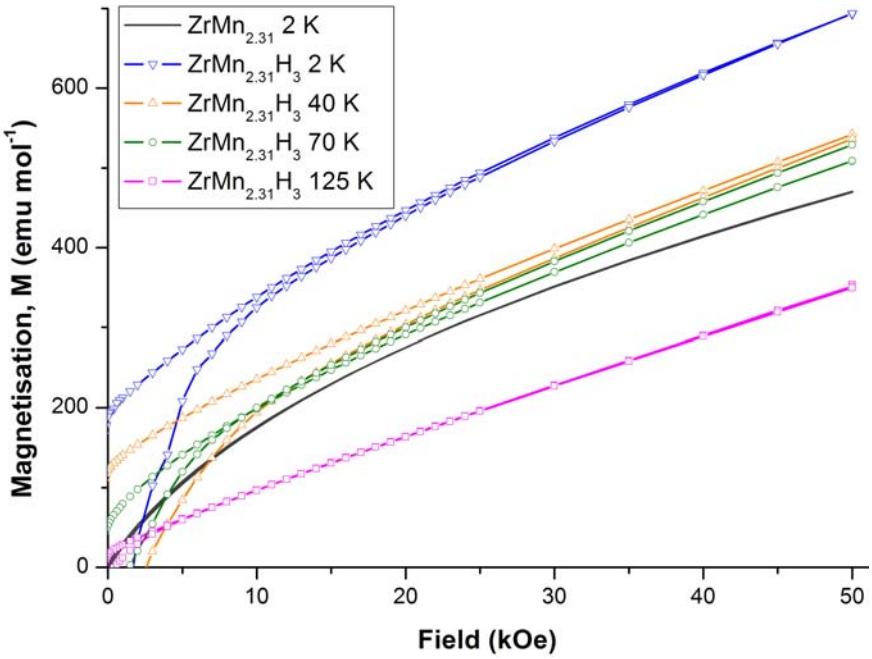

Figure 3.33: *A hysteresis plot at several temperatures for cycled, hydrided $ZrMn_{2.31}H_3$, showing data from the first quadrant only. Relative errors are smaller than the data points. The field dependence of the molar magnetisation (up to 50 kOe) is shown at 2 K, 40 K, 70 K and 125 K as indicated on the graph. For comparison, the field dependence of the alloy, $ZrMn_{2.31}$, at 2 K is shown as a solid gray line.*

It can be seen from Figure 3.33 that the field dependence of the magnetisation for $ZrMn_{2.31}H_3$ does not follow a linear relation between 2 K and 125 K, which

is as expected for a magnetically ordered material. The $M(H)$ data at 2 K show significant hysteresis and the high coercivity indicates that the hydride is a hard magnet. As the temperature increases, the hysteresis loss – the area enclosed by the $M(H)$ curves – gradually decreases. It should be noted that, as was observed for $ZrMn_{2.06}$, the magnetisation of the virgin alloy at 2 K does not linearly vary with the field, indicating that the hydrogen-free system is not paramagnetic and may be on the threshold of a low-temperature magnetic transition.

	W_H	H_C (Oe)	M_r (emu mol^{-1})
alloys:			
$ZrMn_{2.06}$	$3.06(5) \times 10^4$	170(2)	15.8(2)
$ZrMn_{2.13}$	$2.94(5) \times 10^4$	34(1)	1.47(3)
$ZrMn_{2.18}$	$8.5(3) \times 10^4$	55(2)	1.97(8)
$ZrMn_{2.31}$	$5.49(4) \times 10^4$	83(1)	2.49(2)
$ZrMn_{2.44}$	$1.19(1) \times 10^4$	206(2)	3.47(3)
dehydrides:			
$ZrMn_{2.06}$	$5.21(5) \times 10^4$	230(2)	9.59(9)
$ZrMn_{2.44}$	$2.01(2) \times 10^5$	489(4)	10.0(1)
hydrides:			
$ZrMn_{2.06}H_3$	$7.72(3) \times 10^4$	48(2)	$4.7(2) \times 10^2$
$ZrMn_{2.13}H_3$	$3.16(8) \times 10^4$	384(9)	311(1)
$ZrMn_{2.18}H_3$	$1.21(1) \times 10^5$	$1.12(1) \times 10^3$	144(1)
$ZrMn_{2.31}H_3$	$2.36(2) \times 10^5$	$1.94(2) \times 10^3$	175(1)
$ZrMn_{2.44}H_3$	$4.22(1) \times 10^5$	2826(8)	132.4(4)

Table 3.14: *The hysteresis parameters measured at 2 K across the series $ZrMn_{2+x}-H$. For $x = 0.13$, 0.18, 0.31 and 0.44, the hysteresis behaviour was measured for the virgin alloys and the cycled hydrides; the dehydrided material was only measured for x=0.44. Data for the nearly stoichiometric series $ZrMn_{2.06} - H$ are shown for comparison.*

Table 3.14 shows that the superstoichiometric hydrides with $x > 0.06$ are all hard magnets, with coercivity values significantly larger than that of the stoichiometric hydride. As H_C is proportional to the density and average energy of the pinning sites [69], it is evident that an increase in the manganese content is therefore related to an enhancement of magnetic strain in the hydrides. This is in accordance with the earlier observations on trends in relative magnetisation with x, where it was noted that superstoichiometry heightened several competing coupling tendencies —a situation that would surely exacerbate the magnetic strain in the structure. The trends in coercivity are shown in Figure 3.34, where it can be seen that the coercivities of the $ZrMn_{2+x}$ hydrides vary linearly with x. For the hydrogen-free materials, which exhibited a small but significant hysteresis, H_c was comparatively much smaller and increased only slightly as the degree of superstoichiometry rose.

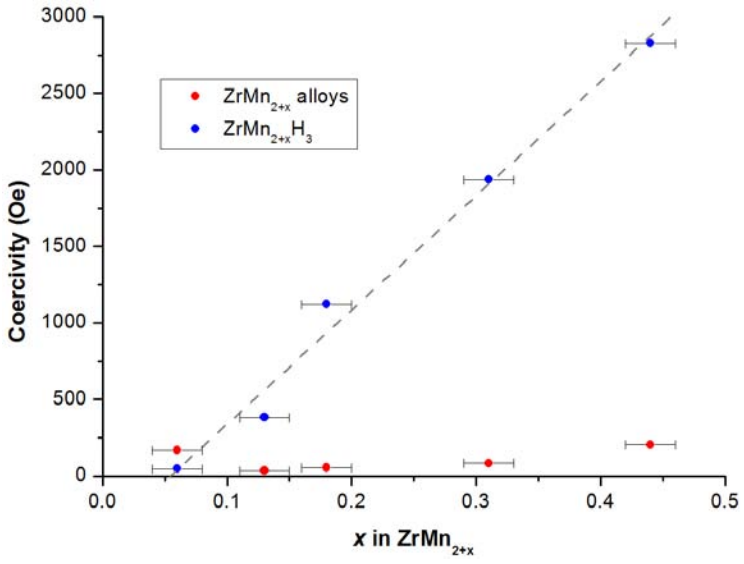

Figure 3.34: *A plot of the variation of in the coercivity against x for the alloys $ZrMn_{2+x}$ and the hydrides $ZrMn_{2+x}H_3$. Relative errors in H_C are smaller than the data points. Although the value of H_C for the alloy series does not vary with x, the dependence of H_C on x for the hydrides is described by a linear trend (indicated with a dashed black line).*

Across the $ZrMn_{2+x}H_3$ series, the magnetic remanence decreases with x, as

shown in Table 3.14. This may be related to a decrease in the amount of magnetocrystalline anisotropy for the superstoichiometric hydrides, and is likely a result of the disorder introduced by the manganese substitution. This magnetic strain and disorder that is found in the $ZrMn_{2+x}-$ H system is further manifested in the increased hysteresis loss with x in the hydride phase. For the alloy, the hysteresis loss initially increases with x, and then begins to decrease around $x = 0.18$.

A comparison of the amount of hysteresis loss in the virgin alloy and the cycled, dehydrided material is also instructive – as the data for the $ZrMn_{2.44}$ system show, the cycling process increases the hysteresis loss 10-fold. Similar data for the nearly stoichiometric materials reveal only a doubling of W_H upon cycling. As no structural change has occurred (both are the alloy and the dehydride are hydrogen-free phases with nearly identical lattice parameters) the amplification of hysteresis loss can only be attributed to an increase in the number of domains, the density of the pinning sites, or both. A peak profile analysis of the diffraction data of the $ZrMn_{2.06}$ and $ZrMn_{2.44}$ dehydrided materials (see Section 3.8.3 for further details) revealed significant decrepitation and crystallite size reduction in both cases. Although the magnitude of the crystallite size did not vary with x, the crystalline strain in the superstoichiometric $ZrMn_{2.44}$ was approximately double that of $ZrMn_{2.06}$. Thus the increased hysteresis loss brought about by the cycling process results not only from a substantial crystallite size reduction, leading to a multiplication of the number of domains, but also from an increase in the number of pinning sites, which is certainly related to the crystalline strain in the material. As the crystalline strain increases with x across the $ZrMn_{2+x}$ series, so too does the hysteresis loss.

Compiled Arrott plots for the $ZrMn_{2+x}$ alloy series and the $ZrMn_{2+x}H_3$ hydride series are shown in Figures 3.35 and 3.36, respectively. Considering the $M(H)$ behaviour of the alloys first, it is evident that for all values of x, a fitted curve will posses a negative $y-$intercept. This implies that the saturation magnetisation is zero and that the alloys are not magnetically ordered. As both the thermomag-

netic data and the hysteresis curve suggest that a magnetic transition is imminent in this system, it is expected that a series of Arrott curves with temperatures less than 2 K would have gradually increasing $y-$intercepts, with the point at which the intercept became positive marking the transition temperature. As the manganese content increases, however, the reverse trend is observed: the slope of the Arrott curves become steeper, shifting the corresponding $y-$intercepts further away from zero. It may be concluded, that the superstoichiometric alloys undergo the transition to ferrimagnetism at lower temperatures than $ZrMn_{2.06}$, with a T_c that is dependent on x: much like for the $ZrMn_{2+x}-$ H hydride series, as Figure 3.30 showed. Indeed, the Arrott intercepts of the $ZrMn_{2+x}$ alloys decrease linearly with x, suggesting that $T_c(x)$ would be linear as well.

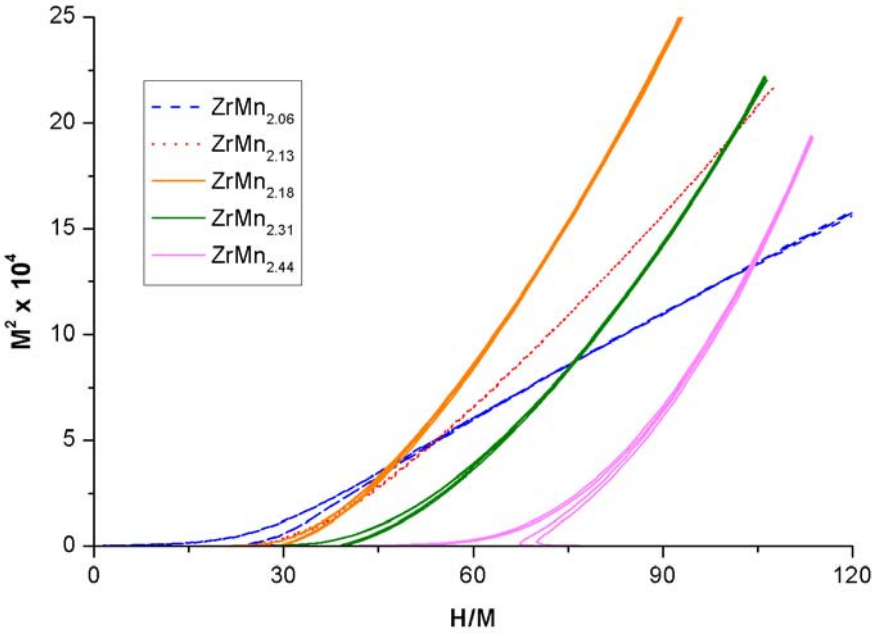

Figure 3.35: *An Arrott plot for series of $ZrMn_{2+x}$ alloys at 2 K, with the square of the molar magnetisation, M, on the y-axis and the applied field, H (in Oe), over M, on the x-axis. Data are shown as solid colored lines for the alloys with $x = 0.18$, 0.31 and 0.44 (the alloy with $x = 0.13$ is shown as a dotted line). Relative errors are smaller than the data points. The Arrott plot for the nearly stoichiometric alloy, in a dashed blue line, is shown for comparative purproses.*

This postulate about the variation in T_c of $ZrMn_{2+x}$ allows reinterpretation of their hysteresis behaviour. Across the range of manganese concentrations in these

alloys, their hysteresis behaviour at 2 K was analysed. A small hysteresis was observed, as is expected for a system slightly above its transition temperature, due to the appearance of short-range order and small clusters of spins. However, the further the temperature of a system is from a magnetic transition, the less substantial that this effect will be. Thus, the hysteresis loss in $ZrMn_{2+x}$ as measured at 2 K might be expected to decrease as x increases due to the shift of T_c to gradually lower temperatures. On the other hand, this trend towards a reduction in W_H with x is opposed by the disorder and strain that the manganese substitution causes, which (as noted above) would lead to a rise in W_H with x The interplay between these two competing tendencies has brought about the observed parabolic trend in hysteresis loss across the $ZrMn_{2+x}$ series.

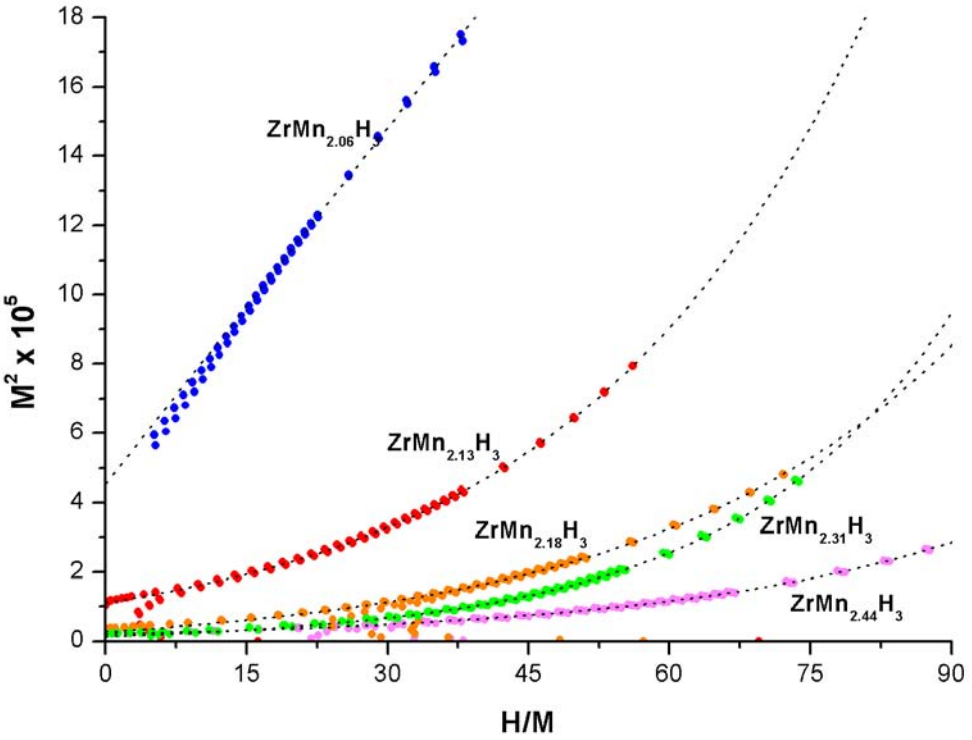

Figure 3.36: *An Arrott plot for series of $ZrMn_{2+x}H_3$ hydrides at 2 K, with the square of the molar magnetisation, M, on the y-axis and the applied field, H (in Oe), over M, on the x-axis. Data are shown as colored symbols for x = 0.13, 0.18, 0.31, and 0.44 (relative errors are smaller than the data points) and were fitted by an exponential trend (shown as a dashed black line). The data for the nearly stoichiometric hydride (blue circles) are shown for comparison, and were fitted with a linear trend instead.*

Moving to the compiled Arrott plot for the $ZrMn_{2+x}H_3$ series (shown in Figure 3.36) it is immediately evident that an increase in manganese content brings about substantial deviation from the expected linear dependence of M^2 on $\frac{H}{M}$. The data for the nearly stoichiometric hydride could be easily fitted with a simple linear trend line, whilst the superstoichiometric data sets required the use of an exponential relationship to achieve a satisfactory fit. Although deviation from linearity in the Arrott plot may be caused by a variety of factors, the expected disorder that would be brought about by manganese substitution is certain to create the kind of curvature seen for the $ZrMn_{2+x}$ hydrides in Figure 3.36 [74]. This is in accordance with the observed hysteresis trends for the superstoichiometric hydrides detailed above, where it was noted that the upsurge of H_C with x was caused by increased magnetic strain.

The Arrott plots for the superstoichiometric hydrides also reveal that the $y-$intercept of the curves fitted to the 2 K data vary with x: as the manganese content increases, the intercept drops closer towards zero. In all cases, the value of the $y-$intercept remains positive, indicating that the system possesses a spontaneous magnetisation. The values of M_s extracted from these Arrott intercepts agree remarkably well with those derived from the hysteresis plots and reported in Table 3.12 – a variation of less than 1% was noted in all cases. It is therefore quite clear that M_s decreases with x in the $ZrMn_{2+x}H_3$ series.

3.10.2.1 Proposed model for magnetic order in $ZrMn_{2+x}$ and $ZrMn_{2+x}H_3$

The experimental data reviewed in the previous section provide several powerful clues as to the nature of the magnetic ordering in the $ZrMn_{2+x}-$ H system, summarised here:

- The $\chi^{-1}(T)$ data for both the hydrided and the hydrogen-free phase can be fitted to the 'Néel hyperbola' for all values of x, indicating that these compounds are ferrimagnetic. The transition temperature of the alloys was

below 2 K in all cases and thus could not be precisely determined, whilst for the hydrides the transition temperature decreased as the manganese content increased. It was also found that the width of the transition in the superstoichiometric hydrides expanded with manganese content, indicating a rise in the magnetic strain and disorder of the system.

- The exchange integrals extracted from the fitted Néel hyperbolae provided some insight into the nature of the ordering in the system. For the superstoichiometric alloys, the exchange integrals vary little with x and indicate that the coupling on the A sublattice is strongly antiferromagnetic, the $B-B$ coupling is virtually non-existent, and that the inter-sublattice exchange is weakly antiferromagnetic. The chief difference between these trends and those observed from the hydrided compounds is the rise in the $B-B$ coupling. For the superstoichiometric hydrides, J_{BB} is the largest exchange in the system and is very strongly positive; however, the strength of the coupling decreases slightly with increasing manganese substitution.

- Analysis of the magnetisation field dependence revealed that the hydrides were hard magnets with a significant magnetocrystalline anisotropy that decreased slightly as x increased. The coercivity showed a linear dependence on x, and was highest for the most superstoichiometric compound as a result of the disorder induced by manganese substitution. This increase in strain and disorder with manganese content was also manifested by a rise in the hysteresis loss.

- The magnetisation behaviour of the superstoichiometric alloys at 2 K revealed a very small hysteresis in each case, with substantial deviation from the expected linear $M(H)$ behaviour. The small hysteresis suggested the formation of short-range spin correlations at the threshold of long-range magnetic order, in agreement with the susceptibility data. A parabolic trend was observed for the hysteresis loss of these alloys, attributed to the competition

between a decrease in T_c with x and an increase in disorder with x.

- Examination of the relative magnetisation curves of the superstoichiometric hydrides revealed the interplay of several competing coupling tendencies. The shape of the magnetisation curves, in view of the assumed ferrimagnetism, suggested that one sublattice has a strong ferromagnetic coupling and the second has a small negative magnetisation that becomes more pronounced with increasing x.

- Arrott plots of the hydrides at 2 K verified their magnetism and provided values for M_s, demonstrating a decrease in spontaneous magnetisation with increased manganese substitution. The disorder caused by this substitution was manifested in the curvature of the superstoichiometric Arrott plots.

- The Arrott plots of the alloys at 2 K also showed significant curvature as a result of magnetic disorder, and indicated that the materials were non-magnetic. Whilst M_s was zero for all values of x, it was evident that the less superstoichiometric materials were closer to a magnetic transition than those containing higher amounts of manganese. The T_c of the hydrogen free $ZrMn_{2+x}$ phase was below 2 K in all cases and is postulated to diminish in a linear fashion as x increases.

Fitting parameters of the Néel hyperbolae were used to derive λ and μ, the relative fractions of atoms on the A and B sublattices, as well the exchange constants relating them, for each member of the $ZrMn_{2+x}-$ H system. As was observed for the nearly stoichiometric system, λ was always much larger than μ, indicating that the A sublattice contained more atoms than the B sublattice; however, for both phases, the ratio of $\mu : \lambda$ increased with the manganese content. Using the assumption made for the nearly stoichiometric system that the A sublattice consists of manganese atoms on the $2a$ sites, and the B lattice is formed by the substituted manganese atoms on the $4f$ site, good agreement was obtained between the calcu-

lated number of atoms on the B sublattice and the actual number of substitutional manganese atoms in the system.

The negative J_{AA} exchange integral indicates that the A sublattice is preferentially antiferromagnetically ordered. A perfect antiferromagnetic coupling of the $2a$ manganese atoms would result in a zero net moment on the A sublattice at 0 K, suggesting that the observed saturation magnetisation must arise solely from the B sublattice of $4f$ manganese atoms. Thus, the experimentally determined magnetic moment for the $ZrMn_{2+x}H_3$ hydrides at 2 K reported in Table 3.12 can be divided by the number of substitutional manganese atoms in order to obtain the moment per manganese atom. The results of this calculation are shown in Figure 3.37.

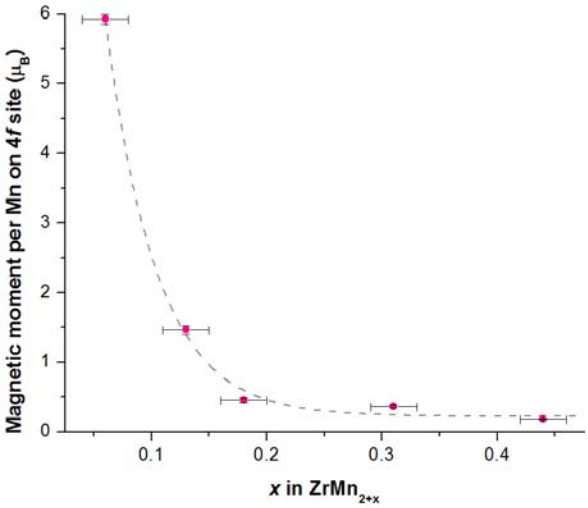

Figure 3.37: *A plot of the magnetic moment per manganese atom against x for the series* $ZrMn_{2+x}H_3$*, with* $x = 0.06, 0.13, 0.18, 0.31$ *and 0.44. The calculation of the magnetic moment per atom assumes that the observed moment arises entirely from the substitutional 4f manganese atoms. A dashed grey line describes the exponential trend in the moment with x.*

For $ZrMn_{2.06}H_3$, the moment per manganese atom is 5.9 μ_B, corresponding roughly to expected magnetic moment for Mn^{2+} $(3d^5)$ of 5 μ_B. The magnetic moment significantly drops in value for the super-stoichiometric hydrides, however, as the exponential trend in Figure 3.37 shows. This apparent decrease in the moment of the manganese atoms is likely a result of two synergistic phenomena: an increase in the alloy-to-hydride ratio with x, and the appearance of a net negative magnetisation on the A sublattice due to competing coupling tendencies.

It has already been noted herein that $ZrMn_{2+x}H_3$ is only metastable at room temperatures and pressures, existing

in equilibrium with its parent alloy *via* Equation 3.2. The higher the manganese content, the more favourable the dissociation of the hydride becomes, and as shown by the X-ray diffraction in Section 3.6.2, a significant amount of the alloy phase is found in all of the nominally 'hydrided' samples for $x > 0.06$. When calculating the magnitude of magnetisation for $ZrMn_{2+x}-$ H samples, it was always assumed that the material was single phase $ZrMn_{2+x}H_3$: although certainly an inaccurate description, it was used for the sake of consistency as it was impossible to determine the exact ratio of the alloy and hydride phases in each sample at the time of measurement. This assumption would not affect determination of properties like T_c, but would dilute the magnitude of the observed magnetisation.

As was noted in the relative magnetisation versus reduced temperature plot for $ZrMn_{2+x}$ hydrides in the previous section, the net magnetisation of the superstoichiometric hydrides appears to result from the combination of one strongly ferromagnetic sublattice and one sublattice with a weak negative magnetisation that increases with x. The exchange integrals indicate that the strong ferromagnetic coupling results from the B sublattice of $4f$ manganese atoms; thus, the negative magnetisation must arise on the A sublattice. Although the J_{AA} coupling is antiferromagnetic and would favour a case in which the manganese $2a$ moments align antiparallel and cancel out completely at low temperatures, the J_{BB} coupling strength is much stronger and may in some cases of competing coupling tendencies bring about a spin flip on the A sublattice from the preferred antiparallel alignment. This would create a small negative magnetisation on the A sublattice, which would presumably grow as the concentration of $4f$ atoms (and the incidence of these forced spin flips) increased. This negative magnetisation, if unaccounted for, would effectively decrease the observed saturation magnetisation and therefore the calculated moment per manganese atom. Moreover, these competing tendencies would be expected to increase the disorder and strain in the hydrides as the level of manganese substitution increased; as noted above, a tendency towards strained magnetic disorder was observed experimentally for the $ZrMn_{2+x}H_3$ series.

When these two factors impacting the net magnetisation are taken into account, it may postulated that the observed decrease in moment with x shown in Figure 3.37 is superficial. Although it cannot be proven at this time, it is likely that the magnetic moment per manganese atom is constant across the $ZrMn_{2+x}H_3$ series.

The trend towards increasing magnetic strain and disorder in the superstoichiometric hydrides may also contribute to the experimentally observed reduction in T_c with x. Moreover, as the onset of a magnetic transition is defined as the point at which the exchange integrals J_{ij} can overcome kinetic energy (see Section 2.2.2), the observed decrease in J_{BB} with x will also cause a reduction in T_c with x. Evidence for the plausibility of the observed linear variation of T_c with x can be found in the work of Brückner *et al.* [96] on the Laves phase $ZrFe_{2+x}$, where it was observed the the transition temperature of this ferromagnetic material varied linearly with the iron content.

The experimental evidence suggests that both the hydrided and hydrogen-free phases of the $ZrMn_{2+x}-$ H system are ferrimagnetic and will manifest localised moments on the A sublattice (manganese on $2a$ sites) and on the B sublattice (substitutional manganese on the $4f$ site). The 'critical distance' theory discussed for the nearly stoichiometric hydride in Section 3.10.1.1 still holds here: the manganese $2a-2a$, $2a-4f$ and $4f-4f$ distances cited for $ZrMn_2-$ H are fractionally smaller for the superstoichiometric system (due to lattice contraction) but still exceed the minimum distance of 2.86 Å for manganese moment localisation. However, the large difference in transition temperature between the $ZrMn_{2+x}$ series (less than 2 K) and the $ZrMn_{2+x}H_3$ series ($174-190$ K) indicates a shift in stability of the magnetic structure upon hydriding. Although the study of Rotter *et al.* [21] on the possible magnetic frustration in the $ZrMn_2$ alloy did not consider the superstoichiometric structure, it is evident that the disorder caused by manganese substitution would only further increase the frustration in the system. The observed decrease in transition temperature with x for the $ZrMn_{2+x}$ alloys verifies this postulate. As noted for the stoichiometric alloy, the absorption of hydrogen by

$ZrMn_{2+x}$ and the concomitant lattice expansion that occurs may act to reduce the frustration of the manganese moments in the system and create a more accessible magnetically ordered state.

3.10.3 Magnetism of the substoichiometric $ZrMn_{1.65}-H$ system

The magnetic behaviour of the substoichiometric $ZrMn_{1.65}-H$ system was examined over the temperature range 2 to 300 K; the as-synthesised alloy, as well the cycled hydride and dehydrided material, were all analysed. Figure 3.38 shows the variation in molar susceptibility with temperature for the three materials. The alloy and the dehydrided sample had very similar magnetic behaviour: the initial susceptibility rose gradually as temperature decreased from 300 K, resembling a Pauli paramagnet, but then with an upturn in χ at very low temperatures. Table 3.15 reports the observed susceptibilities for the system; the similarities to the trend in $\chi(T)$ for nearly stoichiometric alloy reported in Section 3.10.1 – and the reduction in magnitude of χ_{5K} upon manganese depletion – are noted. The value of the susceptibility at 300 K for $ZrMn_{1.65}$ is slightly less than what was found earlier for $ZrMn_{2.06}$, indicating a decrease in the Fermi level density of states with a reduction in manganese content. This follows the trend of a rising $D(\epsilon_F)$ with manganese content that was observed for the superstoichiometric hydrides in Section 3.10.2.

For the hydride, the magnetic behaviour below 225 K mirrored that of the alloy, with a susceptibility that increased slowly with decreasing T. At $T = 212$ K, the hydride undergoes a magnetic transition, and the susceptibility below this point depended upon the thermal history: when cooled in a magnetic field prior to measurement, the susceptibility escalated intensely over a narrow temperature range before continuing to rise slowly as the temperature was further reduced. However, when the hydride is cooled in the absence of a magnetic field, the susceptibility below the transition temperature sharply peaks at 188 K and then decreases with

	$ZrMn_{1.65}$ alloy	$ZrMn_{1.65}H_3$
χ_{300K} (emu mol^{-1} Oe^{-1})	$1.461(1) \times 10^{-3}$	$3.788(2) \times 10^{-3}$
χ_{Max} (emu mol^{-1} Oe^{-1})	$2.548(6) \times 10^{-3}$	$1.273(2) \times 10^{-1}$
T of χ_{Max} (K)	5 ± 5 K	188 ± 2 K
T_C (K)		212
W_H	$1.84(2) \times 10^4$	$1.7(1) \times 10^4$
H_C (Oe)	181(5)	50(4)
M_r (emu mol^{-1})	0.74(2)	$4.0(2) \times 10^2$
[1]M_S (emu mol^{-1})		508(6)

[1]M_S was determined from the saturation at 2 K of $M(H)$.

Table 3.15: *Susceptibilities, transition temperatures, and magnetic moments for the $ZrMn_{1.65} - H$ alloy and hydride. The hysteresis parameters - loss, coercivity, remanence, and saturation magnetisation - at 2 K are also shown.*

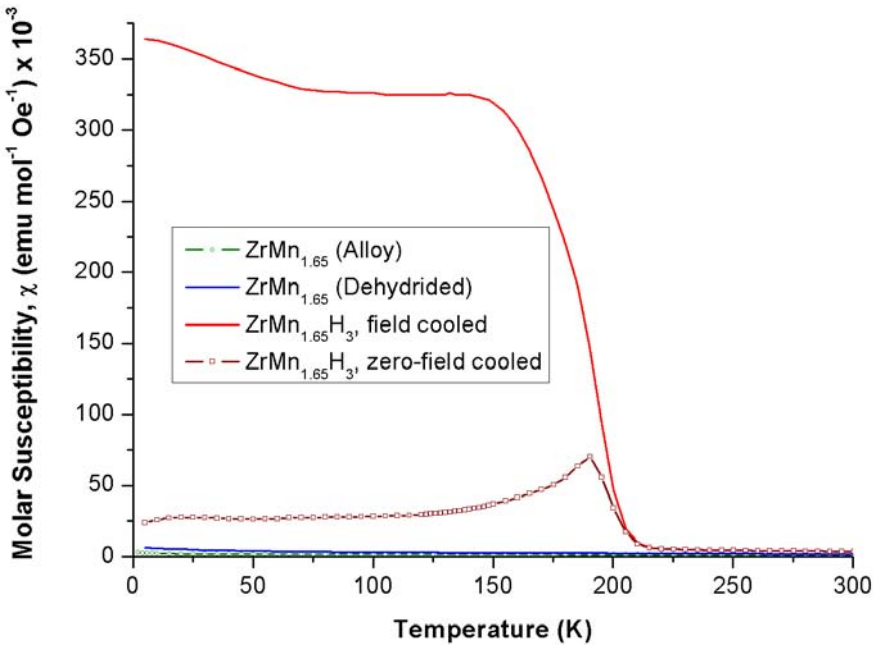

Figure 3.38: *A thermomagnetic analysis for the system $ZrMn_{1.65} - H$, with molar susceptibility against temperature from 2 to 300 K. The alloy (green line with circles) and dehydrided sample (blue line) were cooled to 2 K in a field of 1000 Oe before measurement in the same field. $ZrMn_{1.65}H_3$ was measured both when cooled in absence of field (dark red line with squares) and cooled in field (red line). Relative errors are smaller than the data points.*

temperature. When compared with the $\chi(T)$ data for the nearly stoichiometric hydride, the contraction of the temperature width of the transition upon zirconium substitution is evident. Table 3.15 reports the observed susceptibilities for the hydride.

The $\chi^{-1}(T)$ data for the $ZrMn_{1.65}-$ H system follow the same ferrimagnetic curvature as those for the nearly stoichiometric and superstoichiometric systems. Both the hydrogen-free and the hydrided phase were successfully fitted with the Néel hyperbola equation (see Equation 2.34) as shown in Figure 3.39. Although the ferrimagnetic transition for the hydride is evident, it appears that the hydrogen-free phase is on the threshold of a transition, with a T_c below 2 K, the lowest temperature that was accessed in this experiment. Table 3.16 reports the values of the Néel fitting parameters for the $ZrMn_{1.65}$ alloy and its hydride.

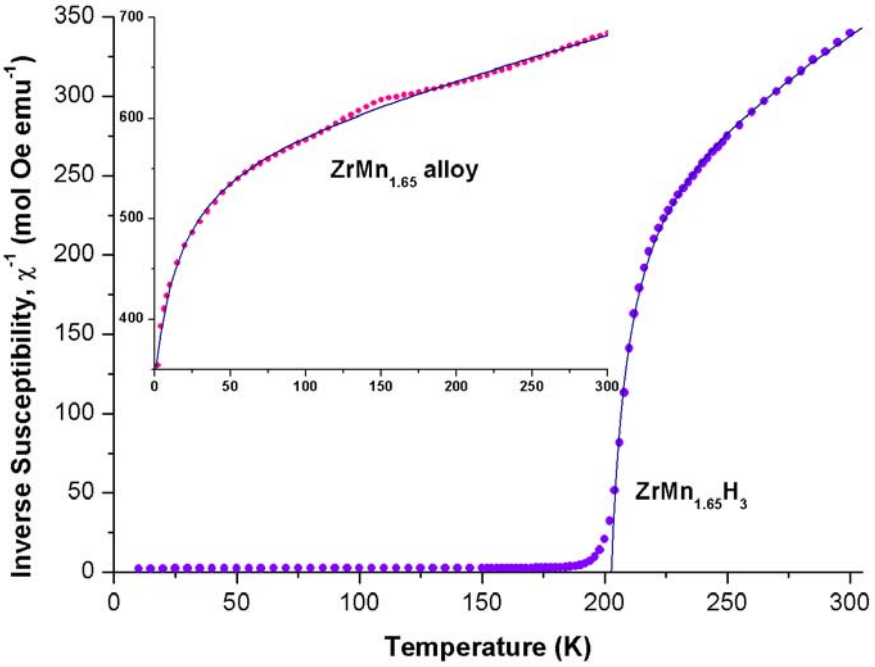

Figure 3.39: *A plot of the temperature dependence of the inverse molar susceptibility for $ZrMn_{1.65}H_3$ cooled and measured in a field of 1000 Oe. The purple dots are experimental data, whilst the solid navy line is a fit to the Néel ferrimagnetism model. Inset is the inverse susceptibility for the alloy $ZrMn_{1.65}$, cooled and measured in a field of 1000 Oe - the pink dots are experimental data, whilst the solid navy line is again a fit to the Néel ferrimagnetism model. In both plots, relative errors are smaller than data points.*

As described in Section 2.2.4, the fitting parameters of the Néel hyperbola can be easily transmuted into exchange integrals J_{ij}, which are reported in 3.16. For the $ZrMn_{1.65}$ alloy, the dominant coupling in the system is the antiferromagnetic $A-A$ exchange. The inter sublattice exchange is also antiferromagnetic, but is much weaker, and the $B-B$ exchange is the smallest in the system, with only a faint antiparallel coupling. In contrast, the $B-B$ exchange in the hydride tends very strongly to parallel alignment and is 100 times stronger than any other exchange constant in the system. For $ZrMn_{1.65}H_3$, the A sublattice retains its antiferromagnetic exchange, but is weaker than that observed in the alloy. The intersublattice exchange retains an antiparallel preference upon hydriding, but now is of approximately the same magnitude as J_{AA}.

The field dependence of the magnetisation for $ZrMn_{1.65}H_3$ is shown in Figure 3.40, with the hysteresis parameters at 2 K summarised in Table 3.15. At all temperatures studied (up to 125 K) the hydride exhibits a significant hysteretic behaviour, with a non-linear dependence of $M(H)$ that confirms the magnetic ordering in the material. As $H_c < 125$ Oe, $ZrMn_{1.65}H_3$ is a soft magnet like the nearly stoichiometric hydride, though the hysteresis is reduced upon manganese depletion —the hysteresis loss at 2 K is approximately 6 times smaller for the substoichiometric hydride. This hysteresis is

Néel ferrimagnetism model: $\frac{1}{\chi} = \frac{T}{C} - \frac{1}{\chi_o} - \frac{\sigma}{T-\theta}$		
	alloy $ZrMn_{1.65}$	*hydrided* $ZrMn_{1.65}H_3$
C	2.51(8)	1.11(7)
χ_o	0.00174(1)	0.0022(1)
σ	$4.2(3) \times 10^3$	$1.9(2) \times 10^3$
θ	$-18(1)$	195.5(5)
λ_{AA}	$-5.9(6) \times 10^2$	$-9.9(1) \times 10^2$
λ_{AB}	$-1.3(1) \times 10^2$	$-2.7(3) \times 10^2$
λ_{BB}	$-27(3)$	$1.4(1) \times 10^4$
J_{AB}	$-66(7)$	$-1.4(1) \times 10^2$
J_{AA}	$-4.4(5) \times 10^2$	$-74(7)$
J_{BB}	$-20(2)$	$1.0(1) \times 10^4$

Table 3.16: *Calculated fitting parameters from the Néel ferrimagnetism model used to describe the observed temperature dependence of the* $\chi^{-1}(T)$ *data for the* $ZrMn_{1.65}$ *alloy and its hydride,* $ZrMn_{1.65}H_3$.

characterised by a large magnetic remanence, indicating that the structure has a strong magnetic anisotropy; the small coercivity value implies that magnetic strain is not a major source of loss.

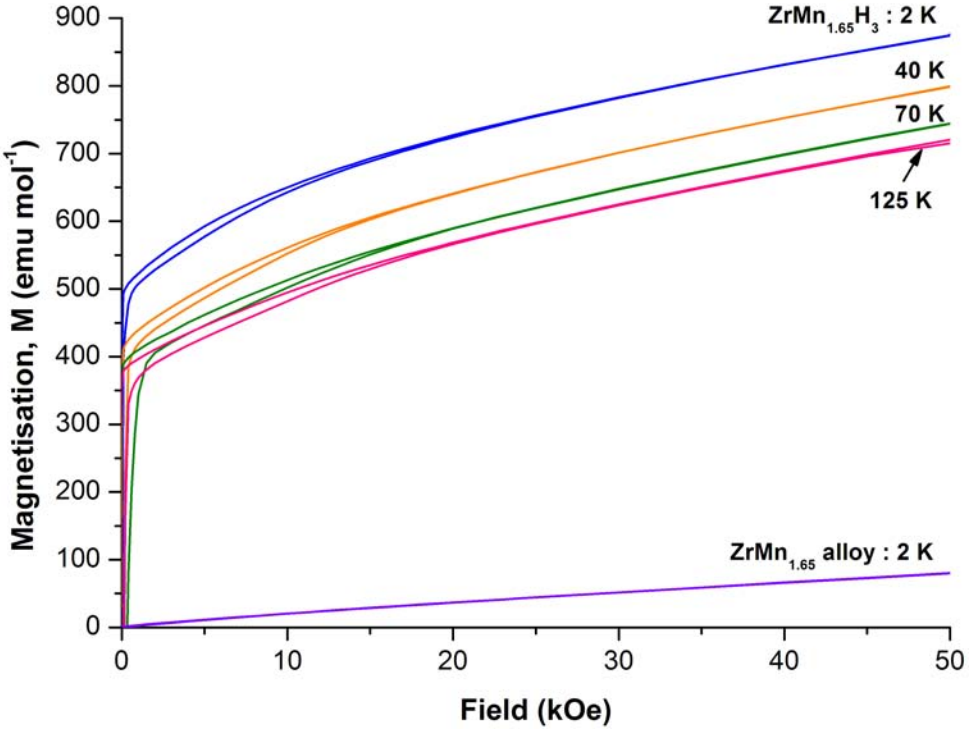

Figure 3.40: *A plot of the field dependence up to 50 kOe of the molar magnetisation for $ZrMn_{1.65}H_3$, showing the first quadrant of data only. M(H) data are shown at temperatures of 2 K, 40 K, 70 K and 125 K as indicated on the graph. For comparison, the field dependence of the magnetisation for the alloy $ZrMn_{1.65}$ at 2 K is also shown. Relative errors are smaller than data points.*

Although not evident on the scale of Figure 3.40, the alloy $ZrMn_{1.65}$ shows a measurable deviation from the expected linear $M(H)$ behaviour of a paramagnet. It exhibits a small hysteresis, with negligible remanence but a substantial coercivity, contributing to a hysteresis loss as large as that reported for the hydride; these values are detailed in Table 3.15. The magnitude of the $ZrMn_{1.65}$ hysteresis, as measured by W_H, is several times smaller than was reported for the $ZrMn_2$ alloy. Nonetheless, this hysteresis may indicate the onset of short-range ordered magnetic clusters, heralding the possibility of a very low temperature magnetic transition. A significant amount of magnetic strain and disorder is exhibited in

the substoichiometric alloy at 2 K, as the large coercivity value indicates.

These $M(H)$ data can be easily translated into Arrott plots, which are shown in Figure 3.41. Although they show some curvature at very low fields, the data for the hydrides with $H > 5$ kOe are easily described by linear functions and have positive $y-$intercepts, indicating that the hydride is magnetically ordered. The spontaneous magnetisation extracted from the $y-$intercept of the fit at 2 K was found to be 502 emu mol^{-1}, which agrees excellently with the value reported in 3.15, which was derived from the hysteresis graph.

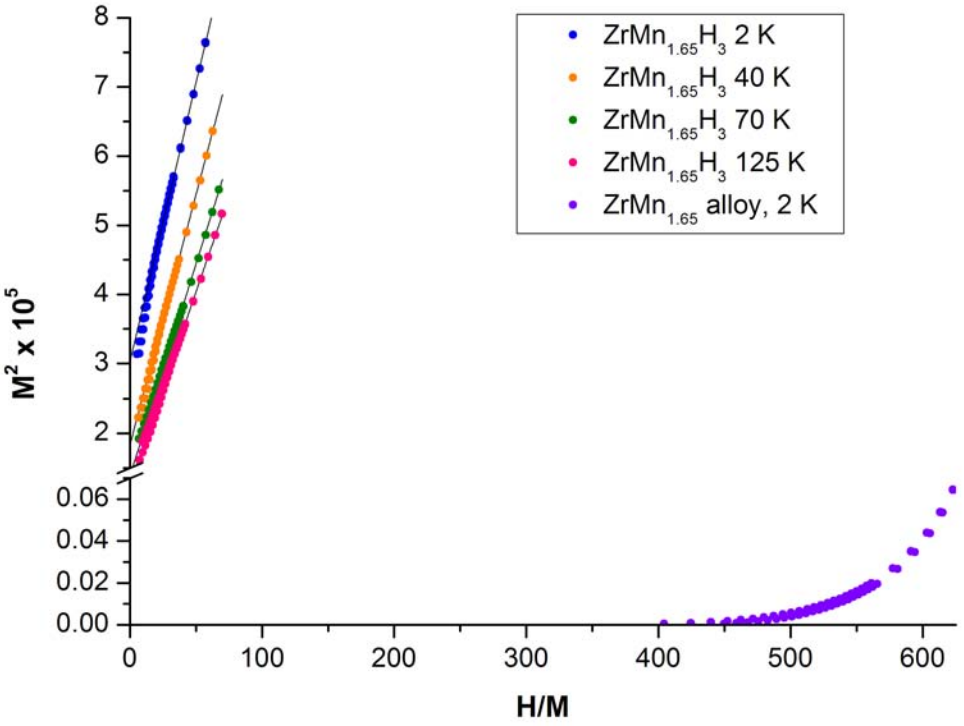

Figure 3.41: *A compiled series of Arrott plots for the alloy $ZrMn_{1.65}$ and $ZrMn_{1.65}H_3$, with the square of the molar magnetisation M on the y-axis and the applied field, H, in Oe, over M, on the x-axis. Relative errors are smaller than data points. The data for the hydride were successfully fitted to a linear model (fits shown as dotted black lines) at all temperatures measured (2 K, 40 K, 70 K and 125 K).*

Figure 3.41 shows that the Arrott plot for $ZrMn_{1.65}$ at 2 K is substantially curved, and could not be described by a linear function. If fitted with an appropriate exponential function, it is obvious that the $y-$intercept of this trendline

would be negative, indicating that the structure possesses no spontaneous magnetisation. However, as the $M(H)$ and $\chi^{-1}(T)$ data indicated that the system may be on the threshold of a magnetic transition, it is expected that measurement of the Arrott plots at lower temperatures would show a series of $y-$intercepts gradually approaching zero up to the transition temperature. Just as was suggested by the high coercivity of the alloy's magnetic hysteresis, the curvature in the Arrott plot may result from the magnetic disorder and strain in the system.

3.10.3.1 Proposed model for magnetic order in substoichiometric $ZrMn_{1.65}$ and its hydride

Clues towards the nature of the magnetic ordering in the $ZrMn_{1.65}-$ H system can be garnered from these experimental findings, which are summarised below:

- The $\chi^{-1}(T)$ data for both the hydrided and the hydrogen-free phase can be fitted to the 'Néel hyperbola' described by Equation 2.34, indicating that these compounds are ferrimagnetic. A transition temperature of 212 K was identified for the hydride, whereas both the dehydrided material and the virgin alloy, which are magnetically very similar, appear to undergo a magnetic transition below 2 K.

- Analysis of the magnetisation field dependence revealed that the hydride was a soft magnet with a large magnetocrystalline anisotropy. The magnetisation behaviour of the alloy at 2 K revealed a very small hysteresis with substantial deviation from the expected linear $M(H)$ behaviour, suggesting the formation of short-range spin correlations at the threshold of long-range magnetic order.

- Arrott plots of the hydrided material verified its magnetism and provided a value for M_s; the Arrott plots of the alloy material showed that whilst M_s was zero at 2 K, the system may have been on the verge of sustaining a spontaneous magnetisation.

Fitting parameters of the Néel hyperbolae were used to derive λ and μ, the relative fractions of atoms on the A and B sublattices, as well the exchange constants relating them. For the alloy and the hydrided material, μ was found to be 0.009 and 0.014, respectively, indicating that the A sublattice is much larger than the B sublattice. Using the model established for the nearly stoichiometric system, in which the A sublattice consists of manganese atoms on the $2a$ sites, and the B lattice is formed by substituted manganese atoms on the $4f$ site, it is calculated that approximately $0.5 - 0.7$ % of the atoms on the $4f$ site must be manganese.

For the substoichiometric system, it would be expected that no manganese would substitute onto the $4f$ site as the system is manganese deficient; indeed, the models for the crystal structure of $ZrMn_{1.65}$ and its hydride (see Section 3.3.3 and 3.6.3) assume that this site is fully occupied by zirconium. However, a recent *ab initio* study on $ZrMn_2$ by Chen *et al.* [31] revealed that the formation of a $ZrMn_2$ supercell with an Mn^{Zr} antisite defect is actually lower in energy, by 0.2 kJ (mol of atoms)$^{-1}$, than the formation of a supercell without a defect. The result seems unphysical but was carefully checked by the authors; moreover, it goes some distance towards explaining the ready substitution of Mn for Zr in this compound and the difficulty in obtaining an exactly stoichiometric $ZrMn_2$ material. This study continued on to report that the congruent melting point of the Zr-Mn binary system was 32.8 at. % Zr, not 33.3 as would be expected for a line phase $ZrMn_2$ structure, suggesting that C14 phase formed at the congruent melting point would have a $4f$ site that contained 1.5 % manganese atoms.

These theoretical finding suggest that even in the substoichiometric $ZrMn_{2+x}$–H system a very small amount of manganese substitution on the $4f$ site should be expected. Thus, the calculations from the fitted Néel hyperbolae which suggest that $ZrMn_{1.65}$ and its hydride contain a $0.5 - 0.7$ % replacement of Mn for Zr on the $4f$ site is not unreasonable; and although such a substitution was not crystallographically determined, it would be difficult to accurately verify such a small fractional occupancy. Using the previously determined $6h$ and $2a$ occupancies and

assuming that the $4f$ site has a fractional occupancy of 0.006 Mn and 0.994 Zr, the composition of the substoichiometric phase is recalculated to be $ZrMn_{1.66}$ —not significantly different from the result of $ZrMn_{1.65}$ obtained when the $4f$ fractional occupancy is neglected. It is therefore reasonable to use the same ferrimagnetic model, with the A sublattice of Mn $2a$ atoms and the B sublattice of Mn $4f$ atoms, for both $ZrMn_{2.06}-$ H and $ZrMn_{1.65}-$ H.

As the experimental evidence shows, both $ZrMn_{1.65}$ and its hydride are ferrimagnetic, with the chief difference between the two being a shift in the transition temperature. The 'critical distance' theory discussed for the nearly stoichiometric hydride in Section 3.10.1.1 suggests that a localised moment can be expected on the $2a$ and $4f$ manganese atoms for both the hydrided and the hydrogen-free phase: the distances between nearest neighbours cited for the $ZrMn_{2.06}-$ H system will be slightly larger in $ZrMn_{1.65}-$ H as the unit cell has increased in size. The shift in stability in between the hydrided and hydrogen-free phase may be caused by the relief of strain in the structure upon hydrogen absorption: the observed decrease in coercivity upon hydriding indicates that $ZrMn_{1.65}H_3$ is less magnetically strained than $ZrMn_{1.65}$. It can be postulated that, much like the $ZrMn_{2.06}-$ H system, the hydrogen-free phase is magnetically frustrated, becoming ferrimagnetic only at very low temperatures, whilst the absorption of hydrogen acts to relieve this frustration and create a more accessible magnetically ordered state.

3.11 The Magnetic Crystal Structure of the $ZrMn_{2+x}-$ H system

As was discussed in Section 2.2.8, the scattering of neutrons by atomic nuclei has both a nuclear structure factor component and a magnetic structure factor component as a result of the neutron's magnetic moment. Thus, neutron diffraction data of $ZrMn_{2+x}H_3$ collected below its magnetic T_c will contain additional reflections resulting from the ordered ferrimagnetic structure: indeed, the neutron diffraction data of $ZrMn_{2.13}-$ D collected at 10 K in Figure 3.21 show such a set of unmatched intensities that cannot be explained using the normal room-temperature structure.

Although the magnetic data collected using the SQUID shine useful insight into the nature of the magnetic ordering in the $ZrMn_{2+x}H_3$ system, providing even a net magnetic moment m, the necessary use of powdered samples throughout this thesis has negated the possibility of deconvoluting m into its directional components m_x, m_y, m_z. Without this information, it is difficult to envisage the arrangement of the atomic magnetic moments in the known crystal structure. The program McPhase, discussed in Section 2.2.9, was used to create a link between the experimental data and the magnetic crystal structure: by simply inputting the derived J_{ij} values obtained in Section 3.10, and the crystal structure that was developed in Section 3.6, the magnetic structure and macroscopic magnetic behaviour of $ZrMn_{2.06}H_3$ can be predicted.

Figure 3.42 shows the predicted thermomagnetic properties and the magnetic structure at 160 K of $ZrMn_{2.06}H_3$ as calculated by the McPhase program, overlaid with the experimental thermomagnetic behaviour of $ZrMn_{2.06}H_3$. The algorithm was run between 10 K and 280 K, in 15 K step sizes, at an isotropic applied field of 1000 Oe. The magnetic model was constructed using the parameters of the $P6_3/mmc$ structure for $ZrMn_{2.06}$ given earlier in Table 3.3, with all the non-magnetic atoms (hydrogen, zirconium, and manganese on the $6h$ sites) deleted. According to the experimental findings detailed earlier, localised moments arise only on the $2a$ manganese atoms and the substitutional manganese on the $4f$ sites; the derived ferrimagnetic J_{ij} values for these two sites were also input into the model. Trial and error suggested that the best agreement was obtained when the manganese atoms were modelled as Mn^{2+} using a simple Brillouin function. As the McPhase program cannot handle fractional occupancies, the $4f$ site was said to be fully occupied, with J_{BB} then 'diluted' by multiplication with the site's fractional occupancy. Attempts to calculate magnetic behaviour for variations on this model – *e.g.* with moments on the $6h$ and $4f$ sites, or just on the $2a$ and $6h$ sites – were unsuccessful, yielding no stable magnetic structures over the range of the tested experimental parameters.

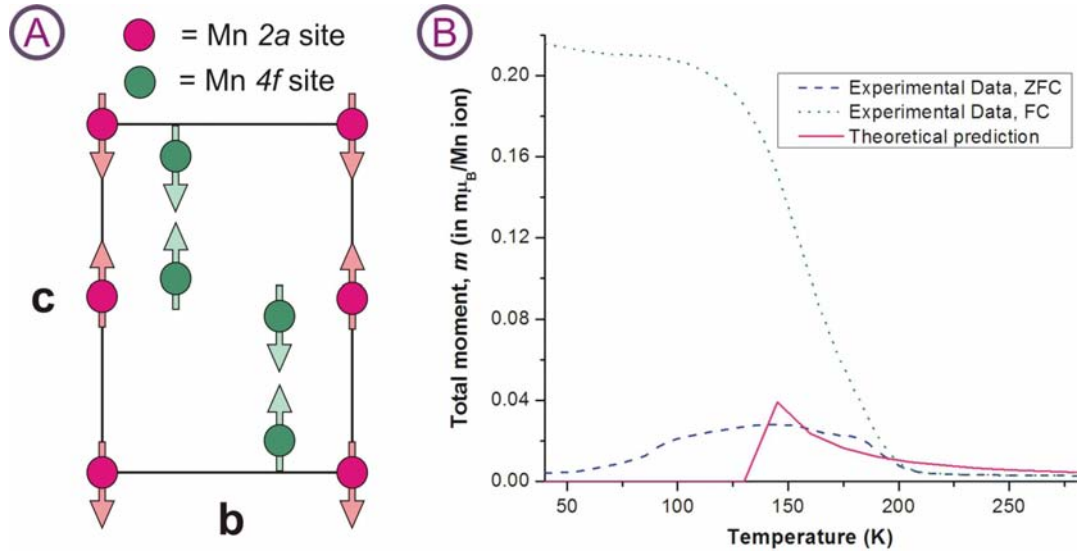

Figure 3.42: *A diagram of the predicted magnetic structure of* $ZrMn_{2.06}H_3$ *((A) on the left) and the thermomagnetic behaviour of this predicted structure as compared to experimental data ((B) on the right). The magnetic structural model depicts the* $P6_3/mmc$ *space group, sliced down the* $(10\bar{1}0)$ *plane, with only the magnetic manganese atoms on the* $2a$ *site (pink) and the* $4f$ *site (cyan) shown. The arrows indicate the relative direction of the magnetic moments on these atoms. The graph on the right compares the ZFC thermomagnetic data predicted from this structure using the McPhase program (solid pink line) with the experimentally determined thermomagnetic data for* $ZrMn_{2.06}H_3$*, measured at a field of 1000 Oe.*

Good agreement was obtained between this predicted thermomagnetic behaviour and the zero-field cooled experimental data: the computational program predicts a sharp peak in the magnetisation at 145 K at a moment of 0.0397 mμ_B/Mn (below this temperature, the program could not find a stable magnetic structure) whereas the experimental data show a broader peak at 144 K with a moment of 0.0277 mμ_B/Mn. The deviation between these two peaks is within the expectations for comparison between theoretical predictions and experimental data and is likely caused by structural defects and strains in the real $ZrMn_{2.06}$−H system. This close accord validates the proposed ferrimagnetic model of an A sublattice of Mn atoms on $2a$ sites and a B sublattice of substitutional $4f$ manganese atoms; moreover, the McPhase program indicates a possible magnetic structure for this model as shown in Figure 3.42. The magnetic moments in this structure are aligned along the $c-$axis, with a spin-flip occurring between successive sheets of Mn $2a$ atoms;

the Mn $4f$ atoms are also predicted to be antiferromagnetically aligned. Although the predicted arrangement of the $2a$ atoms agrees with the experimental findings, that of the $4f$ atoms does not and is likely an artifact of the procedure required to input a fractional occupancy: it is more probable that the substitutional manganese atoms will be ferromagnetically aligned in this structure as the large J_{BB} value (see Table 3.10) indicates.

This combination of experimental and theoretical findings led to the proposed magnetic structure of $ZrMn_{2+x}H_3$ shown in Figure 3.43; all non-magnetic atoms have been omitted. The unit cell volume is twice that of the original crystal structure due to a doubling of the $c-$axis, with the magnetic symmetry giving the Shubnikov space group of $P\bar{3}m'1$. In the initial structural model, the moments of successive planes of Mn $2a$ atoms were set as 5.5 μ_B and -5.5 μ_B, with the Mn $4f$ atoms carrying an equal moment of 5.5 μ_B. This model was compared to the neutron powder diffraction data for the $ZrMn_{2+x}-$ D system collected at 10 K on the GEM beamline during experiment RB920147 (see Section 3.9 for more details) and refined using the Rietveld method. The GSAS program with the EXPGUI interface, which is discussed in Section 2.2.8, handled the computational aspects of these refinements.

Only the nearly stoichiometric $x = 0.06$ and superstoichiometric $x = 0.13$ members of the $ZrMn_{2+x}-$ D system were analysed; the diffraction data for the substoichiometric deuteride ($x = -0.35$) were not of sufficient intensity to be reliably refined. The data were fitted using two phases: the $ZrMn_{2+x}D_y$ $P6_3/mmc$ structure, restricted to produce only nuclear reflections, with initial values as those refined from the neutron data at 300 K in Tables 3.7 and 3.8; and the $P\bar{3}m'1$ structure shown in Figure 3.43, restricted to produce only magnetic reflections. The fractional occupancies of the substitutional manganese site (the $4f$ site in the nuclear structure) were assumed to be the same as in the 300 K structure, for

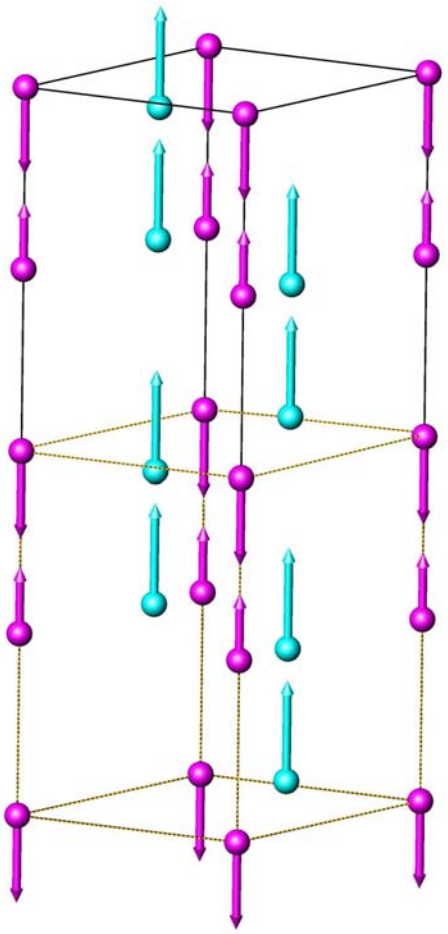

Figure 3.43: *A diagram of the magnetic crystal structure of* $ZrMn_{2+x}H_3$*, showing the arrangement of the magnetic atoms and the directions and relative sizes of their moments within the* $P\bar{3}m'1$ *unit cell (heavy black lines). The outline of the original* $P6_3/mmc$ *unit cell of the nuclear structure is indicated by a dashed yellow-black line within the magnetic cell; the Mn atoms on the 2a sites of this cell are shown in pink, whereas Mn atoms on the 4f sites are shown in cyan.*

both magnetic and nuclear phases. The cell parameters of the nuclear phase were refined first, along with the atomic positions and thermal parameters, and are reported in Table 3.17. The atomic positions of the magnetic phase were constrained to match those of the nuclear phase; however, the lattice parameters of the magnetic phase were freely refined and are reported with the full structural parameters in Table 3.18.

Once the unit cell parameters had been fixed, the magnetic moments were refined, with the following constraints: $m(Mn1) = m(Mn2)$ and $m(Mn4) = m(Mn5) = m(Mn6) = m(Mn7)$. For the $ZrMn_{2.06}$ deuteride, the refined moments for Mn1, Mn2, and Mn3 are reported in Table 3.18, but the moments of Mn4 through Mn7 could not be reliably refined, likely as a result of the low fractional occupancy on this site. In the case of the $ZrMn_{2.13}$ deuteride, none of the magnetic moments could be accurately refined and thus the values determined from the nearly stoichiometric deuteride were arbitrarily used.

Parameter	$ZrMn_{2.09}D_{2.91}$	$ZrMn_{2.13}D_{3.14}$
a (Å)	5.3803(4)	5.3638(4)
c (Å)	8.7348(9)	8.709(1)
R_{wP}	1.52	7.38
$4f$ $(\frac{1}{3}, \frac{2}{3}, z)$	0.0638(2)	0.0709(4)
Zr1 occ.	0.97	0.94
Mn3 occ.	0.03	0.06
B_{eq} (Å^2)	0.00092(4)	0.0043(6)
Mn1, $2a$ $(0, 0, 0)$	-	-
B_{eq} (Å^2)	0.00092	0.0043
Mn2, $6h$ $(x, 2x, \frac{1}{4})$	0.8340(3)	0.8359(6)
B_{eq} (Å^2)	0.0071(8)	0.0022(5)
D1, $24l$ (x, y, z)	0.078(4), 0.315(2), 0.585(1)	0.046(1), 0.334(1), 0.548(2)
D1 occ.	0.210(3)	0.220(1)
B_{eq} (Å^2)	0.47(5)	0.011(9)
D2, $12k$ $(x, 2x, z)$	0.424(1), 0.590(1)	0.435(1), 0.6322(8)
D2 occ.	0.338(2)	0.366(2)
B_{eq} (Å^2)	0.53(4)	0.032(7)
D3, $6h$ $(x, 2x, \frac{1}{4})$	0.408(1)	0.468(1)
D3 occ.	0.368(3)	0.356(2)
B_{eq} (Å^2)	0.60(7)	0.14(9)

Table 3.17: *Refined unit cell parameters and atomic positions, as determined via neutron diffraction at 10 K, for the deuterided, cycled $ZrMn_{2+x} - D$ series with $x = 0.06, 0.13$. The parameters given are for the $P6_3/mmc$ structure with nuclear reflections only; no magnetic component was included.*

Parameter	$ZrMn_{2.09}D_{2.91}$	$ZrMn_{2.13}D_{3.14}$
a (Å)	5.365(1)	5.3334(7)
c (Å)	17.430(6)	17.554(9)
R_{wP}	1.24	6.00
Mn1, $1a$ $(0,0,0)$	-	-
moment (μ_B)	$-4.5(3)$	-4.5
Mn2, $1b$ $(0,0,\frac{1}{2})$	-	-
moment (μ_B)	$-4.5(3)$	-4.5
Mn3, $2c$ $(0,0,z)$	0.25	0.25
moment (μ_B)	3.1(2)	3.1
Mn4, $2d$ $(\frac{1}{3},\frac{2}{3},z)$	$z_{nuclear}(=0.0638)$	$z_{nuclear}(=0.0709)$
Mn4 occ.	0.03	0.06
moment (μ_B)	5.5	5.5
Mn5, $2d$ $(\frac{1}{3},\frac{2}{3},z)$	$0.25 - z_{nuclear}$	$0.25 - z_{nuclear}$
Mn5 occ.	0.03	0.06
moment (μ_B)	5.5	5.5
Mn6, $2d$ $(\frac{1}{3},\frac{2}{3},z)$	$0.5 + z_{nuclear}$	$0.5 + z_{nuclear}$
Mn6 occ.	0.03	0.06
moment (μ_B)	5.5	5.5
Mn7,$2d$ $(\frac{1}{3},\frac{2}{3},z)$	$0.75 - z_{nuclear}$	$0.75 - z_{nuclear}$
Mn7 occ.	0.03	0.06
moment (μ_B)	5.5	5.5

Table 3.18: *Refined unit cell parameters and atomic positions, as determined via neutron diffraction at 10 K, for the deuterided, cycled $ZrMn_{2+x} - D$ series with $x = 0.06, 0.13$. The parameters given are for the $P\bar{3}m'1$ structure with magnetic reflections only; the R_{wP} values cited are for a combined nuclear and magnetic fit.*

To discuss first the refinement of the purely nuclear reflections, the refined structures at 10 K of the $ZrMn_{2+x}D_y$ C14 phase, shown in Table 3.17, can be readily compared with the refined structures at 300 K, shown in Tables 3.7 and 3.8. In accordance with expected thermal expansion, the volumes of low-temperature structures – $V = 218.97$ ($ZrMn_{2.09}D_{2.91}$), $V = 217.00$ ($ZrMn_{2.13}D_{3.14}$) – are smaller than the volumes of the room temperature structures. The metal atom positions have not shifted significantly in either phase upon temperature reduction, although the isotropic thermal parameters have decreased. Conversely, the deuterium atom positions have been notably altered, with much smaller thermal parameters than in the room temperature phase, suggesting that the locations determined at 10 K may be more reflective of the actual deuterium positions in the C14 structure. In the case of the superstoichiometric deuteride, the relative occupancies of the sites have also changed marginally upon temperature reduction, with slightly less deuterium inhabiting the $24l$ site and slightly more on the $12k$ site; the relative occupancies in the nearly stoichiometric deuteride were not statistically different from the room temperature structure.

For both deuterides, the D4 position identified in the room temperature structure could not be reliably refined, suggesting that the diffraction data were not sufficiently intense to extract information on a position with such a small fractional occupancy. Due to the absence of the D4 site in the 10 K structure, the refined deuterium concentration in these structures appears to be marginally less than that in the room temperature structure; in reality, this variance is not significant and it can be expected that the actual number of deuterium atoms per unit cell does not vary with temperature.

Considering now the magnetic reflections, it can be seen that the $P\bar{3}m'1$ Shubnikov space group relates directly to the nuclear unit cell, being simply a doubling of the $P6_3/mmc$ structure along the $c-$axis. The lattice parameters of the magnetic cell were freely refined and, for both the nearly stoichiometric and superstoichiometric structures, independently arrived at values very near to

$a_{magnetic} = a_{nuclear}$ and $c_{magnetic} = 2c_{nuclear}$. Based on this agreement, the atomic positions were not refined and instead were constrained to match the previously determined positions of the nuclear structure. The refined magnetic moments of the $ZrMn_{2.09}D_{2.91}$ structure, which the scaled arrows in Figure 3.43 represent, illustrate a system with a ferromagnetically aligned B sublattice composed of Mn^{2+} ions on $4f$ sites with $m = 5.5\ \mu_B/Mn^{2+}$ and an imperfect antiferromagnetic A sublattice composed of Mn^{2+} ions on $2a$ sites with a net negative moment with $m = -1.44\ \mu_B/Mn^{2+}$. This model agrees excellently with the findings of the magnetic investigations summarised earlier in Sections 3.10.1.1 and 3.10.2, particularly in regards to the reduced magnetisation curve of Figure 3.32, which indicated that the A sublattice was likely to carry a small, negative magnetisation.

Figure 3.44 shows the collected diffraction pattern at 10 K, along with the calculated fit, for $ZrMn_{2.09}D_{2.91}$; as is evident from the difference plot, the agreement for the combined nuclear and magnetic structure is quite good and showed a significant improvement in R_{wP} (1.52 to 1.24) as compared to when only the nuclear structure was used. It should be noted that two particularly intense areas in the difference plot actually result from experimental factors: the sharp peak at $d = 2.14$ is due to the vanadium can, and the broad feature spanning $2.47 \leq d \leq 2.56$ results from the cryostat module. Even considering these corrections, it can be seen that the calculated magnetic structure is not a perfect match to the observed data; it is likely that the magnetic strain and disorder in this system, which were commented on earlier, play an important role here. Local variations in the manganese-to-zirconium ratio across the microstructure are certain to cause variations in the ordering scheme due to the competing exchange integrals in the system, which may give rise to magnetic supercells or other complex ordering arrangements. This unaccounted for disordered variation in the magnetic structure may cause an increase or reduction in intensity of the existing magnetic reflections, or even entirely create new peaks; if a large magnetic cell was used, with more variation in the individual moments incorporated, in order to reflect this disorder, then it is likely that a more satisfactory fit could be obtained.

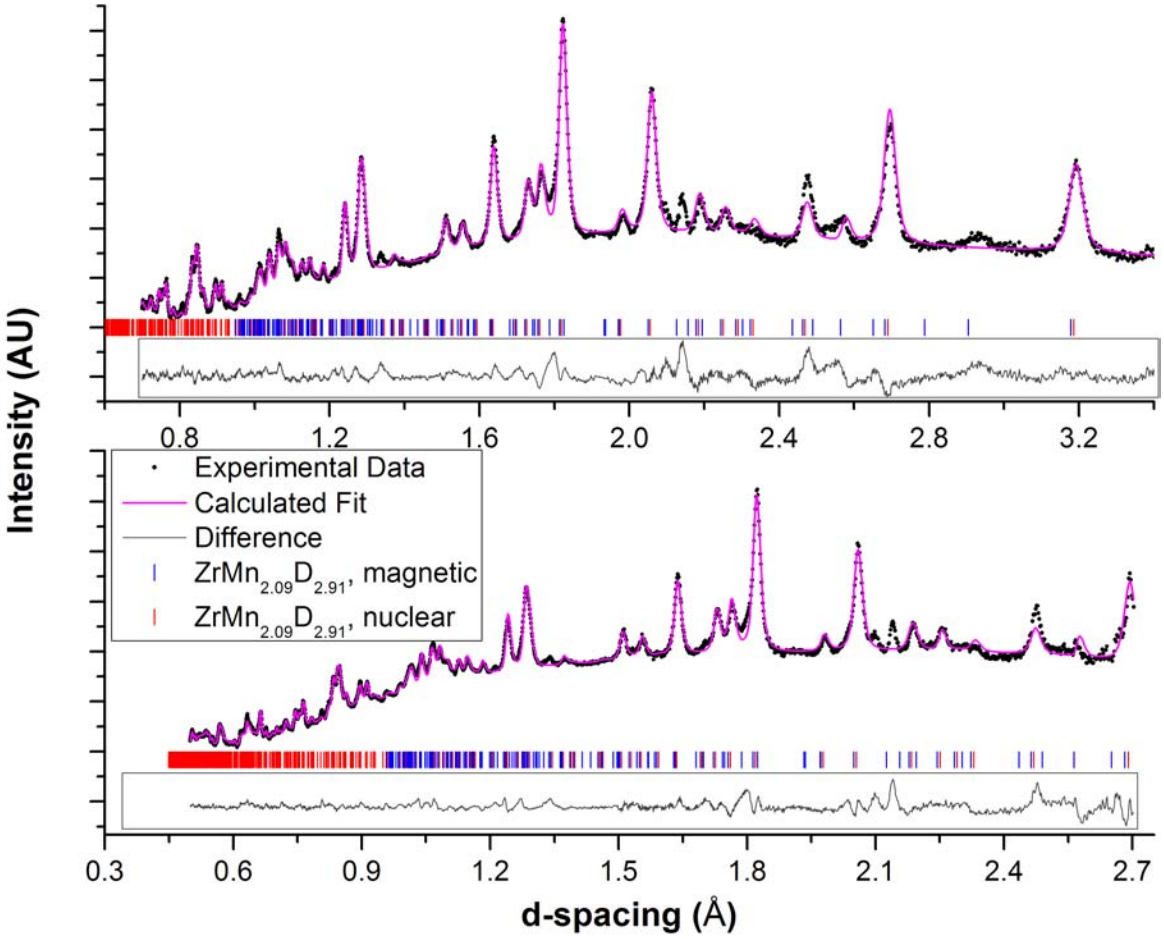

Figure 3.44: *Experimental data (black dots), calculated fits (pink lines) and difference plots (grey lines enclosed in boxes) for the refinement of* $ZrMn_{2.09}D_{2.91}$ *from neutron diffraction data collected at 10 K from bank 4 (top) and bank 5 (bottom) of the ISIS GEM diffractometer. The Bragg peak positions of the nuclear (red) and magnetic reflections (blue) are shown by vertical tick marks.* $R_{wP} = 1.24$

This magnetic disorder becomes more significant in the superstoichiometric deuterides, as the magnetic data in Section 3.10.2 on the $ZrMn_{2+x}H_3$ system have already indicated. It can be seen from Figure 3.45, which shows the collected diffraction pattern and calculated fit at 10 K for $ZrMn_{2.13}D_{3.14}$, that the proposed magnetic structure model does not accurately describe the experimental data. The tickmarks indicate that the $P\bar{3}m'1$ structure is likely to be the correct unit cell; however, the mismatch in intensities signifies that there may be errors either in the atomic positions or the local magnetic moments within the structure. The

magnetic study on the superstoichiometric hydrides indicated a strong tendency towards increasing magnetic disorder and strain as the level of manganese substitution in the system increased; moreover, the decrease in J_{BB} with x in the $ZrMn_{2+x}H_3$ series suggests that spin flips on the B sublattice may be more likely in the superstoichiometric system. Together, this implies that the simple magnetic model given in Figure 3.43 does not completely describe the superstoichiometric members of the $ZrMn_{2+x}-$ D system: although it is beyond the scope of this work, it is expected that a large supercell capable of allowing for these spin flips and disordered moments would provide a more precise magnetic structure model.

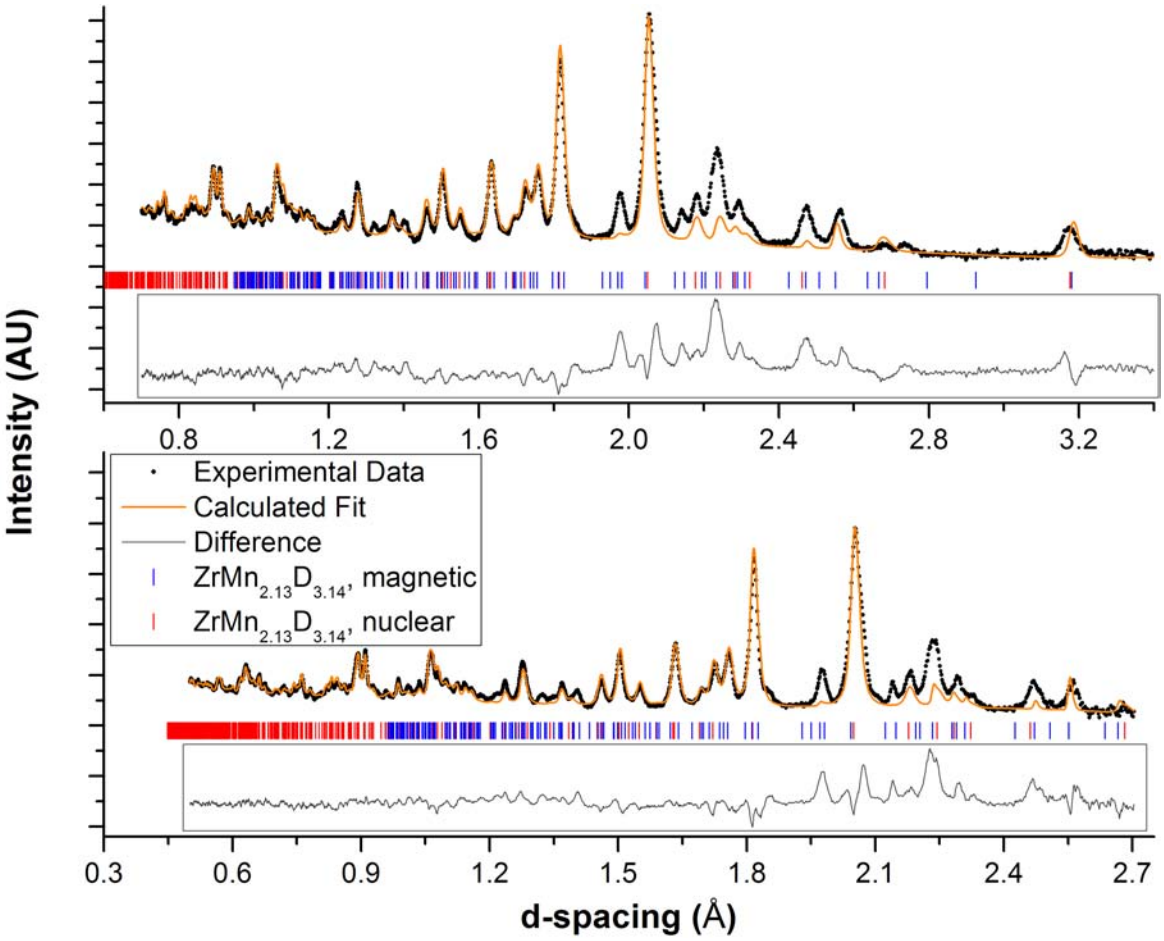

Figure 3.45: *Experimental data (black dots), calculated fits (orange lines) and difference plots (grey lines enclosed in boxes) for the refinement of* $ZrMn_{2.13}D_{3.14}$ *from neutron diffraction data collected at 10 K from bank 4 (top) and bank 5 (bottom) of the ISIS GEM diffractometer. The Bragg peak positions of the nuclear (red) and magnetic reflections (blue) are shown by vertical tick marks.* $R_{wP} = 6.00$

Although the substoichiometric deuteride could not be analysed at this stage, it is expected that its magnetic structure would closely resemble that of the $ZrMn_{2.06}-$ D system. This assumption is based on the analysis of the magnetic data, summarised in Section 3.10.3.1, which suggested that $ZrMn_{1.65}H_3$ was magnetically very similar to $ZrMn_{2.06}H_3$. An even better fit to the proposed magnetic model is expected in this case, since the level of manganese substitution on the $4f$ site is lower – approximately 1.5% of the $4f$ sites are occupied by Mn – which would cause less disorder; this is supported by the low value of the magnetic strain found for the substoichiometric hydride in Section 3.10.3.

3.12 Electronic and Dielectric Properties of $ZrMn_{2+x}$ ($-0.35 \leq x \leq 0.44$) and its hydrides

In order to examine the electronic and dielectric properties of the $ZrMn_{2+x}$ system and how these change upon hydrogen absorption, the cycled, dehydrided $ZrMn_{2+x}$ compounds, with $x = -0.35$, 0.06, 0.13, 0.18, 0.31 and 0.44, and their hydrided counterparts (the synthesis of which are described in Section 3.4) were analysed in a microwave cavity resonator. The design and operation of this resonator is described in Section 2.3.4; for the measurement of the $ZrMn_{2+x}-$ H series the 'collapsed cylinder' model discussed in Section 2.3.3 was used. In all cases, the dielectric properties of the materials were determined at room temperature only.

3.12.1 Model Verification via Microwave Studies on nearly stoichiometric $ZrMn_{2.06}-H$

The accuracy and validity of the collapsed cylinder model were tested over the course of this doctorate work, as Section 2.3.4.1 summarises; nonetheless, it was relevant to consider if the assumptions inherent in the model were appropriate for the $ZrMn_{2+x}-$ H system in particular. The first boundary condition for the model states that the particle size must be much smaller than the wavelength of the electromagnetic field resonating in the cavity; for the 2.5 GHz hairpin used

in this work, that translates into a restriction of particle sizes less than 0.12 m. The second boundary condition mandates that the particle size must also be much smaller than the skin depth: as discussed in Section 2.3.4.1 , this is not precisely known for the $ZrMn_{2+x}-$ H system, but can be estimated to be approximately 12 μm. From the peak profile analysis on the diffraction data of the $ZrMn_{2+x}-$ H system in Section 3.8.3, an estimate of the crystallite size for these materials can be garnered and was found to be approximately 55 ± 12 nm for both the hydrided and dehydrided members of the system. This method of size calculation involves many assumptions and is not a precise measure; nevertheless, it can be said with some confidence that the particle sizes in the $ZrMn_{2+x}-$ H system satisfy the boundary conditions of the collapsed cylinder model.

Figures 3.46 and 3.47 show the resonance spectra for the microwave conductivity measurement on $ZrMn_{2.06}$ and $ZrMn_{2.06}H_3$ in the electric field antinode and magnetic field antinode, respectively. Qualitatively, the shift in the resonance spectra in the electric field antinode from that of the empty cavity is quite different between the hydrided and hydrogen-free phases. Conversely, they are nearly indistinguishable in the magnetic field antinode and, as a result of this, only the results of the electric field antinode measurements will be discussed for $ZrMn_{2+x}-$ H system.

The large resonance frequency shifts induced by $ZrMn_{2.06}$ and its hydride when introduced into the electric field of the resonator suggest that both become substantially polarised, as would be expected for a metallic material. Both phases also contain significant loss components, as exhibited by the increase in the bandwidth of the resonance frequency, with the hydrided phase being more lossy than the dehydrided phase. The numerical values of Δf and $\Delta\Gamma$ for $ZrMn_{2.06}$ and $ZrMn_{2.06}H_3$ in electric field antinode are summarised in Table 3.19; each value given for f and Γ represents an average of at least six separate measurements, with the standard deviation between these measurements given in the table.

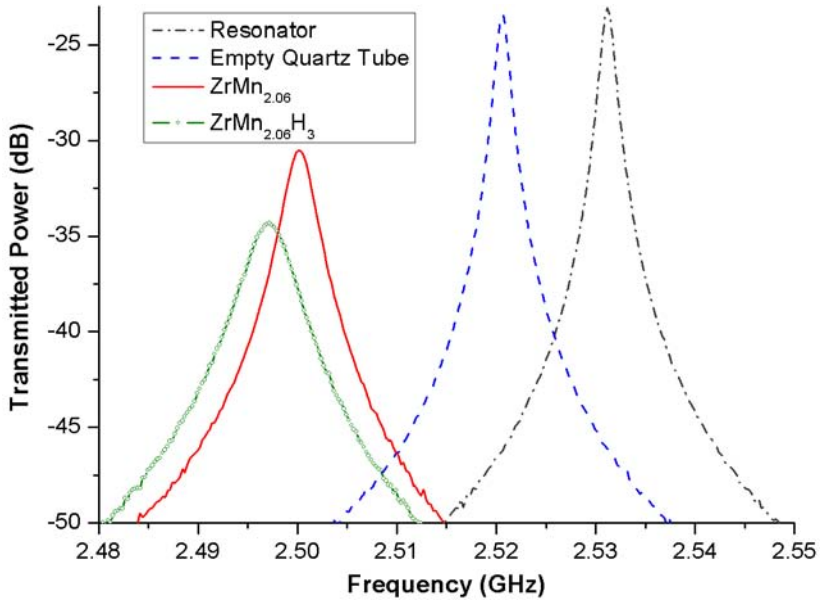

Figure 3.46: *Resonance spectra for the microwave conductivity measurement on $ZrMn_{2.06}$ (red line) and its hydride (green line with circles), showing transmitted power versus frequency in the electric field antinode of the cavity. The spectra for the empty cavity (broken grey line) and an empty quartz tube, used to contain the compounds (dashed blue line), are shown for comparison. Relative errors are smaller than data points.*

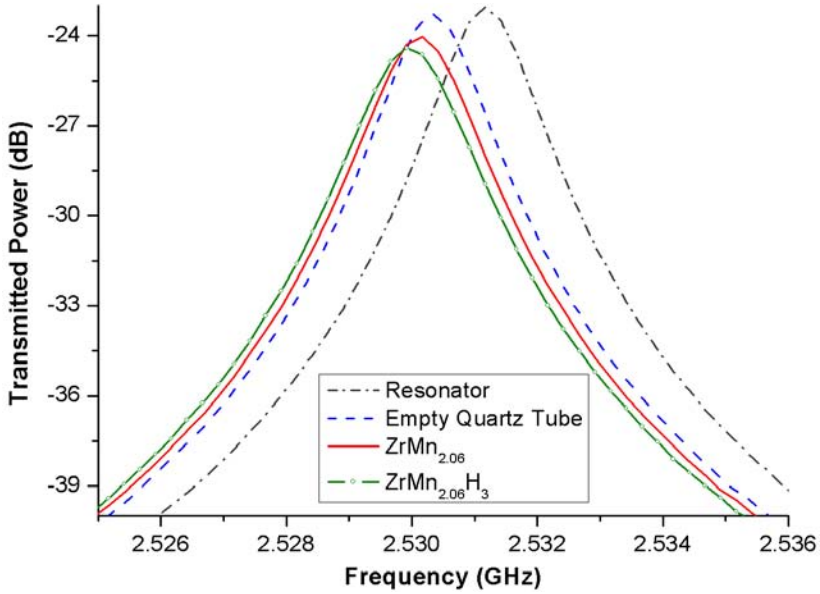

Figure 3.47: *Resonance spectra for the microwave conductivity measurement on $ZrMn_{2.06}$ (red line) and its hydride (green line with circles), showing transmitted power versus frequency in the magnetic field antinode of the cavity. The spectra for the empty cavity (broken grey line) and an empty quartz tube, used to contain the compounds (dashed blue line), are shown for comparison. Relative errors are smaller than data points.*

	f (Hz)	Γ (Hz)	ε_{1eff}	ε_{2eff}	$\tan\delta_{eff}$	σ_{eff} (Ω^{-1} m^{-1})
$ZrMn_{2.06}$	$2.49979(9) \times 10^9$	$3.20(2) \times 10^6$	10(1)	−1.7(3)	0.17(3)	0.23(5)
$ZrMn_{2.06}H_3$	$2.4970(1) \times 10^9$	$5.28(4) \times 10^6$	15(2)	−11(2)	0.7(1)	1.5(3)
Empty resonator	$2.53116(5) \times 10^9$	$1.407(2) \times 10^6$				

Table 3.19: *Measured microwave resonance parameters in the electric field antinode for nearly stoichiometric $ZrMn_{2.06}$ and its hydride, as compared to the resonance parameters of the empty cavity. The extracted dieletric constants, loss tangent and effective conductivity for the $ZrMn_{2.06} - H$ series is also shown.*

Table 3.19 also reports the permittivity, loss tangent and conductivity calculated from these resonance spectra for the $ZrMn_{2.06}-$ H system. The real part of the permittivity, ε_{1eff}, relates to the polarisability and at microwave frequencies would contain components due both the electronic and ionic polarisability; the very strong polarisation of both $ZrMn_{2.06}$ and $ZrMn_{2.06}H_3$ in the electric field suggests that the applied field is readily opposed by the distortion of the conduction electrons. The imaginary part of the permittivity, ε_{2eff}, directly relates to the population of this conduction electron band and shows that the hydride is substantially more conducting than the dehydrided material. As a result of both the model's assumptions and the powdered nature of the samples, the calculated σ_{eff} value for $ZrMn_{2.06}$ is much lower than the reported conductivity of 5.12×10^5 Ω^{-1} m^{-1} for the bulk alloy at 300 K [21]. Finally, examination of the ratio between the real and imaginary parts of the permittivity give the loss tangent, which relates to the energy lost in the polarisation process. This loss tangent increases in $ZrMn_{2.06}$ upon hydriding and is likely related to both an anisotropy in the polarisability of the material and to the ionic polarisability of hydrogen. This ionic polarisability stems from the high mobility of hydrogen in the $ZrMn_{2.06}-$ H system, which has

been previously demonstrated *via* quasielastic neutron spectroscopy [24].

3.12.2 Microwave Studies on the $ZrMn_{2+x}$– H ($-0.35 \leq x \leq 0.44$) series

Microwave resonance spectra were collected for the series of cycled, dehydrided $ZrMn_{2+x}$ materials ($x = -0.35$, 0.13, 0.18, 0.31 and 0.44) and their hydrides, the results of which are in Table 3.20. Each sample was separately measured at least six times and the frequency shift and bandwidth change for each of these measurements, as compared to the empty cavity, was averaged and its standard deviation determined. Estimations of the errors on the extracted electronic and dielectric values proved more difficult; Section 2.3.4.1 details a method for approximating these errors, which was used to calculate the error bars in Figure 3.48.

The change in the frequency shift and the bandwidth increase of the microwave resonance in the $ZrMn_{2+x}$– H series showed a clear dependence on x for both the hydrided and hydrogen free phases. It is evident from Table 3.20 that $\Delta\Gamma$ increases as the level of substitution increases in both the dehydrided and hydrided phases; this holds both for zirconium substitution in the substoichiometric system, and for manganese substitution in the superstoichiometric system. The magnitude of the frequency shift caused by sample insertion, $|\Delta f|$, drops as x increases for both $ZrMn_{2+x}$ and $ZrMn_{2+x}H_3$, although there is some variation in the dehydrided data set.

Translation of these frequency shifts and bandwidth changes into permittivity and conductivity values provides a more telling picture of the changes that occur in the system. Comparison of Tables 3.20 and 3.19 demonstrates that there is a reduction in the real part of the permittivity as x increases across the $ZrMn_{2+x}$ series, indicating a diminishing polarisability of the dehydrided materials as the manganese content increases, with ε_{1eff} of $ZrMn_{1.65}$ almost twice as large as for $ZrMn_{2.06}$. The polarisability of a crystal may be expressed approximately as the product of the polarisabilities of the atoms within it, multiplied by the local electric field at each lattice site [56]. The polarisability of the $ZrMn_{2+x}$ system can

therefore be approximated by a sum of the polarisabilities of the atoms within it and, since zirconium, as a larger atom with an easily deformed electron cloud, is more polarisable than manganese, it is readily seen that an increase in x will reduce the overall polarisability of the system [56].

	Δf ($\times 10^7$ Hz)	$\Delta\Gamma$ ($\times 10^5$ Hz)	ε_{1eff}	ε_{2eff}	$\tan\delta_{eff}$	σ_{eff} ($\Omega^{-1}\mathrm{m}^{-1}$)
dehydrides:						
$ZrMn_{1.65}$	−3.42(2)	17.4(8)	17(2)	−5(1)	0.31(5)	0.7(1)
$ZrMn_{2.13}$	−2.901(8)	9.3(1)	6.8(8)	−0.49(9)	0.072(1)	0.07(1)
$ZrMn_{2.18}$	−3.07(3)	18.3(4)	8.5(9)	−1.4(3)	0.16(2)	0.19(4)
$ZrMn_{2.31}$	−2.93(1)	19.02(7)	7.2(8)	−1.1(2)	0.16(2)	0.16(3)
hydrides:						
$ZrMn_{1.65}H_3$	−3.768(2)	12.8(9)	26(3)	−79(9)	3.0(5)	1.7(3)
$ZrMn_{2.13}H_3$	−3.547(4)	5.6(3)	39(4)	−7(1)	0.17(3)	0.14(3)
$ZrMn_{2.18}H_3$	−3.05(2)	34.8(4)	8.4(9)	−2.7(5)	0.32(5)	0.06(1)
$ZrMn_{2.31}H_3$	−3.036(7)	21.2(3)	8.5(9)	−1.6(3)	0.19(3)	0.034(7)
$ZrMn_{2.44}H_3$	−2.779(6)	17.7(3)	5.7(7)	−0.7(1)	0.12(2)	0.015(3)

Table 3.20: *Measured microwave resonance parameters in the electric field antinode for the series $ZrMn_{2+x}$ and its hydrides, with $x = -0.35, 0.13, 0.18, 0.31, 0.44$. Extracted dieletric constants, loss tangents and effective conductivities are given.*

A similar trend in ε_{1eff} versus x is observed for the hydrided members of the $ZrMn_{2+x}$ series, with the polarisability of the hydride decreasing as the amount of manganese in the system increases. Within error, the real part of the permittivity, and therefore the polarisability, was observed to escalate upon the addition of hydrogen for all values of x. This may in part be due to the high ionic mobility of hydrogen in the $ZrMn_{2+x}-$ H system.

The loss tangent in the hydrogen-free $ZrMn_{2+x}$ materials did not vary significantly with x except in the case of the substoichiometric $ZrMn_{1.65}$, where $\tan\delta_{eff}$

was approximately double that of the rest of the series. In all cases, the loss tangent is enhanced by a factor of two to four upon hydriding, such that $\tan\delta_{eff}$ decreases slightly across the $ZrMn_{2+x}H_3$ series. The addition of hydrogen may increase the dielectric loss of the material as a result of the ionic polarisability of the hydrogen ion, which would be expected to demonstrate significant energy loss in an alternating electric field at microwave frequencies [56]. Moreover, there may be an anisotropic contribution to the polarisation loss in the hydrides, much as was previously observed in their magnetic behaviour. The marginal decline of $\tan\delta_{eff}$ across the superstoichiometric hydride series, as well as the previously noted decrease in ε_{1eff} with x, results simply from reduction in the number of hydrogen atoms per unit cell as the manganese content increases, discussed earlier in Section 3.8.1. In the case of the $ZrMn_{1.65}-$ H system, in which both the hydrogen free and hydrided phase are significantly more lossy than the nearly stoichiometric material, it can be concluded that the substitution of zirconium for manganese has introduced a major source of dielectric loss in the material.

Figure 3.48 displays the change in effective conductivity for the $ZrMn_{2+x}-$ H system with x; showing that conductivity varies with manganese content in an approximately exponential function. Conversely, for the dehydrided materials, shown in the same figure, the conductivity is invariant (within error) across the series with $x \geq 0$, and increases slightly from this value in the case of the substoichiometric phase. The similarity between the trend in σ_{eff} with x for $ZrMn_{2+x}H_3$, and the observed dependence of the magnetic moment, m, on x, documented in Figure 3.37 should be noted: it is likely that for both of these measurements, the drop-off in magnitude with increased manganese content results not from a shift in intrinsic values, but can at least partially be attributed to an increase in the alloy-to-hydride ratio in the sample as the superstoichiometry increases. Although efforts were made to collect microwave resonance spectra as soon as possible after hydriding was complete, it is inevitable that for the materials with higher manganese content that some amount of hydrogen was lost *via* the equilibrium reaction described in Equation 3.2.

However, the difference in conductivity values for $ZrMn_2H_3$ and $ZrM_{1.65}H_3$ cannot be dismissed *via* this hydrogen loss explanation: both hydrides have been shown, *via* X-ray diffraction and thermodynamic measurements in Sections 3.6 and 3.5, to be stable at room temperature and atmospheric pressure. It is difficult to quantify the exact measure of hydrogen lost in the superstoichiometric hydrides, but if the variation in hydride concentration could be accounted for, it is reasonable to expect the trend in σ with x to follow a linear decrease. This assumption is made on the basis that a steady variation in the Zr:Mn ratio would chiefly effect the number of valence electrons, with structure remaining invariant, and indeed the concentration of conduction electrons will determine the material's conductivity.

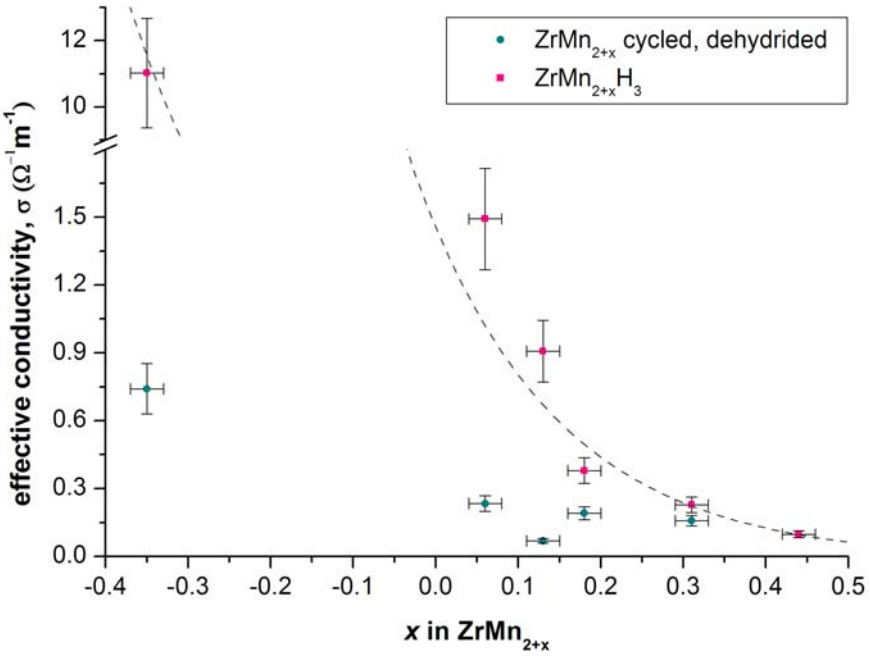

Figure 3.48: *A plot of the effective conductivity, as determined from microwave resonance measurements, against x for the series $ZrMn_{2+x}H_3$ (pink squares) and cycled, dehydrided $ZrMn_{2+x}$ (turquoise circles). A dashed grey line acts as a guide to the eye to exhibit the trend in the hydride data.*

A detailed analysis of the causes behind the observed trends in conductivity in the $ZrMn_{2+x}-$ H system is difficult to make without analysis of the electron density of states (DOS) for the alloy and a view to how this changes upon hydriding and upon alteration of the manganese content. Although there exists detailed

electronic structure studies for the $ZrMn_2$ alloy [32] and for the $ZrMn_2$ hydride [97], the computational methods used to derive these two structures are quite different, making a direct comparison non-facile. The DV-Xα cluster method used to analyse the hydride assumed a composition of $ZrMn_2H_{0.5}$, which is clearly far short of the actual hydrogen concentration in the hydrided phase; moreover, the semi-empirical method used yielded only a crude approximation of the actual electronic structure. There is clearly a need for a suitable theoretical study on the $ZrMn_{2+x}-$ H system that explores the effect of both manganese and hydrogen on the electronic structure; unfortunately, such a study was beyond the scope of this thesis.

These microwave resonance measurements investigating the effect of both hydrogen and x on the electrical properties of the $ZrMn_{2+x}-$ H system have demonstrated several previously unobserved trends:

- Both the hydrided and the hydrogen free members of the $ZrMn_{2+x}-$ H system are metallic conductors, showing a large polarisation in the electric field antinode of the resonator, along with significant dielectric loss in each case.

- The hydrogen-free material $ZrMn_{2+x}$ showed little variation in dielectric properties with x. The polarisability declines with increasing manganese content as a result of the reduced polarisability of manganese as compared to zirconium; the conductivity also decreases slightly.

- Regardless of the zirconium to manganese ratio in the metal, the hydrided material has an enhanced polarisability and a greater dielectric loss than the hydrogen-free phase, as a result of the hydrogen's ionic polarisability and an anisotropy in the structure. An increase in electrical conductivity concomitant to the hydriding process has also been observed, which cannot be appropriately described without further study into the theoretical electronic structure of the $ZrMn_{2+x}-$ H system.

3.13 Summary and Conclusions

To summarise, a series of $ZrMn_{2+x}$ intermetallic compounds were synthesised *via* arc-melting, then hydrided and cycled to produce the $ZrMn_{2+x}H_3$ series. The thermodynamic data indicated that the hydrides thus formed became increasingly unstable as x increased; moreover, X-ray diffraction revealed that the superstoichiometric hydrides possessed significant crystalline strain that was invariant across the $ZrMn_{2+x}H_3$ series. For the hydrogen-free phases, the strain was lowest for the nearly line phase, and increased with x for the superstoichiometric compounds. Analysis of the X-ray diffraction data proved the formation of the hydride phases and showed that hydrogen was accommodated in interstitial sites of the existing C14 metal lattice *via* anisotropic lattice expansion. The structural study also allowed x to be determined, as well as allowing the identification of the substitutional models for both the superstoichiometric and substoichiometric systems. Comparison of the crystal structure across the $ZrMn_{2+x}$ series showed that the volume of the $P6_3/mmc$ unit cell decreased linearly with x; a similar trend was observed for the hydrides but was not linear due to the concomitant depletion in the amount of hydrogen per unit cell as the manganese content rose.

Room temperature neutron diffraction provided the deuterium positions and occupancies within the $ZrMn_{2+x}D_y$ series and, while the structures of the nearly stoichiometric and superstoichiometric deuteride agreed well with previous studies, the novel exploration of the substoichiometric deuteride structure revealed that zirconium substitution created two new deuterium sites in the structure.

A new interpretation on the magnetic behaviour of $ZrMn_{2.06}$ and $ZrMn_{2.06}H_3$ revealed that both were Néel ferrimagnets, where the hydrogen-free phase underwent a very low temperature transition (< 2 K) and the hydrided phase had a $T_c = 224$ K. Both systems were described on the basis of an A sublattice, composed of antiferromagnetically aligned manganese atoms on the $2a$ lattice sites, and a B sublattice, composed of ferromagnetically aligned substitutional manganese atoms on the $4f$ site. It was shown that even in the case of a nominally

stoichiometric and substoichiometric phase, replacement of zirconium by a small fraction of manganese on the $4f$ site is highly favourable. The low transition temperature of the alloy was ascribed to frustration of the magnetic moments, which hydriding at least partially relieves due to both the hydrogen-induced lattice expansion and possibly indirect exchange with the manganese atoms. When cooled in the absence of a field, the hydride was shown to exhibit spin glass behaviour, demonstrating the competing coupling tendencies and the continued presence of magnetic frustration.

The superstoichiometric and substoichiometric alloys and hydrides could be described by the same magnetic model as for $ZrMn_{2.06}-$ H system. In the case of the superstoichiometric hydrides, the ferrimagnetic T_c decreased linearly as the manganese content grew; moreover, the width of the ferrimagnetic transition also increased with x as a result of enhanced strain and disorder in the highly superstoichiometric system. Analysis of the $M(H)$ data confirmed the effect of manganese content on magnetic strain in the hydrides and suggested a similar trend in both strain and T_c in the superstoichiometric alloys. With the proliferation of the substituted manganese atoms on $4f$ site came a rise in competing coupling tendencies in the system, causing this magnetic strain; these effects are suspected to cause substantial deviation from the magnetic structure model described for the nearly stoichiometric $ZrMn_{2.06}-$ H system.

The substoichiometric alloy was shown to be magnetically very similar to the $ZrMn_{2.06}$ alloy; derivation of the Néel fitting constants showed that a very small fraction of manganese atoms were present on the $4f$ site in the substoichiometric system. The magnetic behaviour of the hydride indicated that it was missing the significant strain contributions of the superstoichiometric hydrides, due to the absence of these competing exchange tendencies.

Combination of these experimental magnetic data with a theoretical modelling program enabled the construction of a simple magnetic crystal structure, which was based on a doubling of the nuclear unit cell with Shubnikov symmetry $P\bar{3}m'1$.

Refinement of low temperature neutron diffraction data provided evidence that this model was a good description of the magnetic order in the nearly stoichiometric $ZrMn_{2.06}-$ H system. However, the diffraction data of the superstoichiometric deuteride proved more difficult to fit with this model, and it suspected that a larger supercell would more effectively describe the competing coupling tendencies and magnetic strain and disorder in the system.

Finally, the $ZrMn_{2+x}$ series and their hydrides were measured in a microwave cavity resonator, and their dielectric permittivity and conductivity at room temperature determined. Both the hydrogen free and hydrided phases were found to be metallic conductors undergoing a large polarisation in the electric field; this polarisation decreased as the manganese content increased, and also was enhanced by hydrogen absorption. The $ZrMn_{2+x}$ hydrides were more lossy than the dehydrided materials, as a result of the ionic polarisability of hydrogen and the anisotropy of the structure. Calculation of an effective conductivity value revealed that, for all values of x, the conductivity increased concomitant to the hydriding process, with the conductivity of both the hydrided and hydrogen free phases diminishing as the level of superstoichiometry increased.

Several important conclusions can be drawn from this collected body of data, the first of which involves the general effect of nonstoichiometry on the $ZrMn_{2+x}-$ H system. Following the guidance in Pearson's Handbook [92] that composition dependencies of lattice parameters for intermetallic compounds differ between sub- and superstoichiometric regions, this work has separately analysed the structural trends in the manganese-deficient and manganese-excess $ZrMn_{2+x}-$ H systems; moreover, this separation has been followed for examination of magnetic and electronic trends as well.

In general, the properties of the hydrogen-free superstoichiometric $ZrMn_{2+x}$ series either followed a linear variation with x or were invariant against manganese substitution; properties for which $f(x)$ was a simple linear relationship include the lattice parameters of the $P6_3/mmc$ unit cell, the crystalline strain, and the

ferrimagnetic transition temperature. For many of the magnetic properties of the $ZrMn_{2+x}$ series, a clear dependence on manganese content was observed, but the relationship could not be linearly described due to the simultaneous influence of multiple phenomena —consider, for example, $W_H(x)$, where the effect of both a rise in disorder and a decline in T_c with x brought about a parabolic dependence. Once these additional factors have been accounted for, however, it is clear that the addition of excess manganese to the $ZrMn_{2+x}$ system alters its properties in a predictable, linear fashion. The variations caused by manganese substitution can be easily traced back to either the atomic size difference between manganese and the zirconium it replaces, or to the growth in the number of valence electrons that an increase in the manganese-to-zirconium ratio engenders.

The addition of hydrogen to the superstoichiometric $ZrMn_{2+x}$ series does not destroy this simple linear dependence of properties on x; rather, the general effect of hydrogen is to linearly shift these relationships. Consider the crystal structure of $ZrMn_{2.06}H_3$, which is formed by the expansion of the original metal C14 lattice: the volume of the hydrided $ZrMn_{2+x}H_3$ unit cell shows an exponential dependence on x. However, if the decline in the number of hydrogen atoms per unit cell could be accounted for, this is expected to reduce to a linear trend much like that observed for the hydrogen-free series. This unit cell expansion forms the foundation of the hydrogen-induced magnetic changes in the system: the enlarged lattice is thought to reduce magnetic frustration in the system, shifting the T_c of the magnetically ordered state some 200 K as compared to the $ZrMn_{2+x}$ alloys. Supporting this postulate, the hydrided $ZrMn_{2+x}$ series shows the same linear $T_c(x)$ dependence as the parent alloys.

The hydriding reaction also brings about an increase in the conductivity of the $ZrMn_{2+x}-$ H system, demonstrating that the addition of hydrogen goes beyond a simple lattice expansion effect. Although the conductivity declines with x, it is unclear to what extent this is caused by the reduction of the hydrogen concentration in the system. It is evident that there is an increase in the number of conduction

electrons concomitant to the hydriding process, but without a detailed electronic structure to refer to, it is difficult to comment further.

For the substoichiometric $ZrMn_{2+x}-$ H system, the general variation in properties upon zirconium substitution is less clear; the size of the data set (*viz.* one substoichiometric sample) did not enable the determination of $f(x)$ as for the superstoichiometric series. There is, however, no persuasive reason to assume that the variation in properties across the $ZrMn_{2+x}-$ H system upon zirconium substitution will not follow a predictably linear trend as per manganese substitution: although the mathematical nature of the $x > 0$ and $x < 0$ relationships differ, since the substitutional model has altered, the variation in atomic size and valence electron concentration should continue to describe the changes that occur.

Across the characterisation studies performed on the $ZrMn_{2+x}-$ H system, it was evident that the strain and disorder in the system were enhanced by deviation from $x = 0$. The strain in the crystal structure of the hydrogen free phase increased for $x > 0$; as well, the magnetic strain was heightened only by manganese substitution, supporting the model in which the $6h$ manganese site, on which zirconium substitutes, does not exhibit a localised moment. Hydriding increased the crystalline strain in such a way that it was invariant with x, suggesting that the lattice expansion had relieved some degree of the strain caused by atomic substitution. The rise in magnetic strain upon hydriding varied linearly with x, and the exchange integrals verified that the substitutional atoms played a significant role in creating competing coupling tendencies and additional magnetic stresses in the system. This heightened strain and disorder as the $ZrMn_{2+x}-$ H system veered from perfect stoichiometry affected many properties of the system, and further convoluted an examination of the changes induced by atomic substitution and hydrogen addition.

To conclude, this detailed characterisation study of the $ZrMn_{2+x}-$ H system has shone new insight into the alterations caused both by an off-stoichiometry in the metal atoms, and by the addition of hydrogen to the system. It has been shown

that varying the zirconium to manganese ratio does not bring about a paradigm shift in the system: within the range over which the C14 structure is retained, the addition of excess manganese or zirconium causes a predictable, linear variance in the crystallographic, magnetic and electronic properties of the system. These changes are easily explained on the basis of the difference in atomic size between manganese and zirconium, the change in the number of valence electrons that each carries, and the strain and disorder introduced by the atomic substitution. Nor does the addition of hydrogen alter the system significantly: the $P6_3/mmc$ structure is retained as the structure expands to accommodate hydrogen in interstitial sites. This lattice expansion has been shown to be the chief cause of ferrimagnetism in the hydride; although the hydrogen free phase is also ferrimagnetic, the transition temperature to this ordered state is below 2 K, and difficult to observe experimentally. An increase in conductivity concomitant to the hydriding process reveals that hydrogen addition must also have some electronic effect on the system, too. It can therefore be concluded that whilst the major change brought about by hydrogen addition is simply an expansion of the crystal structure, the hydrogen does not act purely as null dilutant —there exist subtle electronic alterations connected with the hydriding process as well.

3.14 Future Work

Over the course of this study, additional research pathways opened up which could not be explored within the scope of this thesis; these are detailed here.

Analysis of the composition of the $ZrMn_{2+x}$ alloys and their hydrides *via* an independent third means would have been a useful verification of x values calculated through X-ray diffraction. X-ray fluorescence, energy dispersive X-ray analysis, or inductively coupled plasma mass spectroscopy are all possible methods of exploring the manganese-to-zirconium ratio in these systems.

X-ray diffraction of the substoichiometric alloy revealed the presence of a minor

impurity phase, tentatively identified as 'ZrMn'; determination of the full structure of this phase was difficult, considering its low concentration and the overlap of its crystalline reflections with those of the $ZrMn_{2+x}$ phase. Considering that this ZrMn phase is not found in the phase diagram and has not been previously indexed, an in-depth study into synthesis and characterisation of ZrMn would be academically fruitful.

Examination of $\sigma(T)$ data can provide telling clues as to the electronic structure of a material; unfortunately, the microwave resonator used in this study could not be used for variable temperature dielectric measurements. Alteration of the resonator so as to allow low temperature determinations of σ_{eff} for the $ZrMn_{2+x}-$ H series would certainly prove useful; moreover, it would be interesting to examine the behaviour of the $ZrMn_{2+x}H_3$ series in the magnetic field antinode of the resonator below the magnetic transition temperature. As previously noted, a theoretical study of the electronic structure of the $ZrMn_{2+x}-$ H system, and how it varies with manganese content and upon hydrogen absorption, could allow additional insight into the nature of the conductivity changes that were observed.

On a final note, there is scope for additional low-temperature neutron diffraction in order to study the magnetic structure of the $ZrMn_{2+x}D_y$ series. As detailed previously, more complex magnetic modelling using an expanded supercell, with scope for the disorder and competing coupling tendencies that were experimentally observed, could provide a better fit to the neutron diffraction data of the superstoichiometric deuterides. It would also be interesting to examine the diffraction data of a deuteride that had been cooled below its transition temperature whilst in a magnetic field, as this should resolve much of the magnetic disorder within the system —the data collected in this thesis were cooled in the absence of a field, and effectively reflect the spin glass state. Finally, examination of the low temperature neutron diffraction of the substoichiometric deuteride, with comparison to the data collected herein for the nearly stoichiometric and superstoichiometric deuteride, would provide a useful verification of the proposed magnetic structure.

Chapter 4

CRYSTALLOGRAPHIC, MAGNETIC AND ELECTRONIC PROPERTIES OF ZRV_2 AND ITS HYDRIDES

> But why, some say, the moon? Why choose this as our goal? And they may well ask why climb the highest mountain? Why, 35 years ago, fly the Atlantic? Why does Rice play Texas?
>
> We choose to go to the moon in this decade and do the other things, not because they are easy, but because they are hard, because that goal will serve to organize and measure the best of our energies and skills, because that challenge is one that we are willing to accept, one we are unwilling to postpone, and one which we intend to win, and the others, too.
>
> *-President John F. Kennedy, Address at Rice University, Texas on 12 September 1962.*

4.1 Introduction and Scope

The intermetallic compound ZrV_2, a C15 Laves Phase structure, was introduced in Section 1.2.2. Initial interest in the material was sparked by its superconducting behaviour below 9 K [36]; however, its hydrogen absorption capacity makes the material attractive for a variety of technological applications as well. This hydride is unique amongst the Laves phase intermetallic hydrides for the both the ease with which hydrogen absorption occurs, and the high amount of hydrogen it can absorb —up to 6 hydrogen atoms per formula unit [20, 41]. However, even small amounts of hydrogen, on the order of 1.3 hydrogen atoms/f.u., destroys the

superconductivity in ZrV_2 and renders it a simple Pauli paramagnet [44, 45].

Hydrogen dissolves as a solid solution in ZrV_2 with an expansion of the parent $Fd\bar{3}m$ unit cell to accommodate the interstitial hydrogen, but no other structural change [40]. At room temperature, the hydrogen atoms are disordered over the *2A2B* and *1A3B* sites, but an extensive series of crystallographic studies [41–43] has revealed that there exists a complex system of ordered hydrogen superstructures at low temperatures. The hydrogen-free alloy also undergoes a low-temperature cubic-to-rhombohedral martensitic transition, which may be associated with the observed superconductivity [38, 82].

The following chapter will present a detailed examination of the ZrV_2- H system, with an investigation of the hydrogen-induced changes over a range of fundamental properties. These will include the hydriding thermodynamics, room temperature crystal structures, magnetic behaviour, superconductivity, dielectric properties and the electrical conductivity. In addition to gathering together an array of previously investigated phenomena and analysing them together for the first time, with a view towards discerning the role of hydrogen, this chapter will also present an entirely novel study of the dielectric properties and conductivity of the ZrV_2- H system. The chapter will conclude with a summary and discussion of these properties, commenting on the general effect of hydriding in this Laves phase system.

4.2 Formation of the ZrV_2 alloy

The alloy ZrV_2 was synthesised *via* arc-melting, as described in Section 2.4.3, with the inclusion of an annealing step to help secure a homogeneous, single-phase, C15 structure. As discussed by Pan *et al.* [98], an ingot of ZrV_2 quenched from the melt may contain not only the C14 polymorph, but also a variety of superstructures formed by layer stacking faults due to the relative stability of the hexagonal and cubic phases in the Zr-V system. X-ray diffraction of the ground, annealed material

was used to monitor the annealing process and determine when the desired C15 phase was obtained.

4.3 Crystallographic Features of the ZrV_2 alloy

The most stable structure of the intermetallic compound ZrV_2 at room temperature is the C15 Laves phase, with space group $Fd\bar{3}m$ and structural parameters as given in Table 1.2. An atomic diagram of the C15 unit cell is shown in Figure 4.5 (page 200). As was discussed in Section 1.2.2, the C14 polymorph, which forms at high temperatures, can be readily secured at normal temperatures by rapidly cooling the Zr-V melt, due to the small difference in the relative stabilities of the C15 and C14 phases [26]. As an annealing step was included in this work in order to exclude metastable phases, such as the hexagonal polymorph, only the crystallographic features of the cubic phase will be discussed herein.

The crystalline structure of the as-synthesised and annealed ZrV_2 alloy (see Section 4.2 for synthetic details) was examined *via* synchrotron X-ray diffraction on the I11 beamline at the Diamond Light Source – a full description of the instrument and the experimental parameters can be found in Section 2.1.2.1. The collected synchrotron data were analysed using the Rietveld method described in Section 2.1.4; an R_{wP} of 5.728 was obtained for a fit containing the C15 Laves phase structure of ZrV_2 as the major phase, along with several impurities. Three impurity phases were successfully fitted to the diffraction data: the C14 polymorph of ZrV_2, the vanadium starting material with dissolved zirconium, Zr_xV_{1-x} ($x = 0.05$), and an oxygen-stabilised ternary phase $Zr_3V_3O_x$. The observed diffraction pattern and calculated fit are shown in Figure 4.1, along with the relative weight percent of each phase.

In the refinement process of the C15 ZrV_2 structure, the metal atoms were constrained to the $8a$ and $16d$ sites of the $Fd\bar{3}m$ space group as in the reported structure [38]; as there were no free atomic coordinates due to the site symmetry,

only the global lattice parameters and the thermal parameter of each atom could be refined. The C14 ZrV_2 phase was fitted using the atomic coordinates of the ideal C14 Laves phase structure with space group $P6_3/mmc$ [11], which was not further refined, and only the lattice parameters and the thermal parameter of each atom were freely determined.

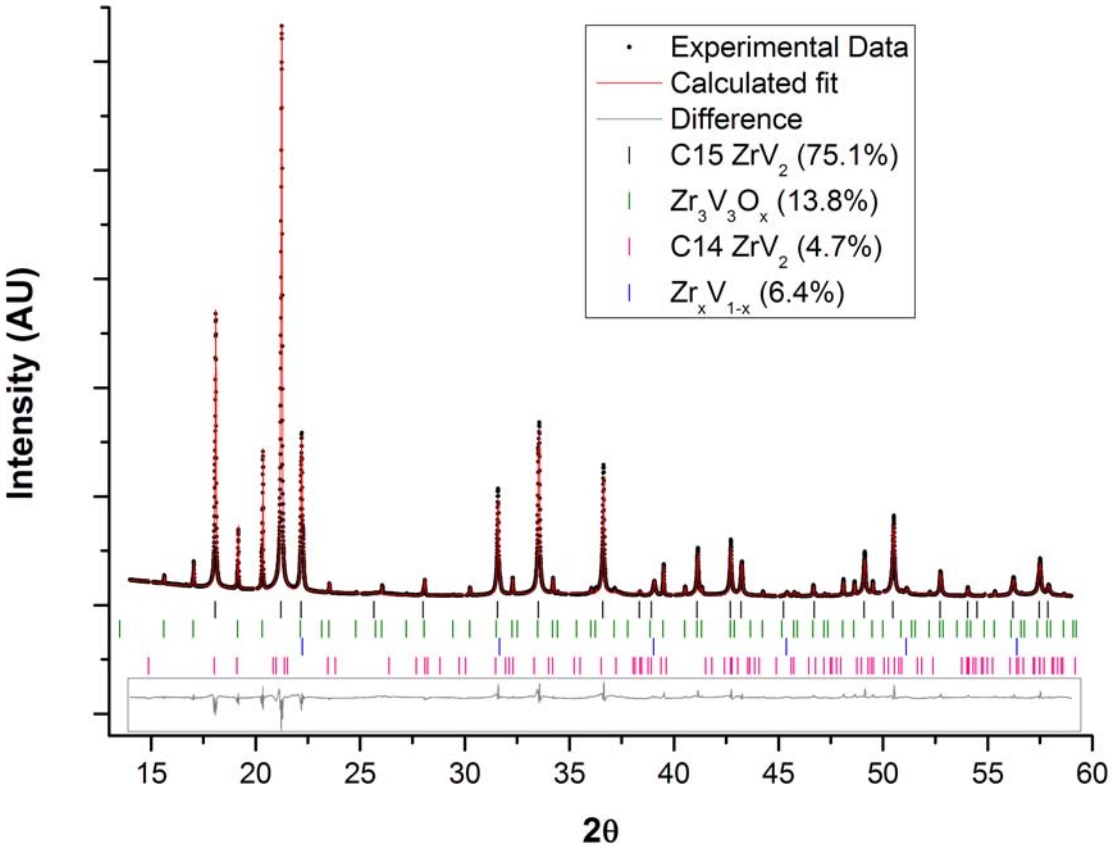

Figure 4.1: *Room temperature synchrotron diffraction pattern for the virgin alloy ZrV_2. Although the major phase is C15 ZrV_2, several impurities are present and the relative weight percent of each phase is indicated in the legend. The Bragg peak positions of all the fitted phases are shown by vertical tick marks. The difference plot between the experimental data (black points) and calculated fit (red solid line) is shown as a grey line enclosed in a box.* $R_{wp}(alloy) = 5.728$.

The Zr_xV_{1-x} impurity was constrained to the $Im\bar{3}m$ space group [99], with x set to 0.05, as the Zr-V binary phase diagram indicated this to be the upper limit of zirconium solubility in vanadium [26]. Atomic positions of Zr and V

in this phase were constrained by symmetry, so only the lattice parameters and one thermal parameter (assumed to be equal for both atoms) were refined. The ternary $Zr_3V_3O_x$ phase was fitted using the $Fd\bar{3}m$ space group, with atoms located on the $48f$, $32e$, $16d$, and $16c$ sites as in the reported structure [100]; those atomic coordinates not limited by the site symmetry were freely refined. The occupancy of the oxygen atom was also refined without restriction, as were the lattice parameters and the thermal parameter of each atom.

In addition to the structural parameters of these phases, the scale factors and weight percent of each phase was also refined. Full structural parameters for the C15 ZrV_2 phase are reported in Table 4.1 (on page 206), as well, the structural parameters of $Zr_3V_3O_x$ are given in Table 4.2 (on page 207). The remaining impurity phases are suitably described simply by their refined lattice parameters: for Zr_xV_{1-x}, $a = 3.0300(1)$ Å, and for C14 ZrV_2, $a = 5.2764(7)$ Å, $c = 8.914(2)$ Å.

4.4 Synthesis of the ZrV_2 hydride and the dehydrided material

4.4.1 Hydriding ZrV_2

Hydrogen was added to annealed ZrV_2, using the hydriding apparatus described in Section 2.4.5, at a variety of temperatures and hydrogen pressures. Figure 4.2 illustrates the absorption of hydrogen against pressure in ZrV_2, at a temperature of 290°C and a constant hydrogen flow rate of 10 sccm. The reaction chamber was evacuated before this hydriding reaction began, yet even at 290°C, hydrogen absorption began immediately upon introduction of H_2 into the chamber, as the flat-line region at low pressure in Figure 4.2 demonstrates. The precise hydriding pressure at 290°C therefore could not be determined. Moreover, as this hydriding temperature represents the upper limits of the apparatus, and the hydrogen flow could not be reduced further, the hydriding pressure could not be accurately measured at any temperature for the ZrV_2- H system.

The ease with which ZrV_2 absorbs hydrogen is reflected in the literature, with Shaltiel *et al.* [20] noting a hydriding pressure for the intermetallic compound of less than 10^{-8} bar at 80°C. Pebler and Gulbransen [37] found that, when hydriding ZrV_2 at 286°C, equilibrium could not be established in a reasonable time below 10^{-6} bar, at which point the alloy had already absorbed 1.8 moles of hydrogen/f.u.; extending the pressure to 1.3 bar increased the hydrogen concentration to 3.0 moles of hydrogen/f.u. These results agree excellently with the hydrogen absorption behaviour observed herein for ZrV_2.

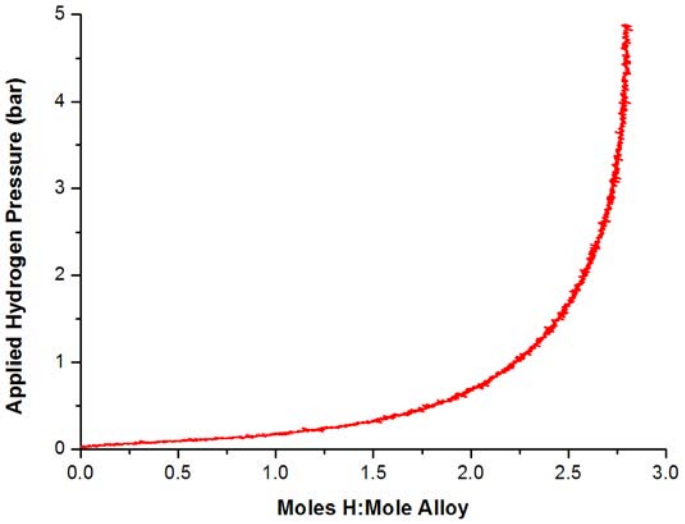

Figure 4.2: *A plot of the pressure-composition isotherm of ZrV_2 at 290°C, showing the amount of hydrogen absorped per mole of alloy against the applied hydrogen pressure. The experiment began with the hydrogen-free alloy under vacuum pressure. Hydrogen gas was then added at a rate of 10 sccm and pressure in the sealed reaction chamber increased until line pressure (5 bar) was reached, at which point 2.8 moles of hydrogen per mole of alloy had been absorbed, corresponding to a composition of $ZrV_2H_{2.8}$.*

4.4.2 Cycling and the Dehydriding Reaction

The apparatus described in Section 2.4.5 was also used to remove hydrogen from the ZrV_2- H system; Figure 4.3 shows a sample dehydriding plot for this reaction. If it is assumed that all of the weight lost over the course of the dehydriding reaction is due to hydrogen gas released from the hydrogen, a concentration of 2.8 moles of hydrogen per mole of ZrV_2 is obtained.

It is apparent from Figure 4.3 that a small amount of hydrogen desorption begins almost immediately, with the rate steadily increasing once 75°C has been

surpassed. However, as the temperature was raised to 350°C, the hydrogen desorption continued. This temperature represents the upper limit of the hydriding apparatus and not necessarily the point of full dehydriding of the ZrV_2H_x phase; thus, to ensure full hydrogen removal, this dehydrided sample was heated up to 650°C on a high vacuum line for one hour. Careful monitoring of the pressure changes revealed a small degree of gas desorption that could not be quantitatively measured on this vacuum line, nevertheless confirming that the dehydriding reaction up to 350°C, outlined in Figure 4.3, was itself quite near to completion.

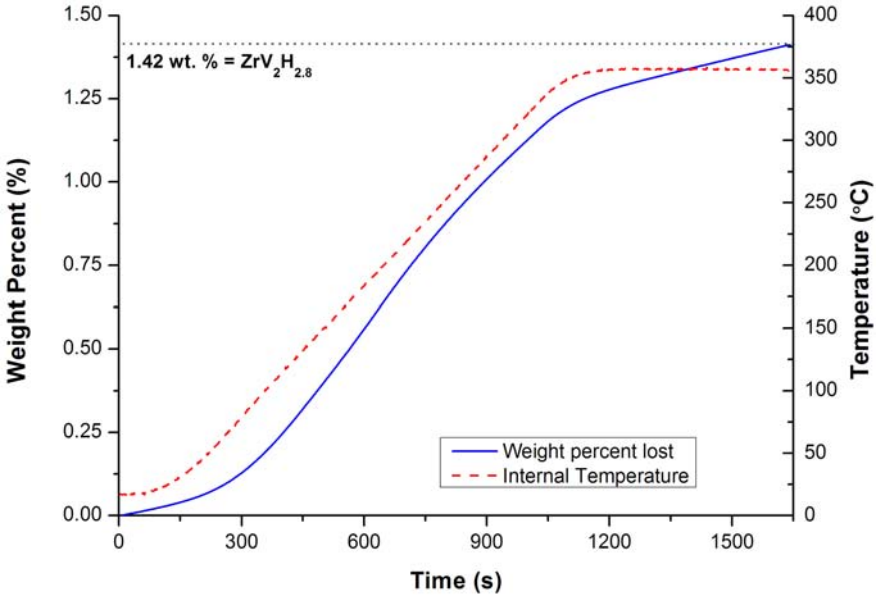

Figure 4.3: *A sample dehydriding trace for the ZrV_2 hydride against time, showing internal temperature (red dashed line) and weight percent lost from the sample (solid blue line). The dashed black line indicates the expected amount of hydrogen to be lost for a total hydrogen concentration of $ZrV_2H_{2.8}$.*

These experimental observations of hydrogen removal from $ZrV_2H_{2.8}$ agree with the thermal desorption spectra series collected by Stern *et al.* [101]. They noted that hydrogen desorption from ZrV_2H_x began at approximately 50°C, reaching a peak at 280°C, 330°C and 720°C and then tailing off in intensity, with a small amount of hydrogen desorption continuing until 900°C. The structure of the hydrogen desorption spectra was ascribed to variation in binding energy across the

differing sites of hydrogen absorption in ZrV_2- H [101]. The lower temperature desorption peaks observed by Stern *et al.* [101] concur with the data presented in Figure 4.3; however, the desorption peak at 720°C was beyond the limits of the apparatus used in this work. The temperature discrepancies between the published work, suggesting temperatures up to 900°C are needed to achieve total dehydriding, and those observed in this work may be due to an equilibration effect: Stern *et al.* [101] collected their dehydriding spectra in just 800 seconds, whilst the range up to 350°C was explored herein over twice that time period, and was followed by an hour-long vacuum heating at 650°C.

Several hydriding and dehydriding cycles had to be carried out before the full capacity of the ZrV_2 alloy was realised: repeated experimentation found this ranged between six and eight cycles. Figure 4.4 illustrates the increase in hydrogen capacity with the number of cycles carried out for the ZrV_2- H system. After six hydrogen absorption/desorption cycles, the alloy reversibly absorbs 2.8 hydrogen atoms per ZrV_2 formula unit; as no increase in capacity is observed upon further cycling, this can be taken as the total hydrogen capacity under the equipment limitations. The pressure limitations of the hydriding apparatus restricted the hydrogen capacity that could be observed in ZrV_2- H: it should be noted that the published studies on $ZrV_2D_{4.5}$ and $ZrV_2H_{4.7}$ were so obtained under pressures of 30 bar of deuterium [40] and 32 bar of hydrogen [101], respectively. If higher hydrogen pressure could have been accessed in this work, then it is likely that absorption of upwards of 5 hydrogen atoms per formula unit would have been observed.

The design of the hydriding apparatus used herein, whilst sufficient to accomplish the task of hydriding and dehydriding ZrV_2, could not be used to collect suitable thermodynamic data on this intermetallic hydride as the limits on pressure and temperature prevented the collection of hydriding pressures over a range temperatures. The hydriding enthalpy and entropy therefore cannot be presented for the ZrV_2- H system. However, as the absorption of hydrogen occurs *via* dis-

solution into the lattice and no distinct hydride phase forms, it is expected that a true $P(x)$ plateau will not form, preventing the assembly of a van't Hoff construction (and extraction of ΔH_H and ΔS_H) under any experimental conditions. Support for this comes from the early work of Pebler and Gulbransen [37], where it was found that no hydriding plateau was observed for the ZrV_2- H system, even up to 798°C.

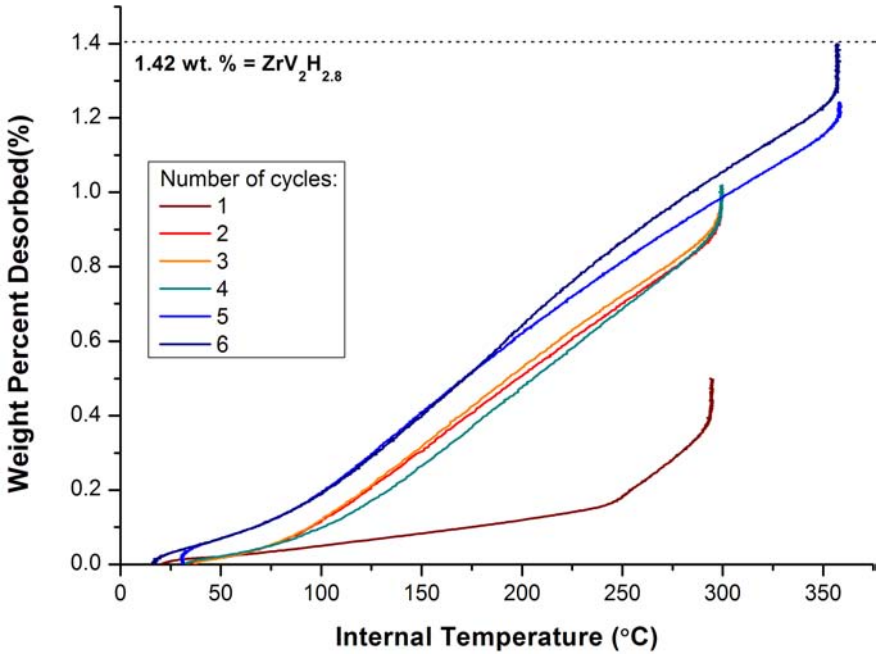

Figure 4.4: *A plot of the effect of cycling on $ZrV_2 - H$. The percentage of weight lost from the hydrided sample is shown on the y-axis, and the internal temperature of the reaction chamber is on the x-axis. Desorption traces, all carried out under identical conditions, are shown starting from the hydrided virgin alloy (1^{st} cycle) until the point of full decrepitation (6^{th} cycle). The dashed line indicates the expected amount of hydrogen to be lost for a total hydrogen concentration of $ZrV_2H_{2.8}$.*

4.5 Crystallographic Features of the ZrV_2- H hydrides

4.5.1 Published Structures of ZrV_2H_x

Hydrogen is accommodated in the $Fd\bar{3}m$ unit cell of the parent C15 intermetallic ZrV_2 *via* an isotropic lattice expansion with no change in symmetry; structural parameters for $ZrV_2D_{4.5}$ are given in Table 1.2. Three types of tetrahedral interstices

exist in this structure: one surrounded by two zirconium and two vanadium atoms (*2A2B*), one with one zirconium vertex and three vanadium vertices (*1A3B*), and one surrounded by four vanadium atoms (*4B*). An atomic diagram of the C15 unit cell, showing an example of each of these interstices, is shown in Figure 4.5.

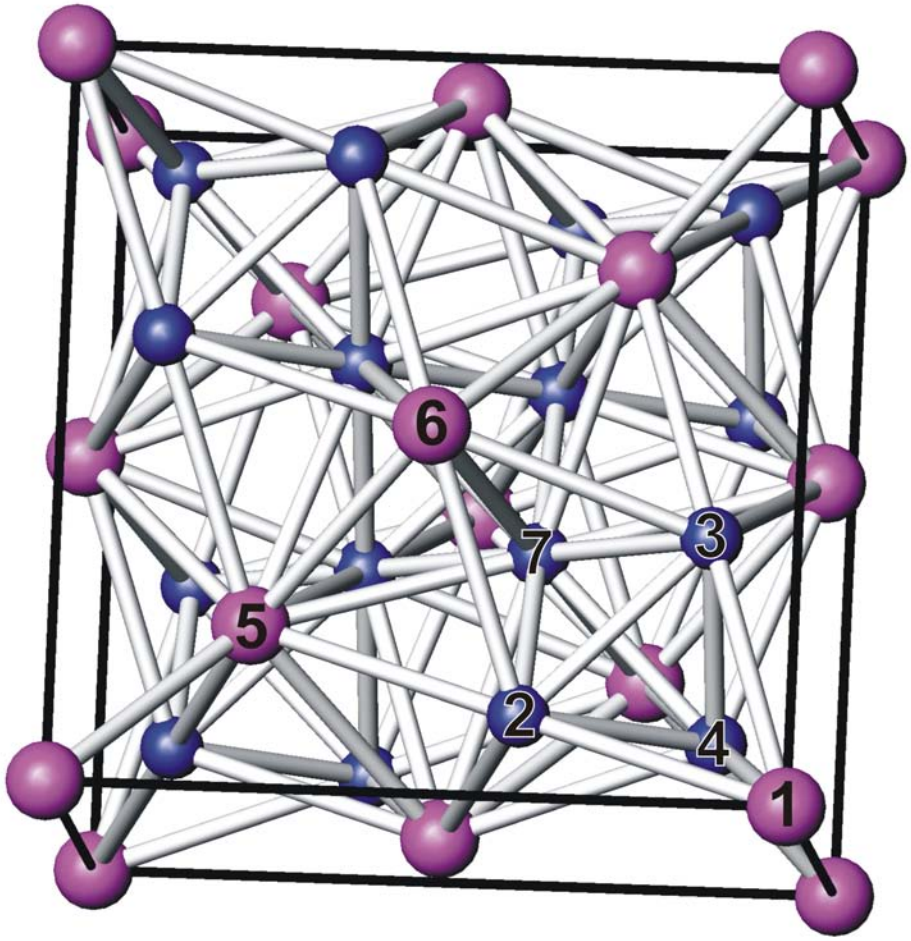

Figure 4.5: *A diagram of the C15 cubic structure of ZrV_2, showing the arrangement of the zirconium atoms (pink spheres) and vanadium atoms (dark blue spheres) within the unit cell (heavy black lines). Nearest-neighbour atoms are connected by thin white cylinders as a guide to the eye. The atoms labelled 1, 2, 3 and 4 form a 1A3B type tetrahedral interstice, as do the atoms labelled 2, 3, 6 and 7; whilst the atoms 2, 5, 6 and 7 form a 2A2B interstice. An example of a 4B type interstice is shown by the tetrahedron formed by atoms 2, 3, 4 and 7.*

Choice of interstice for hydrogen occupation is dependent on both geometric factors (*e.g.* size of interstitial hole) and chemical factors (*e.g.* strength of

hydrogen-metal interaction at each vertex) [40]. On this basis, the *2A2B* site has the lowest binding energy in ZrV_2H_x and is exclusively occupied up to $x = 2.5$; beyond this hydrogen concentration, the *1A3B* site, which is only slightly higher in energy, is successively filled [14, 40]. The $4B$ site is never occupied, even up to $x = 6$, likely as a result of small size of this interstice [41]. Didisheim *et al.* [40] have noted that the distribution of the deuterium atoms amongst the occupied sites is not random, and shows short-range correlations that form an infinite network of diffusion paths; the relative occupancies of the sites is then decided by the choice of diffusion paths and number of nearest neighbours.

A crystallographic study of the low-temperature hydride superstructures has been thoroughly explored by a number of previous researchers [41–43]. Nevertheless, a brief discussion of those superstructures which are stable at or near to room temperature is merited. Note that for ease of reference to the published work the superstructures discussed herein are labelled according to their propagation vector k, where k corresponds to high symmetry points of the reciprocal lattice of the disorder structure [43]; the theory of such superstructures was introduced earlier in Section 2.1.1.1. The most stable superstructures of the ZrV_2H_x system are: $x = 2$, described by the propagation vector $k = (\frac{1}{2}, \frac{1}{2}, \frac{1}{2})$ [42], $x = 3$ with propagation vector $k = (0, 0, 1)$ [43], and $x = 4$ with propagation vector $k = 0$ [43]. The superstructures with $k = (\frac{1}{2}, \frac{1}{2}, \frac{1}{2})$ and $k = 0$ exist above 300 K and have wide homogeneity ranges in their hydrogen contents, whilst the $k = (0, 0, 1)$ superstructure has a narrow hydrogen range and disappears above 200 K.

The superstructure $ZrV_2H_{2+\delta}$, with $-0.8 < \delta < 0.2$, crystallises in a monoclinic cell that is displaced with respect to the disordered, C15 cubic cell *via*

$$\begin{pmatrix} a \\ b \\ c \end{pmatrix}_{monoclinic} = \begin{pmatrix} \frac{1}{2} & -1 & \frac{1}{2} \\ \frac{1}{2} & 0 & -\frac{1}{2} \\ \frac{1}{2} & 1 & \frac{1}{2} \end{pmatrix} \begin{pmatrix} a \\ b \\ c \end{pmatrix}_{cubic} \tag{4.1}$$

where the hydrogen atoms in this phase are ordered over the *2A2B* interstices, of which six non-equivalent sites exist due to the $I4_1/amd$ unit cell symmetry [42].

These sites are then successively filled on the basis of Westlake's criteria regarding the maximum $H-H$ distance of 2.1 Å [15]. This superstructure is stable in the range $75 < T < 300$ K, and most likely exists down to lower temperatures as well [102].

The tetragonal $k = 0$ superstructure, ZrV_2H_4, crystallises in the $I4_1/a$ space group, with a unit cell that is oriented with respect to the C15 cell as follows

$$\begin{pmatrix} a \\ b \\ c \end{pmatrix}_{tetragonal} = \begin{pmatrix} \frac{1}{2} & \frac{1}{2} & 0 \\ -\frac{1}{2} & \frac{1}{2} & 0 \\ 0 & 0 & 1 \end{pmatrix} \begin{pmatrix} a \\ b \\ c \end{pmatrix}_{cubic} \tag{4.2}$$

The hydrogen atoms are dispersed over the *2A2B* interstices, where the occupancies vary as a function of temperature [103]; however, as compared to the disordered cubic structure, the hydrogens are displaced by ~ 0.05 Å, corresponding to a repulsion of nearest-neighbour hydrogen atoms [43]. This superstructure is stable until 340 K, although full ordering of the phase does not occur until 230 K [103].

Finally, the monoclinic hydrogen superstructure ZrV_2H_3, with $k = (0, 0, 1)$, is related to the C15 cubic cell through the transformation

$$\begin{pmatrix} a \\ b \\ c \end{pmatrix}_{monoclinic} = \begin{pmatrix} \frac{1}{2} & \frac{1}{2} & 0 \\ -\frac{1}{2} & \frac{1}{2} & 0 \\ -\frac{1}{2} & -\frac{1}{2} & 1 \end{pmatrix} \begin{pmatrix} a \\ b \\ c \end{pmatrix}_{cubic} \tag{4.3}$$

where the hydrogen atoms are located on the *2A2B* interstices in the $P2_1/c$ unit cell, and are not relatively displaced from their disordered positions in the C15 structure [43]. Nominally, this structure is not stable above 200 K; however, there exists an incommensurate phase between $k = 0$ and $k = (0, 0, 1)$, and at hydrogen concentrations intermediate between these two superstructures, fragments of both may be seen to exist near room temperature [43].

4.5.2 Structural study on the hydride of ZrV_2- H system

The crystalline structure of the hydrided ZrV_2- H material (which was taken from a sample that had been cycled 13 times – see Section 4.4.1 for further synthetic details) was examined on the I11 beamline at Diamond, under the same experimental parameters as the crystallographic study of the ZrV_2 alloy described in Section 4.3. The collected data were analysed using the Rietveld method described in Section 2.1.4; an R_{wP} of 9.741 was obtained for a multi-phase fit consisting of two expanded C15 hydrides with differing hydrogen concentrations, the $k = 0$ and the $k = (0, 0, 1)$ hydride superstructures, a hydrided version of the same $Zr_3V_3O_x$ phase found in the parent alloy, and minor fractions of Zr_xV_{1-x} ($x = 0.05$), and the hydrogen-free C14 polymorph of ZrV_2. The collected synchrotron diffraction pattern of the hydrided ZrV_2 material, the calculated fit to these data, and the relative fractions of each of these phases are shown in Figure 4.6.

During the refinement of the two C15 ZrV_2H_x structures, the metal atoms were constrained to the $8a$ and $16d$ sites of the $Fd\bar{3}m$ space group as in the reported structure [40]; as there were no free atomic coordinates due to the site symmetry, only the global lattice parameters and the thermal parameter of each atom could be refined. Atomic positions and occupancies of the hydrogen atoms could not be determined (see Section 2.1.2 for a discussion of the difficulty in determining hydrogen locations using X-ray diffraction) but the hydrogen concentration in the phase was determined using its lattice parameters: as a solid solution, x in ZrV_2H_x is a linear function of the cubic a parameter [37]. Once the amount of hydrogen had been thus determined, the hydrogen positions and occupancies were assumed from published deuteride phases of similar concentrations [40, 104]. The full structural parameters of these two hydrides are given in Table 4.1.

It should be noted that the simultaneous presence of two or more cubic ZrV_2H_x disordered phases of varying x is to be expected in the unsaturated ZrV_2- H system, as noted previously by Däumer *et al.* [44]. Despite a 72 hour anneal under hydrogen gas in an attempt to secure a single phase sample, these workers

observed the simultaneous coexistence of two ZrV_2H_x phases with differing x in their hydrided ZrV_2 samples.

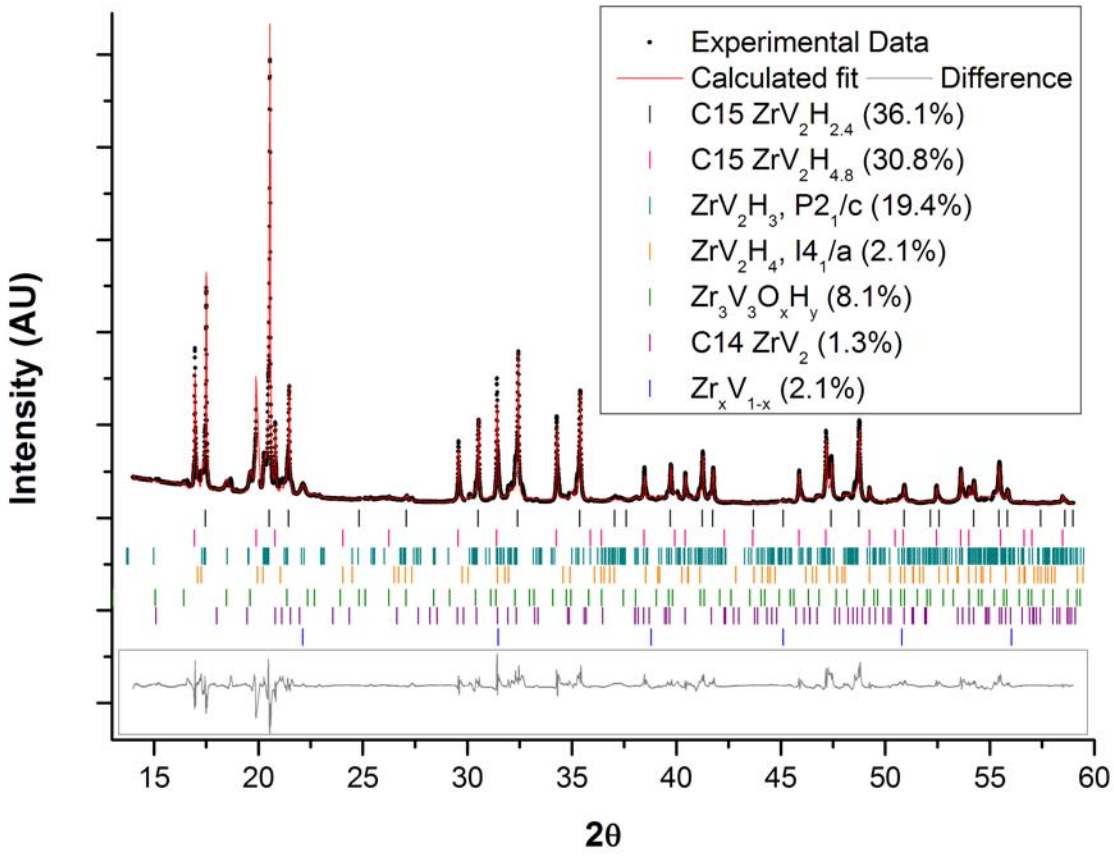

Figure 4.6: *Room temperature synchrotron diffraction pattern for the hydrided $ZrV_2 - H$. Although the major phases are the C15 hydrides $ZrV_2H_{2.4}$ and $ZrV_2H_{4.8}$, several impurities, as well as two hydride superstructures, are present, and the relative weight percent of each phase is indicated in the legend. The Bragg peak positions of all the fitted phases are shown by vertical tick marks. The difference plot between the experimental data (black points) and calculated fit (red solid line) is shown as a grey line enclosed in a box.* $R_{wP} = 9.741$.

The diffraction data of the ZrV_2- H hydride were originally modelled with all three of the hydrogen superstructure phases known to exist at or near room temperature; *viz.* the $k = (\frac{1}{2}, \frac{1}{2}, \frac{1}{2})$, $k = 0$, and $k = (0, 0, 1)$ superstructures. The atomic positions and occupancies were taken from the published structures [42, 43], and only the lattice parameters and phase fractions were determined. No fraction of the $k = (\frac{1}{2}, \frac{1}{2}, \frac{1}{2})$ superstructure could be reliably refined; however, both the $k = 0$ – tetragonal ZrV_2H_4 – and the $k = (0, 0, 1)$ – monoclinic ZrV_2H_3 –

superstructures were present in the diffraction data. The metal atoms of both these phases were completely restricted by the site symmetry, and the hydrogen positions could not be determined *via* X-ray diffraction, so only the lattice parameters of the phases and the thermal parameters of each atom were freely determined. The lattice parameters of the superstructure phases were refined as:

- ZrV_2H_3, propagation vector $k = (0, 0, 1)$: space group $P2_1/c$, lattice parameters $a = 5.4530(5)$ Å, $b = 5.4462(5)$ Å, $c = 9.5474(7)$ Å, $\beta = 125.273(4)°$.

- ZrV_2H_4, propagation vector $k = 0$: space group $I4_1/a$, lattice parameters $a = 5.5096(9)$ Å, $c = 7.934(3)$ Å.

The lattice parameters of these superstructures are in close agreement with the previously published structures [43]. Irodova *et al.* [43] note that in the regime of a hydrogen concentration and/or temperature intermediate between the $k = 0$ and $k = (0, 0, 1)$ end member phases, fragments of both superstructures coexist, with strong broadening of the diffraction peaks. Significant lattice broadening and distortion was noted in the data herein for the reflections ascribed to $k = 0$ and $k = (0, 0, 1)$ superstructures, as evidenced by the imperfect fit of the calculated model around these peaks in Figure 4.6. This observed peak broadening, combined with the presence of both superstructure phases, supports the theory proposed by Irodova *et al.* [43] that the end member $k = 0$ and $k = (0, 0, 1)$ superstructures coexist in regions of intermediate hydrogen concentration and/or temperature.

The C14 ZrV_2 phase was fitted using the atomic coordinates of the ideal C14 Laves phase structure of space group $P6_3/mmc$ [11], which was not further refined, and the lattice parameters were assumed to be equal to those of the C14 ZrV_2 phase observed in the alloy. For the Zr_xV_{1-x} impurity ($x = 0.05$), with space group $Im\bar{3}m$ [99], the atomic coordinates were constrained by site symmetry and the lattice parameters were assumed to be equal to those of the Zr_xV_{1-x} phase in the alloy material. The ternary $Zr_3V_3O_xH_y$ phase was fitted using the $Fd\bar{3}m$ space group, with metal and oxygen atoms located on the $48f$, $32e$, $16d$, and $16c$ sites

as in the reported structure [100]; those atomic coordinates not limited by the site symmetry were freely refined. The occupancy of the oxygen atom was also refined without restriction, as were the lattice parameters and the thermal parameters of each atom. As the hydrogen positions and occupancies could not be determined, the total hydrogen concentration was first determined *via* examination of the cubic lattice parameter (in a similar method as to the cubic ZrV_2H_x phase) and then hydrogen positions and occupancies assumed from a published deuteride phase of similar concentration [100]. The full structural parameters of this oxygen-stabilised hydride phase are given in Table 4.2.

Parameter	*ZrV_2 (alloy)*	*ZrV_2 (dehydride)*	*$ZrV_2H_{2.4}$*	*$ZrV_2H_{4.8}$*
Instrument	Diamond	Diamond	Diamond	Diamond
Wavelength, λ (Å)	0.82656	0.82656	0.82656	0.82656
a (Å)	7.4448(2)	7.4445(1)	7.6944(1)	7.9363(1)
V (Å^3)	412.62(1)	412.59(1)	455.54(2)	499.86(3)
R_{wP}	5.728	5.831	9.741	9.741
Zr1, 8a site $(0,0,0)$	-	-	-	-
B_{eq} (Å^2)	0.14(1)	0.18(2)	0.3	0.11(4)
V1, 16d site $(\frac{5}{8},\frac{5}{8},\frac{5}{8})$	-	-	-	-
B_{eq} (Å^2)	0.22(2)	0.29(2)	0.3	0.11(4)

Table 4.1: *Structural parameters for the alloy ZrV_2, its hydrides $ZrV_2H_{2.4}$ and $ZrV_2H_{4.8}$, and the corresponding dehydrided compound. All structures crystallised in the $Fd\bar{3}m$ space group, and were determined from room temperature synchrotron diffraction patterns.*

The relative phase fraction of impurities in the hydrided material has increased only marginally, as compared to the X-ray diffraction data of the parent alloy

shown in Figure 4.1; this likely a result of minor atmospheric exposures that may have occurred whilst transferring the sample between the hydriding apparatus and the glovebox, or of gas impurities in the atmosphere of the glovebox itself.

Parameter	$Zr_3V_3O_x$	$Zr_3V_3O_xH_y$
a (Å)	12.1746(3)	12.611(1)
V (Å^3)	1804.53(5)	2005.8(2)
Zr1, 48f site $(x, 0, 0)$	0.1909(2)	0.185(1)
B_{eq} (Å^2)	0.21(3)	0.96(6)
V1, 32e site (x, x, x)	0.8285(2)	0.825(1)
B_{eq} (Å^2)	0.15(9)	0.40(9)
V2, 16d site $(\frac{5}{8}, \frac{5}{8}, \frac{5}{8})$	-	-
B_{eq} (Å^2)	0.14(9)	1.4(3)
O1, 16c site $(\frac{1}{8}, \frac{1}{8}, \frac{1}{8})$, occ.	0.99(6)	0.99(3)
B_{eq} (Å^2)	0.66(9)	0.5

Table 4.2: *Structural parameters for the oxygen-stabilised ternary phase, $Zr_3V_3O_x$, and its hydride, $Zr_3V_3O_xH_y$. Both structures crystallised in the $Fd\overline{3}m$ phase, and were determined from the room temperature synchrotron diffraction patterns of the ZrV_2 alloy and hydrided ZrV_2H_x, respectively.*

Comparison of diffraction data of the hydrided material against the ZrV_2 alloy reveals that the hydriding process has not brought about significant peak broadening in the cubic ZrV_2H_x phases, excepting in the case of the superstructures, as discussed earlier. Comparison can again be made to the $ZrMn_2-$ H system, where the hydrogen cycling of the material induced a large increase in peak width, which could be ascribed to a size effect (see Section 3.8.3 for details). A peak profile analysis could not be successfully carried out on either major ZrV_2H_x phase,

leading to the conclusion that no significant decrepitation occurs upon hydriding in the ZrV_2- H system. Due to the isotropic nature of the volume expansion that occurs upon hydriding, the creation of significant strain concomitant to the hydriding process is not expected in this material, thus removing a major cause of the decrepitation phenomena.

The overall hydrogen concentration of the hydrided ZrV_2 sample was determined by summing the individual hydrogen concentrations of each of the four ZrV_2H_x structures present, and then dividing by the appropriate phase fraction. This method revealed that the net hydrogen content of the ZrV_2H_x material was $x = 2.8$, a value that is in excellent agreement with the experimental measurements of hydrogen desorption in the ZrV_2- H system which were presented in Section 4.4.2.

4.6 Crystallographic Features of the cycled, dehydrided ZrV_2

The crystalline structure of the dehydrided ZrV_2 compound was also examined on the I11 beamline at Diamond. Section 4.4.2 details the preparation of this material; it should be noted that the sample used for this crystallographic study was passed through 14 hydriding/dehydriding cycles, and then was subjected to a secondary dehydriding in vacuo at 650°C. The collected synchrotron data were analysed using the Rietveld method as per the ZrV_2 alloy discussed in Section 4.3, following a nearly identical refinement procedure: the data were fitted with a majority phase of C15 ZrV_2, the three impurities previously discussed (C14 ZrV_2, Zr_xV_{1-x}, and $Zr_3V_3O_x$) and one additional impurity phase, $\alpha-$Zr, which was not found in the original alloy diffraction data. No amount of any ZrV_2H_x phase could be reliably refined, suggesting that the dehydriding reaction had gone to completion.

The atom positions and parameter refinement of the first four phases follow exactly from that described previously for the alloy. The $\alpha-$Zr phase was fitted

using the $P6_3/mmc$ room temperature structure described by Swanson *et al.* [89]; although the position of the zirconium atom is restricted by symmetry, the lattice parameters of the phase and the atomic thermal parameter were freely refined. The scale factors and weight percent of each phase in the dehydrided material were also determined. Figure 4.7 gives the observed diffraction pattern and the calculated fit for dehydrided ZrV_2, along with the relative phase fraction of each of the five phases in the data.

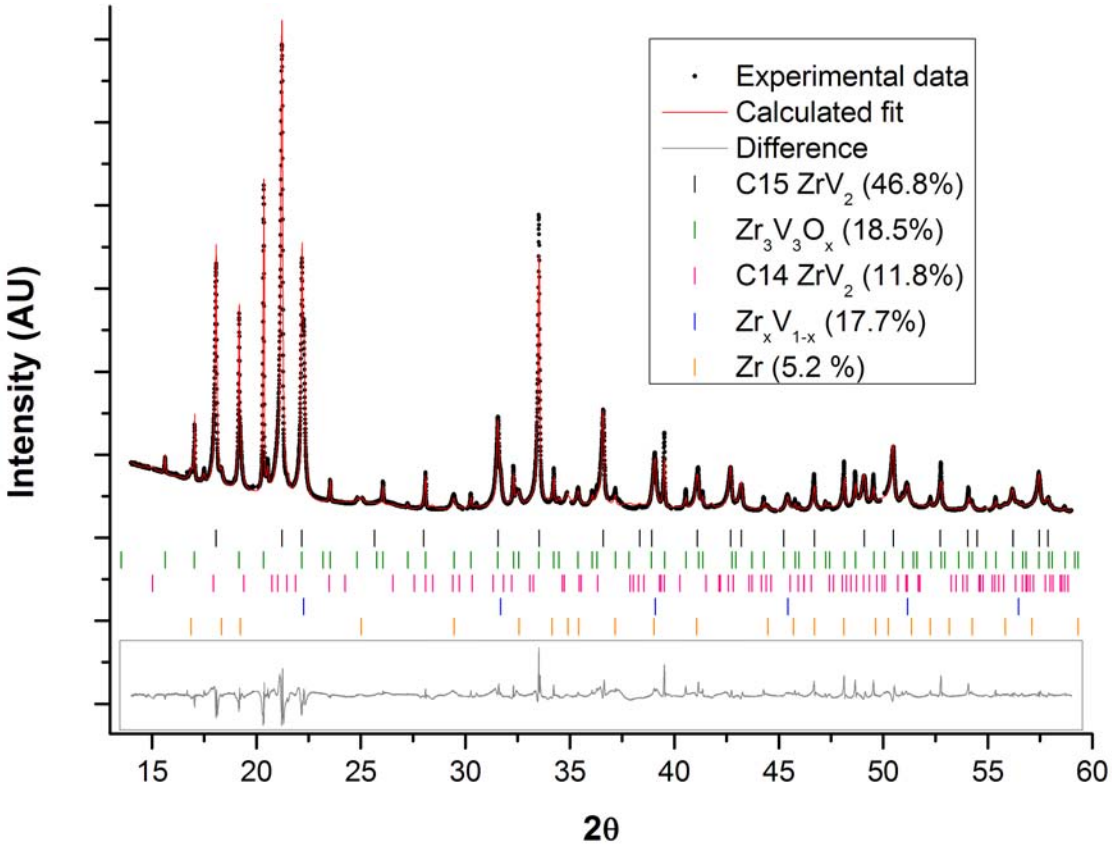

Figure 4.7: *Room temperature synchrotron diffraction pattern for the cycled, dehydrided ZrV_2. Although the major phase is C15 ZrV_2, several impurities are present and the relative weight percent of each phase is indicated in the legend. The Bragg peak positions of all the fitted phases are shown by vertical tick marks. The difference plot between the experimental data (black points) and calculated fit (red solid line) is shown as a grey line enclosed in a box.* $R_{wP} = 5.831$.

The structural parameters of the primary ZrV_2 C15 phase from the dehydrided

material are given in Table 4.1 and, although the parameters of the $Zr_3V_3O_x$ structure determined from this synchrotron pattern are not shown, they do not deviate significantly from those given in Table 4.2 for the same phase in the alloy diffraction data. The refined lattice parameters of the remaining impurity phases are: Zr_xV_{1-x}, $a = 3.0263(7)$ Å, C14 ZrV_2, $a = 5.3016(9)$ Å and $c = 8.709(2)$ Å, and $\alpha-$Zr, $a = 3.2513(2)$ Å and $c = 5.1875(7)$ Å.

The ready formation of impurities in the Zr-V system has been previously observed by a number of workers: Moncton [38] noted the presence of 'extra lines' in the diffraction pattern of the ZrV_2 alloy that could not be explained, Didisheim *et al.* [40] found a few percent of $Zr_3V_3N_x$ in their diffraction data, Keiber *et al.* [105] identified a 3% impurity of $Zr_3V_3O_x$ *via* X-ray diffraction, and Bogdanova *et al.* [41] recorded that 7% of their nominally ZrV_2 alloy was actually Zr_xV_{1-x}. It is worthwhile to mention that these impurities were discovered in ZrV_2 compounds that had been thoroughly annealed, a process which might normally be expected to remove these secondary phases. These data suggests that the presence of phases additional to the desired C15 structure in the ZrV_2 compounds studied herein, whilst slightly detrimental to a characterisation study, may be difficult to avoid entirely.

There is some discrepancy in the literature concerning the oxygen-stabilised ternary phase, $Zr_3V_3O_x$. Whilst some workers [105] have reported the presence of this structure as an admixture to the normal C15 ZrV_2 phase, others [40] have instead noted the presence a nitrogen-stabilised ternary phase, $Zr_3V_3N_x$, of identical structure. Unfortunately, the use of X-ray diffraction did not allow $Zr_3V_3O_x$ to be reliably distinguished from $Zr_3V_3N_x$: attempts to refine the diffraction data with either phase resulted in no significant change in R_{wP}. For consistency, the phase will be herein described as $Zr_3V_3O_x$ despite the O/N ambiguity. Regardless of nature of the stabilising third atom in this structure, the method of its formation remains unclear, as the ZrV_2 compound was handled under argon atmosphere at all times. It is possible that minute exposures to atmospheric air may have oc-

curred, particularly during transfer between equipment, which may be the origin of this $Zr_3V_3O_x$ impurity.

Comparison of the diffraction data of the alloy and the dehydrided ZrV_2 in Figures 4.1 and 4.7 reveals that the cycling process has contributed significantly to the concentration of impurities in the ZrV_2 material. The increase in the phase fraction of $Zr_3V_3O_x$ may be simply accredited to increased exposure to oxygen leaks in the apparatus over time, but the cause of the growth in the other phases remains unclear. It is possible that the increase in weight percent of Zr_xV_{1-x}, and the emergence of $\alpha-$ Zr, may be due to the partial disproportionation of ZrV_2. The rise in the phase fraction of the C14 polymorph may be a result of the high temperatures used to dehydride the ZrV_2- H material; as the hexagonal phase may be readily obtained at room temperature *via* fast cooling from temperatures where it is thermodynamically stable [38, 39]. Evidence that high temperatures caused the disproportionation of ZrV_2 is found in the diffraction data of the hydride in Figure 4.6: this material underwent no disproportionation and was similarly subjected to a large number of hydriding-dehydriding cycles, but did not undergo a high-temperature 650°C vacuum anneal.

A qualitative comparison of the diffraction data of the virgin alloy and dehydrided ZrV_2 furthermore suggests that, unlike the $ZrMn_2-$ H system, this material does not undergo significant decrepitation upon repeated hydrogen cycling. A full peak profile analysis (as described in Section 2.1.4) on the ZrV_2 phase in the dehydrided material could not be successfully completed, as the size parameters consistently refined to the maximum value allowed by the calculation; this is in accordance with a visual analysis of the dehydrided powder, in which the grain sizes appeared no different from those of the original alloy. Although full microstructural characterisation to determine the exact particle size was beyond the scope of this work, Stern *et al.* [101] have previously shown that the particles in a cycled, dehydrided ZrV_2 sample range from $10 - 100$ μm in diameter, which agrees with these observations.

Finally, the lattice parameters of the major C15 ZrV_2 phase in the alloy and the dehydride material are, within error, identical. This indicates that the ZrV_2 phase in the dehydrided material contains no hydrogen, as the presence of interstitial hydrogen atoms dissolved in the intermetallic compounds would be manifested in a lattice expansion [37]. It is therefore clear that the dehydriding reaction described in Section 4.4.2 has gone to completion, successfully removing all hydrogen from the material. The revelation that dehydriding can be accomplished using a maximum temperature of 650°C is in contrast to the study of Stern *et al.* [101], which suggested that temperatures of upwards of 900°C was required to dehydride ZrV_2H_x.

The refined C15 structure of the ZrV_2 phase in the dehydrided and alloy materials agrees excellently with the previously published description of the cubic ZrV_2 phase, which is summarised in Section 1.2.2.

4.7 Magnetic and Superconducting Behaviour in the ZrV_2-H system

At room temperature, both ZrV_2 and its hydride ZrV_2H_x are simple Pauli paramagnets, with the susceptibility of the hydride being lower than that of the intermetallic compound [46]. At 300 K, the susceptibility of the intermetallic compound is 9.8×10^{-4} emu mol^{-1} Oe^{-1}, whilst the corresponding value for hydride with $x = 5.2$ is 7.8×10^{-4} emu mol^{-1} Oe^{-1} [46]. This reduction in χ stems from a depletion of the number of states at the Fermi level upon hydrogen absorption, $N(\epsilon_F)$, where the amount of hydrogen in the unit cell is proportional to the shift in susceptibility [45]. For hydrides with $x > 1.3$, the systems shows no long range order down to 2 K and continues to behave as a paramagnet [45]. However, the hydrogen-free material [36] and those ZrV_2H_x hydrides containing low amounts of hydrogen [44] act as superconductors below 8.8 K, and readily expel magnetic flux when cooled in a field to below this transition temperature.

In terms of its superconducting properties, ZrV_2 is a type II superconductor with $H_{c1} = 3.2$ kOe and $H_{c2} = 230$ kOe [44, 46]. Däumer *et al.* [44] studied the

low-concentration hydrides of $Zr_{0.5}Hf_{0.5}V_2H_x$ and found that, as x increased from 0 to 1.1, the superconducting T_c was reduced only slightly from the hydrogen-free value of 8.8 K; however, once the hydrogen concentration exceeded 1.1, the superconducting T_c became vanishing small (estimated to be less than 1.5 K). Geibel *et al.* [45], with a view to carrying out a similar test of the T_c dependence of x in ZrV_2H_x, synthesised a range of hydrides with hydrogen amounts ranging between 0 and 1.2 and measured a decrease in T_c with x. However, subsequent structural characterisation of these materials revealed that, below 260 K, they segregated into a mixture of ZrV_2 and $ZrV_2H_{1.3}$, with the pure $x = 1.3$ hydride showing no superconducting behaviour down to 2 K. These authors concluded that hydrogen absorption of any quantity lead to a destruction of the superconductivity, with the superficial observed decrease in T_c with x assigned simply to a reduction in the phase fraction of ZrV_2 in the mixed material.

4.7.1 Magnetic behaviour of ZrV_2 and $ZrV_2H_{2.8}$

The magnetic behaviour of the ZrV_2- H system was examined over the temperature range 2 to 300 K; the as-synthesised alloy, as well as the cycled hydride and the dehydrided material, were all analysed. Figure 4.8 shows the variation in molar susceptibility with temperature for the alloy and the hydride; whilst Figure 4.9 depicts the same data for the dehydrided material. The susceptibilities and relevant transition temperatures of these materials are summarised in Table 4.3, along with the values of the critical field for the superconducting samples.

The thermomagnetic analysis revealed that, above 8 K, the ZrV_2 alloy behaves mostly as a simple paramagnet, with no significant difference between the zero-field cooled and the field cooled data. A step in the susceptibility was observed below 125 K, corresponding with the point of the martensitic transition [45]; this drop in susceptibility has been previously shown to be related to the reduction in the density of states that accompanies the change in structure [106]. The room temperature susceptibility, as shown in Table 4.3, agrees excellently with the

published value of Fujii *et al.* [46]. At 8 K, the alloy undergoes a superconducting transition, as exhibited by the sudden exclusion of magnetic flux and the drop to negative susceptibility values, as if diamagnetic.

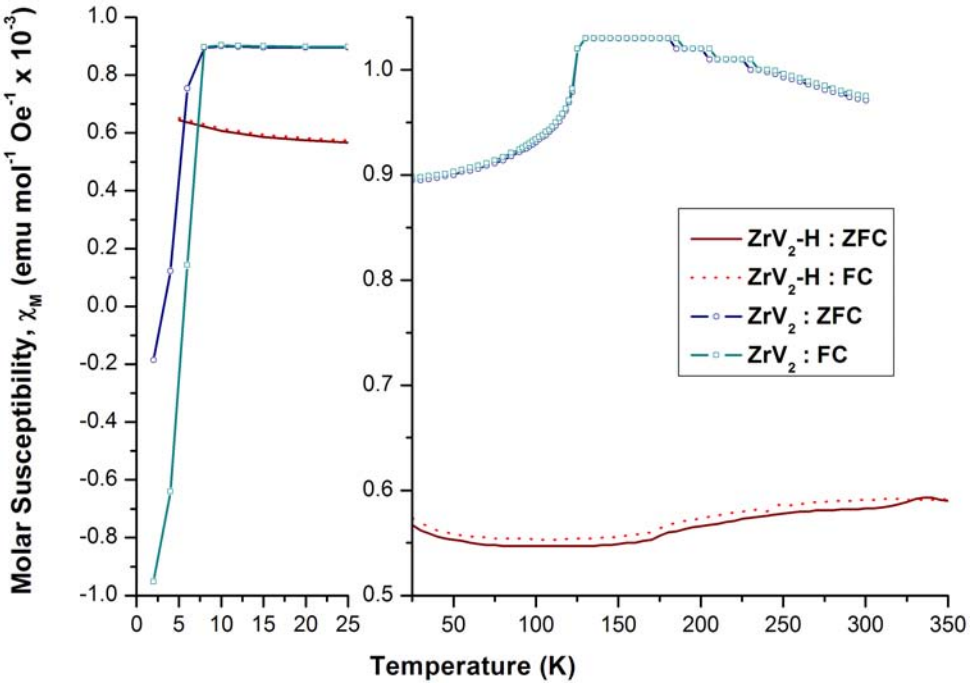

Figure 4.8: *Thermomagnetic analysis of the $ZrV_2 - H$ system from 2 K to 350 K, showing the magnetic behaviour of the alloy (blue lines) and the cycled hydride (red lines). Both samples were cooled to 2 K under two conditions: zero-field cooled (ZFC) and field cooled at 10000 Oe (FC). Under both regimes, the sample was then measured on warming under a field of 10000 Oe. Relative errors are smaller than data points.*

The dehydrided material was qualitatively very similar to the virgin alloy in terms of its magnetic behaviour. The martensitic step at 125 K was far less pronounced in this sample, and the susceptibility was observed to increase slightly as the superconducting transition was approached; nonetheless, the superconducting T_c was unchanged from the alloy. The differences between the dehydrided sample and the original alloy may be ascribed to the presence of impurities, as were noted in the crystallographic study in Section 3.7. These impurities act to dilute the cubic ZrV_2 phase, weakening the martensitic transition; additionally, the slight increase in χ above 40 K may be a paramagnetic contribution from one of the

impurity phases. A further result of the dilution of the cubic ZrV_2 phase is the decrease in χ_{300K} as compared to the parent alloy.

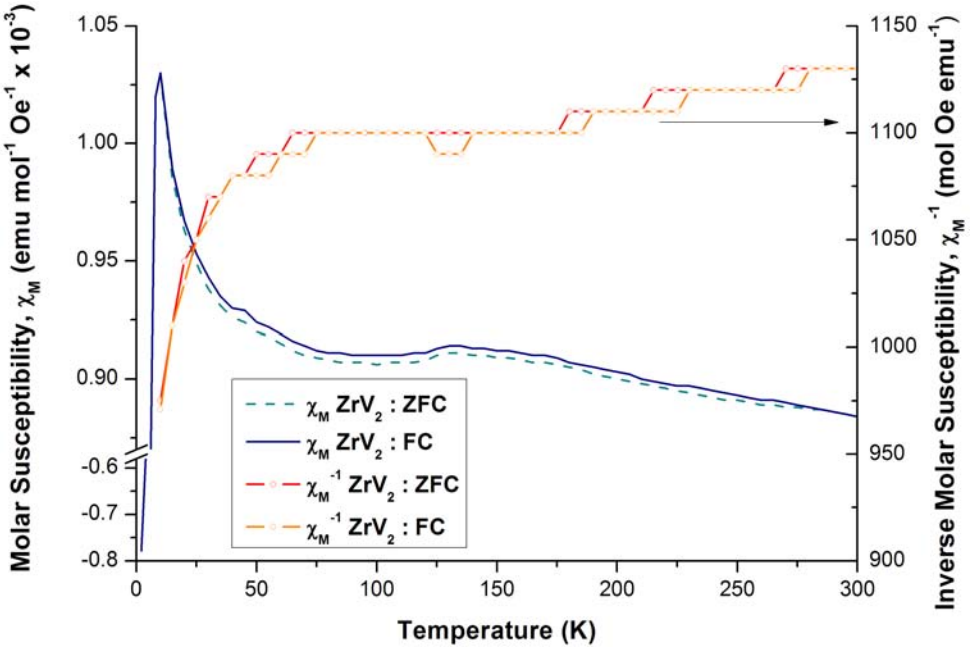

Figure 4.9: *Thermomagnetic analysis of the cycled, dehydrided ZrV_2, showing the variation in the molar susceptibility, as well as its inverse, from 2 K to 300 K. The sample was cooled to 2 K under two conditions: zero-field cooled (ZFC) and field cooled at 10000 Oe (FC). For both regimes, the molar susceptibility (left axis) was measured on warming under a field of 10000 Oe, where the ZFC and FC data are shown as a cyan dashed line and a dark blue line, respectively. Corresponding to the right axis is the inverse molar susceptibility, in red and orange lines, respectively, for the ZFC and FC measurements. Relative errors are smaller than data points.*

To address the contribution of the impurity phases to the magnetic measurements of the ZrV_2- H system, the nature of the magnetic ordering in $\alpha-$ Zr, $\alpha-$ V (which should closely resemble $Zr_{0.5}V_{0.95}$), and $Zr_3V_3O_x$ and its hydride are considered. According the CRC Handbook [81], both elemental zirconium and vanadium are weak paramagnets with room temperature susceptibilities of 1.20×10^{-4} emu mol^{-1} Oe^{-1} and 2.85×10^{-4} emu mol^{-1} Oe^{-1}, respectively. Zirconium is a very low T superconductor ($T_c = 0.61$ K) and vanadium is a type II superconductor, with a T_c of 5.40 K [81]. Considering the low percentage of these impurities in the materials studied, and the weak paramagnetic moment they exhibit, the effect of a

minor percentage of zirconium or vanadium on the measured magnetic behaviour of the ZrV_2- H system will be negligible. Unfortunately, the magnetic properties of $Zr_3V_3O_x$ and its hydride are not available, although a room temperature neutron diffraction study [100] of the hydride did not reveal any magnetic reflections or diffuse paramagnetic scattering. Zr_3V_3O is a superconductor with $T_c = 7.5$ K [81].

	ZrV_2 alloy	ZrV_2 dehydride	$ZrV_2H_{2.8}$
χ_{300K} (emu mol^{-1} Oe^{-1})	$9.751(1) \times 10^{-4}$	$8.844(1) \times 10^{-4}$	$5.908(2) \times 10^{-4}$
χ_{10K} (emu mol^{-1} Oe^{-1})	$9.033(2) \times 10^{-4}$	$1.0292(1) \times 10^{-3}$	$6.072(1) \times 10^{-4}$
^1T_M (K)	125 ± 5	120 ± 5	-
^2T_C (K)	8 ± 2	8 ± 2	-
H_{c1} (Oe)	$1.50(7) \times 10^3$	$4.0(2) \times 10^2$	-
H_{c2} (Oe)	> 50000	$2.5(1) \times 10^4$	-

[1] Temperature of the martensitic transition

[2] Temperature of the superconducting transition

Table 4.3: *Experimentally observed susceptibilities and transition temperatures for the $ZrV_2 - H$ series. Data for the virgin alloy, the cycled, dehydrided material, and the hydride are given. The critical field values at 2 K, for those materials exhibiting superconductivity, are also shown.*

The $\chi(T)$ behaviour of the hydrided $ZrV_2H_{2.8}$ material differs little from an ideal paramagnet, excepting two small steps in susceptibility at 340 K and 180 K. These steps are likely to result from structural transitions within the ZrV_2- H system. Previous crystallographic studies have shown that the most stable hydrogen superstructure – the $k = 0$ structure – transitions to a fully disordered state at 340 K [43]; therefore, the step in susceptibility at 340 K may be attributed to a partial structural transition from the cubic ZrV_2H_x phase to the ZrV_2H_4 tetragonal superstructure. Irodova *et al.* [43] have shown that at intermediate temperatures between 340 K and 200 K, the $k = 0$ and $k = (0, 0, 1)$ superstructures coexist in varying concentrations, thus explaining the gradual decline in χ in this

temperature range, whilst the drop in susceptibility at 180 K may result from the end step of this transition. Down to the lowest temperature measured (5 K) the hydrided material exhibits no signs of superconductivity.

Figure 4.10 shows the variation in magnetisation against the applied field strength for the virgin alloy and the cycled, dehydrided ZrV_2, both at 2 K. Both materials exhibit type II superconductivity, with H_{c1} and H_{c2} clearly reduced by the effect of cycling. The critical field values of the ZrV_2 alloy agree well the published values [44, 46]: H_{c1} is slightly lower than the literature value, but is within error, and the published data indicates that H_{c2} is 230 kOe, well beyond the upper field magnitude tested herein. The provenance of the $M(H)$ disparities between the dehydrided ZrV_2 sample and the original alloy is not clear, but may result from the reduction in the relative percentage of the cubic phase within the material.

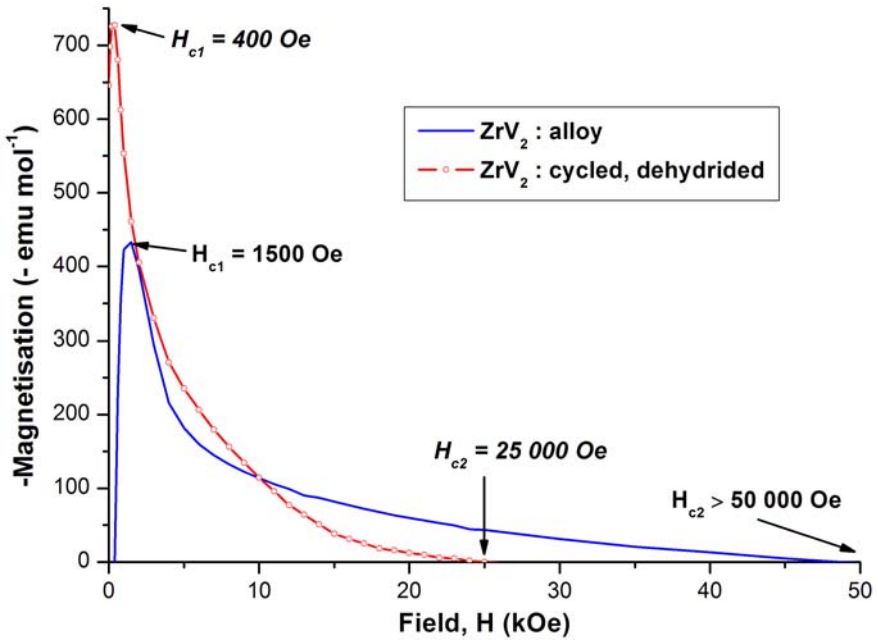

Figure 4.10: *A plot of the dependence of magnetisation, M on the applied field, H, for the alloy ZrV_2 (blue line) and a cycled, dehydrided ZrV_2 sample (red line with open circles) at 2 K, showing the fourth quadrant only. Both materials exhibit type II superconductivity; the critical fields H_{c1} and H_{c2} are shown. Note that the magnetisation scale is expressed in negative units, in order to emphasise the diamagnetic nature. Relative errors are smaller than data points.*

The $M(H)$ behaviour of the ZrV_2 hydride is shown in Figure 4.11. It is evident that at 2 K, a small amount of flux expulsion occurs, signalling the presence of a superconductor; this is likely caused by either the 1.3 wt. % of the hydrogen-free ZrV_2 that is present in the hydrided material, as the X-ray diffraction data in Figure 4.6 show, or the 2.0 wt. % of Zr_xV_{1-x} ($x = 0.05$). Excepting the anomalous superconductor contribution at 2 K, the magnetisation of $ZrV_2H_{2.8}$ increases linearly with the applied field and shows little variation with temperature, as expected for a Pauli paramagnet.

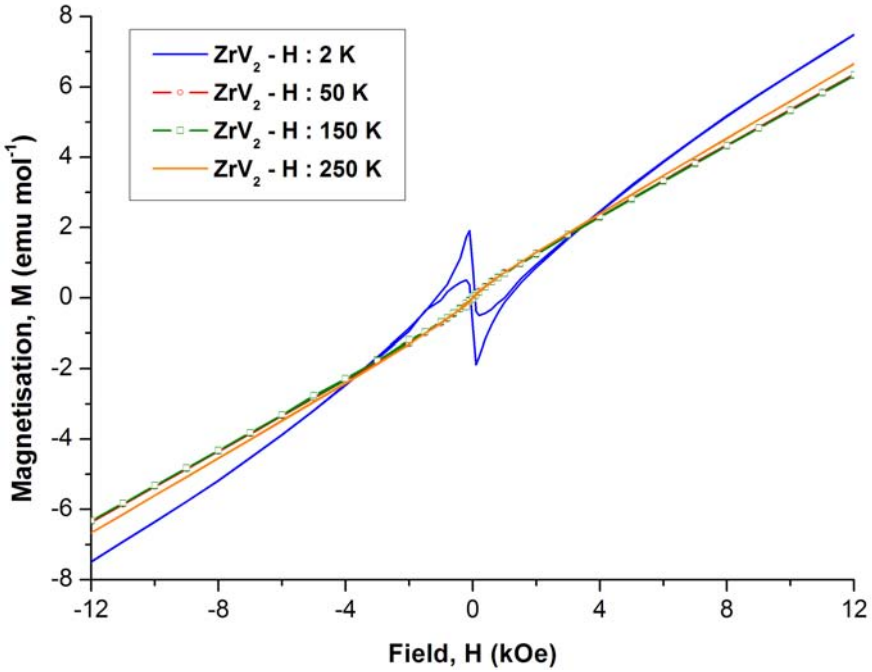

Figure 4.11: *A plot of the dependence of magnetisation, M on the applied field, H, for the hydrided $ZrV_2H_{2.8}$ material at 2 K (blue line), 50 K (red line with open circles), 150 K (green line with open squares), and 250 K (orange line). Relative errors are smaller than data points.*

The field dependence of the magnetisation for the ZrV_2- H system can be easily translated into a series of Arrott plots, as shown in Figure 4.12 for the measurements at 50 K. Although they show some curvature at low fields, the data for both the alloy and the dehydrided ZrV_2 material can be described by linear functions and have large, negative intercepts, indicating that they are not magnetically ordered. The Arrott plot for the hydrided material is substantially more curved

than those for the hydrogen free materials, and cannot be accurately fitted to a linear function; nonetheless, it is evident that any mathematical description of the trend in the M^2 versus $\frac{H}{M}$ data of the hydride would yield a negative intercept, and therefore no spontaneous magnetisation.

Close examination of Figure 4.12 reveals that the dehydrided material is subject to a larger degree of low-field curvature than the virgin alloy. Although deviation from linearity in an Arrott plot may be caused by many phenomena, the consideration of this data in conjunction with the previously detailed crystallographic studies in Section 4.3 and 4.6 suggests that microstructural inhomogeneities are the most plausible origin of this. A similar explanation may be applied to the curved Arrott plot of the hydride, due to the number of structurally distinct ZrV_2H_x phases in this material.

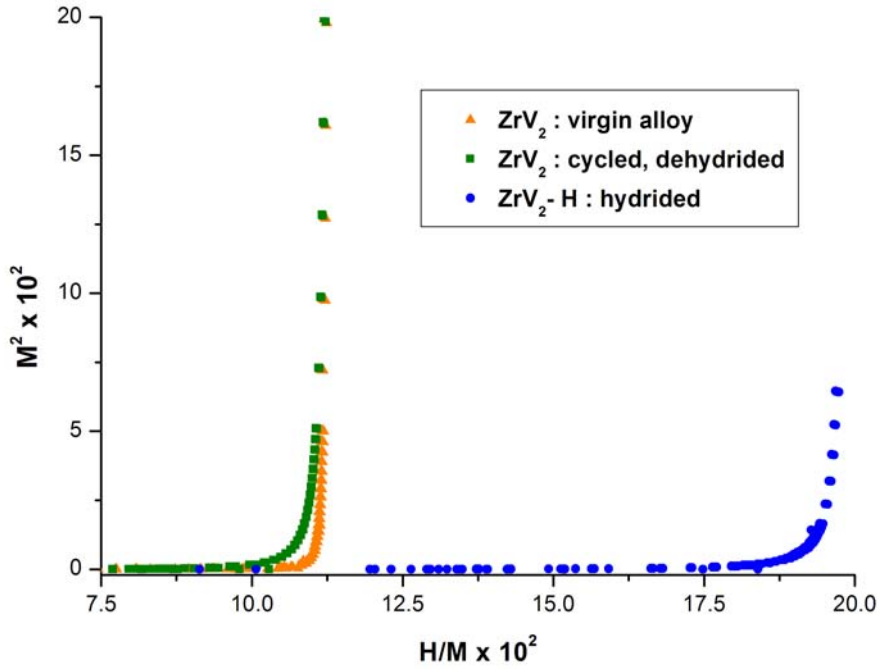

Figure 4.12: *An Arrott plot for the $ZrV_2 - H$ system at 50 K, with the square of the molar magnetisation, M, on the y-axis and the applied field, H (in Oe), over M, on the x-axis. Data are shown for the virgin alloy (orange triangles), the cycled, dehydrided material (green squares), and the hydrided material, $ZrV_2H_{2.8}$ blue circles). Relative errors are smaller than data points.*

4.8 Electronic and Dielectric Properties of the ZrV_2-H system

Microwave resonance spectra were collected for the cycled, dehydrided ZrV_2 material, and the hydrided material with net hydrogen concentration $ZrV_2H_{2.8}$; the synthesis of these materials is discussed in Section 4.4. The spectra in the electric field is shown in Figure 4.13, whilst the spectra in the magnetic field is given in Figure 4.14; summarised results of these measurements are given in Table 4.4. Each sample was separately measured at least six times, and the frequency shift and bandwidth change for each of these measurements, as compared to the empty cavity, averaged and its standard deviation determined. Estimation of the errors on the extracted electronic and dielectric values proved more difficult; Section 2.3.4.1 details an appropriate method for estimating these errors.

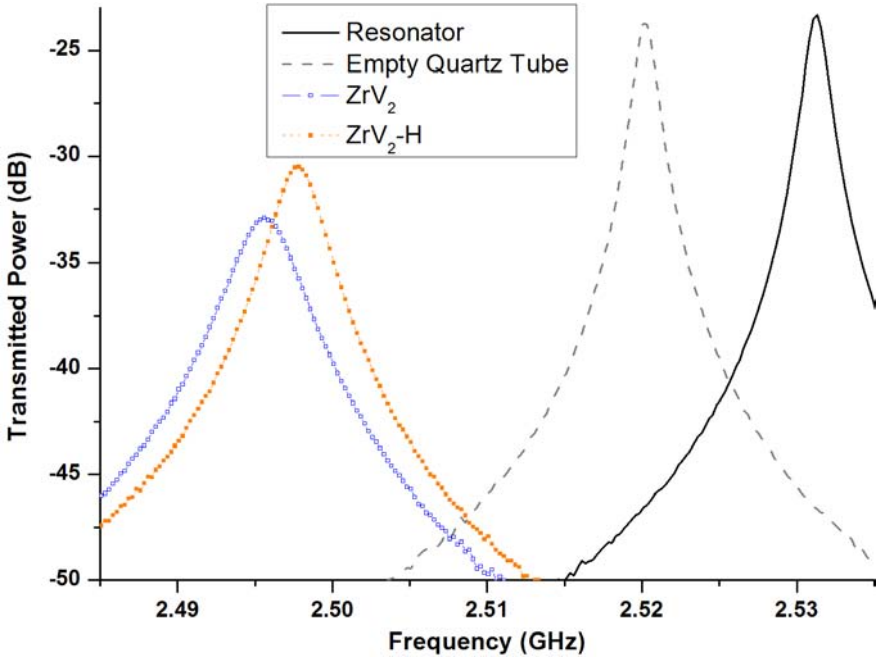

Figure 4.13: *Resonance spectra for the microwave conductivity measurement on ZrV_2 (blue line with open squares) and its hydride (orange line with closed squares), showing transmitted power versus frequency in the electric field antinode of the cavity. In addition to the measured compounds, the spectra for the empty resonator cavity (black line) and an empty quartz tube, used to contain the compounds (broken grey line), are shown for comparison. Relative errors are smaller than data points.*

The large resonance frequency shifts induced by ZrV_2 and its hydride when inserted into the electric field antinode of the resonator indicates that both materials are substantially polarised in an electric field. This polarisation is expected for metals, due to the ready movement of the free conduction electrons to oppose the applied electric field. The increase in bandwidth, as compared to the empty resonator, denotes the presence of significant loss components, with the dehydrided material showing more dielectric loss than the hydrided material. Qualitatively, the behaviour of ZrV_2 and $ZrV_2H_{2.8}$ are easily distinguished within the electric field antinode; whereas the measurements in the magnetic field antinode are more difficult to separate.

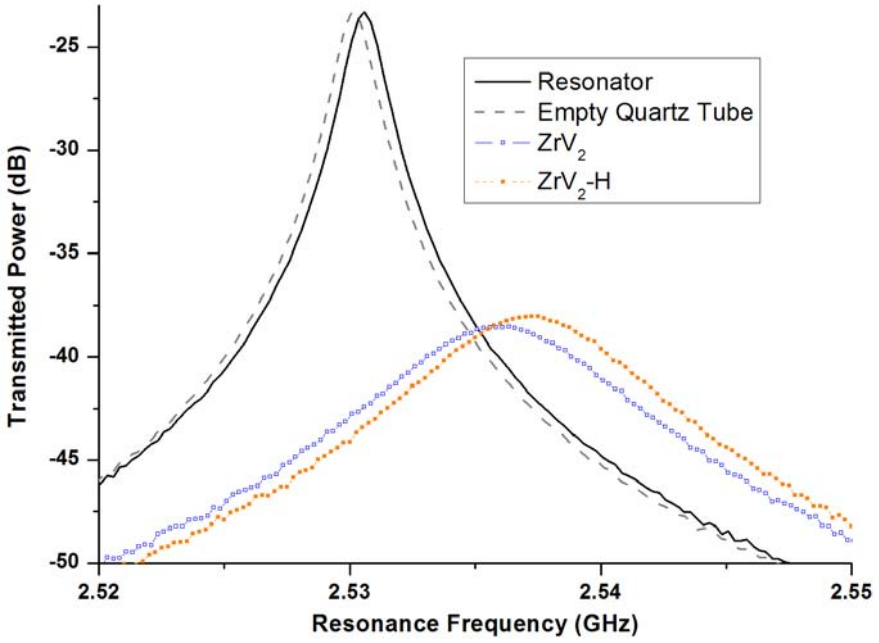

Figure 4.14: *Resonance spectra for the microwave conductivity measurement on ZrV_2 (blue line with open squares) and its hydride (orange line with closed squares), showing transmitted power versus frequency in the magnetic field antinode of the cavity. In addition to the measured compounds, the spectra for the empty resonator cavity (black line) and an empty quartz tube, used to contain the compounds (broken grey line), are shown for comparison. Relative errors are smaller than data points.*

When introduced into the magnetic field antinode ZrV_2 and its hydride, which, for the purposes of this qualitative treatment behave identically, display a slight

increase in resonance frequency compared to the empty cavity, and a large bandwidth expansion. The bandwidth increase, typical for metals in a magnetic field, stems from the high metallic conductivity and eddy current losses, and may also be related to magnetic losses, if $\mu \neq 1$. The positive frequency shift is related to the effective reduction in cavity volume, resulting from partial screening of the metal particles: this screening only arises in particles with a radius larger than the skin depth, where the core of these particles is shielded from the external magnetic field, causing a drop in the apparent volume of the resonator. As the skin depth of ZrV_2 is 10 μm (see Section 2.3.4.1), this suggests that some portion of the ZrV_2 particles must have a diameter greater than approximately $25-30$ μm; as the skin depth of the hydride is not known, it is assumed that the same clause applies to the $ZrV_2H_{2.8}$ material as well.

In the case of a frequency shift in the magnetic field antinode, the distribution of particle radii is more telling than the average size: the net effect of an assembly of particles on the resonance frequency can be described by an effective particle radius, a_{eff}, which is defined by

$$a_{eff}^2 = \frac{\int_0^\infty [r^5 f(r)]\, dr}{\int_0^\infty [r^3 f(r)]\, dr} \tag{4.4}$$

where $f(r)$ is a function that describes the particle radii distribution [79]. It is evident that for expected forms of $f(r)$ – *e.g.*, a log-normal distribution – a_{eff} will be much larger than the average particle size, creating a situation where a few, much larger particles can dominate the observed resonance frequency shift in the magnetic field.

The question of particle size is relevant to determining the suitability of the 'collapsed cylinder' model for the study of the ZrV_2- H system. As discussed in Section 2.3.4.1, two boundary conditions must be fulfilled: the first states that the particle size must be much smaller than the wavelength of the electromagnetic field resonating in the cavity; for the 2.5 GHz hairpin used in this work, this translates

into a restriction of particle sizes to less than 0.12 m. The second boundary condition mandates that the particle radius must also be smaller than the skin depth, *viz.* 10 μm. As the magnetic field data in Figure 4.14 showed; however, this second condition cannot be completely fulfilled, due to the observance of a small, positive frequency shift when the sample is inserted into the cavity. Stern *et al.* [101] have previously estimated the particle diameter in cycled, dehydrided ZrV_2 to range from $10-100$ μm, but did not quantify the distribution of sizes. Any particle of diameter less than $25-30$ μm will be within the boundary conditions; thus, if the assumption is made that most of the ZrV_2 particles are within this range, the observed frequency shift in the magnetic field must be due to a very few, large particles.

	ZrV_2 dehydride	$ZrV_2H_{2.8}$
Δf ($\times 10^7$ Hz)	$-3.58(4)$	$-3.44(6)$
$\Delta\Gamma$ ($\times 10^5$ Hz)	4.0(8)	2.0(6)
ε_{1eff}	15(2)	20(2)
ε_{2eff}	$-25(5)$	$-8(2)$
$\tan\delta_{eff}$	1.6(2)	0.40(6)
σ_{eff} (Ω^{-1} m^{-1})	3.4(7)	1.1(2)

Table 4.4: *Measured microwave resonance parameters in the electric field antinode for cycled, dehydrided, ZrV_2 and the hydrided $ZrV_2H_{2.8}$, showing the shift in bandwidth and frequency in each case, as compared to the resonance parameters of the empty cavity. The extracted dielectric constants, loss tangent and effective conductivity for the ZrV_2-H system are also shown.*

To lend support to this postulate, the magnitude of an induced frequency shift can be related to the corresponding reduction in effective cavity volume by comparing it to the shift caused by a steel ball bearing of known volume. This calculation reveals that the apparent volume decrease brought about by the insertion of ZrV_2 into the magnetic field amounts to 1.27 mm^3. In comparison, the volume of the ZrV_2 sample that was used in this measurement was 25.6 mm^3, as estimated from its mass and the theoretical density of the unit cell. It is therefore clear that less than 5 % of the sample is shielded from the magnetic field, sustaining the above theory that the vast majority of the particles in the ZrV_2 sample are within the skin depth limit, and thus fulfill the boundary

conditions of the collapsed cylinder model.

A more exacting description of the dielectric behaviour of ZrV_2 and its hydride can be gleaned by translating these bandwidth and frequency shifts into permittivities, loss tangents and effective conductivities. These data are given in Table 4.4. Examining the permittivity values, it can be seen that the real part of the permittivity increases upon the addition of hydrogen, indicating improved polarisability; as ε at microwave frequencies is expected to contain both electronic and ionic components, it is probable that the observed rise in ε_{1eff} stems from an amplification of the ionic factor. The polarisability of hydrogen, combined with its high mobility in the disordered ZrV_2H_x system [107], is the most likely case of this increase.

The imaginary part of the permittivity, ε_{2eff}, directly relates to the population of the conduction electron band and shows that the hydride is substantially less conducting than the dehydrided material. As a result of both the model's assumptions and the powdered nature of the samples, the calculated σ_{eff} value for ZrV_2 is much lower than the reported conductivity of $1.11 \times 10^7\ \Omega^{-1}\ m^{-1}$ for the bulk alloy at 300 K [82]. Finally, examination of the ratio between the real and imaginary parts of the permittivity gives the loss tangent, which relates to the energy lost in the polarisation process. This loss tangent is higher in the dehydrided material, perhaps as a result of the slight disproportionation and impurity of this phase indicated by the crystallographic study in Section 4.6.

Elucidating the origin of the hydrogen-induced decline in conductivity in the ZrV_2- H system may be simplified by reference to published electronic density of state diagrams for C15 ZrV_2 [106] and the cubic $ZrV_2H_{0.5}$ [14]. Unfortunately, detailed density of state diagrams for disordered ZrV_2H_x at higher hydrogen concentrations is not available, due to difficulties in describing the electronic structure of the lattice-gas behaviour of hydrogen in these systems [108]. Hong *et al.* [14] have explored the effect of hydrogen on the electronic structure of ZrV_2 *via* a first principles, local-density-functional calculation and found that, with hydrogen ab-

sorption, $N(\epsilon_F)$ is lowered by $\sim 20\%$ as shown in Figure 4.15. This downward shift, which is likely the cause of the particularly strong binding of hydrogen in this compound, is expected to be more pronounced at higher hydrogen concentrations; however, it is not expected to shift the Fermi level past the well-defined valley separating the bonding and anti-bonding states. Hong *et al.* [14] furthermore showed that the interstitial hydrogen atom in $ZrV_2H_{0.5}$ is in a negative charge state, due to charge donation from the host metal to hydrogen.

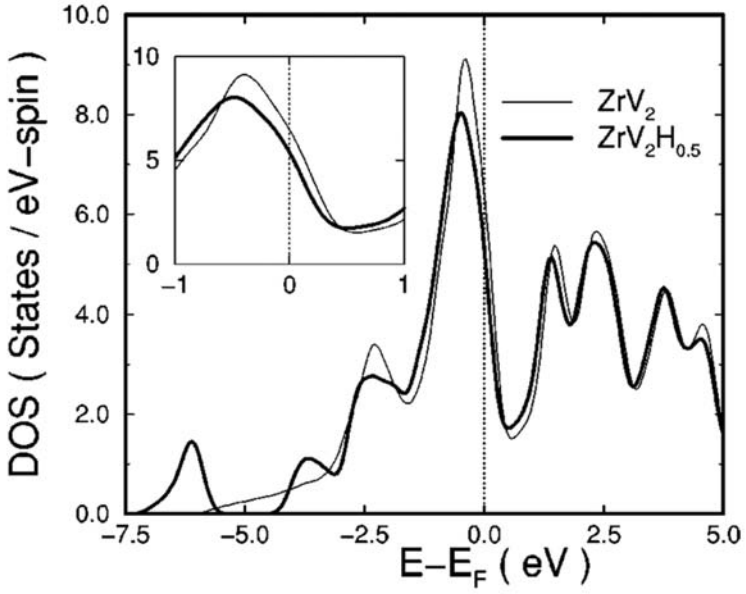

Figure 4.15: *The total density of states for ZrV_2 and $ZrV_2H_{0.5}$. Figure from* [14].

This theorised charge donation from metal to hydrogen may explain the observed decrease in conductivity upon hydrogen addition. The negative (or partially negative) charged state of the hydrogen atom would be accomplished *via* electron transfer from the metal, thus depleting the conduction electron band and triggering a drop in conductivity concomitant to the hydriding process.

4.9 Summary and Conclusions

To summarise, the intermetallic compound ZrV_2 was synthesised *via* arc-melting, then cycled with hydrogen to produced a hydrided material with net hydrogen

content $ZrV_2H_{2.8}$. Hydrogen was absorbed so readily by ZrV_2 that accurate data on the hydriding thermodynamics could not be collected; moreover, high temperatures were required to remove the hydrogen from this system and obtain the cycled, dehydrided material. X-ray diffraction indicated that, in addition to the C15 ZrV_2 phase, the virgin alloy contained several minor impurity phases, the phase fractions of which were increased significantly as a result of the dehydriding process. Structural characterisation of the hydride revealed the same incidence of impurity phases as was observed in the parent alloy, along with a plethora of ZrV_2H_x phases: these included two disordered ZrV_2H_x ($x = 2.4$, 4.8) cubic phases formed by isotropic expansion of the parent metal substructure, as well as two ordered hydride phases with propagation vectors $k = 0$ and $(0, 0, 1)$. A peak profile analysis of the C15 ZrV_2H_x phases, as well as the C15 ZrV_2 phase in the cycled, dehydrided material, revealed that no significant peak broadening had occurred upon hydrogen cycling.

Magnetic measurements on the ZrV_2- H system indicated that the hydrided material behaved as a simple Pauli paramagnet down to 5 K, showing small variations in $\chi(T)$ that could be tied to order-disorder transitions in the ZrV_2H_x structure. The alloy and the dehydrided compound both demonstrated type II superconducting behaviour, with a T_c of 8 K; the critical fields of the cycled material differed slightly from the virgin alloy, likely as a result of the disproportionation and impurities created by the high temperature dehydriding process. Similarly, close examination of the Arrott plots revealed that the dehydrided structure exhibited increased low-field curvature, also caused by these microstructural inhomogeneities. For all three components of the ZrV_2- H system, the Arrott plots at 50 K could be fitted with linear functions possessing a large, negative magnetisation, indicating that both hydrided and hydrogen-free ZrV_2 were not magnetically ordered.

Finally, the hydrided $ZrV_2H_{2.8}$ and its cycled, dehydrided counterpart were measured in a microwave cavity resonator, and their dielectric permittivities and

conductivities at room temperature determined. Both materials were found to be metallic conductors undergoing a large polarisation in the electric field; however, it was revealed that the hydriding process induced a decrease in the conductivity. Comparison with published density of state diagrams suggested that this hydrogen-induced drop in conductivity resulted from charge transfer from the host metal to the hydrogen atom, effectively depleting the conduction electron band. A qualitative analysis of the frequency shift induced by introduction of ZrV_2 and $ZrV_2H_{2.8}$ into the magnetic field suggested that the small, positive frequency shift was caused by a few very large particles in these materials.

Several important conclusions can be drawn from this collected body of data, the first of which concerns the effect of a high-temperature treatment under vacuum on the stability of ZrV_2. To ensure total hydrogen removal from the $ZrV_2H_{2.8}$ material, it was subjected to an additional dehydriding step at 650°C in vacuo; however, X-ray diffraction later revealed that this dehydrided sample contained a significantly increased phase fraction of impurities as compared to the parent hydride. Additionally, the appearance of an $\alpha-$ Zr phase, and an augmentation of the Zr_xV_{1-x} ($x = 0.05$) phase fraction, indicated that segregation of ZrV_2 had occurred. This reduction in the relative percentage of ZrV_2 in the material lead to a dilution of the superconductivity in the dehydrided material, as the $M(H)$ data revealed, as well as the manifestation of low-temperature paramagnetic contributions in the thermomagnetic analysis, resulting from the impurity phases. It is evident from these findings that the dissolution of hydrogen in this compound is so favourable as to make its complete removal difficult to achieve whilst still retaining the integrity of the parent intermetallic compound.

The action of cycling hydrogen through the ZrV_2- H system was not found to beget substantial decrepitation. X-ray diffraction data of the hydrided and the dehydrided C15 phases did not exhibit a peak broadening effect, which may have heralded a crystallite size reduction; moreover, measurements in the magnetic field antinode of the microwave cavity resonator suggested that a few large particles

were present in both samples. This lack of decrepitation may result from the isotropic nature of the hydrogen-induced lattice expansion, which, as compared to an anisotropic expansion, is not expected to generate significant crystalline strain and stress in the system.

Hydrogen addition to the ZrV_2 intermetallic compound induced several electronic and magnetic changes in the system. Crystallographically, the hydrided material exists as a solid solution of hydrogen in the parent ZrV_2 compound; the hydrogen atoms are accommodated at interstitial sites *via* a simple lattice expansion that is proportional to the amount of hydrogen absorbed. Although the original intermetallic compound is a superconductor, hydrogen addition was found to destroy the superconductivity; it has been postulated [45] that this results from the reduced influence of spin fluctuations and the drop in the electron-phonon coupling strength in ZrV_2H_x. Furthermore, the absorption of hydrogen results in a drop in $N(\epsilon_F)$, with electron transfer from the metal to the hydrogen atom spurring a consequent decrease in the conductivity of the hydride. Clearly, despite the lacklustre structural changes that occur, the addition of hydrogen to ZrV_2 induces several interesting electronic and magnetic changes.

4.10 Future Work

The unfortunate time limits inherent in a doctorate work necessitated that several interesting side projects related to this work had to be overlooked in favour of the pursuit of the main thesis. These additional research questions are detailed here, in the hope that they may be pursued in the near future.

Crystallographic analysis of the ZrV_2 alloy revealed that it was not a single phase, C15 structure as desired. Although many other researchers who have synthesised this intermetallic compound noted the same problem, it does not necessarily follow that the cubic structure cannot be obtained in a pure, single phase form. A detailed experimental study on reducing the concentration of impurities

in the ZrV_2 alloy, covering the effect of variables such as annealing time, temperature, atmosphere, *etc.*, could provide a new route for synthesising pure ingots of the C15 structure.

There is additional scope for improvement of the experimental method in the synthesis of the hydrides ZrV_2H_x. As discussed earlier in Section 4.4.1, the custom built hydriding apparatus that was used in this work could not accurately measure hydriding pressures in the ZrV_2- H system. However, if higher temperatures could be accessed – for example, with the addition of a new furnace to the apparatus – it is possible that the temperature might be raised to a point where the hydriding pressure could be accurately measured. A similar goal could also be accomplished with the use of a mass flow controller able to restrict very small flow rates, thus enabling the addition of minute aliquots of hydrogen to the reaction chamber. Although the expense of these alterations was beyond the scope of this project, it would be worthwhile to pursue in order to gain a more lucid understanding of the hydriding thermodynamics in the ZrV_2- H system. Moreover, tighter control on the hydride synthesis process with these equipment modifications would allow selection of the precise hydrogen content x in ZrV_2H_x; this would in turn open a pathway into examining how the crystallographic, electronic and magnetic properties of this system vary with x.

On a final note, it would be interesting to examine the $\sigma(T)$ dependence of the ZrV_2- H system, as this can provide telling clues as to the electronic nature of a material. Unfortunately, it was not possible to use the microwave resonator at variable temperatures. Alteration of the resonator so as to allow low temperature determinations of σ_{eff} for the ZrV_2- H system would certainly prove useful; moreover, it would be interesting to examine the behaviour of the dehydrided ZrV_2 in the electric field antinode of the resonator below the superconducting transition temperature. In conjunction with the previous note regarding the synthesis of a range of hydrides ZrV_2H_x, a study of the dependence of conductivity on x could certainly prove fascinating.

Chapter 5

CRYSTALLOGRAPHIC, MAGNETIC AND ELECTRONIC PROPERTIES OF $ZRCR_2$ AND ITS HYDRIDES

> Some books are to be tasted, others to be swallowed, and some few to be chewed and digested. *Sir Francis Bacon, 'Of Studies' from "The Essays of Francis Bacon"*

5.1 Introduction and Scope

$ZrCr_2$ was discovered some fifty years ago [47], but controversy over the nature of its thermodynamically stable structure at room temperature persisted well into the 1980s [48, 109] due to polymorphism between the C14, C36 and C15 Laves phase structures. Although the Zr-Cr phase diagram [26] gives the cubic C15 phase as the most stable allotrope of $ZrCr_2$ up to 1592°C, the hexagonal structures are easily stabilised by rapidly cooling the melt [110], with this structural degeneracy also leading to the ready appearance of layered superstructures and stacking faults [48]. The intermetallic compound is a simple Pauli paramagnet down to 4.2 K [51] and experimental determinations of its conductivity have not yet been reported.

Both the hexagonal and cubic intermetallic compounds reversibly absorb hydrogen up to a concentration of approximately 3 hydrogen atoms/formula unit, where $ZrCr_2-$ H is a two-phase system, consisting of the hydride $ZrCr_2H_3$ and the parent alloy [20,37]. This hydride is an expanded form of the original intermetallic compound, and, in the case of the cubic phase, the hydrogen atoms are disordered over the *2A2B* interstitial sites [49]. The application of higher pressures results in the formation of a solid solution hydrided phase, $ZrCr_2H_{3+x}$, $0 < x \leq 1$ [20] ,

with the additional hydrogen atoms accommodated on the less favourable *1A3B* sites as well [111]. In terms of its magnetic behaviour, the addition of hydrogen increases the room-temperature susceptibility of the system three-fold, but otherwise causes no shift from the observed Pauli paramagnetism of $ZrCr_2$ [51]. Although its electronic properties have not been explored experimentally, a recent theoretical investigation [52] suggested that the hydrogenic electron remains bound to the proton and may be considered localised —a finding that may have interesting implications for hydrogen-induced changes in the conductivity of the $ZrCr_2-$ H system.

The following chapter will present a detailed examination of the $ZrCr_2-$ H system, carefully examining the effect of hydrogen over an array of fundamental properties. These include the hydriding thermodynamics, crystal structure, magnetic behaviour, superconductivity, dielectric properties and electrical conductivity. Novel and valuable contributions will include an exploration of the low temperature magnetic properties of the system, including a possible superconducting transition, and a study of the dielectric properties and electrical conductivity for $ZrCr_2$ and its hydride. The chapter will conclude with a summary and discussion of these properties, with a view to determining the role of hydrogen in this system.

5.2 Formation of the $ZrCr_2$ alloy

The alloy $ZrCr_2$ was synthesised *via* arc-melting, as described in Section 2.4.3, with the inclusion of an annealing step to help secure a homogeneous, single, C15 structure. As discussed by Mestnik Filho *et al.* [48], an ingot of $ZrCr_2$ quenched from the melt may contain not only the C14 or C36 polymorph, but also a variety of superstructures formed by layer stacking faults due to the relative stability of the hexagonal and cubic phases in the Zr-Cr system. X-ray powder diffraction of the ground, annealed material was used to monitor the annealing process and determine when the desired C15 phase was obtained.

5.3 Crystallographic Features of the $ZrCr_2$ alloy

5.3.1 Published structures of the $ZrCr_2$ intermetallic compound

At room temperature and standard pressure, the most stable polymorph of the $ZrCr_2$ intermetallic compound is the C15 Laves phase [26], with space group $Fd\bar{3}m$ and structural parameters as given in Table 1.3; however, the high-temperature C14 and C36 phases are readily secured under standard conditions by rapidly cooling the Zr-Cr melt [48]. As an annealing step was included in this work in order to exclude such metastable phases, it is principally the cubic polymorph that will be discussed herein.

The polymorphism of $ZrCr_2$ and the close relative stability of the C14, C15 and C36 structures has been shown to lead to the formation of other ordered superstructures based on the fundamental layers of the Laves phases. As discussed in Section 1.1.2, the Laves phase polymorphs are all formed of a common set of layers, where the stacking sequence of these layers differs in each structure [12]. Figure 1.2, which illustrates the arrangement of the A atoms in the C14, C15 and C36 polymorphs, shows that that the A sublattice can be divided into three shared layers; and, if the B sublattice is also included, the Laves phases are then seen to be constructed from a common set of six different layers [13]. Following the notation of Komura [13] regarding the labelling of the AB_2 layers , the stacking sequence of the C14 structure is AB', the C15 structure is ABC, and the C36 structure is $AB'A'C$. Stacking faults in Laves phase compounds may lead to the formation of other ordered structures from these same layers: in MgCuAl, for example, X-ray diffraction revealed diffuse reflections from a five-layer $ABCAB'$ structure and a nine-layer $AB'ABC'BCA'C$ structure, intermixed with the predominant peaks of the C14 and C36 phases [13].

Several workers [109, 111] have previously noted unexplained additional reflections, or mismatched intensities to the known Laves phase reflections, in their analysis of the X-ray diffraction data of $ZrCr_2$. Mestnik Filho *et al.* [48] have the-

orised that these inconsistencies arise from ordered Laves phase-type structures with nonstandard stacking sequences, like the five- and nine-layer structures discussed above. It is plausible that these phases may form *via* slips and stacking faults over the course of crystallisation; however, upon the addition of hydrogen, these layers stacking defects are no longer apparent [48].

5.3.2 Structural study of the $ZrCr_2$ alloy

The crystalline structure of the as-synthesised and annealed $ZrCr_2$ alloy (see Section 5.2 for synthetic details) was examined *via* X-ray synchrotron diffraction on the ID31 beamline at the ESRF —a full description of the instrument and the experimental parameters can be found in Section 2.1.2.1. The collected synchrotron data were analysed using the Rietveld method described in Section 2.1.4; an R_{wP} of 23.618 was obtained for a fit containing the C15 Laves phase structure of $ZrCr_2$ as the major phase, along with the C14 and C36 polymorphs as minor phases.

In the refinement process of the C15 $ZrCr_2$ structure, the metal atoms were constrained to the $8a$ and $16d$ sites of the $Fd\bar{3}m$ space group as in the reported structure [49]; as there were no free atomic coordinates due to the site symmetry, only the global lattice parameters could be refined. The C14 $ZrCr_2$ phase was fitted using the atomic coordinates of the ideal C14 Laves phase structure with space group $P6_3/mmc$ [11], which was not further refined, and only the lattice parameters were freely determined. The C36 phase was also fitted using the idealised atomic coordinates of the standard Laves phase structure [11] which were not further refined; just the lattice parameters of the $P6_3/mmc$ unit cell were determined.

In addition to the structural parameters of these phases, the scale factors and weight percent of each phase was also refined. The observed diffraction data and calculated fit are shown in Figure 5.1, along with the relative weight percent of each phase. Full structural parameters for the C15 $ZrCr_2$ phase are reported in Table 5.2 (see page 244), whilst the structures of the minor C14 and C36 phases

are suitably described simply by their refined lattice parameters: for C14 $ZrCr_2$, $a = 5.1026(4)$ Å and $c = 8.3106(7)$ Å, and for C36 $ZrCr_2$, $a = 5.103(5)$ Å and $c = 16.617(9)$ Å.

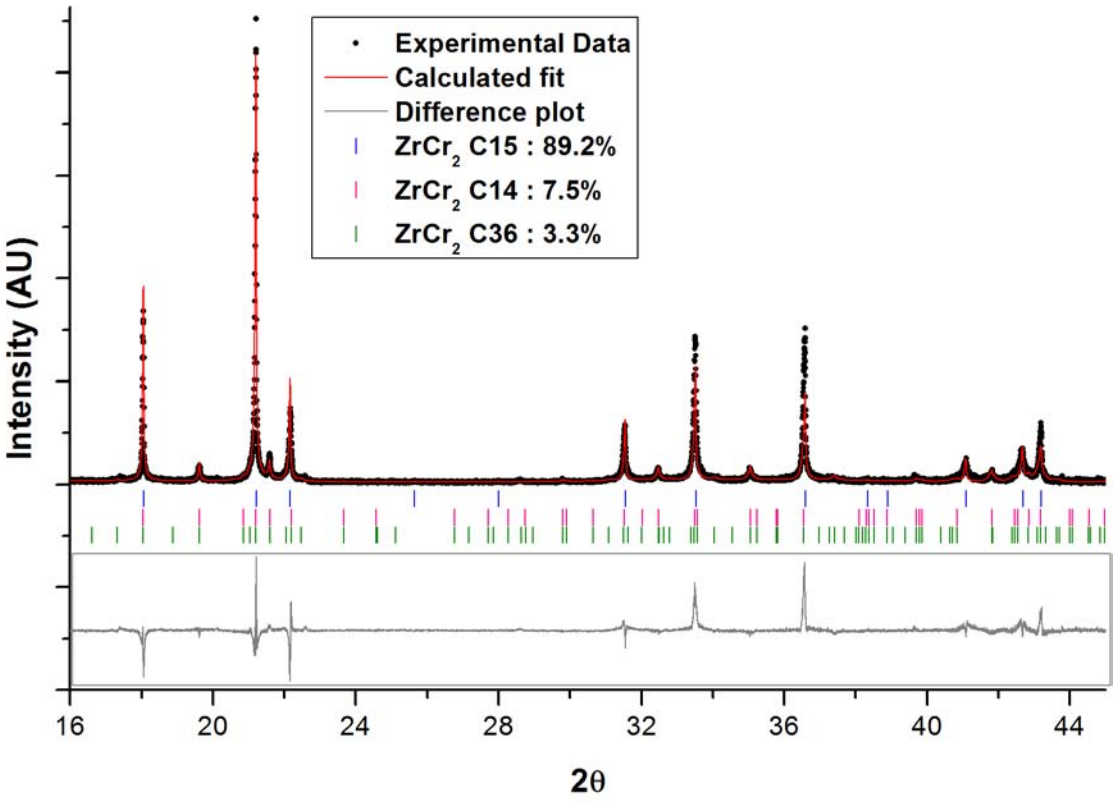

Figure 5.1: *Room temperature synchrotron diffraction pattern for the alloy $ZrCr_2$. Although the major phase is C15 $ZrCr_2$, both the C14 and C36 polymorph are also present, with the relative weight percent of each phase indicated in the legend. The Bragg peak positions of all the fitted phases are shown by vertical tick marks. The difference plot between the experimental data (black dots) and calculated fit (solid red line) is shown as a grey line enclosed in a box.* $R_{wP} = 23.618$.

Given the relative stabilities of the three Laves phase structures in the $ZrCr_2$ intermetallic compound, it is not surprising that a small percentage of the C14 and C36 phases persisted in the alloy material even despite the annealing step. In addition to this, the difference plot from the calculated fit to the observed diffraction data for the alloy reveals significant peak mismatches between the measured intensities and the expected intensities for many of the C15, C14, and C36 reflections. Following the analysis of Mestnik Filho *et al.* [48], both the structural degeneracy

in the sample and the mismatched *hkl* intensities suggest the occurrence of layer stacking faults in the $ZrCr_2$ compound. Modelling these Laves phase-type ordered structures is computationally demanding, involving the construction of large supercells with non-uniform stacking of the six Laves phase layers to cover every plausible stacking fault or slip and such an analysis, whilst academically intriguing, was beyond the scope of this work. Given that no other reasonable phase – *i.e.*, the starting materials or oxides thereof, or trace impurities in the reagents – could be reliably fit to the mismatched intensities, and given their clear overlap with reflections of the three $ZrCr_2$ Laves phase structures, a reasonable conclusion can therefore be drawn that the poor fit of the collected diffraction data of the alloy results from the mixture of the primary C15 phase with a number of unresolved, ordered Laves-phase type structures with unknown stacking sequences.

Related to the presence of these additional phases resulting from layer stacking faults was the inability to refine the thermal parameters of the C14, C15 and C36 $ZrCr_2$ structures. The significant unmatched intensities for many of the structural reflections interfered with the refinement process and generated negative thermal parameters as the program attempted to minimize the residual S_y. The thermal parameters of all atoms were therefore fixed at $B_{eq} = 0.4$ Å^2, a reasonable room temperature value for a metal atom; although the eventual inclusion of the other layered structures contributing to these diffraction peaks in the refinement model would allow an accurate determination of these values.

5.4 Synthesis of the $ZrCr_2$ hydride and the dehydrided material

5.4.1 Hydriding of $ZrCr_2$

Hydrogen was added to the annealed $ZrCr_2$ alloy using the hydriding apparatus described in Section 2.4.5, at a variety of temperatures and pressures. Figure 5.2 gives a series of pressure-composition isotherms for a well-cycled sample of $ZrCr_2$, illustrating the absorption of hydrogen from 0 to 6.5 bar at temperatures ranging

from 95 to 170°C. Hydriding cycles were carried out at other temperatures, but these data are not shown here for clarity and conciseness —qualitatively, they resemble the isotherms shown in Figure 5.2 and follow the expected trends in temperature. The pcT plot shows the formation of a distinct plateau at all temperatures measured, indicating that the $ZrCr_2-$ H system contains a miscibility gap. Determination of the critical temperature was beyond the scope of this work, but is certainly below the lowest hydriding temperature measured herein of 240°C.

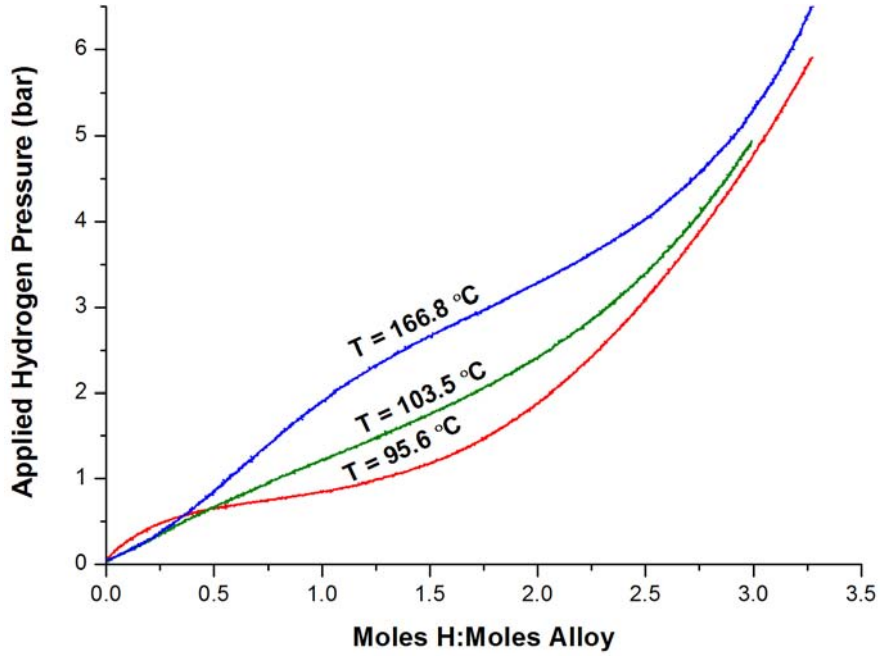

Figure 5.2: *A pcT plot of the $ZrCr_2-H$ system, showing the absorption of hydrogen at temperatures between 95 and 170° C and pressures from 0 to 6.5 bar. The exact hydriding temperature for each isotherm is indicated on the plot.*

It is evident from Figure 5.2 that the intermetallic compound absorbs $\sim$ 3 moles of hydrogen by the end of the plateau, in accordance with the formation of $ZrCr_2H_3$. At higher pressures, hydrogen continues to dissolve in the system; this is especially evident for the isotherm at 166.8°C, which absorbed 3.26 moles of hydrogen per mole of alloy by the time the line pressure of 6.5 bar had been reached. At all temperatures examined, the hydriding pressure in the plateau

region is not invariant against hydrogen content, with the degree of plateau sloping increasing with the hydriding temperature. The plateau pressure at 95.6°C can be estimated as 0.75 bar, by taking a reading at the midpoint of the plateau. The hydriding pressures measured herein deviates substantially from the values of Shaltiel *et al.* [20], although it worthwhile to note that they report estimates from the published data of Pebler and Gulbransen [37]; direct examination of the work of Pebler and Gulbransen reveals that at 98.7°C, they recorded a hydriding pressure of 0.53 bar. This value compares relatively favourably with the pressure measured herein at 95.6°C, and the slight discrepancy may be due to a difference in structure: the C14 polymorph was studied in these previous works, as opposed to the C15 structure examined herein.

5.4.2 Cycling and the dehydriding reaction

The dehydriding of $ZrCr_2H_x$ was also carried out using the apparatus described in Section 2.4.5; Figure 5.3 represents a sample data set from such a reaction. If it is assumed that all of the weight lost over the course of the dehydriding experiment in Figure 5.3 is due to desorbed hydrogen gas, then the calculated composition of the original hydride becomes $ZrCr_2H_{3.4}$, which is within expectations. As the dehydriding data show, the rate of hydrogen loss is not significant below approximately 80°C; above this temperature, the hydride is unstable at atmospheric pressure and begins to release hydrogen gas. Once this point of destabilisation has been reached, the reaction proceeds quickly as the temperature escalates, and the hydrogen-free $ZrCr_2$ is returned within a matter of minutes.

The kinetics of the dehydriding reaction can be more readily examined *via* the analysis of a peak shift plot, as shown in Figure 5.4. This figure illustrates the rate at which gas, presumed to be hydrogen, is desorbed from the sample as the heating rate is varied. At the fastest heating rate tested, 36 K/min, the material is completely dehydrided within eight and a half minutes, with the desorbed gas flow exhibiting a broad maximum around 156°C. However, as the rate of heat-

ing is decreased and additional time for equilibration between the heater and the sample allowed, the resolution of this 'thermal desorption spectra' improves. The desorbed gas trace collected at 29 K/min exhibits a large sharp peak at 233°C, followed by a small, broader peak at 317°C which slowly tapers off with increasing temperature. The shape of this desorption curve suggests that the initial peak, describing approximately 84% of the total volume desorbed, consists of the less strongly bound hydrogen atoms, and is followed by a higher temperature desorption of those hydrogen atoms sturdily bound at the more favourable sites of the hydride.

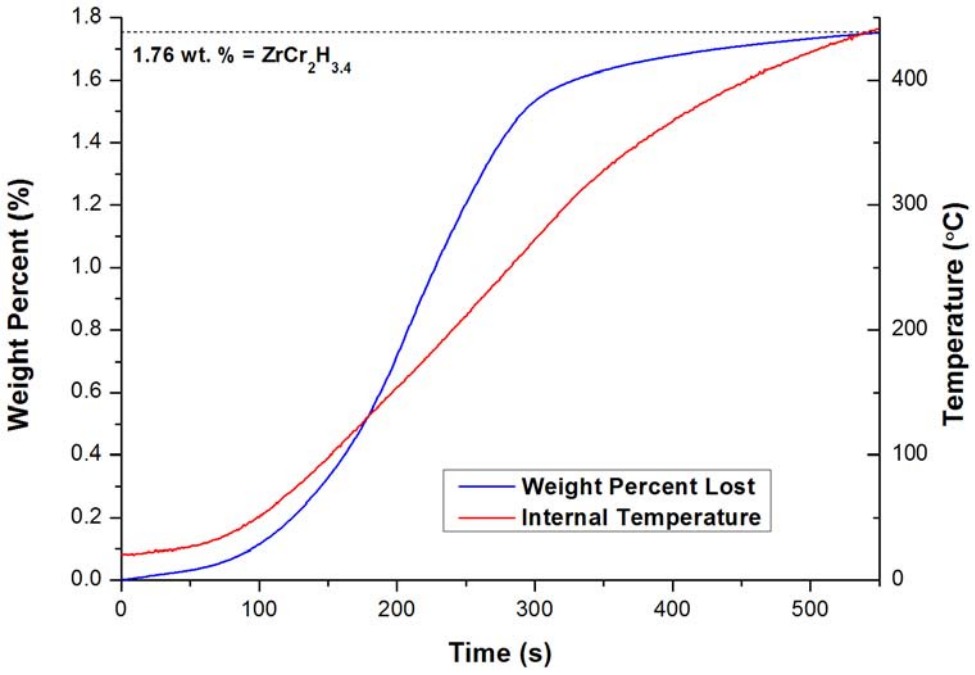

Figure 5.3: *A sample dehydriding trace for $ZrCr_2H_{3.4}$, showing the weight percent of gas desorped from the sample (blue) and the internal temperature of the reaction chamber (red) against time. The dashed line indicates the expected amount of hydrogen to be lost - 1.76 weight percent hydrogen - which corresponds to a composition of $ZrCr_2H_{3.4}$.*

Unfortunately, no data on the cycling of this system can be presented. It was found during the course of experimentation that, once the $ZrCr_2$ alloy had been suitably activated, the compound immediately absorbed its full capacity of hydrogen gas. The dehydriding trace presented in Figure 5.3 is in fact the data from

the very first hydrogen absorption/desorption cycle of this material. Although fifteen hydriding cycles were carried out on the $ZrCr_2-$ H system, no improvement or decline in hydriding capacity or rate of hydrogen absorption or removal was observed. This finding, which has not been previously commented on in the literature, suggests the possibility that $ZrCr_2$ is not subject to decrepitation upon the addition of hydrogen to the system. The ease with which the full hydriding capacity is reached furthermore implies strong diffusion of hydrogen in the system; indeed, anomalously high mobility down to 78 K has been been previously revealed *via* NMR measurements [112] for the $ZrCr_2-$ H system.

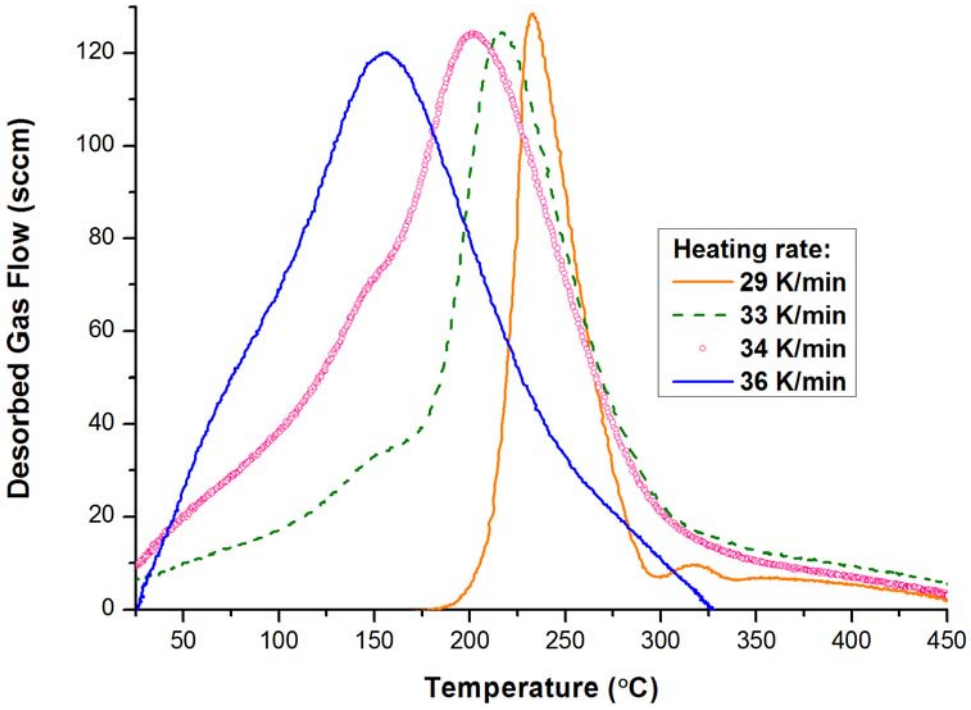

Figure 5.4: *A peak shift plot for the $ZrCr_2 - H$ system, showing the desorbed gas flow from the hydrided sample against the internal temperature, at a variety of heating rates as detailed in the legend. The amount of gas desorped (calculated as the difference between the flow rate of output gas and the flow rate of input gas) is expressed as a flow rate in sccm.*

5.5 Hydriding Thermodynamics of the $ZrCr_2-$ H system

Although examination of the pressure-temperature isotherms of the $ZrCr_2-$ H system provides an initial view into the stability of $ZrCr_2H_3$, the translation of

these data into the fundamental quantities of enthalpy and entropy can give a quantitative picture of the thermodynamics of the hydriding reaction. A plot of the natural logarithm of the plateau pressure, p_H, against the hydriding temperature, T_H, should yield a linear trend and allow the determination of the hydriding enthalpy, ΔH_H, and the hydriding enthalpy, ΔS_H *via* the van't Hoff relationship (Equation 1.1).

Figure 5.5 illustrates a van't Hoff plot for the $ZrCr_2-$ H system, showing the best-fit linear trend line to the experimental data. The extracted enthalpy and entropy values from this best-fit line are given in Table 5.1. As the sloping hydriding plateau indicates that ΔH_H varies with hydrogen concentration, the hydriding pressures incorporated into the van't Hoff plot were consistently selected at the composition $ZrCr_2H_{1.5}$. Table 5.1 also reports published values for the enthalpy and entropy of this system for the purposes of comparison: the thermodynamic calculations carried out in this work yield values that are slightly higher than those of Pebler and Gulbransen [37], which again may simply be an artifact of the difference in hydride stability between the C14 structure studied by those authors and the C15 hydride studied herein.

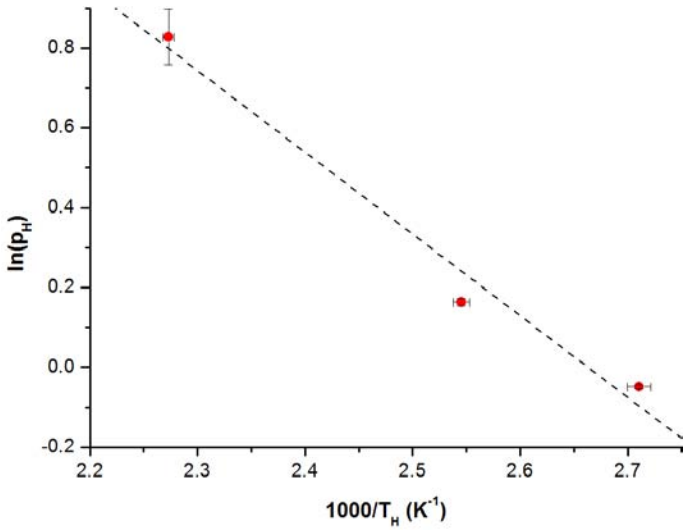

Figure 5.5: *A van't Hoff plot of the $ZrCr_2-H$ system, with the natural logarithm of the plateau pressure on the y-axis and the inverse of the hydriding temperature on the x-axis. Plateau pressures were taken at a concentration of 1.5 hydrogens per formula unit. A dashed line indicates the best fit to the experimental data (shown as red dots).*

	ΔH_H **(kJ/mol H_2)**	ΔS_H **(J (K·mol H_2)$^{-1}$)**
C15 $ZrCr_2-$ H (This work)	$-17(2)$	$-45(6)$
C14 $ZrCr_2-$ H [37]	-21.8	-55.3

Table 5.1: *Values of the hydriding enthalpy and entropy for $ZrCr_2 - H$ system, as determined from the van't Hoff construction. Hydriding pressures for this calculation were taken at the midpoint of the plateau ($H = 1.5$) for each temperature. Also shown are published entropy and enthalpy values, for comparative purposes.*

5.6 Crystallographic Features of the $ZrCr_2H_x$ hydride

5.6.1 Published Structures of $ZrCr_2H_x$

Hydrogen is accommodated in the $Fd\bar{3}m$ unit cell of the parent C15 intermetallic compound $ZrCr_2$ *via* an isotropic lattice expansion with no change in symmetry; structural parameters for $ZrCr_2D_{3.8}$ are given in Table 1.3. Three types of tetrahedral interstices exist in this structure: one surrounded by two zirconium and two chromium atoms (*2A2B*), one with one zirconium vertex and three chromium vertices (*1A3B*), and one surrounded by four chromium atoms (*4B*). An atomic diagram of the C15 unit cell of ZrV_2, showing an example of each of these interstice types, was shown in Figure 4.5 in Chapter 4, and provides an excellent depiction of the atomic structure of the analogous cubic $ZrCr_2$ compound.

The choice of interstice for hydrogen occupation is dictated by both geometric (*e.g.* size) and chemical (*e.g.* strength of metal-hydrogen interaction at each vertex) factors. Hong *et al.* [14] have shown *via* a first principles local-density-functional calculation that the binding energy of hydrogen is lowest at the *2A2B* site, but that the *1A3B* site is only slightly higher in energy. This is physically manifested in the room temperature C15 structure of $ZrCr_2H_x$ as a site preference for hydrogen on the *2A2B* site, up to $x \approx 3.5$; at higher concentrations, binding to the *1A3B* site becomes competitive and hydrogen begins to occupy that site as well [111].

As the temperature drops towards 250 K, rearrangement of the hydrogen atoms on these sites occurs and the *1A3B* site is gradually depopulated in favour of the *2A2B* site [49]. This shift in hydrogen site occupancy anticipates the structural transition at 250.2 K to an ordered, monoclinic phase of nominal composition $ZrCr_2H_4$: in this low temperature structure, the metal substructure is unchanged from the C15 polymorph, but the hydrogen atoms are ordered about the metal atoms, forming a distorted two-capped trigonal prism about the zirconium atoms and a tetrahedral or saddle-type coordination about the chromium atoms [49]. The configuration of the hydrogen atoms in this ordered superstructure is reminiscent of the hydrogen-metal anion complexes formed by several alkali-transition metal hydrides, *e.g.* the $[NiH_4]^{4-}$ complex of Mg_2NiH_4 [49]. Kohlmann *et al.* [49] have shown that the low-temperature $ZrCr_2H_4$ modification crystallises in the $C2/c$ space group, with $a = 9.3816(1)$ Å, $b = 5.4445(1)$ Å, $c = 9.3495(1)$ Å, and $\beta = 108.846(1)°$.

5.6.2 Structural study of the $ZrCr_2$ hydride

The synchrotron X-ray diffraction data of the cycled, hydrided $ZrCr_2H_x$ compound were collected on the ID31 beamline at the ESRF, under the same conditions as the diffraction data for the $ZrCr_2$ alloy as described in Section 5.3. The synthesis of the hydride is described in Section 5.4.1, where the sample in question was passed through fourteen hydriding/dehydriding cycles before characterisation. The collected synchrotron data were analysed using the Rietveld method (see Section 2.1.4), and followed a similar refinement procedure as per the alloy material. The diffraction data of $ZrCr_2H_x$ were fitted with a majority phase of C15 $ZrCr_2H_{3.0}$, along with minor proportions of the hydrided C14 and C36 polymorphs, to obtain an R_{wP} of 19.117.

During the refinement of the cubic $ZrCr_2H_{3.0}$ phase, the metal atoms were constrained to the 8*a* and 16*d* sites of the $Fd\bar{3}m$ space group as in the reported structure; as there were no free atomic coordinates due to the site symmetry, only

the global lattice parameters were refined. Atomic positions and occupancies of the hydrogen atoms could not be determined (see Section 2.1.2 for a discussion of the difficulty in determining hydrogen locations using X-ray diffraction) but the hydrogen concentration in the phase was calculated using the refined lattice parameter: in $ZrCr_2H_x$, hydrogen dissolves as a solid solution for concentrations of x greater than 3 and the cubic lattice parameter is therefore a linear function of x in the range $3 \leq x \leq 4$ [20]. Once the amount of hydrogen had been thus determined, the hydrogen positions and occupancies were assumed from the published deuteride structure [49, 111], with all of the hydrogen atoms accommodated at the *2A2B* interstice on the $96g$ site when $x < 3.5$.

The hydrided C14 hexagonal phase of $ZrCr_2H_x$ was modelled using the atomic coordinates of published room-temperature structure of $ZrCr_2D_{3.8}$ [110]; as the structure of the hydrided C36 analogue was not available, an approximation of the appropriate structure was created using an expanded unit cell containing metal atoms placed as in the ideal C36 structure [11] with lattice parameters initially set to $a_{C36} = a_{C14}$, $c_{C36} = 2c_{C14}$. Due to the low relative weight percents of the structures, the metal atom coordinates were not refined, and only the lattice parameters of each phase were freely varied. The hydrogen atom positions and occupancies of the C14 phase were also not refined; for ease of reference, the hydrided C14 and C36 structures were both assumed to have a total hydrogen concentration of $ZrCr_2H_3$.

The structural parameters of the primary C15 hydride are given in Table 5.2, whilst the refined lattice parameters of the minor C14 and C36 hydride phases are as follows: for C14 $ZrCr_2H_3$ of the $P6_3/mmc$ space group, $a = 5.3766(5)$ Å and $c = 8.7975(9)$ Å, and for C36 $ZrCr_2H_3$, with the same space group, $a = 5.3758(4)$ Å and $c = 17.585(2)$ Å. Figure 5.6 shows the observed diffraction pattern and calculated fit for the hydrided $ZrCr_2H_3$ material, along with the relative phase fractions of each of the three phases.

Parameter	*$ZrCr_2$ (alloy)*	*$ZrCr_2$ (dehydride)*	*$ZrCr_2H_{3.0}$*
Instrument	ESRF	ESRF	ESRF
Wavelength, λ (Å)	0.79996(1)	0.79996(1)	0.79996(1)
a (Å)	7.2069(2)	7.2075(2)	7.59395(6)
V (Å^3)	374.33(3)	374.42(3)	437.93(1)
R_{wP}	23.618	24.273	19.117
Zr1, 8a site $(0,0,0)$	-	-	-
B_{eq} (Å^2)	0.4	0.4	0.4
Cr1, 16d site $(\frac{5}{8},\frac{5}{8},\frac{5}{8})$	-	-	-
B_{eq} (Å^2)	0.4	0.4	0.4

Table 5.2: *Structural parameters for the C15 phase of the alloy $ZrCr_2$, the cycled C15 hydride $ZrCr_2H_{3.0}$, and the corresponding cycled, dehydrided compound. All structures crystallised in the $Fd\bar{3}m$ space group, and were determined from room temperature synchrotron diffraction patterns.*

The crystallographic study on the hydrided $ZrCr_2H_x$ material suggests that the relative proportion of the C15, C14 and C36 phases has not been altered as compared to the phase fraction of these phases in the diffraction data of the alloy (see Figure 5.1). However, the poor quality of the fit to the diffraction data in both cases does not allow a detailed analysis of these relative phase fractions. All three phases have absorbed hydrogen *via* a simple lattice expansion, with no change in symmetry. Although there exists no published data on the C36 hydride with which to compare the structure determined herein, the refined lattice parameters of the C14 hydride agree with those published by Irodova *et al.* [110]. The overall hydrogen content of the hydrided material $ZrCr_2H_x$ is approximated to be $x = 3$, based on the calculation of the hydrogen content in the cubic phase

and the estimations of the hydrogen content in the hexagonal phases.

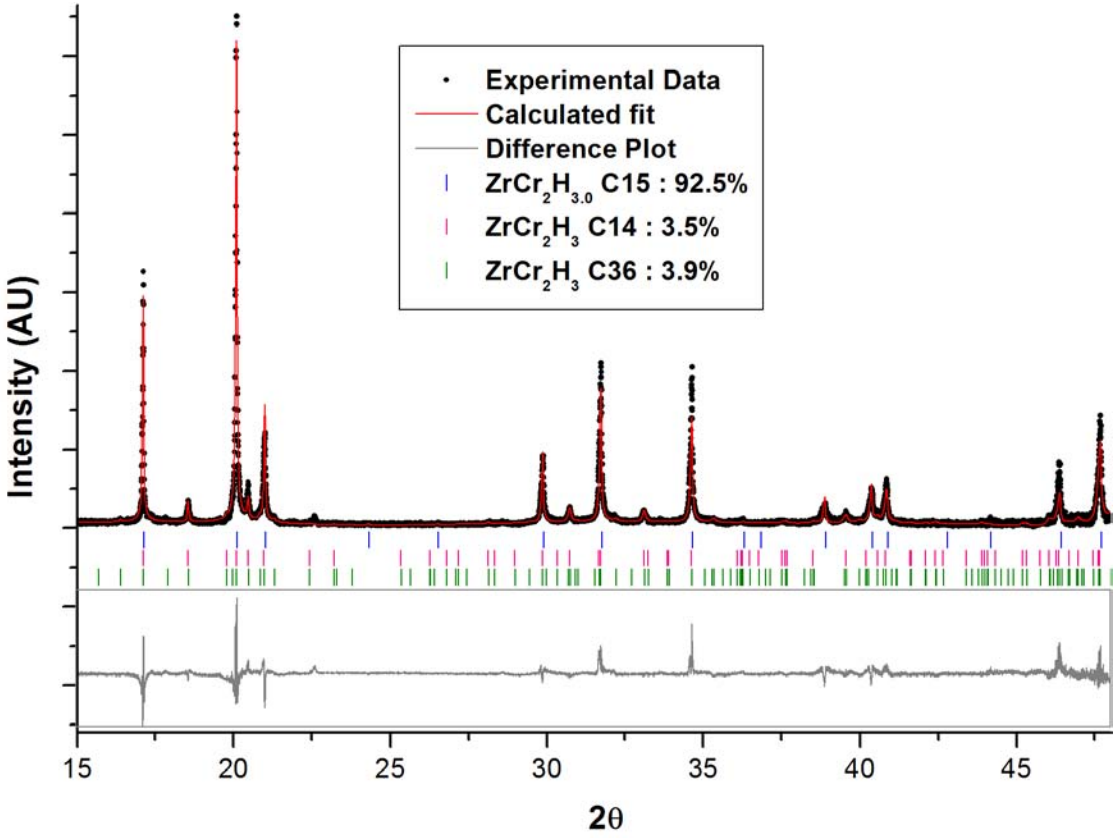

Figure 5.6: *Room temperature synchrotron diffraction pattern for the cycled, hydrided $ZrCr_2H_3$. Although the major phase is C15 $ZrCr_2H_{3.0}$, both the C14 and C36 hydrides are also present, with the relative weight percent of each phase indicated in the legend. The Bragg peak positions of all the fitted phases are shown by vertical tick marks. The difference plot between the experimental data (black dots) and calculated fit (solid red line) is shown as a grey line enclosed in a box.* $R_{wP} = 19.117$.

This calculated hydrogen content is lower than the hydrogen content of the $ZrCr_2-$ H system that was measured during the dehydriding reaction. As detailed in Section 5.4.2, $ZrCr_2$ has a reversible hydrogen capacity of 3.4 hydrogen atoms per formula unit under the pressure and temperature limits imposed by the hydriding apparatus. However, $ZrCr_2H_x$ with $x > 3$ has been shown [49] to gradually desorb hydrogen at room temperature, reaching equilibrium at $x \simeq 3$ over a period of days. As the logistical requirements of synchrotron diffraction measurement at

an international facility necessitated that the sample be synthesised some time before measurement (approximately one week elapsed between the final hydriding cycle and measurement) it is plausible that any hydrogen absorbed by the material in excess of 3 H/f.u. was lost by the time the diffraction data were collected.

As was observed for the diffraction data of the $ZrCr_2$ alloy, the difference plot between the observed diffraction data of the hydride and the calculated fit shows significant mismatched intensities for many of the structural reflections of the C14, C15 and C36 phases. This can again be credited to the presence of ordered Laves phase-type structures formed by layer stacking faults. Given the shift of these unmatched reflections as compared to the hydrogen-free data, it is evident that these unresolved layered structures also absorb hydrogen, and to a similar extent as the identified C14, C36 and C15 phases. This finding is in contrast to the report of Mestnik Filho *et al.* [48], where these authors observe a disappearance of the stacking fault structures upon hydrogen addition, with no suitable explanation given.

Finally, visual comparison of the diffraction data for the alloy and the hydride of the $ZrCr_2-$ H system, Figures 5.1 and 5.6, reveals that the width of the diffraction peaks for each of the hydride phases (C14, C15 and C36) has not increased upon repeated cycling of hydrogen through the $ZrCr_2$ material. This suggests that the $ZrCr_2-$ H system is not subject to a hydrogen induced decrepitation. A full peak profile analysis could not be carried out, due to the unresolved phases in the diffraction data.

5.7 Crystallographic Features of the cycled, dehydrided $ZrCr_2$

A crystallographic study of the cycled, dehydrided $ZrCr_2$ compound was also carried out on the ID31 beamline at the ESRF. The synthesis of this material is described in Section 5.4.2, where the sample in question was passed through fifteen hydriding/dehydriding cycles before it was examined. The collected synchrotron

data were analysed using the Rietveld method as per the $ZrCr_2$ alloy, which is described in Section 5.3, and followed an identical refinement procedure: the diffraction data of the dehydrided material were fitted with a majority phase of C15 $ZrCr_2$, along with minor proportions of the C14 and C36 polymorphs, to obtain an R_{wP} of 24.273. No amount of any $ZrCr_2H_x$ phase could be reliably refined, suggesting that the dehydriding reaction had gone to completion.

The refinement of the atomic positions, lattice parameters, weight percents and scale factors of the three $ZrCr_2$ phases in the dehydrided material follows precisely from that described previously for the alloy. The structural parameters of the primary C15 phase are given in Table 5.2, whilst the refined lattice parameters of the minor C14 and C36 phases are as follows: for C14 $ZrCr_2$, $a = 5.1013(4)$ Å and $c = 8.3048(7)$ Å, and for C36 $ZrCr_2$, $a = 5.1072(5)$ Å and $c = 16.629(2)$ Å. Figure 5.7 shows the observed diffraction pattern and calculated fit for the dehydrided $ZrCr_2$ material, along with the relative fractions of each of the three phases.

Comparison of Figures 5.1 and 5.7 reveals that the diffraction data of the dehydrided material are almost identical to those of the original alloy. The relative ratios of the C15, C14 and C36 phases appears to be altered only slightly upon cycling, where the minor difference in phase fractions may be due to the poor quality of the fit in both cases and the presence of unresolved phases. The difference plot between the calculated fit and the observed diffraction data of the dehydrided material shows considerable intensity mismatches to the Laves phase reflections, suggesting the presence of layer stacking faults, as were observed in the diffraction data of the alloy. For a fit using just the three Laves phase structures, the generated R_{wP} value for the refinement of the dehydrided diffraction data is comparable to the R_{wP} value obtained from the refinement of the alloy data: *viz.* 24.273 versus 23.618. The consistency of the quality of fit between these refinements suggests that the cycling process has neither created more stacking faults nor alleviated the existing ones: the relative amount of these ordered Laves-phase type structures appears to be constant between the dehydrided material and the

alloy.

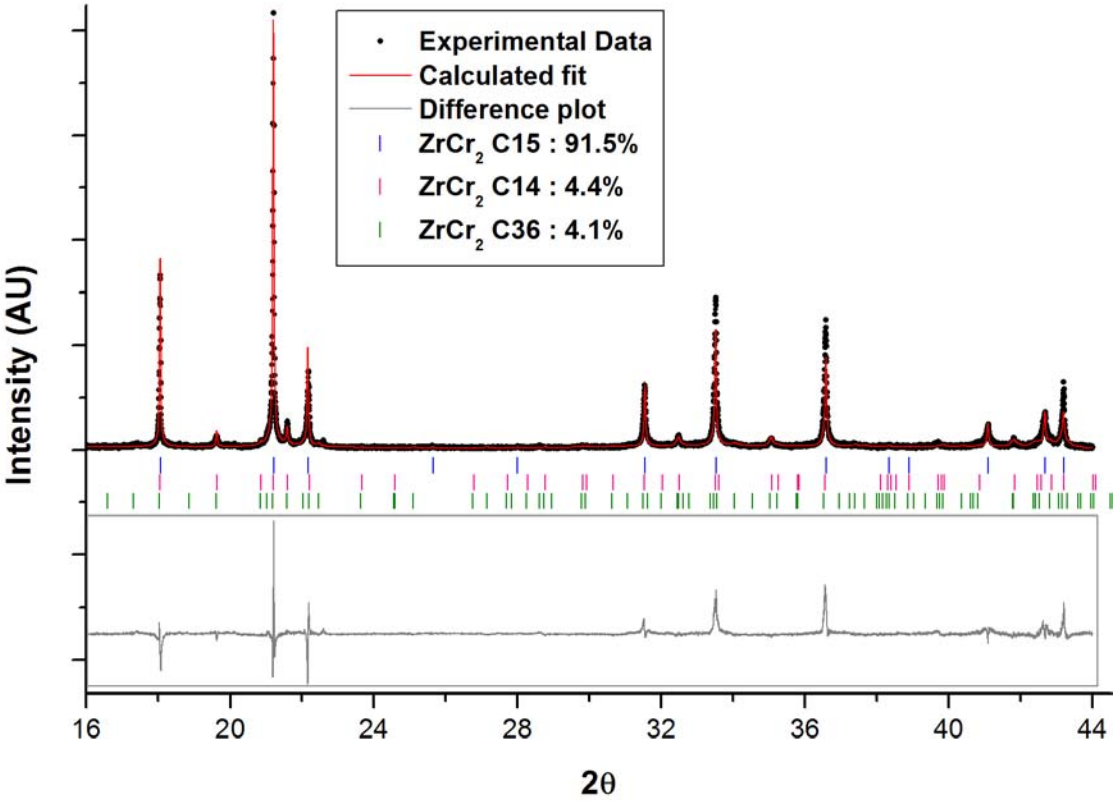

Figure 5.7: *Room temperature synchrotron diffraction pattern for the cycled, dehydrided $ZrCr_2$. Although the major phase is C15 $ZrCr_2$, both the C14 and C36 polymorph are also present, with the relative weight percent of each phase indicated in the legend. The Bragg peak positions of all the fitted phases are shown by vertical tick marks. The difference plot between the experimental data (black dots) and calculated fit (solid red line) is shown as a grey line enclosed in a box.* $R_{wP} = 24.273$.

Visual comparison of the diffraction data for the $ZrCr_2$ dehydride and alloy, shown in Figures 5.1 and 5.7, reveals that the width of the diffraction peaks for each of the hydride phases (C14, C15 and C36) has not increased upon repeated cycling of hydrogen through the $ZrCr_2$ material. This agrees with the peak width observations of the hydrided material discussed above. As a full peak profile analysis could not be carried out, due to the unresolved phases in the diffraction data, further interpretation of the peak widths in the diffraction data is not possible. However, when these considerations are combined with the measurements of the

dehydriding process discussed in Section 5.4.2, where it was shown that no increase in hydrogen capacity appeared in $ZrCr_2$ upon repeated cycling, the absence of a hydrogen-induced decrepitation in the $ZrCr_2-$ H system is suggested.

Finally, the cubic lattice parameter of the C15 $ZrCr_2$ phase – which is identical, within error, for the alloy and the dehydrided material – agrees with the published crystallographic data on this material [49]. Likewise, the refined lattice parameters of the C14 and C36 structures correspond favourably with the reported data [48, 113]; the slight deviations from the values determined herein and those published likely results from the low weight percent of these phases and their convolution with the unmodelled stacking defect structures. The published crystallographic parameters of the cubic polymorph are given in Table 1.3 for ease of reference.

5.8 Magnetic and Superconducting Behaviour in the $ZrCr_2-$ H system

Although a detailed magnetic study on the $ZrCr_2-$ H system has not yet been carried out, it has been shown [51] that both $ZrCr_2$ and its hydride $ZrCr_2H_3$ are simple Pauli paramagnets from 4.2 K to 300 K. The susceptibility of the hydride is slightly higher than that of the intermetallic compound, and Jacob *et al.* [51] report a temperature-independent susceptibility for C14 $ZrCr_2$ of 4×10^{-4} emu mol^{-1} Oe^{-1}, which increases to 1.16×10^{-4} emu mol^{-1} Oe^{-1} upon the addition of hydrogen. Unfortunately, magnetic measurements on the cubic intermetallic compound and its hydride are not available. A magnetic study by Abel and Craig [114] on susceptibilities of some transition metal Laves phase compounds did, however, note that χ_{300K} of $TiCr_2$ differed between the cubic and hexagonal polymorphs, and was $\sim 25\%$ larger in the C15 structure.

The superconductivity of the $ZrCr_2-$ H system has not been previously investigated. The literature reports only one brief reference to the superconductivity of $ZrCr_2$: an early study by Rapp *et al.* [115] of Laves phase compounds, in which they determined that $ZrCr_2$ is not a superconductor down to 0.03 K. Although

these authors report that the structure was 'mainly C15' (no phase fraction or details of other phases given) they note a room-temperature cubic lattice parameter $a = 6.942(2)$ Å, which is much lower than the expected value (see Table 1.3). The superconductivity, or absence thereof, of the hydride phase has not been previously discussed in the literature.

5.8.1 Magnetic behaviour of $ZrCr_2$ and $ZrCr_2H_3$

The magnetic behaviour of $ZrCr_2$ was examined over the temperature range 2 to 300 K; the as-synthesised alloy, as well as the cycled hydride and the dehydrided material, were all analysed. Figure 5.8 shows the variation in molar susceptibility with temperature for the alloy and the hydride; whilst Figure 5.9 depicts the same data for the dehydrided material. The room temperature susceptibilities of these materials are summarised in Table 5.3, along with the values of the critical field for the superconducting samples.

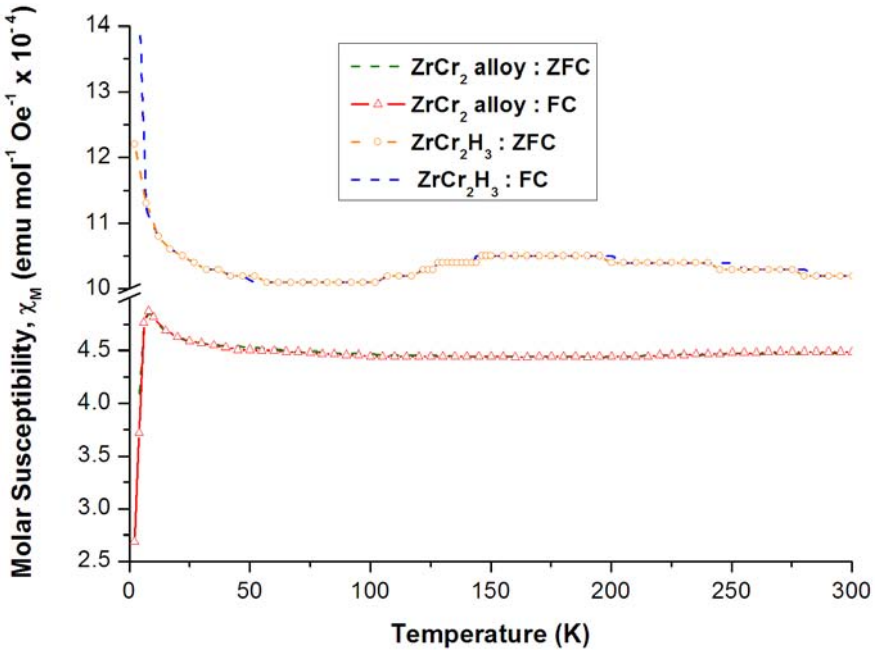

Figure 5.8: *Thermomagnetic analysis of the $ZrCr_2 - H$ series from 2 K to 300 K, showing the magnetic behaviour of the alloy (green and red lines) and the cycled hydride (orange and blue lines). Both samples were cooled to 2 K under two conditions: zero-field cooled (ZFC) and field cooled at 1000 Oe (FC). Under both regimes, the sample was then measured on warming under a field of 1000 Oe. Relative errors are smaller than the data points.*

The thermomagnetic analysis revealed that, above 8 K, the $ZrCr_2$ alloy displays a nearly temperature-independent susceptibility that is consistent with its expected Pauli paramagnetic behaviour. Comparison of the susceptibility measured at room temperature, as reported in Table 5.3, with the published value [114] shows that χ_{300K} determined in this work is 14% larger. Given that the material studied herein was composed of approximately 90% cubic $ZrCr_2$, and that the cited value stems from a measurement of the hexagonal phase, this discrepancy is within expectations.

At 8 K, a sharp drop in susceptibility is observed, consistent with the exclusion of magnetic flux that is associated with a dilute superconducting transition. The susceptibility does not become negative, however; which may indicate that the superconductivity arises from a phase which is only a minor component of this system.

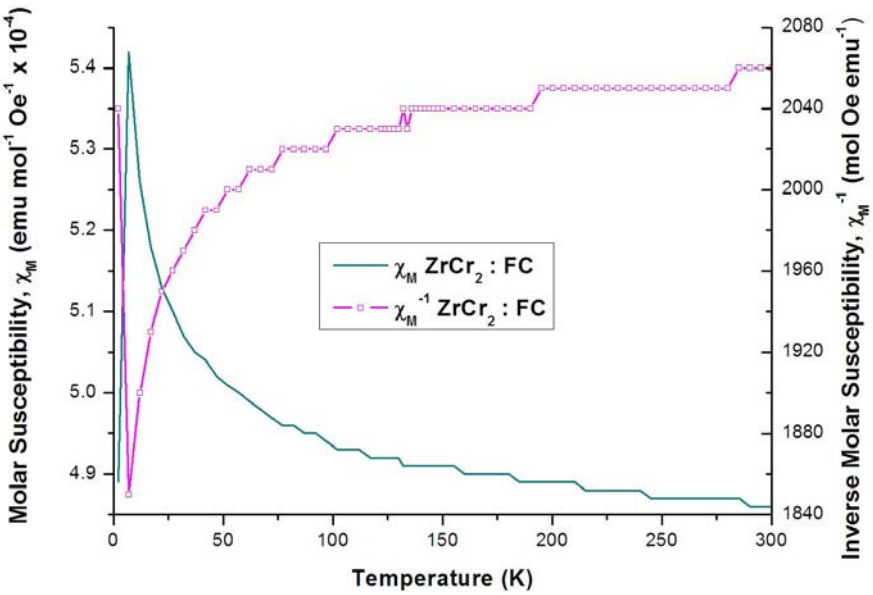

Figure 5.9: *Thermomagnetic analysis of the cycled, dehydrided $ZrCr_2$, showing the variation in the molar susceptibility, as well as its inverse, from 2 K to 300 K. The sample was cooled to 2 K under a field of 1000 Oe (FC), and the molar susceptibility (data as a cyan line, corresponding to the left axis) was then measured on warming under a field of 1000 Oe. Corresponding to the right axis is the inverse molar susceptibility, with the data shown as pink squares connected by a line. Relative errors are smaller than the data points.*

The $\chi(T)$ behaviour of the hydrided material indicated that it was a Pauli paramagnet in the temperature range studied, with a small, broad step in the susceptibility at 146 K. The cause of this step is not known, but may be due to a structural transition: the C15 and C14 hydrides both undergo order-disorder transitions with $T_c \simeq 250$ K and may well undergo other structural alterations of this type at lower temperatures which have not yet been investigated. Alternately, the small shift in susceptibility may be due to hydrogen ordering in the hydrided stacking fault structures. Without low-temperature diffraction data to supplement this $\chi(T)$ data, it is difficult to conclusively identify the nature of this previously unobserved step in the susceptibility curve of $ZrCr_2H_3$. The measured value of χ_{300K} diverges slightly from the value reported by Jacob *et al.* [51], where the 13% difference likely results from alterations in $N(\epsilon_F)$ between the C15 hydride that was examined herein and the C14 hydride that was studied in the cited work.

	$ZrCr_2$ alloy	$ZrCr_2$ dehydride	$ZrCr_2H_3$
χ_{300K} (emu mol^{-1} Oe^{-1})	$4.482(2) \times 10^{-4}$	$4.860(2) \times 10^{-4}$	$1.019(1) \times 10^{-3}$
^1T_C (K)	8 ± 2	7 ± 5	-
H_{c1} (Oe)	200(4)	≈ 0	≈ 0
H_{c2} (Oe)	$3.00(6) \times 10^3$	$3.00(3) \times 10^3$	$3.00(4) \times 10^3$

[1]Temperature of the possible superconducting transition

Table 5.3: *Experimentally observed susceptibilities and transition temperatures for the $ZrCr_2$ alloy, cycled $ZrCr_2H_3$, and the corresponding cycled, dehydrided compound. The critical field values at 2 K, as determined from the hysteresis measurements, are also shown.*

The dehydrided material was qualitatively very similar to the virgin alloy in regards to its magnetic behaviour, as Figure 5.9 shows. As in the alloy, a superconducting transition is observed at approximately 8 K; above this temperature, the susceptibility varies little with temperature and resembles that of a Pauli paramagnet. The susceptibility at 300 K, which is reported in Table 5.3, is insignificantly higher than that of the original alloy. A plot of $\chi^{-1}(T)$ (see Figure 5.9) reveals that

the low-temperature transition in this compound does not appear to be related to a magnetic ordering phenomenon: although the drop in magnetisation below 8 K may have been explained by an antiferromagnetic transition, the shape of the inverse susceptibility curve clearly negates this postulate.

Further indications of superconductivity in this material may be gleaned from analysis of the dependence of the magnetisation on the field strength: a plot of $M(H)$ for the $ZrCr_2-$ H system at 2 K is shown in Figure 5.10. It is evident that at least partial flux exclusion occurs for all members of the system below an applied field of 3 kOe, with the superconducting effect largest for the alloy sample, and smallest for the hydride. The shape of the $M(H)$ curve for the virgin alloy is suggestive of a type II superconductor, and the values of the critical field are reported in Table 5.3, along with the H_{c1} and H_{c2} values for the hydrided and the dehydrided material. The weakly negative value of the magnetisation in the superconducting region for these materials indicates that either the superconducting transition is not complete ($T_c < 2$ K) or that the superconductivity arises from only a minor component of the materials – for example, an impurity phase.

As a crystallographic study (see Section 5.3 and 5.7) suggested that both the alloy and the dehydrided $ZrCr_2$ material in this study contained only C15 $ZrCr_2$, the C14 and C36 polymorphs, and unresolved Laves phase-type structures formed from layer stacking faults, it is likely that the superconducting properties arise from one of these phases. The $ZrCr_2H_3$ material was composed of the hydrided analogues of these same materials, as shown in Section 5.6, with no other impurity phases detected; thus, it is apparent that the addition of hydrogen does not destroy the superconductivity. However, the reduction in intensity of the diamagnetic response of the hydride (as compared to the alloy and the dehydrided material) and the absence of a superconducting transition in the thermomagnetic analysis (see Figure 5.8) suggests the dilution of the superconducting phase in the hydrided material.

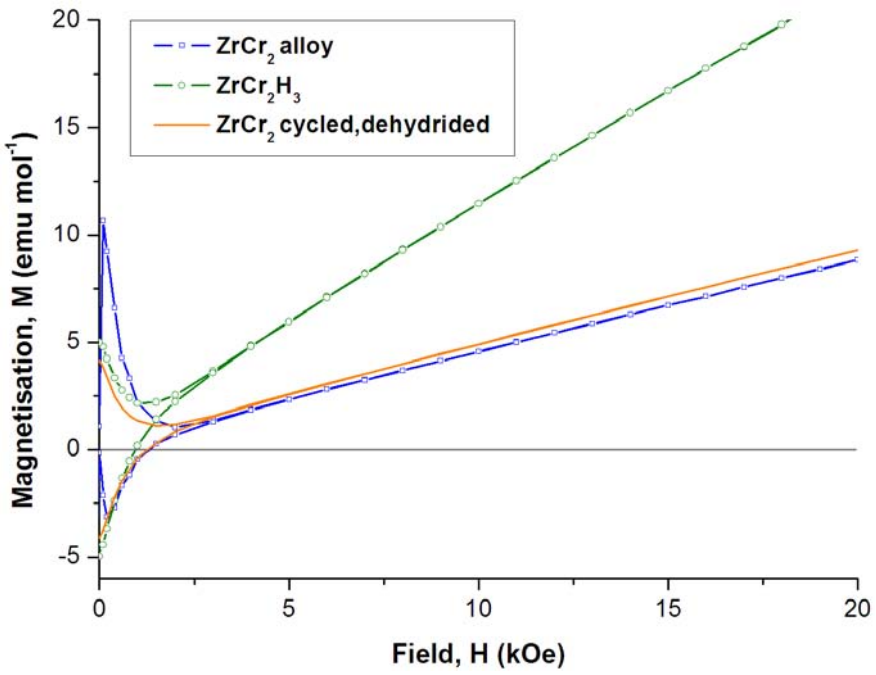

Figure 5.10: *A plot of the field dependence of the magnetisation for the $ZrCr_2 - H$ system at 2 K, showing the first and fourth quadrants only. The data for the alloy are shown as squares connected by a blue line; the dehydrided sample are in orange, and the data for $ZrCr_2H_3$ are shown as circles joined by a green line. Relative errors are smaller than the data points.*

Without a complete structural analysis of the diffraction data due to the presence of unresolved phases, it is difficult to pinpoint the cause of the superconductivity. The only phases for which superconductivity has been explored are the starting reagents – Cr is not a superconductor, and Zr has a very low T_c of 0.61 K [81] – and the C15 alloy, which according to a cursory review by Rapp *et al.* [115], is not superconducting. The electrical properties of the C14 and C36 polymorphs, and particularly of the ordered Laves phase-type structures, has not been previously determined. It is interesting to note, however, that the analogous Cr_xTi_{1-x} alloy is a superconductor, with $T_c = 4.2$ K [81]. Thus, it is plausible to theorise that the observed superconductivity in the $ZrCr_2-$ H system arises from either a hexagonal $ZrCr_2$ structure, or one of the unresolved phases created by layer stacking faults in the known $ZrCr_2$ Laves phase polymorphs. In this case, the appearance of a dilute superconductivity in the hydrided sample can be at-

tributed to a small percentage of $ZrCr_2$ in the sample, of a sufficiently low phase fraction that it could not be satisfactorily refined in the crystallographic analysis.

The magnetisation field dependence of $ZrCr_2H_3$ across a range of temperatures in shown in Figure 5.11, demonstrating the disappearance of the superconductivity at temperatures greater than 2 K. The $M(H)$ behaviour above this point is relatively temperature-independent and increases only slightly with the applied field, which is suggestive of a Pauli paramagnet. This observation is consistent with the thermomagnetic data for $ZrCr_2H_3$, shown in Figure 5.8.

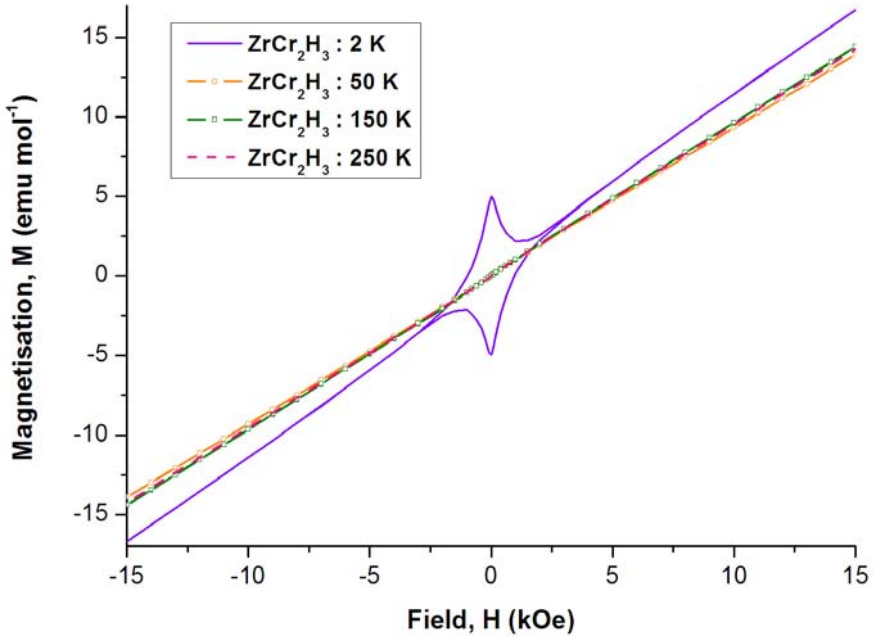

Figure 5.11: *A plot of the field dependence of the magnetisation for $ZrCr_2H_3$ at several temperatures, showing the region from -15 kOe to 15 kOe only. The magnetisation was measured at 2 K (purple line), 50 K (orange line with open circles), 150 K (green line with open squares), and 250 K (pink dashed line). Relative errors are smaller than the data points.*

These $M(H)$ data of the $ZrCr_2-$ H system can be easily translated into a series of Arrott plots: Figure 5.12 illustrates the Arrott plots of the dehydrided $ZrCr_2$ material, along with data from the alloy at 2 K, and Figure 5.13 corresponds to the data for the hydride. Discussing first the plots for the hydrogen-free materials, it is evident that the Arrott plots for the dehydrided $ZrCr_2$ collected

at 50 K and 250 K exhibit substantial low-field curvature, whilst the high field data can be described by a linear trend line. Any linear regression would clearly yield a line with a negative $y-$intercept, indicating that $ZrCr_2$ has zero saturation magnetisation and is not magnetically ordered at these temperatures. The low field curvature likely results from microstructural inhomogeneities in the material, arising from the previously demonstrated structural degeneracy of $ZrCr_2$.

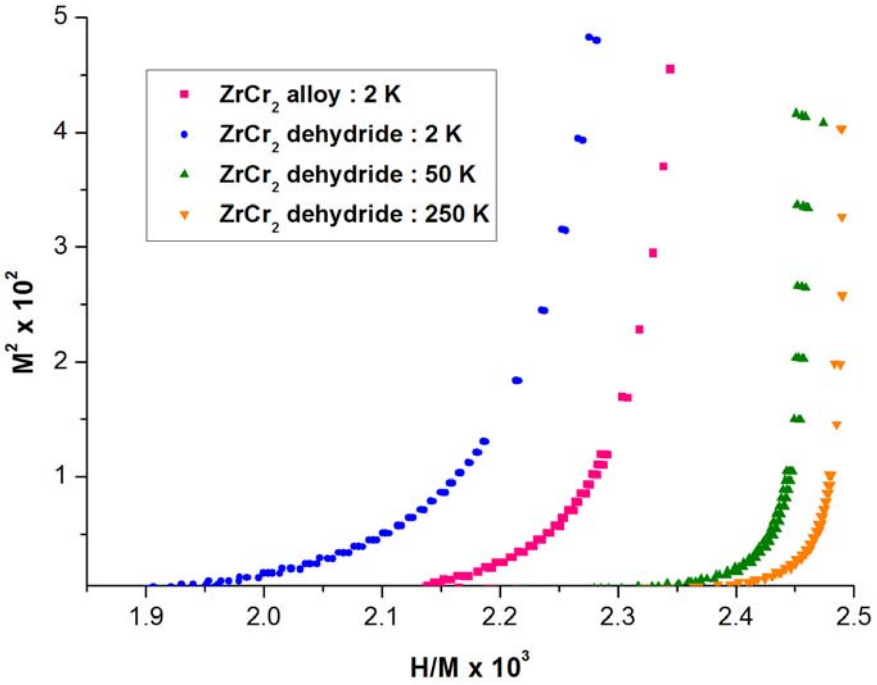

Figure 5.12: *An Arrott plot for the cycled, dehydrided $ZrCr_2$ material at various temperatures, with the square of the molar magnetisation, M, on the y-axis and the applied field, H (in Oe), over M, on the x-axis. Data are shown over the range 2 K - 250 K, as indicated in the legend. An Arrott plot of the virgin alloy at 2 K is shown for comparison. Relative errors are smaller than the data points.*

The 2 K Arrott plots of both the alloy and the dehydrided material deviate substantially from linearity, exhibiting significant high field curvature as compared to the higher temperature $M(H)$ measurements. Although these deviations can be brought about by a variety of causes, it is reasonable to surmise that the high field additions may be due to spin fluctuations in the system, perhaps related to the superconductivity [70]. Regardless of the curvature, any attempt to describe the

data with a linear or exponential expression results in a trendline with a negative $y-$intercept, indicating no magnetically order at 2 K.

The series of Arrott plots collected for $ZrCr_2H_3$, shown in Figure 5.13, are qualitatively very similar to those for the dehydrided material. In the temperature range 50 K to 250 K, the plots show low field curvature, which is related to the distribution of structurally distinct phases in the material. If these deviations are discarded, the data can be described by a linear trendline that will, in all cases, have a negative intercept, thus indicating that the material is not magnetically ordered in this temperature range. The Arrott plot measured at 2 K is vastly different from those collected at higher temperatures, however, and deviates substantially from linearity up to the largest applied field used. As was observed for the hydrogen-free compound, this is likely caused by spin fluctuations related to the observed superconductivity. Although the curvature can be described by an exponential function, the fitted curve yielded a negative $y-$intercept, indicating that $ZrCr_2H_3$ is not magnetically ordered down to 2 K.

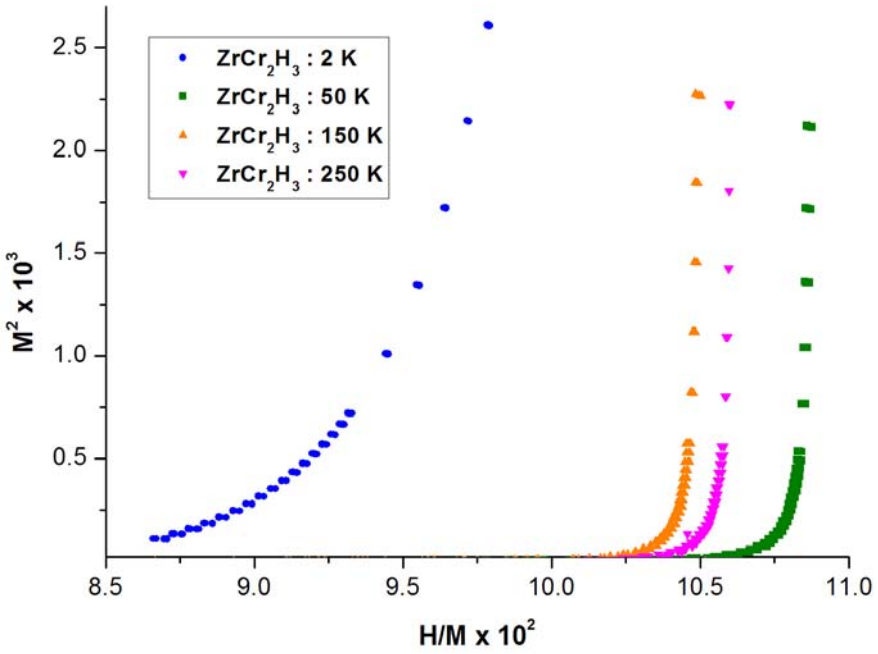

Figure 5.13: *An Arrott plot for the hydrided $ZrCr_2H_3$ at various temperatures, with the square of the molar magnetisation, M, on the y-axis and the applied field, H (in Oe), over M, on the x-axis. Data are shown over the range 2 K - 250 K. Relative errors are smaller than the data points.*

5.9 Electronic and Dielectric Properties of the $ZrCr_2-H$ system

Microwave resonance spectra of the $ZrCr_2-H$ system were collected at room temperature: both the cycled, dehydrided material and $ZrCr_2H_3$ were analysed. The spectra of these two compounds in the electric field antinode is shown in Figure 5.14, whilst the spectra in the magnetic field antinode is shown in Figure 5.15; summarised results of these measurements are given in Table 5.4. Each sample was separately measured at least six times, and the frequency shift and bandwidth change for these measurements, as compared to the empty cavity, was averaged and its standard deviation determined. Estimation of the errors on the extracted electronic and dielectric values proved more difficult; Section 2.3.4.1 details an appropriate method for estimating these errors.

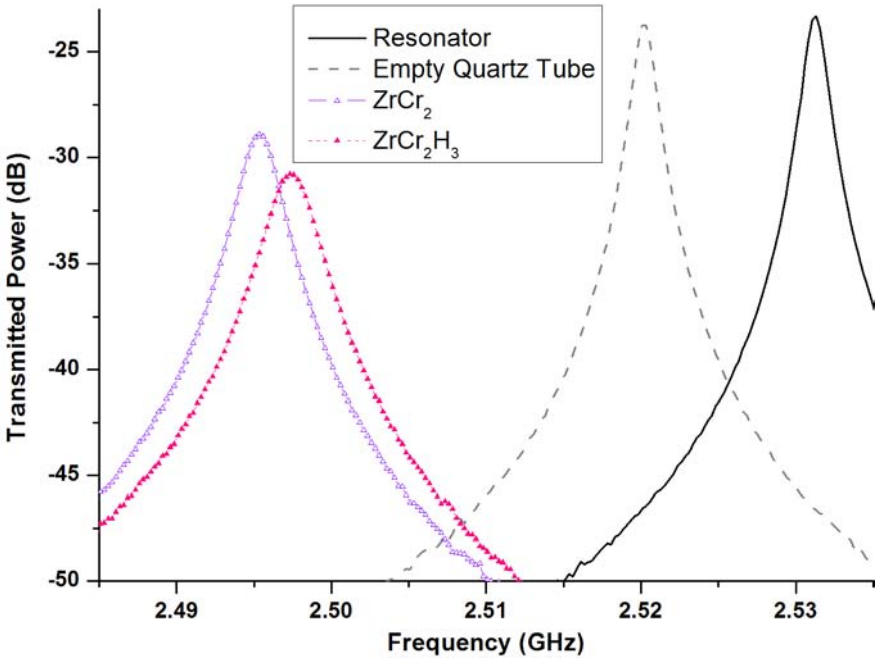

Figure 5.14: *Resonance spectra for the microwave conductivity measurement of $ZrCr_2$ (purple line with open triangles) and its hydride (pink line with closed triangles), showing transmitted power versus frequency in the electric field antinode of the cavity. In addition to the measured compounds, the spectra for the empty resonator cavity (black line) and an empty quartz tube, used to contain the compounds (broken grey line), are shown for comparison. Relative errors are smaller than the data points.*

When inserted into the electric field antinode of the resonator, both $ZrCr_2$ and its hydride produce a large shift in the resonance frequency of cavity, indicating that both materials are substantially polarised in the electric field. This polarisation is in accordance with the expected behaviour of a good metallic conductor, in which the free conduction electrons may readily move to oppose the applied electric field. The insertion of $ZrCr_2$ into the cavity causes an increase in the bandwidth of the resonance frequency peak, due to loss components associated with the polarisation; the hydrided material is slightly more lossy than the intermetallic compound.

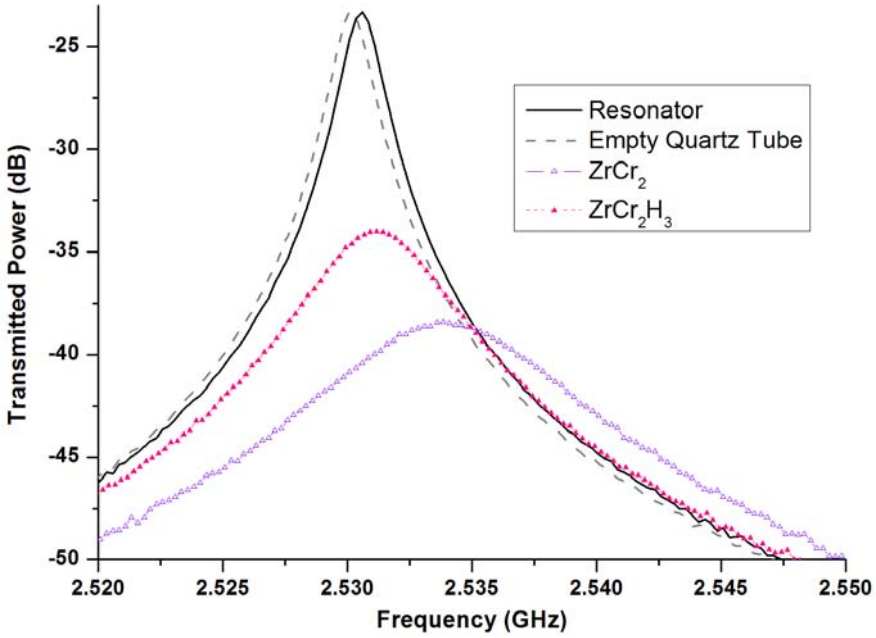

Figure 5.15: *Resonance spectra for the microwave conductivity measurement of $ZrCr_2$ (purple line with open triangles) and its hydride (pink line with closed triangles), showing transmitted power versus frequency in the magnetic field antinode of the cavity. In addition to the measured compounds, the spectra for the empty resonator cavity (black line) and an empty quartz tube, used to contain the compounds (broken grey line), are shown for comparison. Relative errors are smaller than the data points.*

In contrast, the insertion of $ZrCr_2$ into the magnetic field antinode of the resonator brings about an increase in the resonance frequency and an increase in the bandwidth of the signal. The behaviour of the hydride is qualitatively

similar, but diluted – the frequency shift is smaller, and the bandwidth increase less drastic. In both cases, the expansion of the resonance frequency signal stems from eddy current losses that are associated with a high metallic conductivity, and is typical for metals in a magnetic field. This bandwidth increase may also be related to magnetic loss components if the magnetic polarisation, μ, is not 1. The positive frequency shift results from an effective reduction in cavity volume caused by partial screening of the metal particles, where this screening may only arise in particles with a radius larger than the skin depth. In these large grains, the interior of particle will be shielded from the external magnetic field, thus creating an apparent reduction in the volume of the cavity.

As discussed in Section 2.3.4.1, the skin depth of $ZrCr_2$ is not known as its bulk conductivity has not been previously reported. As a rough estimate, it may be approximated using the known skin depths of the related compounds ZrV_2 and $ZrMn_2$:

$$\delta(ZrCr_2) = \frac{\{\delta(ZrV_2) + \delta(ZrMn_2)\}}{2} = 11\ \mu\text{m} \tag{5.1}$$

Using this approximation, any particle with a diameter greater than 25 – 30 μm will be partially shielded in the magnetic field antinode. As the skin depth of $ZrCr_2H_3$ is also unknown, it is assumed herein that this is a suitable size approximation for the shielding of the hydride as well.

As was discussed in Section 4.8, the distribution of particle radii is more telling than the average size of the particles in determining the magnitude of a frequency shift in the magnetic field antinode, due to the mathematical nature of Equation 4.4. A few large particles can dominate the observed resonance frequency of a material; indeed, if the observed resonance shift induced by $ZrCr_2$ in the magnetic field is calibrated against a steel ball of known magnitude, it is readily determined that less 3% of the total sample volume is shielded. The same calculation for $ZrCr_2H_3$ indicates that approximately 0.5% of the hydride is screened against the magnetic field. This quantification indicates that the frequency shift induced by insertion of $ZrCr_2$ and its hydride results from a very small fraction of the total

material in both cases, and can likely be ascribed to a few, much larger particles intermixed amongst a collection of small grains with radii less than the skin depth.

Knowledge of the particle sizes in the $ZrCr_2-$ H system is important in determining the suitability of the 'collapsed cylinder model' for the study of these materials. As discussed in Section 2.3.4.1, two boundary conditions must be fulfilled: the first states that the particle size must be much smaller than the wavelength of the electromagnetic field resonating in the cavity; for the 2.5 GHz hairpin used in this work, this translates into a restriction of particle sizes to less than 0.12 m. The second boundary condition mandates that the particle radius must also be smaller than the skin depth, which is approximated herein as 11 μm. The previous discussion of the frequency shift in the magnetic field antinode revealed that the second condition is not completely fulfilled, with approximately 3% of the dehydrided material, and 0.5% of the hydride, possessing radii larger than the skin depth. However, as the majority of the particles in the $ZrCr_2-$ H system remain within the skin depth limit, the boundary conditions of the collapsed cylinder model are considered to be suitably fulfilled for the purposes of this study.

	$ZrCr_2$ dehydride	$ZrCr_2H_3$
Δf ($\times 10^7$ Hz)	−3.61(2)	−3.42(3)
$\Delta\Gamma$ ($\times 10^5$ Hz)	1.3(3)	1.88(7)
ε_{1eff}	32(3)	20(2)
ε_{2eff}	−27(5)	−7(1)
$\tan\delta_{eff}$	0.84(9)	0.34(5)
σ_{eff} (Ω^{-1} m^{-1})	3.8(7)	0.9(1)

Table 5.4: *Microwave resonance parameters in the electric field antinode for dehydrided $ZrCr_2$ and the $ZrCr_2H_3$, showing the shift in bandwidth and frequency as compared to the resonance parameters of the empty cavity. Extracted dielectric constants, loss tangents and effective conductivities for the $ZrCr_2 - H$ system are given.*

Translation of the bandwidth changes and frequency shifts that occur in the electric field antinode into the fundamental properties of permittivity, loss tangent and effective conductivity provides a quantitative description of the dielectric behaviour of the $ZrCr_2-$ H system. These calculated values are given in Table 5.4. To examine first the permittivities, it can be seen that ε_{1eff} is re-

duced as the intermetallic compound absorbs hydrogen, indicating a reduction in the polarisability. The permittivity at microwave frequencies contains both electronic and ionic components, and as the ionic component is expected to increase concomitant to the hydriding process (due to the polarisability of hydrogen and its ready mobility in this system) there must be a significant decrease in the electronic component to produce the observed net diminishment of ε.

The reduction in electronic polarisability results from a decrease in the population of the conduction electron band; as the imaginary part of the permittivity relates directly to the number of valence electrons, it is therefore expected that $|\varepsilon_{2eff}|$ will decrease as hydrogen is absorbed. This prediction is in accordance with the calculated values; moreover, derivation of σ_{eff} from the permittivity shows that $ZrCr_2H_3$ is substantially less conducting than the hydrogen-free intermetallic compound.

Finally, examination of the ratio between the real and imaginary components of the permittivity yields the loss tangent, $\tan\delta_{eff}$, which relates to energy lost in the polarisation process. $ZrCr_2$ is shown to have a higher loss tangent than its hydride, suggesting that the dehydriding process has introduced additional loss components into the system. The origin of the increased loss is unknown, but may be related to the generation of very small fractions of impurity phases or minor amounts of decrepitation that could not be detected in the crystallographic analysis.

In determining the provenance of the hydrogen-induced drop in conductivity in the $ZrCr_2-$ H system, it is useful to refer to an electronic density of state diagram for this system. Hong *et al.* [14] have applied a first principles, local-density-functional calculation to study a series of ZrM_2 Laves phases and their diluted hydrides $ZrM_2H_{0.5}$, including the C15 structure with M = Cr; unfortunately, band structure diagrams of this system at higher hydrogen concentrations are not available. The calculated total density of states for $ZrCr_2$ and $ZrCr_2H_{0.5}$ is given in Figure 5.16, where it is readily seen that hydrogen absorption shifts the Fermi

level past the well-defined valley separating the bonding and anti-bonding states in this system, causing an increase in $N(\epsilon_F)$ at larger hydrogen concentrations.

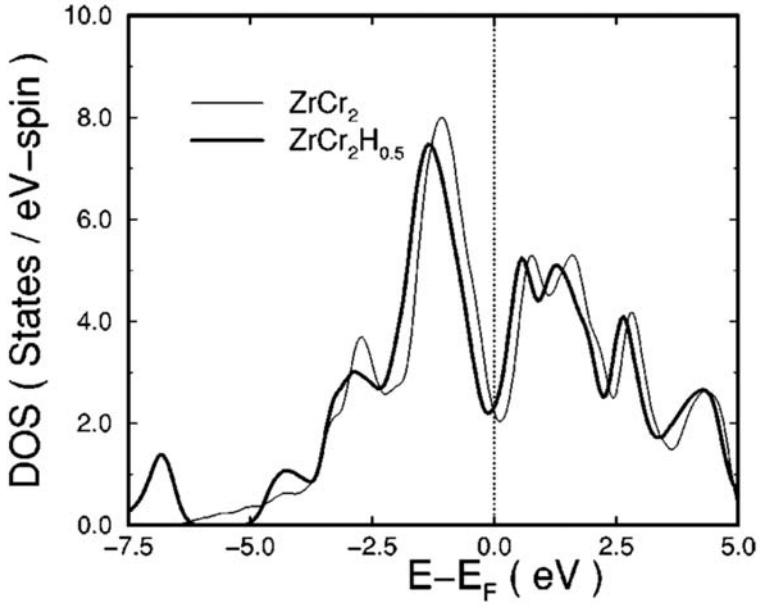

Figure 5.16: *The total density of states for $ZrCr_2$ and $ZrCr_2H_{0.5}$. Figure from* [14].

Hong *et al.* [14] have shown that the interstitial hydrogen atom in $ZrCr_2H_{0.5}$ is negatively charged as a result of charge donation from the host metal to the hydrogen. Supporting the hypothesis that hydrogen is negatively charged, or at least in a neutral state, van Midden *et al.* [52] have analysed the fate of the hydrogenic electron and determined that it remains localised on the hydrogen atom, rather than becoming a free conduction electron. These theoretical results may explain the observed decrease in conductivity upon hydrogen addition: electron transfer from the metal to the hydrogen, to achieve even a partially negative state, would be accomplished *via* depletion of the conduction electron band, which would trigger a drop in conductivity concomitant to the hydriding process.

5.10 Summary and Conclusions

To summarise, the cubic phase of the intermetallic compound $ZrCr_2$ was synthesised *via* arc-melting, then cycled with hydrogen to produce a material with net hydrogen content $ZrCr_2H_3$. Thermodynamic data were collected on the hydriding process during this cycling, and used to calculate the enthalpy and entropy of the hydriding reaction. A crystallographic study on the $ZrCr_2-$ H system revealed that the annealing process on the virgin alloy had not been entirely successful, as a small percentage of the hexagonal Laves phases remained in the material; moreover, the presence of an ordered Laves phase-type type structure formed by layer stacking faults in the original three phases was suggested. These hexagonal impurities and even the stacking fault structures persisted in the hydrided material, absorbing hydrogen to a relatively equal extent as the majority C15 phase; for all phases, hydrogen absorption occurred with no structural change, excepting lattice expansion. X-ray diffraction data of the cycled, dehydrided compound were nearly identical to that of the original alloy, with the same ratio of non-cubic $ZrCr_2$ phases and no evidence of any decrepitation induced by the hydrogen cycling process.

Magnetic measurements on the $ZrCr_2-$ H system indicated that both materials behave as simple Pauli paramagnets down to 8 K, with the hydride having a slightly higher susceptibility than the hydrogen-free phase. Small variations in $\chi(T)$ for $ZrCr_2H_3$ were accredited to structural transitions in the C14 and C15 phases, possibly related to low temperature hydrogen ordering. At 8 K, both $ZrCr_2$ and its hydride underwent a dilute superconducting transition; the weakened flux exclusion that was observed for $ZrCr_2H_3$ suggested that the superconductivity arose from a hydrogen-free $ZrCr_2$ phase that persisted in small quantities upon hydrogen addition. As the cubic phase has been previously shown [115] to be non-superconducting, the observed superconductivity is thought to develop in either the hexagonal C14 or C36 phases, or in the ordered Laves phase-type stacking fault structures. Across the $ZrCr_2-$ H system, the Arrott plots revealed that the materials were not magnetically ordered at all temperatures measured, as

well as suggesting that the superconductivity in this system may be tied to spin fluctuations.

The dielectric permittivities and the effective conductivities at room temperature for cycled, dehydrided $ZrCr_2$ and its hydride were determined using a microwave cavity resonator. Both materials were found to be metallic conductors undergoing a large polarisation in the electric field; however, it was revealed that the hydriding process induced a decrease in the conductivity. Comparison with published density of state diagrams suggested that this hydrogen-induced drop in conductivity resulted from charge transfer from the host metal to the hydrogen atom, effectively depleting the conduction electron band. Finally, qualitative analysis of the frequency shift induced by the introduction of $ZrCr_2$ and $ZrCr_2H_3$ into the magnetic field antinode suggested that the small, positive frequency shift was caused by a few very large particles in these materials.

From these collected data, several important conclusions can be drawn, the first of which is regarding the hydrogen-induced decrepitation that is generally observed in metal-hydrogen systems. In contrast to expectations, $ZrCr_2$ appears to undergo no particle size reduction upon repeated hydrogen cycling. As shown in Section 5.4.2, this intermetallic compound is capable of absorbing its full capacity of hydrogen immediately upon activation, suggesting that hydrogen diffusion through the material occurs so readily that particle cracking does not occur. This unusual behaviour has not been previously commented upon in the literature. The lack of decrepitation may be tied to the isotropic nature of the lattice expansion that occurs concomitant to the hydriding process, which is not expected to generate significant strain in the material as compared to an anisotropic expansion process. It is plausible that the amount of hydrogen that is absorbed is also a factor: 3 hydrogens per formula unit may simply not be enough to cause decrepitation in the $ZrCr_2-$ H system. The 'elasticity' of $ZrCr_2$ is further demonstrated by its structural degeneracy and the variety of Laves phase structures it readily forms. The strain in the lattice that hydrogen-induced expansion would create may also

be released by the creation of stacking faults in the Laves phase structures, where such faults would furthermore permit the ready passage of hydrogen through the material without the need for particle cracking.

This polymorphism presented a minor problem in the samples synthesised herein: despite a long annealing step, the alloy still contained other non-cubic $ZrCr_2$ phases. Although these phases were readily identified *via* X-ray diffraction, the multi-component nature of the sample made a quantitative analysis of the magnetic and electronic properties difficult to achieve. It is evident that either the hexagonal C14/C36 $ZrCr_2$, or the structures formed by stacking faults in these phases, is a hitherto unknown low temperature superconductor, and the flux exclusion that occurs below T_c therefore obscures any possibly interesting magnetic behaviour in the majority cubic phase at this temperature. Moreover, these secondary phases may also contribute to the measured polarisability and conductivity in the $ZrCr_2-$ H system; as these phases have never been explored using a microwave resonance technique before, it is difficult to predict their influence on the measurements. However, as the major phase in the material is the cubic $ZrCr_2$ / $ZrCr_2H_3$, it is assumed that the impact of the secondary phases will be relatively low.

The addition of hydrogen to the $ZrCr_2$ intermetallic compound induces several interesting electronic and magnetic changes. Structurally, the effect of hydrogen is minor —it brings about no change in the symmetry of the crystal structure, as it is accommodated on interstitial sites *via* a simple isotropic lattice expansion. However, magnetic measurements showed that hydrogen absorption more than doubled the room temperature susceptibility of the Pauli paramagnetic material. This can be tied to an increase in $N(\epsilon_F)$, with theoretical studies [14,52] suggesting an electron transfer from the metal host to the interstitial hydrogen atoms as the hydrided phase forms. The novel experimental measurements of conductivity in the $ZrCr_2-$ H system carried out in this work have validated these theoretical predictions, showing a clear decrease in conductivity in the hydrided compound

as compared to the parent intermetallic. It is evident that despite the lack of significant structural alterations, the addition of hydrogen to $ZrCr_2$ brings about a cascade of interesting electronic and magnetic changes.

5.11 Future Work

Several interesting pathways for further research opened up during the course of this investigation; unfortunately, for reasons of both limited funds and restricted time, they could not be pursued. These additional research questions are detailed below and it is hoped that they may be explored in the near future.

As the crystallographic study of the $ZrCr_2-$ H system revealed, the synthesised alloy was not solely composed of the C15 Laves phase structure. As evidenced both by other researchers [48, 109] and the binary phase diagram [26], $ZrCr_2$ readily crystallises in a variety of structures, which makes the generation of a pure, single phase sample rather difficult. Considering the potentially deleterious influence of these secondary phases on the measured properties of this material, a detailed experimental study devoted to obtaining a uncontaminated cubic sample would be worthwhile. Analysis of the variables that may influence the relative concentration of the phases in $ZrCr_2$ – *e.g.* annealing time and temperature, atmosphere during annealing, melting technique – may help to provide a new synthetic route for synthesising pure samples of the C15 structure.

Connected to this polymorphism, an investigation of the ordered Laves phase-type structures that arise in this system due to stacking faults could prove highly fruitful. The crystallographic study carried out in this work was insufficient to resolve these structures and fully identify them. Analysis of the diffuse scattering, perhaps *via* a total scattering technique or PDF analysis, could provide a tool with which the complex structures of these stacking fault phases could be elucidated.

The magnetic study carried out over the course of this work suggested that a superconducting transition occurred in $ZrCr_2$ below 8 K; this transition seemed to

persist in the hydrided material but may simply arise from lingering minute portions of an unhydrided phase. In order to validate the apparent superconductivity, further work needs to be done. Synthesis of a single phase C15 material, as discussed above, will allow verification of whether the superconductivity arises from the cubic phase; if not, synthesis and characterisation of the hexagonal phases should be carried out. Heat capacity measurements, in order to determine the variation in entropy around T_c, will also be useful in proving the existence of superconductivity in these materials.

On a final note, it would be interesting to examine the $\sigma(T)$ dependence of the $ZrCr_2-$ H system, as this can provide telling clues as to the electronic nature of a material. Unfortunately, variable temperature dielectric measurements could not be carried out in the microwave resonator used in this study. Alteration of the resonator so as to allow low temperature determinations of σ_{eff} for the $ZrCr_2-$ H system would certainly prove useful; in particular, it would be interesting to examine the behaviour of the dehydrided $ZrCr_2$ in the electric field antinode of the resonator below the apparent superconducting transition temperature. Analysis of resistivity changes near T_c would provide a valuable tool in verifying the superconductivity in $ZrCr_2$.

Chapter 6

SUMMARY AND CONCLUSIONS

> One never notices what has been done; one can only see what remains to be done. *Marie Curie in a letter to her brother, 1894*

6.1 Summary of the results obtained

The discussion of this doctorate work began with an introduction to the crystal chemistry of metal hydrides in *Chapter 1*. Previous studies of the ZrM_2- H systems (M = V, Cr, Mn) were summarised with an emphasis on their crystallographic, magnetic and electronic properties, particularly those that had not yet been thoroughly explored.

In *Chapter 2*, the experimental methods used to explore these crystallographic, magnetic and electronic properties were introduced. A detailed description of the synthesis and characterisation techniques was given, along with a discussion of the relevant theory underpinning these methods.

Hydrogen-induced changes in the properties of the $ZrMn_{2+x}-$ H system were the focus of *Chapter 3*. The crystal structure, magnetic ordering and dielectric properties of the nearly stoichiometric $ZrMn_{2.06}$ intermetallic compound were explored in detail, and then contrasted against a similar study of $ZrMn_{2.06}H_3$. The hydriding thermodynamics were also discussed. A synchrotron X-ray diffraction study revealed that hydrogen absorption in this system occurred with no change in symmetry of the parent C14 Laves phase structure: the base metal sublattice was conserved, undergoing only an anisotropic lattice expansion. This anisotropic expansion triggered a hydrogen-induced decrepitation in the system, which was further aggravated by cycling. Neutron diffraction revealed that deuterium was

accommodated on the *2A2B* interstitial sites in the structure. This lattice expansion was also connected to the ferrimagnetism ($T_c = 224$ K) of $ZrMn_{2.06}H_3$, where the addition of hydrogen brought about a dramatic shift in the ferrimagnetic transition temperature as compared to $ZrMn_{2.06}$, a frustrated ferrimagnet of similar ordering, with $T_c < 2$ K. Both the hydrided and the hydrogen-free phases were shown to be good metallic conductors with a large polarisation in the electric field. The addition of hydrogen brought about an increase in the electrical conductivity of the $ZrMn_{2.06}-$ H system, along with a rise in dielectric loss.

In addition to the effect of hydrogen on the nearly stoichiometric $ZrMn_{2.06}$, the role of manganese in the properties of the off-stoichiometric $ZrMn_{2+x}$ compounds and their hydrides was also examined, over the composition range $-0.35 \leq x \leq 0.44$. The $ZrMn_{2+x}$ materials crystallise in the same C14 Laves phase structure as the line phase, with off-stoichiometry accomplished *via* atomic substitution on the existing zirconium or manganese sites for the super- or substoichiometric compounds, respectively. As x increases in the superstoichiometric compounds, the hydrogen absorption capacity of $ZrMn_{2+x}$ was found to decrease, with the stability of the hydride following suit. Neutron diffraction of the substoichiometric deuteride revealed that zirconium substitution created new interstitial sites for hydrogen absorption.

Similar to the nearly stoichiometric system, $ZrMn_{2+x}$ was shown to be a very low T (less than 2 K) frustrated ferrimagnet, with T_c decreasing and disorder increasing as x rises. The addition of hydrogen relieves frustration in the system and increases the ferrimagnet T_c; as per the hydrogen-free compounds, T_c was shown to decrease linearly with x, whilst the magnetic strain increased. Coupled with low-temperature neutron diffraction, this study allowed the magnetic structure of $ZrMn_{2+x}H_3$ to be elucidated for the first time. Finally, a dielectric study of the $ZrMn_{2+x}-$ H system revealed that the conductivity of both the hydrided and the hydrogen-free phase diminished as the amount of manganese in the system increased.

Chapter 4 focused on the crystal structure, superconductivity, magnetism and dielectric properties of ZrV_2 and its hydride. Synchrotron X-ray diffraction revealed that the intermetallic compound crystallised in the cubic C15 Laves phase structure, but was contaminated with several trace impurities. Hydrogen absorption occurred so readily that its thermodynamics could not be determined; in contrast, dehydriding required the application of very high temperatures, which brought about an increase in the impurity fraction and partial disproportionation of ZrV_2, but no decrepitation. X-ray diffraction of the hydrided material revealed that the major phase was C15 ZrV_2H_x ($x = 2.4, 4.8$), an expanded version of the parent metal structure with hydrogen absorbed in *2A2B* and *1A3B* interstitial sites. Several hydrogen-ordered superstructures were also detected in minor proportions. A magnetic study revealed that this hydrogen absorption destroyed the superconductivity of the material: although C15 ZrV_2 is a type II superconductor with $T_c = 8$ K, the hydrided material is a Pauli paramagnet down to 5 K. Measurement of the dielectric properties showed that, although both ZrV_2 and its hydride are metallic conductors, the addition of hydrogen brings about a decrease in the conductivity as a result of charge transfer from the host metal to the hydrogen atom.

Finally, *Chapter 5* explored the properties of the $ZrCr_2-$ H system, with a focus on how the crystal structure, magnetic properties and electrical conductivity are affected by hydrogen absorption. A crystallographic study revealed the polymorphism of this intermetallic compound: although the major phase was the stable C15 structure, traces of the C14 and C36 Laves phase were also detected, along with several ordered Laves-phase type structures that could not be fully refined. These polymorphs were preserved upon hydrogen cycling, with each structure absorbing hydrogen in a similar fashion as the C15 phase; in each case, hydrogen absorption occurred at interstitial sites in the structure, with no change in symmetry. The hydriding thermodynamics of the $ZrCr_2-$ H system were also determined, with the additional finding that hydrogen cycling caused no decrepitation in this system. Investigations of the magnetic behaviour revealed a dilute

superconducting transition at 8 K in both the hydrided and the hydrogen free phases; otherwise, the materials behaved as simple Pauli paramagnets. A study of the dielectric properties of the $ZrCr_2-$ H system showed a hydrogen-induced decrease in conductivity, which when combined with the published band structure of the system, suggested that a partial charge transfer from the metal to the absorbed hydrogen occurred.

6.2 General Conclusions

In consideration of the wide range of hydrogen-induced changes in the ZrM_2- H (M = V, Cr, Mn) systems discussed above, it is clear that the role of hydrogen in these systems is complex. Across the series, the addition of hydrogen induces few changes in the Laves phase crystal structures: in all cases, there is no change in symmetry between the hydrided and hydrogen-free compounds, with the hydrogen atoms accommodated in interstitial sites *via* an expansion of the unit cell. The absorbed hydrogen atoms are mobile at room temperature, diffusing readily through the structures; with temperature reduction, the hydrogen atoms form an ordered network about the base metal substructure in some systems.

As a result of the hydrogen mobility and its loose binding at the interstitial sites, formation of these ZrM_2H_x compounds is easily reversed, and *via* subtle changes in temperature and hydrogen pressure, hydrogen gas can be repeatedly cycled through the systems. Figure 6.1 charts the temperature required to desorb hydrogen over the ZrM_2H_x compounds —the temperatures were taken from Figures 3.4, 4.3, and 5.3, choosing the point at which 90% of hydrogen had been removed in each case. As the nature of M progresses across the $3d$ row, the dehydriding temperature decreases and the hydride formed by ZrM_2 becomes gradually less stable. This relationship can be described by a linear trend as shown in Figure 6.1.

Similar to the trend in stability of the ZrM_2H_x compounds across the range of M, the amount of hydrogen absorbed, x, also varies with the nature of the alloying

element. The hydrogen absorption capacity of the ZrM_2 intermetallic compounds can be taken from their pressure - temperature - composition (pcT) plots, as shown in Figures 3.6 and 5.2 for the $ZrMn_{2.06}$ and $ZrCr_2$ compounds, respectively. In the case of ZrV_2, pcT data could not be collected, so the absorption capacity is estimated from X-ray diffraction data as the hydrogen content of the most significant hydrogen-absorbing phase in the system. From these data, it is evident that the hydrogen capacity of the ZrM_2H_x hydrides decreases as M moves across the 3*d* series: for M = V, $x = 4.8$, for M = Cr, $x = 3.4$ and for M = Mn, $x = 3.2$.

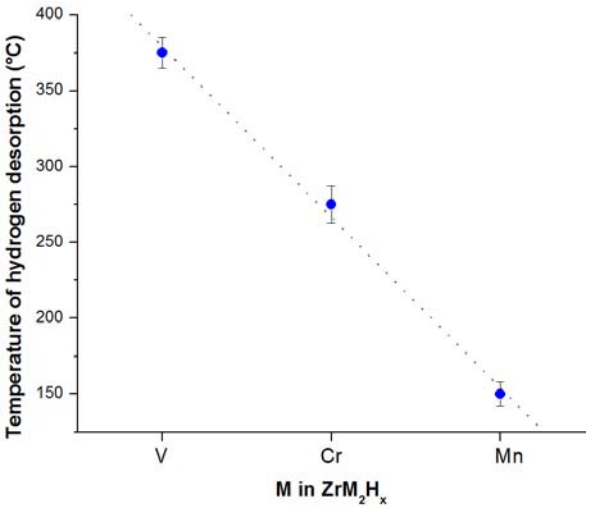

Figure 6.1: *A plot of the temperature of hydrogen desorption in ZrM_2H_x against M. The desorption temperature was taken from dehydriding plots of these hydrides, and in each case was chosen as the point at which 90 % of the total hydrogen content had been removed from the compound. The data are shown as blue circles, with the dotted line indicating the linear fit to this data.*

The magnetic behaviour of the ZrM_2 intermetallic compounds and their hydrides varies widely across the three systems studied; however, at 300 K, both the hydrogen-free and the hydrided members of these systems are all Pauli paramagnets. The room temperature susceptibilities of the ZrM_2H_x compounds, which can be found in Tables 3.12, 4.3, and 5.3, are plotted against M in Figure 6.2. It is readily seen that as the nature of the alloying element is varied across the 3*d* series, the Pauli paramagnetic susceptibility of the hydride increases. This trend can be described by an exponential function, as Figure 6.2 shows.

The novel conductivity measurements on the ZrM_2- H system that were carried out over the course of this thesis revealed that both the hydrided and the hydrogen-free members of this series are metallic conductors across the range of M tested. The electrical conductivity varies according to the nature of M, as shown

by Figure 6.3, which charts the changes in σ_{eff} against M for the ZrM_2 series. These data were taken from microwave resonance measurements, as summarised in Tables 3.19, 4.4, and 5.4. Figure 6.3 also shows the conductivity of the ZrM_2H_x compounds; comparison of these data against the corresponding information for the hydrogen-free materials reveals that the electrical effect of hydrogen absorption varies across the ZrM_2- H systems. In the case of M = V, Cr, the absorption of hydrogen induces a decrease in the electrical conductivity, whilst for M = Mn, there is an increase in the conductivity concomitant to the hydriding process.

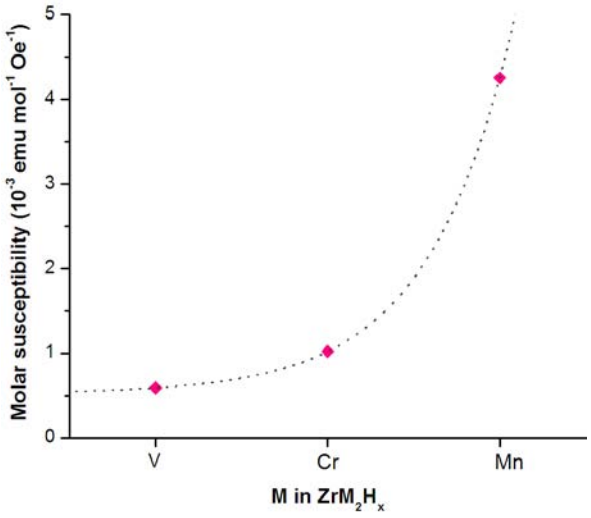

Figure 6.2: *A plot of the molar magnetic susceptibility in ZrM_2H_x against M. The susceptibility was taken at 300 K in each case. The data are shown as pink diamonds, with the dotted line indicating the exponential fit to this data. Relative errors are smaller than the data points.*

These variations in the properties of the ZrM_2- H systems are certainly related, yet there exists no general theory to describe the effect of M (or of hydrogen) on these systems. Moreover, the complexity of the trends suggests that several competing factors may play a role. Although these factors are difficult to deconvolute, the influence of the electronegativity of M on the properties of the ZrM_2- H system might be considered as a first step towards explaining these trends. Using the Allred-Rochow definition of electronegativity, the power of M to attract electrons to itself increases as the 3*d* series is crossed: the electronegativity of V is 1.45, of Cr is 1.56, and of Mn is 1.60 [81]. Contrasted against this, the electronegativity of Zr is 1.22, and of hydrogen is 2.20 [81]. As this definition of electronegativity takes into account the atomic radius [81], it also provides a convenient explanation of the variation in structure in ZrM_2 – as explained in Section 1.1.2, the Laves phases are size factor structures, with choice of the C14, C15 or

C36 phase determined by atomic size and number of electrons. Thus, as the size of M increases across the 3*d* series, the stable room temperature structure of the compound changes from cubic (M = V, Cr) to hexagonal (M = Mn).

The variation in electronegativity will also affect the nature of the hydrogen absorption in the ZrM_2 compounds. As M becomes more electropositive, increased electron transfer from M to the absorbed hydrogen atom can be expected, leading towards an enhancement of the stability of ZrM_2H_x. This electron transfer from the host metal to the hydrogen atom may in turn cause a reduction in the metallic conductivity, as the free conduction electron band is depleted. Therefore, as M progresses across the 3*d* period, the subsequent rise in electronegativity of this alloying element may be expected to trigger a reduction in the stability of the ZrM_2- H hydrides, and an escalation in their electrical conductivity as compared to ZrM_2. As the Pauli susceptibility is proportional to the density of states at the Fermi level, the observed variation in magnetic susceptibility across the ZrM_2H_x series may be further related to these trends.

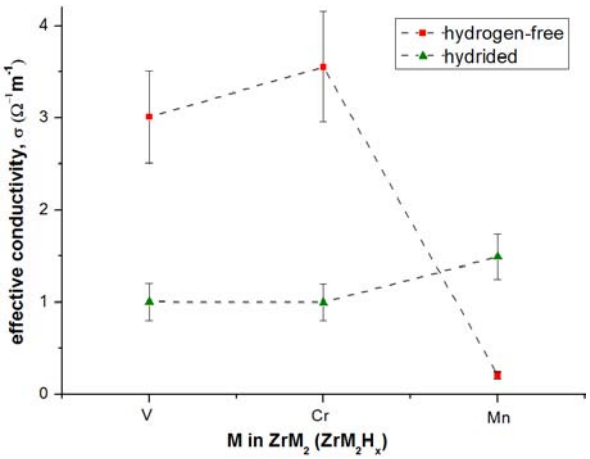

Figure 6.3: *A plot of the effective conductivity in the ZrM_2-H systems against M. The conductivity was determined via microwave resonance measurements at room temperature. The data for the hydrogen-free compounds are shown as red squares, whilst the data for the hydrided compounds are shown as green triangles; the dashed line in both cases acts as a guide to the eye in describing the trend in the data.*

The above qualitative explanation represents only a initial step towards developing a general, descriptive theory of the effect of hydrogen absorption on intermetallic compounds. Construction of a complete theory capable of predicting the properties of a metal hydride are currently beyond the scope of this work, and

would require a rigorous study of an exhaustive range of metal hydrides. The investigation of the ZrM_2-H systems (M = V, Cr, Mn) that was carried out over the course of this doctorate work found that hydrogen absorption caused little structural change in these systems: the symmetry of the parent intermetallic compound was conserved in each case, with hydrogen absorption occurring at interstitial sites *via* expansion of the unit cell. Significant electronic and magnetic alterations occurred concomitant to hydrogen absorption, causing either an increase/decrease in the electrical conductivity or the appearance/disappearance of magnetic phenomena. It can therefore be concluded that whilst the hydrogen addition in ZrM_2-H occurs simply *via* an expansion of the crystal structure, the hydrogen does not act purely as null dilutant —there exist subtle electronic changes connected with the hydriding process as well.

BIBLIOGRAPHY

[1] D. F. Shriver and P. W. Atkins. *Inorganic Chemistry.* Oxford University Press, Oxford, UK, 3rd edition, 1999.

[2] Louis Schlapbach. Introduction. In Louis Schlapbach, editor, *Hydrogen in Intermetallic Compounds*, volume 73 of *Topics in Applied Physics.* Springer-Verlag, Berlin, Germany, 1988.

[3] Annick Percheron-Guégan and Jean-Marie Welter. Preparation of Intermetallics and Hydrides. In Louis Schlapbach, editor, *Hydrogen in Intermetallic Compounds*, volume 73 of *Topics in Applied Physics.* Springer-Verlag, Berlin, Germany, 1988.

[4] Gerfried Wiesinger and Günter Hilscher. Magnetic Properties, Mössbauer Effect and Superconductivity. In Louis Schlapbach, editor, *Hydrogen in Intermetallic Compounds*, volume 73 of *Topics in Applied Physics.* Springer-Verlag, Berlin, Germany, 1988.

[5] K. H. J. Buschow. Magnetic Properties of La_2Ni_7 and its hydride. *Journal of Magnetism and Magnetic Materials*, 40:224, 1983.

[6] K. H. J. Buschow and A. M. van Diepen. Moment formation upon hydrogen absorption in Hf_2Fe. *Solid State Communications*, 31:469, 1979.

[7] Klaus Yvon. Hydrogen in novel solid-state metal hydrides. *Zeitschrift fur Kristallograhie*, 218:108–116, 2003.

[8] Ted B. Flanagan and W. Alan Oates. Thermodynamics of Intermetallic Compound-Hydrogen Systems. In Louis Schlapbach, editor, *Hydrogen in Intermetallic Compounds*, volume 73 of *Topics in Applied Physics.* Springer-Verlag, Berlin, Germany, 1988.

[9] George G. Libowitz. *The solid-state chemistry of binary metal hydrides.* W. A. Benjamin, New York, 1st edition, 1965.

[10] K. H. Buschow, P. C. P. Bouten, and A. R. Miedema. Hydrides formed from intermetallic compounds of two transition metals: a special class of ternary alloys. *Reports on Progress in Physics*, 45:937–1039, 1982.

[11] Roy L. Johnston and Roald Hoffmann. Structure-Bonding Relationships in the Laves Phases. *Zeitschrift fur anorganische und allgemeine Chemie*, 616:105–120, 1992.

[12] Charles Barrett and T. B. Massalski. *Structure of Metals*. Pergamon Press, Oxford, England, 3rd edition, 1980.

[13] Yukitomo Komura. Stacking Faults and Two New Modifications in Mg-Cu-Al System. *Acta Crystallographica*, 15:770–777, 1962.

[14] Suklyun Hong and C. L. Fu. Hydrogen in Laves phase ZrX_2 ($X = V, Cr, Mn, Fe, Co, Ni$) compounds: Binding energies and electronic and magnetic structure. *Physical Review B*, 66:094109, 2002.

[15] D. G. Westlake. A geometric model of stoichiometry and interstitial site occupancy in hydrides (deuterides) of $LaNi_5$, $LaNi_4Al$ and $LaNi_4Mn$. *Journal of the Less Common Metals*, 91:275–292, 1983.

[16] A. C. Switendick. Electronic Band Structures of Metal Hydrides. *Solid State Communications*, 8(18):1463–1467, 1970.

[17] H. Smithson, C. A. Marianetti, D. Morgan, A. Van der Ven, A. Predith, and G. Ceder. First-principles study of the stability and electronic structure of metal hydrides. *Physical Review B*, 66(14):144107, 2002.

[18] D. J. Singh and M. Gupta. Role of H in the magnetism and electronic structure of YFe_2H_4. *Physical Review B*, 69:132403, 2004.

[19] V. N. Svechnikov and V. V. Detkov. *Metallofizika i Noveishie Tekhnologii*, 24:2004, 1976.

[20] D. Shaltiel, I. Jacob, and D. Davidov. Hydrogen absorption and desorption properties of AB_2 Laves-phase pseudobinary compounds. *Journal of the Less Common Metals*, 53(1):117–131, 1977.

[21] M. Rotter, A. Grytsiv, Chen Xing-Qiu, P. Rogl, R. Podloucky, W. Wolf, V. T. Witusiewicz, A. Saccone, H. Noel, M. Doerr, A. Lindbaum, H. Michor, E. Bauer, S. Heathman, W. Kockelmann, and J. Taylor. Structural, thermodynamic, and transport properties of Laves-phase $ZrMn_2$ from X-ray and neutron diffraction and first principles. *Phys. Rev. B: Condens. Matter Mater. Phys.*, 74(22):224109, 2006.

[22] L. Pontonnier, S. Miraglia, D. Fruchart, J. L. Soubeyroux, A. Baudry, and P. Boyer. Structural study of hyperstoichiometric alloys $ZrMn_{2+x}$ and their hydrides. *Journal of Alloys and Compounds*, 186:241–248, 1992.

[23] J-J. Didisheim, K. Yvon, and D. Shaltiel. The distribution of the deuterium atoms in the deuterated hexagonal Laves-phase $ZrMn_2D_3$. *Solid State Communications*, 31:47, 1979.

[24] A. V. Skripov, T. J. Udovic, and J. J. Rush. Hydrogen jump diffusion in C14-type $ZrMn_2H_3$: Quasielastic neutron scattering study. *Physical Review B*, 76(10):104305, 2007.

[25] T. Kodama. An attempt to estimate the extent of the single phase region of the $ZrMn_2$ phase by means of the X-ray diffraction-profile halfwidths. *Journal of Alloys and Compounds*, 256:263, 1997.

[26] Thaddeus B. Massalski, editor. *Binary Alloy Phase Diagrams*. ASM International, Materials Park, Ohio, USA, 2nd edition, 1990.

[27] R. H. Van Essen and K. H. Buschow. Composition and Hydrogen Absorption of C14 Type Zr-Mn Compounds. *Materials Research Bulletin*, 15(8):1149–1155, 1980.

[28] W. Luo, J. D. Clewley, Ted B. Flanagan, and W. A. Oates. Thermodynamic characterization of the Zr-Mn-H system part 1. Reaction of H_2 with single-phase $ZrMn_{2+x}$ C14 Laves phase alloys. *Journal of Alloys and Compounds*, 185(2):321–338, 1992.

[29] N. Nishimiya. Hydriding behaviors and equilibrium properties of Zr-Mn binary alloys. *Materials Research Bulletin*, 21(9):1025–1037, 1986.

[30] F. Pourarian, H. Fujii, W. E. Wallace, V. K. Sinha, and H. Kevin Smith. Stability and Magnetism of Hydrides of Nonstoichiometric $ZrMn_2$. *Journal of Physical Chemistry*, 85:3105–3111, 1981.

[31] Chen Xing-Qiu, W. Wolf, R. Podloucky, P. Rogl, and M. Marsman. Ab initio study of ground-state properties of the Laves-phase compound $ZrMn_2$. *Physical Review B*, 72(5):054440, 2005.

[32] Chen Xing-Qiu, W. Wolf, and R. Podloucky. Coupling of magnetic ordering and vibrational properties. *Phase Transitions*, 80(4-5):445–468, 2007.

[33] H. Fujii, F. Pourarian, and W. E. Wallace. Influence of hydrogen absorption on magnetic ordering in some zirconium-based Laves phase compounds. *Journal of the Less-Common Metals*, 88(1):187–93, 1982.

[34] H. Fujii, M. Saga, and T. Okamoto. Magnetic, Crystallographic and Hydrogen absorption properties of YMn_2 and $ZrMn_2$ hydrides. *Journal of the Less-Common Metals*, 130:25–31, 1987.

[35] J-J. Didisheim and P. Fischer. Structural and magnetic phase transitions in $ZrMn_2D_3$. *Journal of the Less Common Metals*, 103(2):267–275, 1984.

[36] B. T. Matthias, V. B. Compton, and E. Corenzwit. Some new superconducting compounds. *Journal of Physics and Chemistry of Solids*, 19(1-2):130–133, 1961.

[37] A. Pebler and E. A. Gulbransen. Equilibrium Studies on the Systems $ZrCr_2-H_2$, ZrV_2-H_2 and $ZrMo_2-H_2$ between 0 and 900 degrees C. *Transactions of the Metallurgical Society of Aime*, 239:1593–1600, 1967.

[38] D. E. Moncton. Lattice transformation in the superconductivity of ZrV_2 by neutron diffraction. *Solid State Communications*, 13(11):1779–1782, 1973.

[39] J. T. Williams. Vanadium-Zirconium Alloy System. *Transactions of the Metallurgical Society of Aime*, 203:345–350, 1955.

[40] J-J. Didisheim, K. Yvon, D. Shaltiel, P. Fischer, P. Bujard, and E. Walker. The distribution of the deuterium atoms in the deuterated cubic Laves phase $ZrV_2D_{4.5}$. *Solid State Communications*, 32:1087, 1979.

[41] A.N. Bogdanova, A. V. Irodova, D. André, and F. Bouree. The ZrV_2D_6 crystal structure. *Journal of Alloys and Compounds*, 356-357:50–53, 2003.

[42] A. V. Irodova and E. Suard. Evolution of hydrogen superstructure with $k = (\frac{1}{2}\frac{1}{2}\frac{1}{2})$ in $ZrV_2D_{2+\delta}$. *Journal of Alloys and Compounds*, 291(1-2):184–189, 1999.

[43] A. V. Irodova, G. André, and F. Bouree. Phase transition between hydrogen superstructures with $k = (001)$ and $k = 0$ via an incommensurate phase in ZrV_2D_x $(2.8 < x < 3.9)$. *Journal of Alloys and Compounds*, 302(1-2):159–168, 2000.

[44] W. Däumer, H. R. Khan, and K. Lüders. Electronic structure investigated by NMR and superconductivity of cubic Laves phase hydrides: V_2HfH_x and $V_2Hf_{0.5}Zr_{0.5}H_x$. *Physical Review B*, 38(7):4427–4436, 1988.

[45] C. Geibel, W. Goldacker, H. Keiber, V. Oestreich, H. Rietschel, and H. Wühl. Phase transitions, electronic properties, and superconductivity in the system V_2ZrH_x. *Physical Review B*, 30(11):6363–6367, 1984.

[46] H. Fujii., T. Okamoto, W. E. Wallace, F. Pourarian, and T. Morisaki. Influence of hydrogen absorption on magnetic properties of $Zr(Fe_{1-x}V_x)_2$ ternaries. *Journal of Magnetism and Magnetic Materials*, 46:245, 1985.

[47] E. T. Hayes, A. H. Roberson, and M. H. Daves. Zirconium-Chromium phase diagram. *Journal of Metals*, page 304, March 1952.

[48] J. Mestnik Filho, A. W. Carbonari, W. Pendl, J. I. Moura, and R. N. Saxena. X-ray and time differential perturbed angular correlation measurements in $ZrCr_2$ and $ZrCr_2H_3$. *Journal of Alloys and Compounds*, 224(1):60–65, 1995.

[49] H. Kohlmann, F. Fauth, and K. Yvon. Hydrogen order in monoclinic $ZrCr_2H_{3.8}$. *Journal of Alloys and Compounds*, 285(1-2):204–211, 1999.

[50] A. V. Skripov, A. E. Karkin, and A. V. Mirmelstein. Hydrogen-induced anomalies in the heat capacity of C15-type $ZrCr_2H_x$ ($ZrCr_2D_x$). *Journal of Physics: Condensed Matter*, 9:1191, 1997.

[51] I. Jacob, D. Davidov, and D. Shaltiel. Effect of hydrogen absorption on the magnetic properties of some $3d-$Laves phase binary and pseudobinary intermetallics. *Journal of Magnetism and Magnetic Materials*, 20:226–230, 1980.

[52] H. J. P. van Midden, A. Prodan, E. Zupanič, R. Žitko, S. S. Makridis, and A. K. Stubos. Structural and Electronic Properties of the Hydrogenated $ZrCr_2$ Laves Phases. *The Journal of Physical Chemistry C*, 114(9):4221–4227, 2010.

[53] Richard J. D. Tilley. *Crystals and Crystal Structure*. John Wiley and Sons Ltd., Chichester, England, 2006.

[54] L. D. Landau and E. M. Lifschitz. *Statistical Physics*. Addison-Wesley, 1958.

[55] Yu. A. Izyumov and V. N. Syromyatnikov. *Phase Transitions and Crystal Symmetry*. Kluwer Academic, Dordrecht, The Netherlands, 1990.

[56] Charles Kittel. *Introduction to Solid State Physics*. John Wiley and Sons, Inc., 8th edition, 2005.

[57] W. I. F. David, K. Shankland, L. B. McCusker, and Ch. Baerlocher, editors. *Structure determination from powder diffraction data*. International Union of Crystallography, Monographs on Crystallography. Oxford University Press, 2002.

[58] R. L. Snyder, H. J. Bunge, , and J. Fiala, editors. *Defect and Microstructure Analysis from Diffraction*. International Union of Crystallography, Monographs on crystallography. Oxford University Press, 1999.

[59] Philips Analytical B.V., Almelo, The Netherlands. *X'Pert PRO User's Guide*, 3rd edition, 2002.

[60] A. N. Fitch. The high resolution powder diffraction beam line at ESRF. *Materials Science Forum*, 228-231:219–222, 1996.

[61] Nicola Tartoni, Stephen P. Thompson, Chiu C. Tang, Brian L. Willis, Gareth E. Derbyshire, Anthony G. Wright, Stephen C. Jaye, J. Michael Homer, John D. Pizzey, and Anthony M. T. Bell. High-performance X-ray detectors for the new powder diffraction beamline I11 at Diamond. *Journal of Synchrotron Radiation*, 15(1):43–49, Jan 2008.

[62] George Edward Bacon. *Neutron Diffraction*. Monographs on the physics and chemistry of materials. Oxford University Press, 3rd edition, 1975.

[63] L. Koester, H. Rauch, and E. Seymann. Neutron scattering lengths and cross sections of the elements and their isotopes. *Neutron News*, 3(3):29–37, 1992.

[64] P. Day, J. E. Enderby, W. G. Williams, L. C. Chapon, A. C. Hannon, P. G. Radaelli, and A. K. Soper. GEM: The General Materials Diffractometer at ISIS - Multibank Capabilities for Studying Crystalline and Disordered Materials. *Neutron News*, 15:19, 2004.

[65] R. A. Young, editor. *The Rietveld Method*. International Union of Crystallography: Monographs on Crystallography. Oxford University Press, 1993.

[66] Alan Coelho. TOPAS Academic. ©1994-2006.

[67] Fachinformationszentrum (FIZ) Karlsruhe. Inorganic Crystal Structure Database. [Online].

[68] Alan Coelho. *TOPAS Academic: Technical Reference Manual*, 4.1 edition, 2007.

[69] David Jiles. *Introduction to Magnetism and Magnetic Materials*. Chapman and Hall/CRC Press, Boca Raton, USA, 2nd edition, 1998.

[70] Kei Yosida. *Theory of Magnetism*. Springer Series in Solid State Sciences. Springer-Verlag, Berlin, Germany, 1996.

[71] Louis Néel. Propriétés Magnétiques des Ferrites, Ferrimagnétisme et Antiferromagnétisme. *Annales de physique*, 3:137–198, 1948.

[72] J. Samuel Smart. The Néel Theory of Ferrimagnetism. *American Journal of Physics*, 23(6):356–370, 1955.

[73] Anthony S. Arrott. Criterion for Ferromagnetism from Observations of Magnetic Isotherms. *Physical Review*, 108(6):1394, 1957.

[74] E. P. Wohlfarth. Magnetic properties of crystalline and amorphous alloys: A systematic discussion based on the Rhodes-Wohlfarth plot. *Journal of Magnetism and Magnetic Materials*, 7(1-4):113–120, 1978.

[75] A. C. Larson and R. B. von Dreele. General Structure Analysis System (GSAS). Technical Report LAUR 86-748, Los Alamos National Laboratory Report, Los Alamos, New Mexico, 1994.

[76] B. H. Toby. EXPGUI, a graphical user interface for GSAS. *Journal of Applied Crystallography.*, 34:210–213, 2001.

[77] M. Rotter, Lucian Pascut, M. Doerr, P. Fabi, S. Rotter, M. Banks, Duc Manh Le, and R. Schedler. McPhase - a Mean Field Monte Carlo Magnetic Phase Calculation Program.

[78] Gordon L. Squires. *Practical Physics.* Cambridge University Press, Cambridge, England, 4th edition, 2001.

[79] Olivier Klein, Steve Donovan, Martin Dressel, and George Grüner. Microwave cavity perturbation technique: Part I: Principles. *International Journal of Infrared and Millimeter Waves*, 14(12):2423–2457, 1993.

[80] Jean A. Cross. *Electrostatics: Principles, probelms and applications.* Adam Hilger, IOP Publishing Ltd., Bristol, England, 1987.

[81] David R. Lide, editor. *CRC Handbook of Chemistry and Physics.* CRC Press, Boca Raton, 84th edition, 2003.

[82] S. B. Roy. $CeRu_2$ and ZrV_2 - 2 Interesting C15-Laves-Phase Superconductors. *Philosophical Magazine B*, 65(6):1435–1444, 1992.

[83] M. O'Keeffe and M. Valigi. The electrical properties and defect structure of pure and chromium-doped MnO. *Journal of Physics and Chemistry of Solids*, 13:947–962, 1970.

[84] K. L. Aplin. Aspirated capacitor measurements of air conductivity and ion mobility spectra. *Review of Scientific Instruments*, 76:104501–104506, 2005.

[85] A. Pebler and E. A. Gulbransen. Thermochemical and Structural aspects of reaction of hydrogen with alloys and intermetallic compounds of zirconium. *Electrochemical Technology*, 4:211, 1966.

[86] Ted B. Flanagan, H. Noh, W. Luo, and W. A. Oates. Thermodynamic characterization of the Zr-Mn-H system Part 2. Reaction of H_2 with two-phase alloys. *Journal of Alloys and Compounds*, 185:339–351, 1992.

[87] D. Fruchart, J. L. Soubeyroux, and R. Hempelmann. Neutron diffraction in $Ti_{1.2}Mn_{1.8}$ deuterides: Structural and magnetic aspects. *Journal of the Less-Common Metals*, 99:307–319, 1984.

[88] R. M. Waterstrat, B. N. Das, and Paul A. Beck. Phase Relationships in the Titanium-Manganese System. *Transactions of the Metallurgical Society of AIME*, 224:512–518, 1962.

[89] H. E. Swanson and R. K. Fuyat. Standard X-ray diffraction powder patterns II. *Journal of Chemical Physics*, 21:1383–1384, 1953.

[90] L. Y. Zhang and W. E. Wallace. Hydrogenation Characteristics of the Isoelectronic Alloys $ZrMn_2$, ZrCrFe, and ZrVCo. *Journal of Solid State Chemistry*, 74:132–137, 1988.

[91] F. Pourarian, V. K. Sinha, W. E. Wallace, and H. Kevin Smith. Kinetics and thermodynamics of $ZrMn_2-$based hydrides. *Journal of the Less Common Metals*, 88(2):451–458, 1982.

[92] W. B. Pearson. *A Handbook of Lattice Spacings and Structures of Metals and Alloys*. Pergamon Press, 1958. page 39.

[93] E. Clementi, D. L. Raimondi, and W. P. Reinhardt. Atomic Screening constants from SCF Functions. *Journal of Chemical Physics*, 38:2686, 1963.

[94] K. H. J. Buschow and R. C. Sherwood. Magnetic properties and hydrogen absorption in rare-earth intermetallics of the type RMn_2 and R_6Mn_23. *Journal of Applied Physics*, 48(11):4643–4648, 1977.

[95] D. S. Williams, P. M. Shand, T. M. Pekarek, R. Skomski, V. Petkov, and D. L. Leslie-Pelecky. Magnetic transitions in disordered $GdAl_2$. *Physical Review B*, 68(21):214404, 2003.

[96] W. Brückner, R. Perthel, K. Kleinstück, and G. E. R. Schulze. Magnetic Properties of $ZrFe_2$ and $TiFe_2$. *Physica Status Solidi (b)*, 29:211–216, 1968.

[97] T. Matsumura, H. Yukawa, and M. Morinaga. Alloying effects on the electronic structure of the $ZrMn_2$ intermetallic hydride. *Journal of Alloys and Compounds*, 279(2):192–200, 1998.

[98] V. M. Pan, I. E. Bulakh, A. L. Kasatkin, and A. D. Shevchenko. Dielectric phase transitions in the superconducting Cl5 compounds ZrV_2 and HfV_2. *Journal of the Less Common Metals*, 62:157–166, 1978.

[99] R. Kuentzler and H. R. Khan. Low temperature specific heat and superconductivity measurements of $V_{1-x}T_x$; T = Ti, Zr, Hf and $x = 0.013$ and 0.05. *Physics Letters A*, 113(2):89 – 92, 1985.

[100] I. Yu Zavaliy, W. B. Yelon, P. Y. Zavalij, I. V. Saldan, and V. K. Pecharsky. The crystal structure of the oxygen-stabilized η-phase $Zr_3V_3O_xD_{9.6}$. *Journal of Alloys and Compounds*, 309(1-2):75–82, 2000.

[101] A. Stern, S. R. Kreitzman, A. Resnik, D. Shaltiel, and V. Zevin. Thermal desorption spectra of hydrogen from the bulk ZrV_2H_x. *Solid State Communications*, 40(8):837–841, 1981.

[102] V. A. Somenkov and A. V. Irodova. Lattice structure and phase transitions of hydrogen in intermetallic compounds. *Journal of the Less Common Metals*, 101:481–492, 1984.

[103] J-J. Didisheim, K. Yvon, P. Fischer, and P. Tissot. Order-Disorder Phase Transition in $ZrV_2D_{3.6}$. *Solid State Communications*, 38:637, 1981.

[104] A. V. Irodova, G. André, and F. Bouree. Hydrogen redistribution in the solid solutions ZrV_2D_x, $2.2 < x < 2.7$: II. Structure of the intermediate phase: Lattice liquid crystal. A neutron-diffraction study. *Journal of Alloys and Compounds*, 350(1-2):196–204, 2003.

[105] H. Keiber, C. Geibel, B. Renker, H. Rietschel, H. Schmidt, H. Wühl, and G. R. Stewart. Phase instability, spin fluctuations and superconductivity in the C15 compound ZrV_2. *Physical Review B*, 30(5):2542–2546, 1984.

[106] R. M. Klein, W. E. Pickett, D. A. Papaconstantopoulos, and L. L. Boyer. Electronic Structure, Superconductivity, and magnetism in the C15 compounds ZrV_2, $ZrFe_2$ and $ZrCo_2$. *Physical Review B*, 27(11):6721, 1983.

[107] A. V. Skripov, M. Yu Belyaev, S. V. Rychkova, and A. P. Stepanov. Nuclear magnetic resonance study of hydrogen diffusion in $HfV_2H_x(D_x)$ and $ZrV_2H_x(D_x)$. *Journal of Physics: Condensed Matter*, 3(33):6277, 1991.

[108] Yu M. Yarmoshenko, V. N. Kozhanov, V. M. Cherkashenko, E. Z. Kurmaev, and E. P. Romanov. X-ray emission spectra and electronic structure of ZrV_2 and ZrV_2D_x. *Solid State Communications*, 55(1):19–23, 1985.

[109] Hideo Imoto, Motoshige Sasaki, Taro Saito, and Yukiyoshi Sasaki. Equilibrium, X-Ray, and ^{1}H-NMR Studies of the $ZrCr_2H$ System. *Bulletin of the Chemical Society of Japan*, 53(6):1584–1587, 1980.

[110] A. V. Irodova and E. Suard. Order-disorder phase transition in the deuterated hexagonal (C14-type) Laves phase $ZrCr_2D_{3.8}$. *Journal of Alloys and Compounds*, 299:32–38, 2000.

[111] D. Fruchart, A. Rouault, C. B. Shoemaker, and D. P. Shoemaker. Neutron diffraction studies of the cubic $ZrCr_2D_x$ and ZrV_2D_x (H_x) phase. *Journal of Less-Common Metals*, 73:363–368, 1980.

[112] A. V. Skripov and M. Yu Belyaev. Hydrogen mobility in the C15-type compounds $ZrCr_2H_x$. *Journal of Physics: Condensed Matter*, 5(27):4767, 1993.

[113] J. L. Soubeyroux, M. Bououdina, D. Fruchart, and L. Pontonnier. Phase stability and neutron diffraction studies of Laves phases $Zr(Cr_{1-x}M_x)_2$ and their hydrides. *Journal of Alloys and Compounds*, 219(1-2):48–54, 1995.

[114] A. W. Abel and R. S. Craig. Magnetic and structural characteristics of $TiCr_2$, $ZrCr_2$, $HfCr_2$ and the $TiCo_2-ZrCo_2$ and YFe_2-YCo_2 alloy systems. *Journal of the Less Common Metals*, 16(2):77–83, 1968.

[115] Ö. Rapp, J. Invarsson, and T. Claeson. Search for superconductivity in Laves phase compounds. *Physics Letters A*, 50(3):159–160, 1974.

Appendix A

SUPPLEMENTAL CRYSTALLOGRAPHIC, THERMODYNAMIC AND MAGNETIC DATA FOR THE ZRMN$_{2+X}$− H SYSTEMS

A.1 Supplemental Crystallographic Data

A.1.1 X-ray Diffraction Data for the $ZrMn_{2+x}$ (x = 0.13, 0.18, 0.31, 0.44) alloys

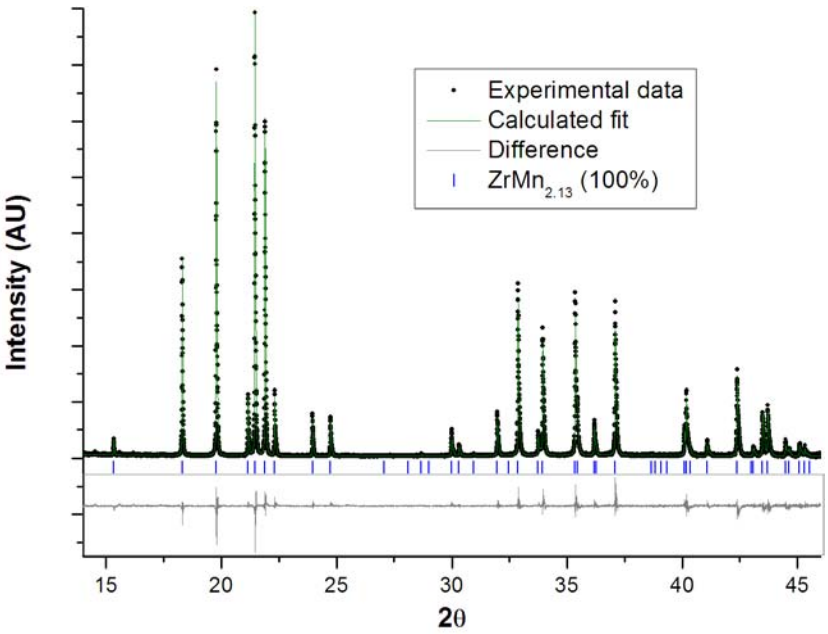

Figure A.1: *Room temperature synchrotron diffraction pattern for the alloy $ZrMn_{2.13}$, which was fitted with solely the C14 $ZrMn_{2.13}$ phase (ticks marks shown at the bottom of the diagram). The difference plot between the experimental data (black points) and calculated fit (green line) is shown as a grey line in a box.* $R_{wP} = 10.320$.

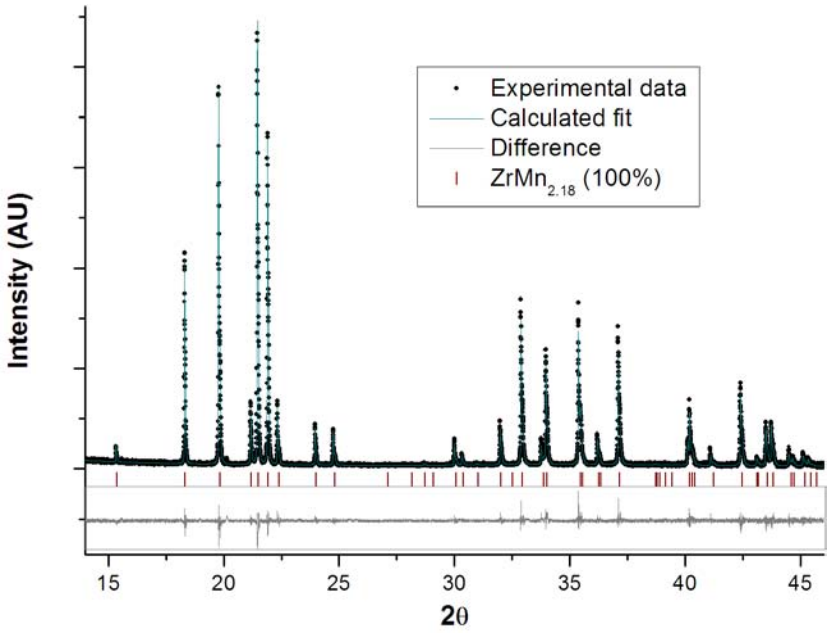

Figure A.2: *Room temperature synchrotron diffraction pattern for the alloy* $ZrMn_{2.18}$*, which was fitted with solely the C14* $ZrMn_{2.18}$ *phase (ticks marks shown at the bottom of the diagram). The difference plot between the experimental data (black points) and calculated fit (cyan line) is shown as a grey line in a box.* $R_{wP} = 10.184$.

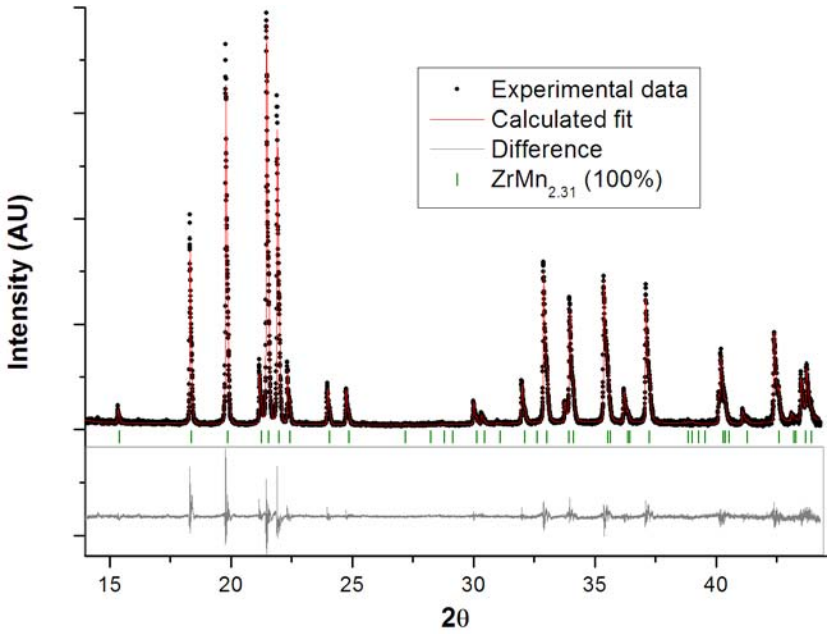

Figure A.3: *Room temperature synchrotron diffraction pattern for the alloy* $ZrMn_{2.31}$*, which was fitted with solely the C14* $ZrMn_{2.31}$ *phase (ticks marks shown at the bottom of the diagram). The difference plot between the experimental data (black points) and calculated fit (red line) is shown as a grey line in a box.* $R_{wP} = 11.043$.

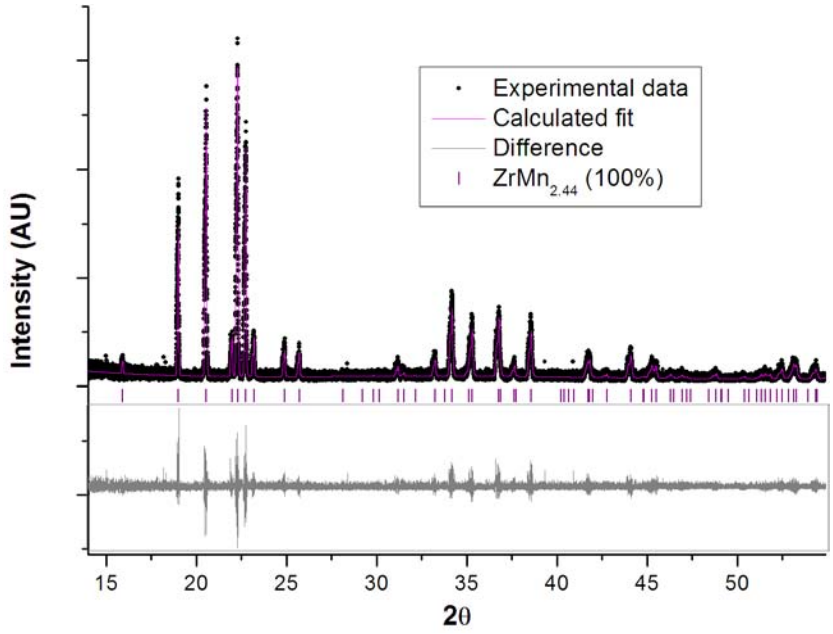

Figure A.4: *Room temperature synchrotron diffraction pattern for the alloy* $ZrMn_{2.44}$*, which was fitted with solely the C14* $ZrMn_{2.44}$ *phase (ticks marks shown at the bottom). The difference plot between the experimental data (black points) and calculated fit (pink line) is shown as a grey line in a box.* $R_{wP} = 17.118$.

A.1.2 X-ray Diffraction Data for hydrided $ZrMn_{2+x}H_3$ ($x = 0.13, 0.18, 0.31$)

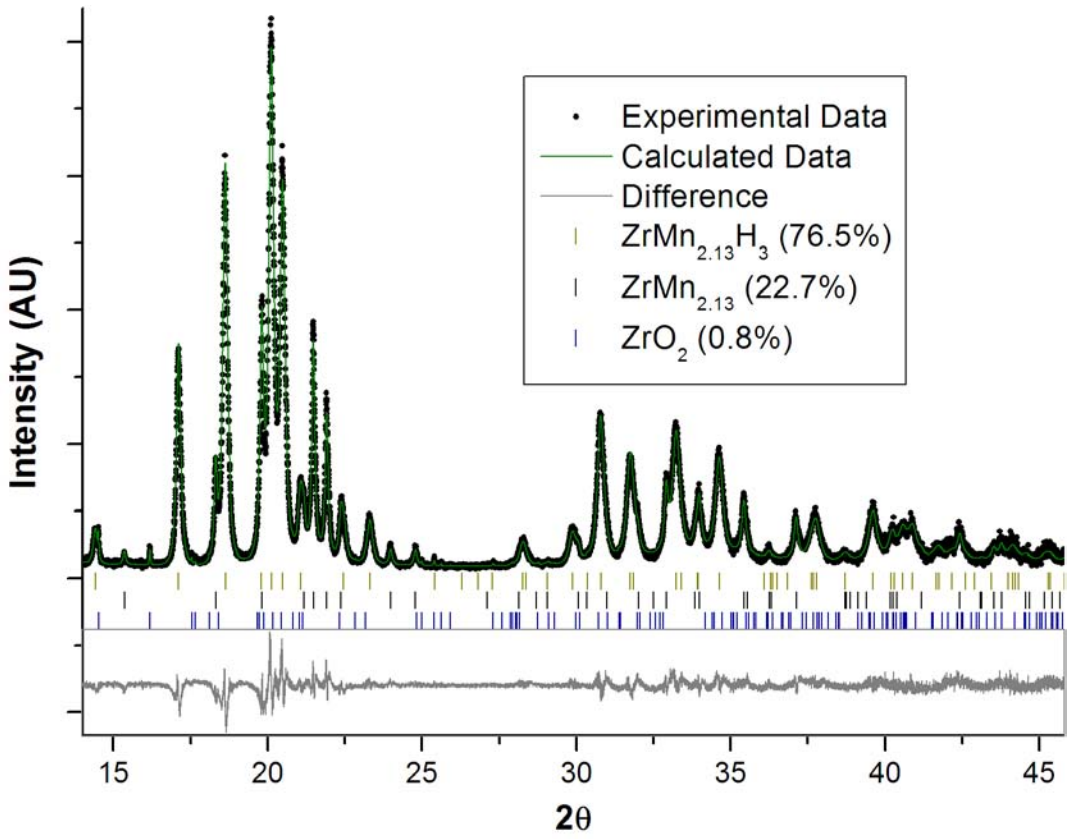

Figure A.5: *Room temperature synchrotron diffraction pattern for the hydrided $ZrMn_{2.13} - H$ sample, which was fitted with a mixture of phases, the ratios of which are given in the legend. The major phase was C14 $ZrMn_{2.13}H_3$, with the ticks marks shown at the bottom in dark yellow. A secondary, hydrogen free phase of $ZrMn_{2.13}$ was also fitted (tick marks in black) along with a trace ZrO_2 impurity (tick marks in navy). The difference plot between the experimental data (black points) and calculated fit (green line) is shown as a grey line in a box. $R_{wP} = 8.141$.*

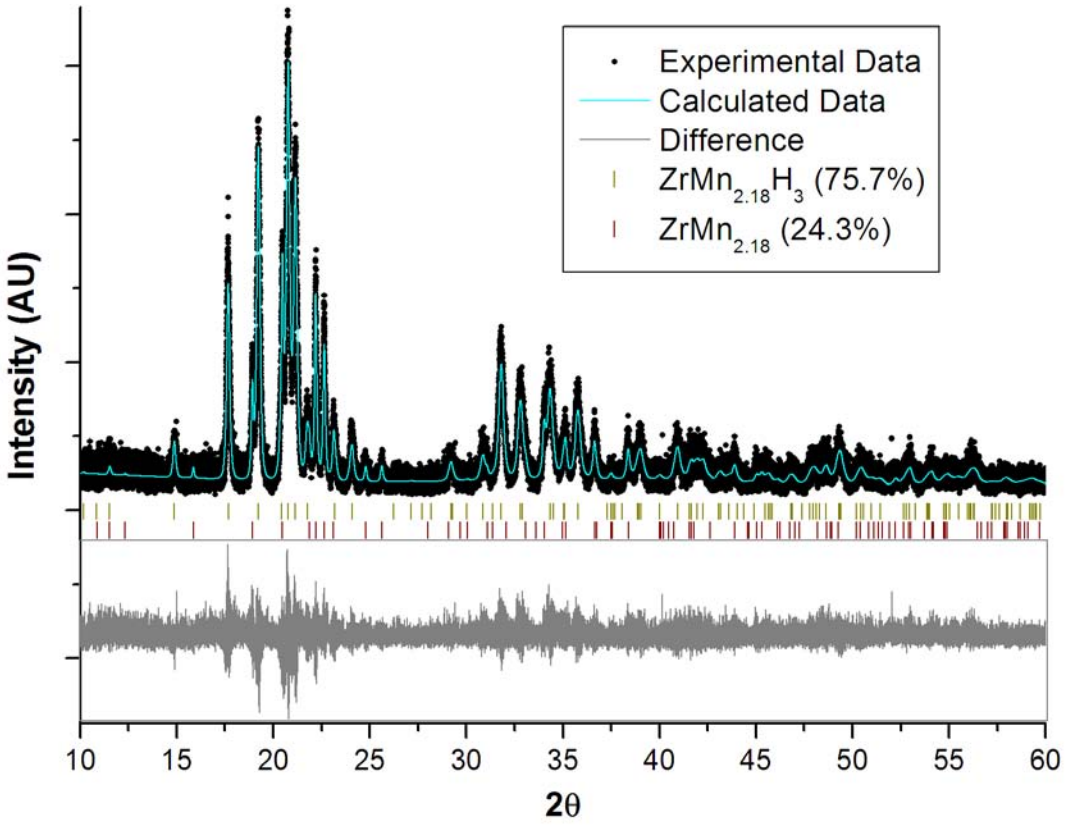

Figure A.6: *Room temperature synchrotron diffraction pattern for the hydrided* $ZrMn_{2.18} - H$ *sample, which was fitted with a mixture of phases, the ratios of which are in the legend. The major phase was C14* $ZrMn_{2.18}H_3$*, with the ticks marks shown at the bottom in dark yellow. A secondary* $ZrMn_{2.18}$ *phase was also fitted (tick marks in red). The difference plot between the experimental data (black points) and calculated fit (cyan line) is shown as a grey line in a box.* $R_{wP} =$ 16.685.

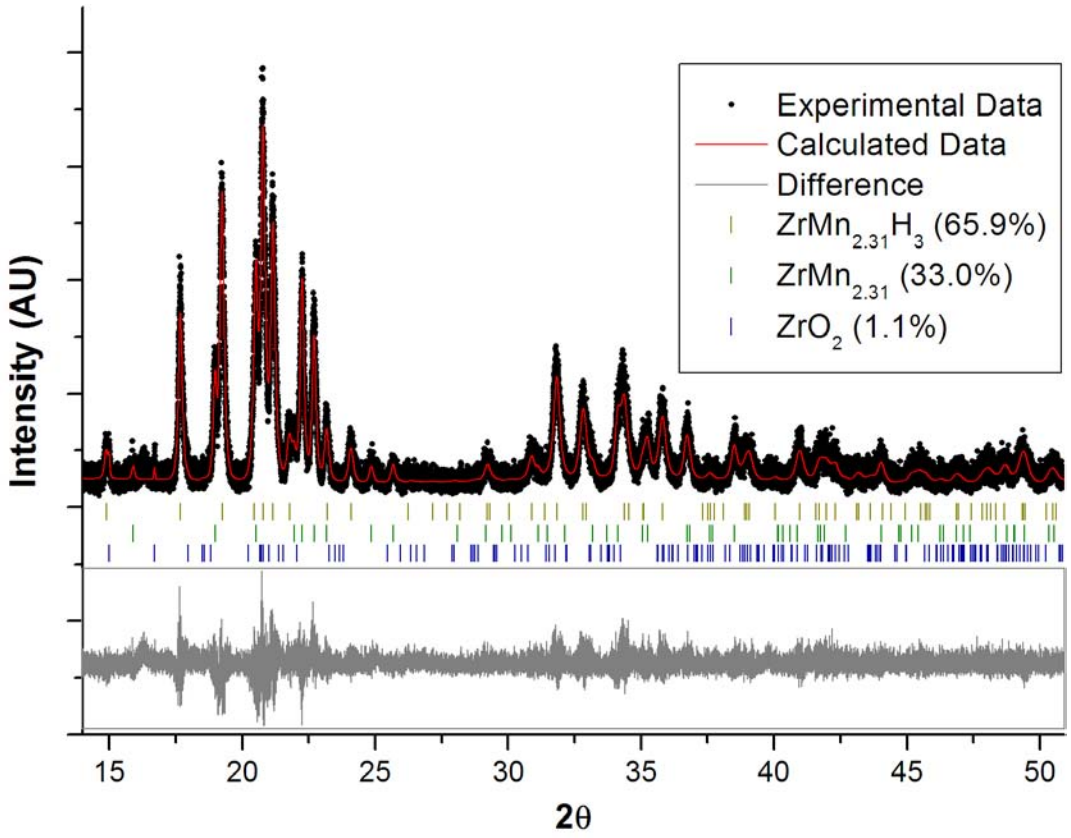

Figure A.7: *Room temperature synchrotron diffraction pattern for the hydrided* $ZrMn_{2.31} - H$ *sample, which was fitted with a mixture of phases, the ratios of which are given in the legend. The major phase was C14* $ZrMn_{2.31}H_3$*, with the ticks marks shown at the bottom in dark yellow. A secondary, hydrogen free phase of* $ZrMn_{2.31}$ *was also fitted (tick marks in green) along with a trace* ZrO_2 *impurity (tick marks in navy). The difference plot between the experimental data (black points) and calculated fit (red line) is shown as a grey line in a box.* $R_{wP} = 15.991$.

A.1.3 X-ray Diffraction Data for the cycled, dehydrided $ZrMn_{2+x}$ *(*$x = 0.13, 0.18, 0.31, 0.44$*) materials*

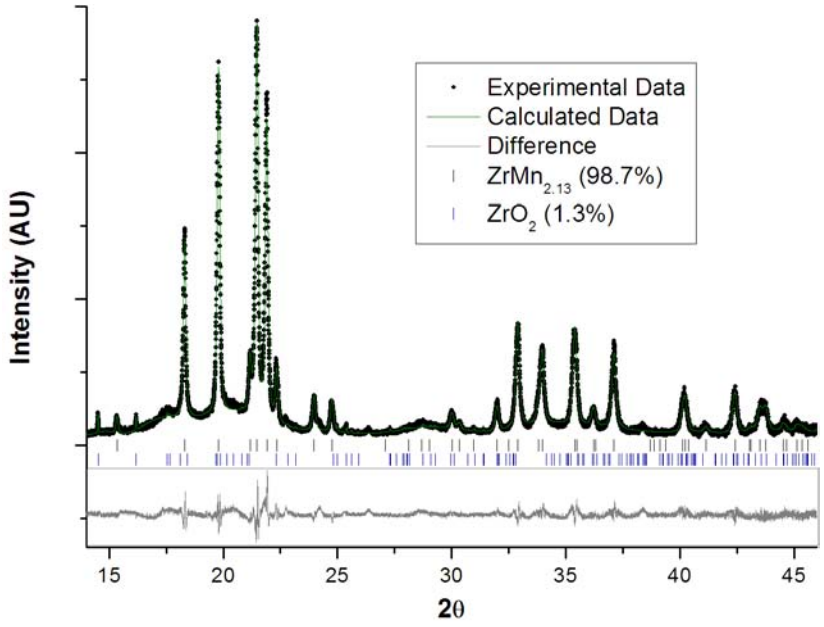

Figure A.8: *Room temperature synchrotron diffraction pattern for the cycled, dehydrided $ZrMn_{2.13}$, which was fitted with the C14 $ZrMn_{2.13}$ phase (ticks marks in black). A trace impurity of ZrO_2 was included, with tick marks for this phase shown in navy. The difference plot between the experimental data (black points) and calculated fit (green line) is shown as a grey line in a box.* $R_{wP} = 8.376$.

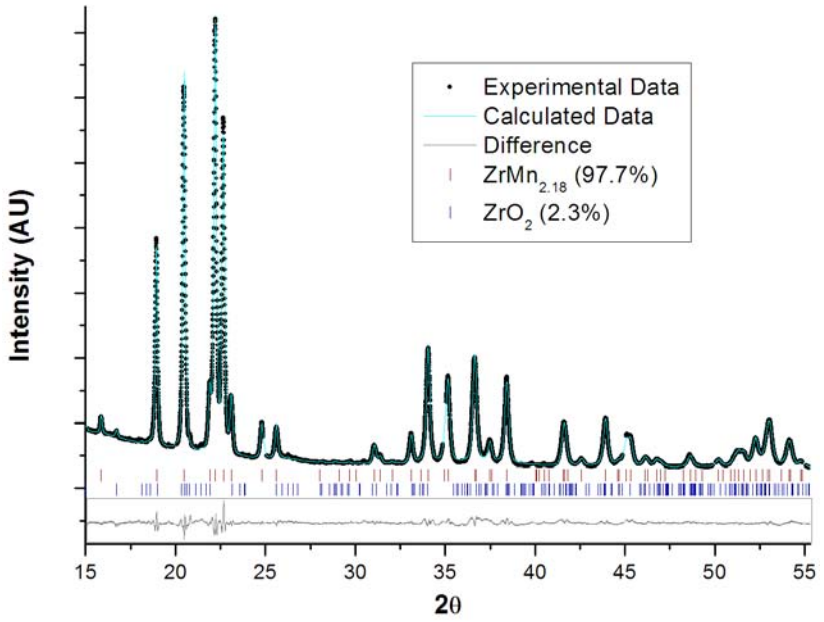

Figure A.9: *Room temperature synchrotron diffraction pattern for the cycled, dehydrided $ZrMn_{2.18}$, which was fitted with the C14 $ZrMn_{2.18}$ phase (ticks marks in red). A trace impurity of ZrO_2 was included, with tick marks for this phase shown in navy. The difference plot between the experimental data (black points) and calculated fit (cyan line) is shown as a grey line in a box.* $R_{wP} = 3.268$.

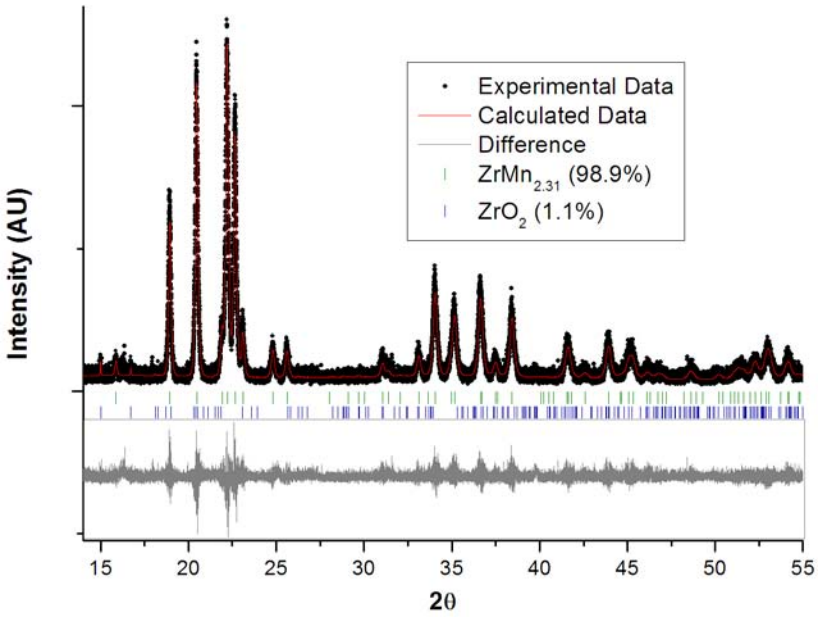

Figure A.10: *Room temperature synchrotron diffraction pattern for the cycled, dehydrided $ZrMn_{2.31}$, which was fitted with the C14 $ZrMn_{2.31}$ phase (ticks marks in green). A trace impurity of ZrO_2 was included, with tick marks for this phase shown in navy. The difference plot between the experimental data (black points) and calculated fit (red line) is shown as a grey line in a box.* $R_{wP} = 15.526$.

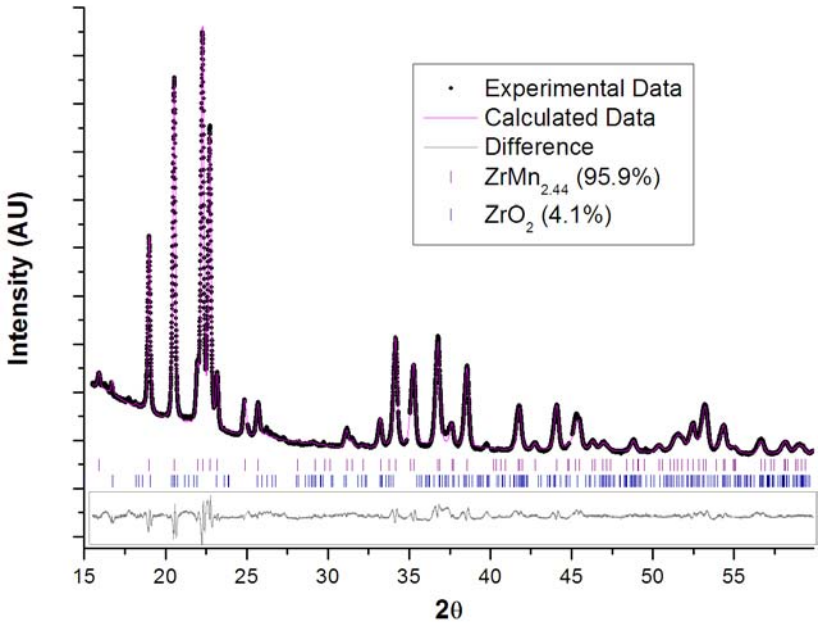

Figure A.11: *Room temperature synchrotron diffraction pattern for the cycled, dehydrided $ZrMn_{2.44}$, which was fitted with the C14 $ZrMn_{2.44}$ phase (ticks marks in purple). A trace impurity of ZrO_2 was included, with tick marks for this phase shown in navy. The difference plot between the experimental data (black points) and calculated fit (pink line) is shown as a grey line in a box.* $R_{wP} = 3.809$.

A.1.4 Neutron Diffraction Data for $ZrMn_{1.69}D_{2.63}$

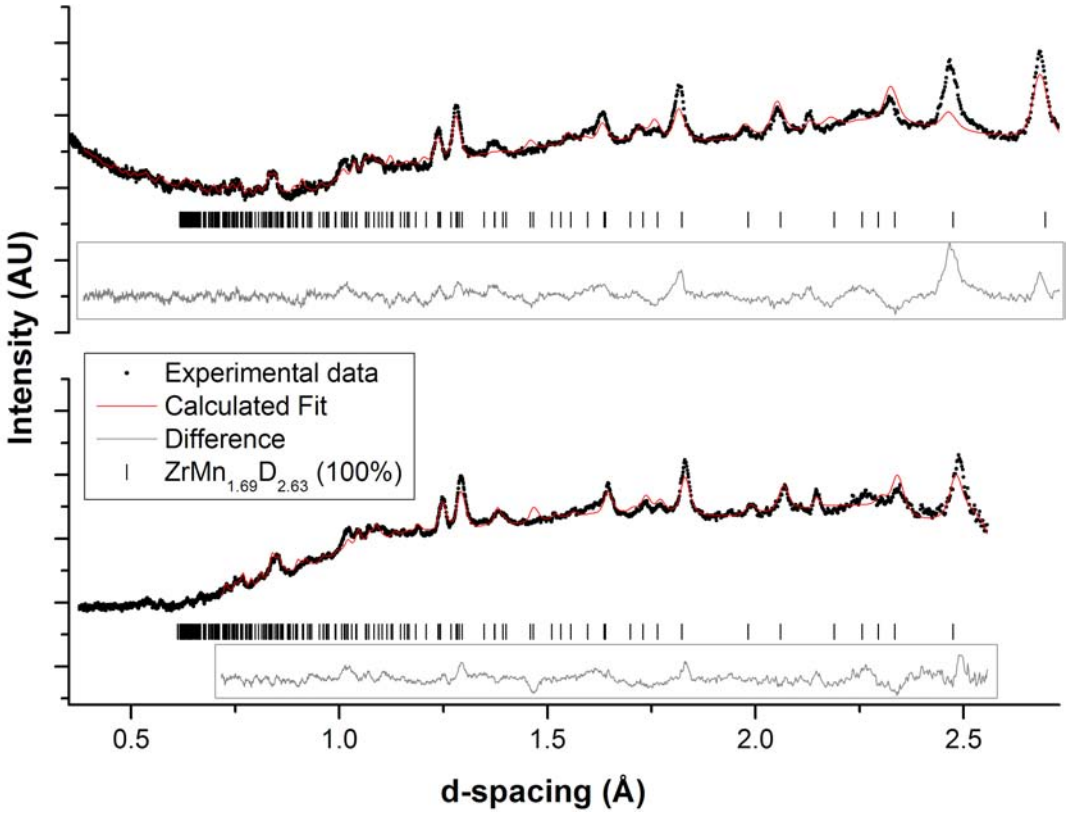

Figure A.12: *Experimental (black dots), calculated (red lines) and difference plots (grey lines enclosed in boxes) for the structural refinement of $ZrMn_{1.69}D_{2.63}$ from neutron diffraction data collected at 300 K at the ISIS GEM difractometer. Shown are data collected on banks 4 (top) and 5 (bottom). The Bragg peak positions of the major deuteride phase is shown by vertical tick marks.* $R_{wP} = 1.536$

A.2 Supplemental Hydriding Thermodynamic Data

A.2.1 Hydriding Pressures and Temperatures across the $ZrMn_{2+x}-H$ ($x = -0.35$, 0.06, 0.13, 0.18, 0.31, 0.44) systems

Plateau Pressure and Temperature in $ZrMn_{2+x}-H$					
$x = -0.35$	$x = 0.06$	$x = 0.13$	$x = 0.18$	$x = 0.31$	$x = 0.44$
	58.7°C	51.2°C		58.2°C	58.5°C
	0.348 bar	0.357 bar		1.53 bar	2.42 bar
		62.9°C		67.7°C	65.1°C
		0.449 bar		1.93 bar	3.76 bar
		71.1°C		71.8°C	78.6°C
		0.56 bar		2.00 bar	4.00 bar
		80.2°C		89.6°C	84.2°C
		0.752 bar		3.20 bar	4.33 bar
90.1°C	99.8°C	94.1°C	97.1°C	95.6°C	
0.499 bar	1.65 bar	1.71 bar	2.44 bar	3.33 bar	
104.9°C			107.3°C		
0.664 bar			2.85 bar		
117.9°C	120.0°C		112.1°C	117.0°C	
0.958 bar	2.04 bar		3.12 bar	4.45 bar	
132.1°C	125.7°C		126.5°C		
1.11 bar	2.38 bar		3.66 bar		

Table A.1: *Hydriding temperatures and concurrent plateau pressures for the $ZrMn_{2+x} - H$ systems with $x = -0.35, 0.06, 0.13, 0.18, 0.31, 0.44$. All measurements were taken at the hydriding plateau midpoint for fully cycled samples.*

A.3 Supplemental Magnetic Data

A.3.1 Inverse Susceptibility Data for the $ZrMn_{2+x}-H$ (x = 0.13, 0.18, 0.31, 0.44) systems

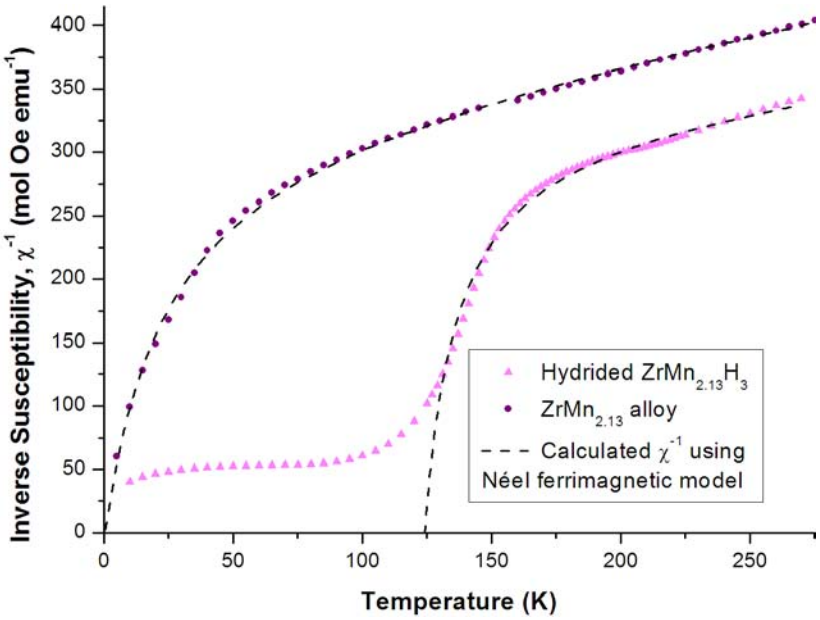

Figure A.13: *A plot of the temperature dependence of the inverse molar susceptibility for the $ZrMn_{2.13}$ alloy (purple dots) and cycled, hydrided $ZrMn_{2.13}H_3$ (pink triangles), both cooled in and then measured in a field of 1000 Oe. The dashed black lines are fits of the data to the Néel ferrimagnetism model.*

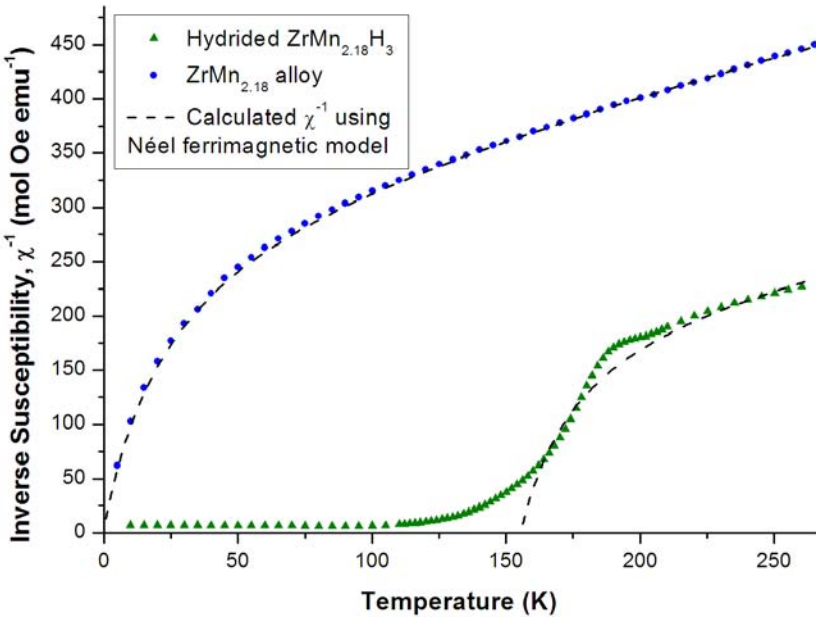

Figure A.14: *A plot of the temperature dependence of the inverse molar susceptibility for the $ZrMn_{2.18}$ alloy (blue dots) and cycled, hydrided $ZrMn_{2.18}H_3$ (green triangles), both cooled in and then measured in a field of 1000 Oe. The dashed black lines are fits of the data to the Néel ferrimagnetism model.*

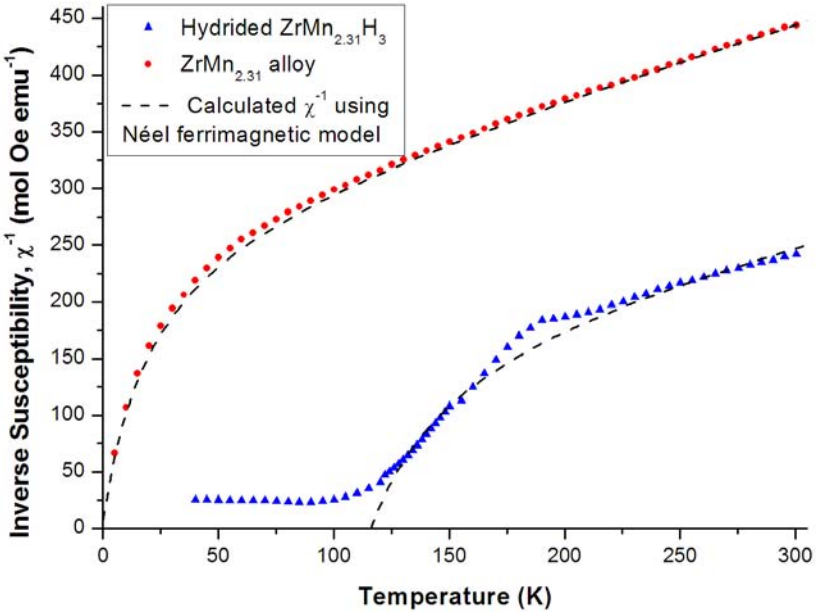

Figure A.15: *A plot of the temperature dependence of the inverse molar susceptibility for the $ZrMn_{2.31}$ alloy (red dots) and cycled, hydrided $ZrMn_{2.31}H_3$ (blue triangles), both cooled in and then measured in a field of 1000 Oe. The dashed black lines are fits of the data to the Néel ferrimagnetism model.*

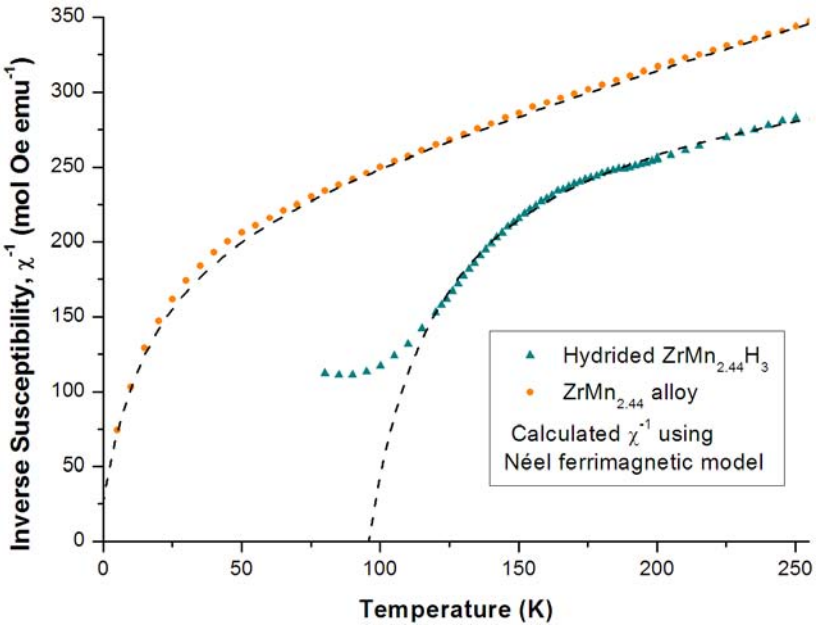

Figure A.16: *A plot of the temperature dependence of the inverse molar susceptibility for the $ZrMn_{2.44}$ alloy (orange dots) and cycled, hydrided $ZrMn_{2.44}H_3$ (cyan triangles), both cooled in and then measured in a field of 1000 Oe. The dashed black lines are fits of the data to the Néel ferrimagnetism model.*

A.3.2 Magnetic Hysteresis of the $ZrMn_{2+x}-H$ ($x = 0.13, 0.18, 0.44$) systems

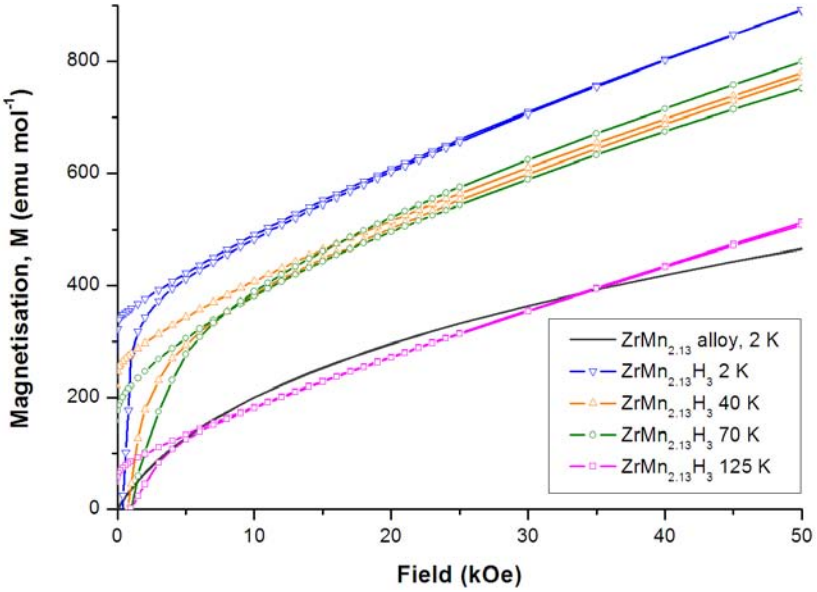

Figure A.17: *A hysteresis plot for cycled, hydrided $ZrMn_{2.13}H_3$, showing data from the first quadrant. The field dependence of the molar magnetisation (up to 50 kOe) is shown at 2 K, 40 K, 70 K and 125 K as indicated on the graph. For comparison, the field dependence of the alloy, $ZrMn_{2.13}$, at 2 K is shown as a gray line.*

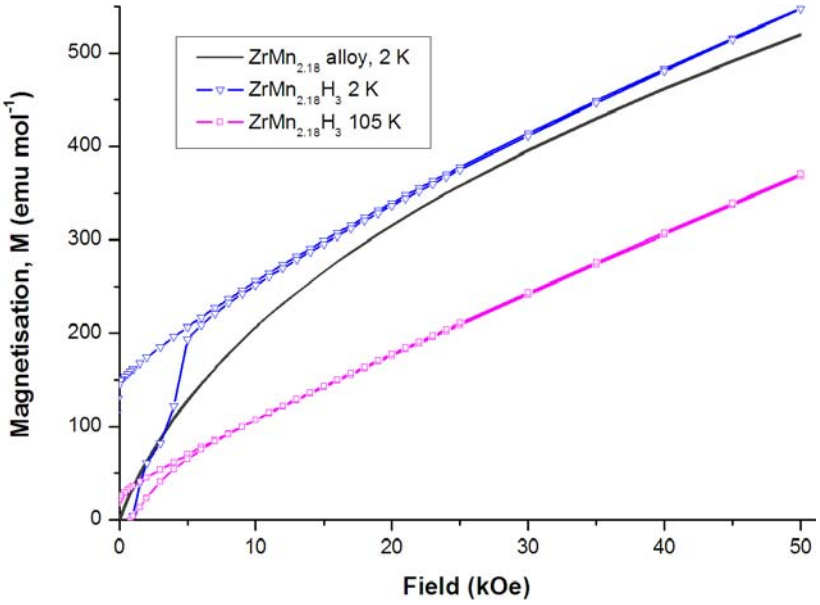

Figure A.18: *A hysteresis plot at several temperatures for cycled, hydrided $ZrMn_{2.18}H_3$, showing data from the first quadrant only. The field dependence of the molar magnetisation (up to 50 kOe) is shown at 2 K and 105 K as indicated on the graph. For comparison, the field dependence of the alloy, $ZrMn_{2.18}$, at 2 K is shown as a solid gray line.*

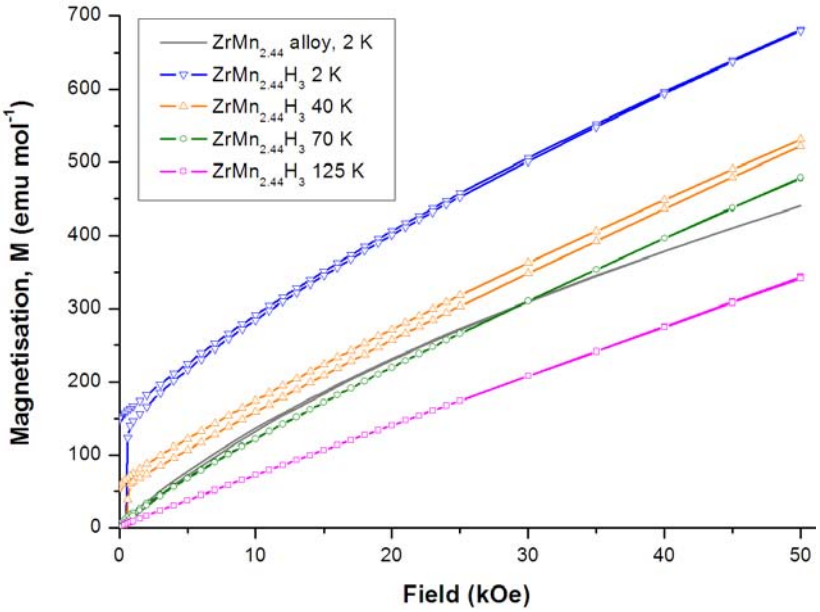

Figure A.19: *A hysteresis plot at several temperatures for cycled, hydrided $ZrMn_{2.44}H_3$, showing data from the first quadrant only. The field dependence of the molar magnetisation (up to 50 kOe) is shown at 2 K, 40 K, 70 K and 125 K as indicated on the graph. For comparison, the field dependence of the alloy, $ZrMn_{2.44}$, at 2 K is shown as a solid gray line.*